



University of Kentucky
UKnowledge

Theses and Dissertations--Mechanical
Engineering

Mechanical Engineering


2017

A PHYSICS-BASED APPROACH TO MODELING WILDLAND FIRE SPREAD THROUGH POROUS FUEL BEDS

Tingting Tang

University of Kentucky, wstc_ttt@live.com

Author ORCID Identifier:

 <http://orcid.org/0000-0003-2022-9884>

Digital Object Identifier: <https://doi.org/10.13023/ETD.2017.027>

[Right click to open a feedback form in a new tab to let us know how this document benefits you.](#)

Recommended Citation

Tang, Tingting, "A PHYSICS-BASED APPROACH TO MODELING WILDLAND FIRE SPREAD THROUGH POROUS FUEL BEDS" (2017). *Theses and Dissertations--Mechanical Engineering*. 84.
https://uknowledge.uky.edu/me_etds/84

This Doctoral Dissertation is brought to you for free and open access by the Mechanical Engineering at UKnowledge. It has been accepted for inclusion in Theses and Dissertations--Mechanical Engineering by an authorized administrator of UKnowledge. For more information, please contact UKnowledge@lsv.uky.edu.

STUDENT AGREEMENT:

I represent that my thesis or dissertation and abstract are my original work. Proper attribution has been given to all outside sources. I understand that I am solely responsible for obtaining any needed copyright permissions. I have obtained needed written permission statement(s) from the owner(s) of each third-party copyrighted matter to be included in my work, allowing electronic distribution (if such use is not permitted by the fair use doctrine) which will be submitted to UKnowledge as Additional File.

I hereby grant to The University of Kentucky and its agents the irrevocable, non-exclusive, and royalty-free license to archive and make accessible my work in whole or in part in all forms of media, now or hereafter known. I agree that the document mentioned above may be made available immediately for worldwide access unless an embargo applies.

I retain all other ownership rights to the copyright of my work. I also retain the right to use in future works (such as articles or books) all or part of my work. I understand that I am free to register the copyright to my work.

REVIEW, APPROVAL AND ACCEPTANCE

The document mentioned above has been reviewed and accepted by the student's advisor, on behalf of the advisory committee, and by the Director of Graduate Studies (DGS), on behalf of the program; we verify that this is the final, approved version of the student's thesis including all changes required by the advisory committee. The undersigned agree to abide by the statements above.

Tingting Tang, Student

Dr. James M. McDonough, Major Professor

Dr. Haluk E. Karaca, Director of Graduate Studies

A PHYSICS-BASED APPROACH TO MODELING WILDLAND FIRE SPREAD
THROUGH POROUS FUEL BEDS

DISSERTATION

A dissertation submitted in partial
fulfillment of the requirements for
the degree of Doctor of Philosophy
in the College of Engineering at the
University of Kentucky

By
Tingting Tang
Lexington, Kentucky

Director: Dr. James M. McDonough, Professor of Mechanical Engineering and
Mathematics
Lexington, Kentucky 2017

Copyright© Tingting Tang 2017

ABSTRACT OF DISSERTATION

A PHYSICS-BASED APPROACH TO MODELING WILDLAND FIRE SPREAD THROUGH POROUS FUEL BEDS

Wildfires are becoming increasingly erratic nowadays at least in part because of climate change. CFD (computational fluid dynamics)-based models with the potential of simulating extreme behaviors are gaining increasing attention as a means to predict such behavior in order to aid firefighting efforts. This dissertation describes a wildfire model based on the current understanding of wildfire physics. The model includes physics of turbulence, inhomogeneous porous fuel beds, heat release, ignition, and firebrands. A discrete dynamical system for flow in porous media is derived and incorporated into the subgrid-scale model for synthetic-velocity large-eddy simulation (LES), and a general porosity-permeability model is derived and implemented to investigate transport properties of flow through porous fuel beds. Note that these two developed models can also be applied to other situations for flow through porous media. Simulations of both grassland and forest fire spread are performed via an implicit LES code parallelized with OpenMP; the parallel performance of the algorithms are presented and discussed. The current model and numerical scheme produce reasonably correct wildfire results compared with previous wildfire experiments and simulations, but using coarser grids, and presenting complicated subgrid-scale behaviors. It is concluded that this physics-based wildfire model can be a good learning tool to examine some of the more complex wildfire behaviors, and may be predictive in the near future.

KEYWORDS: CFD, LES, wildfire modeling, fire spread, porous media

Author's signature: Tingting Tang

Date: February 14, 2017

A PHYSICS-BASED APPROACH TO MODELING WILDLAND FIRE SPREAD
THROUGH POROUS FUEL BEDS

By
Tingting Tang

Director of Dissertation: James M. McDonough

Director of Graduate Studies: Haluk Karaca

Date: February 14, 2017

To my dearest family

ACKNOWLEDGMENTS

Professor James McDonough, for being a great academic advisor and supporting me through these years. In particular, for his most grateful assistance in building up CFD knowledge, developing research skills, and improving scientific writing.

My Committee members: Professors Kozo Saito, Sean Bailey, Jian Yang, and Peter Hislop, for supporting and helpfully guiding me academically and professionally.

Professor Alexandre Martin and fellow students, for creating a cozy lab to stay in, and for their friendship and academic support.

My husband, Zhiyong Li, for loving, supporting, and caring for me through these wonderful years, and for spending lots of time discussing the code problems that I had encountered.

My parents Xuehong Tang and Hui Hu, for their endless love, support, and encouragement throughout my life. My grandparents, aunts, uncles, and cousins on both sides deserve my wholehearted thanks as well.

Lastly, all my lovely friends, for understanding and encouragement, and for making my life a wonderful experience.

TABLE OF CONTENTS

Acknowledgments	iii
Table of Contents	iv
List of Tables	vii
List of Figures	viii
Chapter 1 Introduction	1
Chapter 2 Review of Wildfire Spread Studies	10
2.1 Wildfire spread physics	10
2.1.1 Fuel	11
2.1.2 Ignition	13
2.1.3 Heat transfer	16
2.1.4 Turbulence and fire whirls	18
2.2 Wildfire spread modeling	21
2.2.1 Empirical modeling	25
2.2.2 Quasi-empirical modeling	25
2.2.3 Quasi-physical modeling	27
2.2.4 Detailed physical and multiphase modeling	28
2.2.5 Simulation and mathematical analogue modeling	31
2.2.6 RANS modeling—overview	32
2.2.7 Large-eddy simulation—overview	35
2.3 Summary and conclusions	39
Chapter 3 The Wildfire Spread Model	41
3.1 Governing equations and model features	42
3.2 Synthetic-velocity large-eddy simulation	45
3.2.1 Explicit filtering	46
3.2.2 Small-scale calculations	49
3.2.3 The complete solution	52
3.3 Porosity of fuel beds	54
3.4 Heat release rate	59
3.5 Ignition modeling	65
3.6 Firebrands	70
3.6.1 Firebrand trajectories	72
3.6.2 Firebrand heat transfer and combustion	73
3.7 Summary and conclusions	76

Chapter 4	The Solver	78
4.1	Projection methods	79
4.2	Grid generation	82
4.3	Solution and parallelization of the momentum equations	84
4.3.1	δ -form quasilinearization	86
4.3.2	Spatial discretization	88
4.3.3	Douglas and Gunn time-splitting	90
4.4	Solution and parallelization of the pressure Poisson equation	92
4.4.1	Analysis	93
4.4.2	Jacobi iteration method	97
4.4.3	Point SOR and red-black SOR iteration methods	100
4.5	Parallel performance of the solver with OpenMP	108
4.6	Summary and conclusions	111
Chapter 5	The Poor Man's Navier-Stokes Equations in Porous Media	114
5.1	Analysis	115
5.1.1	Flow regime analysis	115
5.1.2	Derivation	117
5.1.3	Bifurcation analysis	124
5.2	Bifurcation results for variation of β	125
5.3	Bifurcation results for variation of λ and μ	133
5.3.1	Isotropic porous media	133
5.3.2	Anisotropic porous media	136
5.3.3	Sensitivity to initial conditions	139
5.4	Summary and conclusions	143
Chapter 6	A Theoretical Model for the Porosity-Permeability Relationship	145
6.1	Analysis	147
6.1.1	Derivation of permeability formula	148
6.1.2	Further discussion	152
6.2	Lid-driven cavity problem	154
6.2.1	Verification	155
6.2.2	General model results	158
6.3	The natural convection problem	163
6.3.1	Verification	164
6.3.2	General model results	168
6.4	Summary and conclusions	172
Chapter 7	Computations of Wildfire Spread	174
7.1	Numerical details	174
7.2	Grassland fire (simulation 1)	180
7.3	Forest fire	185
7.3.1	Flat terrain (simulation 2)	185
7.3.2	Realistic terrain (simulation 3)	192

7.4	Forest fire with firebrands (simulation 4)	198
7.5	Summary and conclusions	205
Chapter 8	Final Summary, Conclusions and Future Work	207
8.1	Summary	207
8.2	Conclusions	208
8.3	Future work	210
Appendix		213
	Source code for PPE parallelization	213
Bibliography		215
Vita		235

LIST OF TABLES

1.1	Historically significant wildland fires. Data extracted from Statista [6]. .	3
2.1	Fire models. Information extracted from [60].	30
3.1	Stand descriptions of typical forests.	56
3.2	Branch information for deciduous and coniferous trees.	58
3.3	Summary of estimates.	60
3.4	Properties of a typical trunk fuel grid cell.	62
3.5	Properties of a typical canopy fuel grid cell.	64
3.6	Properties of a typical grass fuel grid cell.	65
6.1	Grid function convergence test	156
6.2	Estimation of flow regimes [219]	159
6.3	Comparison of present results with benchmark data from [243]	165
7.1	Summary of the different numerical conditions used for each simulation (Sim.) conducted in this study.	178
7.2	Firebrand properties.	199

LIST OF FIGURES

1.1	A prescribed burn in Canada. Photograph by Cameron Strandberg, distributed under a CC-BY 2.0 license.	2
1.2	A wildfire burns in the Sierra National Forest in the U. S. [2]. Used with permission.	2
1.3	U. S. wildfire statistics. Data extracted from the website of the National Interagency Fire Center.	4
1.4	Overview of wildland fire studies	5
1.5	Sketch of forest fire spread.	8
2.1	Classification of current existing wildfire models.	22
2.2	Summary of current existing wildfire models according to relation with fuel, atmosphere or fire [63]. Used with permission.	23
3.1	Description of a typical forest model.	54
3.2	Description of cells in one large-scale grid cell.	68
3.3	Flow chart of the ignition module.	69
4.1	Sketch of 3-D staggered gridding.	85
4.2	Jacobi iteration for 101^3 grid-point problem: number of cores vs. (a) speedup; (b) elapsed time.	98
4.3	Jacobi iteration in Fortran: problem size vs. efficiency with different number of cores.	99
4.4	Number of cores vs. speedup for 101^3 grid-point problem: (a) point SOR; (b) red-black ordered SOR.	102
4.5	Number of cores vs. elapsed time for 101^3 grid-point problem: (a) point SOR; (b) red-black ordered SOR.	103
4.6	Required iterations vs. problem size for optimal SOR.	104
4.7	Point-SOR for 201^3 grid-point problem: number of cores vs. (a) speedup; (b) elapsed time.	105
4.8	Red-black ordering SOR for 201^3 grid-point problem: number of cores vs. (a) speedup; (b) elapsed time.	105
4.9	Problem size vs. efficiency with different number of cores in Fortran: (a) point SOR; (b) red-black ordered SOR.	106
4.10	Parallel Performance of (a) PPE solver and (b) momentum equation . . .	109
5.1	Relationship between friction factor and Reynolds number [219].	116
5.2	Regime map of β vs. λ_1 . (a) color table, (b) $\gamma = -0.03$, $\lambda_1 = \mu_1$, $\lambda_2 = 0.02$, $\mu_2 = 0.01$, $\lambda_3 = 1.2$, $\mu_3 = 1$	125
5.3	Regime map zoom-ins of Figure 5.2(b). (a) $(\beta, \lambda_1) \in [3, 4] \times [2.5, 3.5]$, (b) $(\beta, \lambda_1) \in [3.16, 3.56] \times [2.7, 2.95]$	126

5.4	Example power spectrum of the 12 non-trivial types of behavior: (a) periodic; (b) periodic w/ different fundamental; (c) subharmonic; (d) phase lock; (e) quasiperiodic; (f) noisy subharmonic; (g) noisy phase lock; (h) noisy quasiperiodic w/ fundamental; (i) noisy quasiperiodic w/o fundamental; (j) broadband w/ fundamental; (k) broadband w/ different fundamental; (l) broadband w/o fundamental.	127
5.5	Example time series of the 12 non-trivial types of behavior: (a) periodic; (b) periodic w/ different fundamental; (c) subharmonic; (d) phase lock; (e) quasiperiodic; (f) noisy subharmonic; (g) noisy phase lock; (h) noisy quasiperiodic w/ fundamental; (i) noisy quasiperiodic w/o fundamental; (j) broadband w/ fundamental; (k) broadband w/ different fundamental; (l) broadband w/o fundamental.	129
5.6	Regime map of β vs. λ_1 . (a) $\gamma = -0.03$, $\lambda_1 = \mu_1$, $\lambda_2 = 0.02$, $\mu_2 = 0.002$, $\lambda_3 = 0.2$, $\mu_3 = 0.02$, (b) zoom in for $(\beta, \lambda_1) \in [2.4, 3.7] \times [2.2, 3.0]$.	130
5.7	Regime map of β vs. γ : (a) $\lambda = \mu = 0$, with $(\Delta\beta, \Delta\lambda_1) = (0.0015, 0.00154)$; (b) $\lambda = 0.2, \mu = 0.02$, with $(\Delta\beta, \Delta\lambda_1) = (0.00148, 0.00133)$; (c) $\lambda = \mu = 0.2$, with $(\Delta\beta, \Delta\lambda_1) = (0.00095, 0.00078)$	132
5.8	Regime maps of λ vs. μ . (a) color table, (b) $\beta_1 = 3.9$, $\beta_2 = 3.87$, $\beta_3 = 3.1$, $\gamma_{12} = \gamma_{13} = \gamma_{21} = \gamma_{23} = 0.3$, $\gamma_{31} = -0.5$, $\gamma_{32} = -0.02$, (c) $\beta = 3.8$, $\gamma = -0.01$, (d) $\beta = 2.5$, $\gamma = -0.48$	134
5.9	Regime maps of λ_1 vs. μ_1 . (a) $\lambda_2 = 0.01$, $\mu_2 = 0.01$, $\lambda_3 = 0.2$, $\mu_3 = 0.3$, (b) $\lambda_2 = 0.02$, $\mu_2 = 0.02$, $\lambda_3 = 1.2$, $\mu_3 = 1.2$	136
5.10	Regime maps of λ_1 vs. λ_3 . (a) $\lambda_2 = \mu_2 = 0.02$, $\mu_1 = \lambda_1$, $\mu_3 = \lambda_3$, (b) $\lambda_2 = 0.02$, $\mu_2 = 0.01$, $\mu_1 = 0.1$, $\mu_3 = \lambda_3$	138
5.11	Behavior of quasiperiodic w/o fundamental for slightly perturbed initial conditions: (a)–(f) time series; (g) & (l) phase portraits.	139
5.12	Behavior of broadband w/o fundamental for slightly perturbed initial conditions: (a)–(f) time series; (g) & (l) phase portraits.	140
5.13	Basins of attraction for bifurcation parameters in (a) Figure 5.11, (b) Figure 5.12.	142
5.14	Time series for large perturbation of initial conditions. Bifurcation parameter values corresponding to (a) & (b) Figure 5.11, (c)&(d) Figure 5.12.	142
6.1	Relationship between entropy production rate and permeability.	152
6.2	Sketch of the 3-D lid-driven cavity problem.	155
6.3	Velocity profiles computed with three different grids: (a) $Re = 100$; (b) $Re = 400$	156
6.4	Velocity profiles through the cavity center, solid lines are calculated solutions and symbols are benchmark solutions [241]: (a) u component along the vertical center line; (b) v component along the horizontal center line.	157
6.5	Velocity profiles for different constant permeabilities, solid lines are calculated solutions, and symbols are solutions from [240]: (a) u component along the vertical center line; (b) v component along the horizontal center line.	158

6.6	Velocity profiles through the cavity center for LDC flow in different porosity media: (a) u component along the vertical line; (b) v component along the horizontal line.	160
6.7	Velocity streamlines in the middle x - y plane.	160
6.8	Permeability (log-scale) and strain rate through the cavity center computed with permeability model and successively increasing porosity: (a) permeability; (b) strain rate.	161
6.9	Permeability distributions (log-scale) of lid driven cavity flows through different porous media in the middle x - y plane.	162
6.10	Strain rates of lid driven cavity flows through different porous media in the middle x - y plane.	163
6.11	Sketch of the cubicle natural convection problem.	163
6.12	Flow patterns for convective flow compared with cite, from left to right: velocity streamlines, u component velocity, v component velocity, temperature.	166
6.13	Streamline, u -component velocity, v -component velocity, isothermal patterns for different Darcy and Rayleigh numbers.	167
6.14	(a) Velocity and (b) temperature profiles through the cavity center for convective flow through different porosity media.	168
6.15	Flow patterns for convective flow through different porous media, from left to right: velocity streamline, u -component velocity, v -component velocity, temperature.	169
6.16	(a) Permeability and (b) strain rate through the cavity center for convective flow through different porosity media.	170
6.17	Permeability of cubicle convective flow through different porosity media in the middle x - y plane, $Ra = 10^4$	171
6.18	Strain rate of cubicle convective flow through different porosity media in the middle x - y plane, $Ra = 10^4$	172
7.1	Profiles of (a) leaf area density a_f ; (b) corresponding permeability values.	176
7.2	Sketch of the computational domain used in this study.	178
7.3	Iso-surfaces of temperature (transparency): 63 °C (87.5%), 100 °C (75%), 160 °C (75%), 230 °C (62.5%), 500 °C (0%), 600 °C (0%) for fire burn at (a) 5 seconds; (b) 40 seconds; (c) 60 seconds; (d) 130 seconds.	181
7.4	Flow field in the x - y plane at $t = 130$ seconds and $z = 100$ m in correspondence of part (d) of Fig. 7.3: (a) Temperature contours and velocity vectors; (b) subgrid-scale streamlines.	182
7.5	Top view of grassfire burn with ignitions lines of (a)(b) 25 m; (c)(d) 50 m; (e)(f) 100 m at 60 seconds (left) and 120 seconds (right).	184
7.6	Iso-surfaces of temperature (transparency): 63 °C (87.5%), 100 °C (75%), 160 °C (75%), 230 °C (62.5%), 500 °C (0%), 600 °C (0%) for fire burn at (a) 10 seconds; (b) 60 seconds; (c) 120 seconds; (d)–(f) 180 seconds; (e) canopy at $y = 6.54$ m; (f) canopy at $y = 12.66$ m.	186

7.7	(a) Velocity vectors in forest for cold flow. Temperature contours and velocity vectors in the x - y planes of (a)(b) $z = 100$ m (top), (c)(d) $z = 50$ m (bottom) at (a)(c) 120 seconds (left) and (b)(d) 180 seconds (right). .	189
7.8	(a) Subgrid-scale streamlines at time 180 seconds and $z = 100$ m; (b) zoom-in of (a).	191
7.9	(a) Terrain viewed from $z+$; (b) terrain viewed from $x+$; (c) computational domain and grids	193
7.10	Iso-surfaces of temperature (transparency): 63°C (87.5%), 100°C (75%), 160°C (75%), 230°C (62.5%), 500°C (50%), 800°C (0%) for canopy fire burn at times: (a) 6 seconds; (b) 80 seconds; (c) 160 seconds; (d) 220 seconds.	195
7.11	Small-scale behaviors at $z=145$ m: (a) Small-scale temperature contours; (b) Small-scale streamlines.	197
7.12	Firebrand trajectories (200) at 100 sec. of simulation 4: (a) 3-D depiction of firebrands with coloring in travel time (second); iso-surfaces of temperature (transparency): 100°C (75%), 160°C (75%), 230°C (62.5%), 500°C (0%), 600°C (0%) (b) side view of the trajectories with coloring in temperature; (c) top view of the trajectories with coloring in mass. . . .	200
7.13	Firebrand trajectories (200) at 150 s of simulation 4: (a) 3-D depiction of firebrands with coloring in travel time (second); iso-surfaces of temperature (transparency): 100°C (75%), 160°C (75%), 230°C (62.5%), 500°C (0%), 600°C (0%) (b) side view of the trajectories with coloring in temperature; (c) top view of the trajectories with coloring in mass. . . .	202
7.14	3-D depiction of 20 firebrand trajectories with iso-surfaces of temperature (transparency): 100°C (75%), 160°C (75%), 230°C (62.5%), 500°C (0%), 600°C (0%): (a) in fixed flow field at 100 s with coloring in travel time; (b) in flow field at 20 s with coloring in temperature; (c) in flow field at 40 s with coloring in temperature.	204

Chapter 1: Introduction

Wildland fire is a general term describing any non-structure fire that occurs in a natural landscape such as a forest, grassland, or tundra which consumes natural fuels and spreads based on environmental conditions (e.g., wind, topography). According to the Fire Executive Council [1], wildland fires are categorized into two distinct types: (1) wildfires; and (2) prescribed fires. Wildfires can be either unplanned ignitions, such as fire caused by lightning, volcanoes, unauthorized and accidental human-caused fires (e.g., arson or campfires), or escaped prescribed fires. A wildfire can also occur in the wildland-urban interface (WUI) where structures and other human developments intermingle with undeveloped wildland or vegetation fuels. On the other hand, prescribed fires or controlled burns are, by definition, planned ignitions. A prescribed burning is designed to allow a naturally occurring fire to play its role in the ecosystem, such as to control insect pests, remove exotic species, and encourage the growth of fire-dependent species.

Figure 1.1 shows a prescribed fire conducted north of Highway 11, Alberta, Canada, in June 2009, courtesy of Cameron Strandberg. It was intended to bring about greater diversity, prevent the spread of mountain pine beetles, and create a fire barrier for any future wildfires. The massiveness and intensity of a typical forest fire are clearly seen in this figure. The bright yellow cylindrical part within the fire plume in the middle-right of the figure is possibly a fire whirl, which is typically about the same height of the trees around it but can be much larger. Also, it is seen, from the trees immersed in the intensively burning fires, that the tree leaves or needles are consumed much faster than the tree trunks and branches. These phenomena can also be observed in an uncontrollable wildfire.

Figure 1.2 shows a human-caused wildfire burning in the Sierra National Forest,



Figure 1.1: A prescribed burn in Canada. Photograph by Cameron Strandberg, distributed under a CC-BY 2.0 license.

U. S., in August 2014, photographed by Palley [2]. One can see that the large-scale fire on the hills spreads from east to west with a shape of the fire plume largely affected by wind and topography, and that the fire seemingly burns more intensely and spreads faster when climbing up the hills due to the updraft buoyancy.



Figure 1.2: A wildfire burns in the Sierra National Forest in the U. S. [2]. Used with permission.

Non-prescribed wildfires also contribute to the balance of ecosystems, but essentially all are suppressed for safety reasons in accord with the long-standing U. S. fire policy [1]. Clearly, wildfires are two-edged swords that promote various vegetation species and ecosystems, but also threaten human lives and property yearly around the world, especially those in the WUI where more and more people now often choose to live, according to Stein et al. [3]. For instance, Guha-Sapir et al. [4] provided the statistics that in 2011, wildfires, along with flood and extreme temperatures, caused over 55,800 deaths in Russia. Extreme fire behaviors such as fire whirls, as studied by Emori and Saito [5] and others, pose a considerable safety hazard to firefighters through increased fire intensity, spot fire frequency, and erratic spread rate. In 2013, the Yarnell Hill fire in Arizona, U. S., killed 19 elite firefighters due to unpredicted spread rate and direction. Statista [6] presents several severe fire events with a number of fatalities during the past hundred years, as shown in Table 1.1. These events took place in different countries, in different months, and on various landscapes, but they usually occur under rather dry and hot weather conditions in summer or fall. Also, forest fires have higher possibility to be disastrous in most of the countries except for Australia, where there are more dry grasslands.

Table 1.1: Historically significant wildland fires. Data extracted from Statista [6].

Date	Fire	Location	Number of fatalities
Oct. 1918	forest fire	United States	1000
Feb. 1983	scrub/grassland fire	Australia	75
May 1987	forest fire	China	191
Sept. 1997	forest fire	Indonesia	240
Aug. 2007	forest fire	Greece	65
Feb. 2009	bush/brush fire	Australia	180

While these fires have not resulted in a large number of fatalities (but still a significant number) compared with other catastrophic tragedies, the area of burned land and economic impact have been significant. Figure 1.3 shows statistics for acres

burned and suppression costs from 2011 to 2015. It is seen that both lightning and human behaviors have caused at least 1 million acres burned every year. Lightning occupies a relatively large portion of land burned since 2012 and had reached 8 million acres by the end of 2015, when the total acres burned are approximately 10 million—the highest in U. S. history. Correspondingly, firefighting costs have soared.

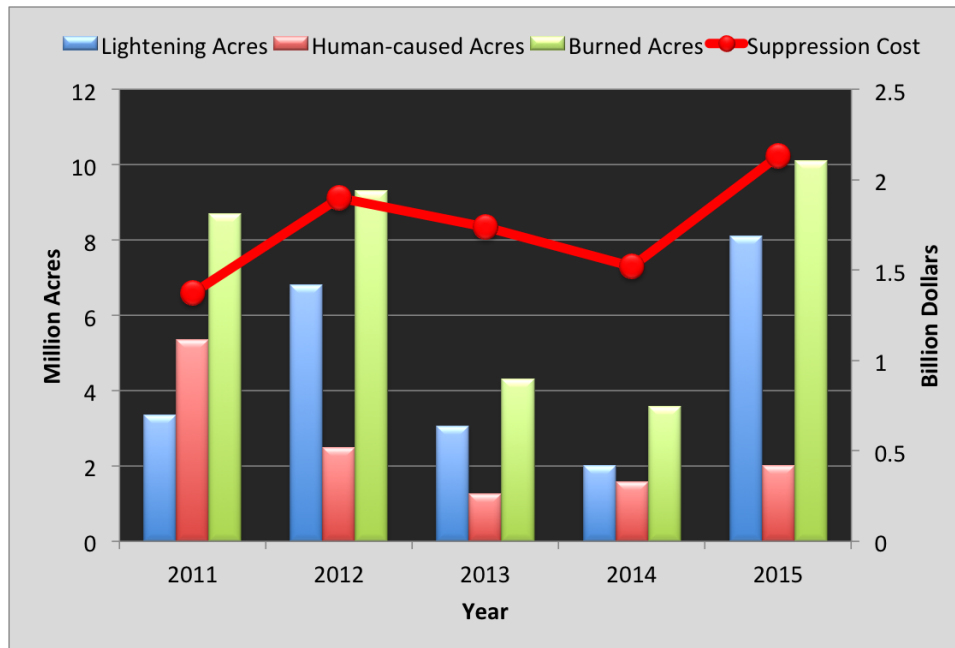


Figure 1.3: U. S. wildfire statistics. Data extracted from the website of the National Interagency Fire Center.

As shown by the red line in Fig. 1.3, the federal firefighting costs (suppression only) have reached more than \$2 billion in 2015. In fact, as summarized by Stephens et al. [7] and Topik [8], the total cost for fire suppression had already exceeded \$2 billion in 2012; federal appropriations for fire suppression and fire operations zoomed from about \$600 million in 1995 to nearly \$3 billion in 2014; and it was said in 2015 that the U. S. Forest Service would spend over 50% of its budget on fire management. One reason for such increasingly intense, dangerous, and expensive fires in the U. S. may be its century-long policy to put out all fires, according to Tullis [9]. In particular, accumulation of dead wood and unburned “ladder fuels” resulting from

fire extinguishment can turn lower-intensity ground fires into hotter canopy fires that are more destructive [9]. Furthermore, Stephens [10] investigated the diverse forest types and conditions in the U. S., and concluded that climate change could have also contributed to increased wildfire area from 1940 to 2000. Wildfires of a size and intensity that only a decade ago were rare are now almost an annual occurrence. In coming decades, with climate warming, forests around the world will likely undergo major landscape-scale vegetation changes, and a better fire policy is called for to respond to such diversity [7].

The study of wildland fires covers a broad range of disciplines. As shown in Fig. 1.4, it is mainly divided into three categories: fire ecology, fire management, and fire behavior. Fire ecology concentrates on the origin of a wildfire and its relationship to the living and non-living environment that surrounds it. Ecologists or foresters

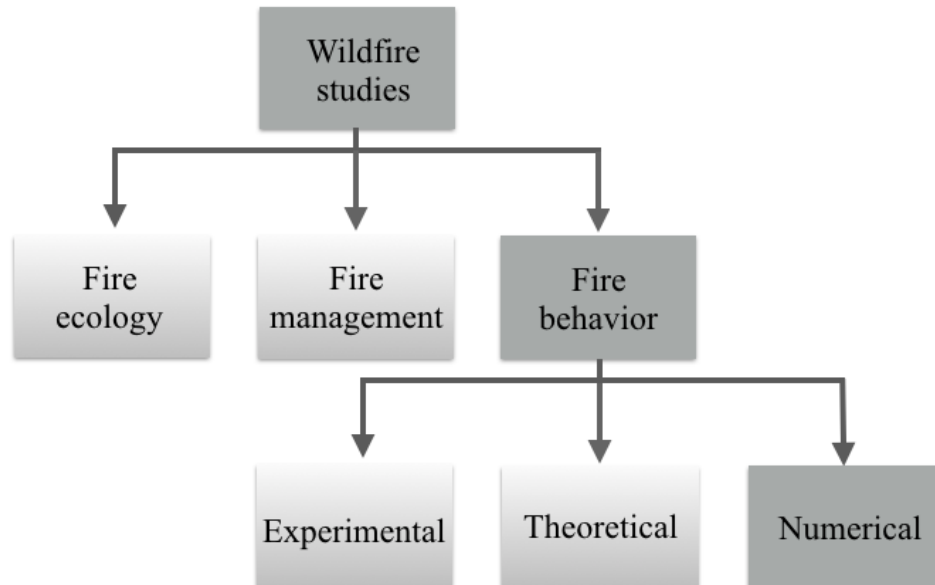


Figure 1.4: Overview of wildland fire studies

usually focus research on fire dependence and adaptation of plants and animals, fire history, fire regimes, and fire effects on ecosystems. Fire management, as suggested by the term, refers to developing tools and/or making policies to effectively and

efficiently manage fires for the sake of society, economy, and ecosystems. Traditional approaches to wildland fire studies are mostly developed in the area of fire ecology and management, which put more emphasis on ecological responses to fire rather than the physical processes of fire itself. Since the 1950s, literature regarding fire behavior has been growing in journals of engineering, geophysics, meteorology, etc. This relatively modern research is more technical in areas, such as combustion, fluid mechanics, heat transfer, and thermodynamics. A comprehensive review as a bridge between traditional and specialized studies was provided by Miyanishi [11].

There are three main techniques for the study of fire behavior: experimental, theoretical/analytical and numerical. Both laboratory and field experiments on fire spread have been performed in the past several decades. They provide physically reliable data for analysis and contribute to the theory of fire spread. For instance, field experiments such as the International Crown Fire Modeling Experiment (ICFME), as introduced by Stocks et al. [12], provide valuable data and insights into the characteristics of crown fires and help to develop better forest fire modeling, such as those investigated by Linn et al. [13]. Scale modeling also plays an important role in designing experiments and theory development. However, it is always difficult and expensive to conduct experimental research on fire spread at the mesoscale, which is usually the size of a real forest fire. Numerical approaches, as adopted in the present study, can be less costly and can model realistic large-scale fires. However, they are heavily based on the (as yet, incomplete) knowledge of physics of fire and sometimes can produce non-physical results. Theoretical approaches are more mathematical and are closely related to both experimental and numerical results.

This dissertation mainly deals with fire behaviors in the fire spread problem. Prediction is key to more effective control of fire spread and intensity. Without a reliable wildfire spread predicting tool, it is difficult, on one hand, to propose safe fire-fighting strategies, and on the other hand, for disaster planners and fire ecologists to

decide which fire to let burn and which should be suppressed. Although many research endeavors, e.g., experiments and modeling, have been devoted to wildfire behavior, Finney et al. [14] [15] assert that the fundamental theory of wildfire spread is still not established. Wildfire spread modeling is thus based on the current understanding of physics. Typically, there are four types of fire spread classified according to the portion of the forest in which it burns:

- **Ground fires:** burn organic matter in the soil beneath surface litter and are sustained by glowing combustion.
- **Surface fires:** spread with a flaming front and burn fuels located at ground level.
- **Crown fires:** burn through the top layer of foliage on a tree—the canopy or crown. The most intense type of fire, and often the most difficult to contain.
- **Spotting fires:** spotting ignition by lofted firebrands, observed in many large-scale fires.

Figure 1.5 is a sketch of a forest fire with nearly all of the types of spread described above, except ground fires which are out of the scope of the current work. Factors such as fuel, wind, terrain, and firebrands are depicted in the figure, and they have largely affected the plume formation and fire spread. It is suggested that a modern fire spread model should at least include all these physics. Current fire behavior models used for operational predictions are semi-empirical, based on the well-known formula developed by Rothermel [16]. They help the U. S. Forest Service and other agencies predict the course of hundreds of fires each year. The relatively crude existing simulations have proved to be useful in certain, usually simpler, situations. However, it is agreed that these models present limited predicting power when facing blazes that seemingly act erratically under a warmer climate, such as the Esperanza

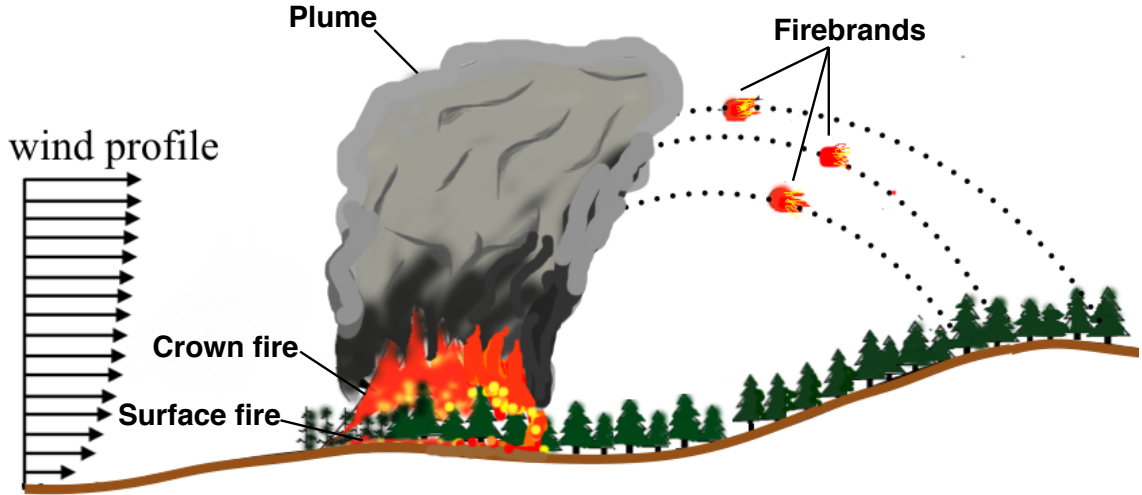


Figure 1.5: Sketch of forest fire spread.

fire in 2006 (Coen and Riggan [17]), and the Yarnell Hill fire in 2013. Therefore, more sophisticated models that can simulate the extreme behavior of fire across entire landscapes are on the horizon (Kintisch [18]). For example, the coupled weather/wildfire model WRF-Fire used by Coen et al. [19], the large-eddy simulation (LES)-based Wildland-Urban Fire Dynamics Simulator (WFDS) developed at the National Institute of Standards and Technology (NIST) by McGrattan et al. [20], and the RANS (Reynolds-averaged Navier–Stokes)-based FIRETEC proposed by Linn et al. [21] have been gaining increasing attention because of their ability to simulate more realistic fire behaviors. It is noticed that almost all existing wildfire LES modeling employs classical eddy-viscosity based subgrid-scale (SGS) models such as Smagorinsky or the dynamic (Smagorinsky) model.

This dissertation research utilizes one of the structural models of multi-scale methods (Weinan and Engquist [22])—synthetic-velocity LES—which utilizes explicit spatial filtering for dissipation (such as in implicit LES) and a chaotic map based model for backscatter, and aims at capturing more details on subgrid-scales. Investigations of forest fire modeling using this form of LES were initially attempted previously for both two-dimensional by McDonough et al. [23] and three-dimensional simulations

by McDonough and Yang [24]. However, neither of these explored details of porous effects of fuel beds and realistic terrains; heat transfer and re-ignition by firebrands were also not considered. These issues will be addressed in the present study. In addition, the run time for many of the more complex models is still far too long to provide any faster-than-real-time applications, even computed in parallel on today's largest supercomputers. However, it is postulated that their more physically-based nature could make them better learning tools and allow them to be used to examine some of the more complex wildfire behaviors, ultimately, being predictive in the near future. Besides, not all field applications require faster-than-real-time output, e.g., planning, training, and risk assessment. This justifies the purpose of this dissertation work. The rest of the dissertation is organized as follows. In Ch. 2, a detailed literature review of fire spread science and modeling is provided. In Ch. 3, the proposed wildfire modeling approach is discussed. In Ch. 4, the algorithm and parallelization of the solver are explained. In Ch. 5, a discrete dynamical system for turbulence modeling is derived and analyzed. In Ch. 6, a theoretical permeability model—another sub-model—is derived and discussed. In Ch. 7, computational results of wildfires are given. Finally, summary and conclusion of the overall work is provided in Ch. 8.

Chapter 2: Review of Wildfire Spread Studies

As mentioned in Ch. 1, the prediction of fire spread is important for fire management and developing efficient firefighting strategies. In this chapter, a fairly comprehensive literature review is provided concerning two main research areas: 1) forest fire physics and fire-related phenomena, and 2) fire spread models. Both of these lead to improved understanding of wildfire science and development of rigorous physical wildfire models, which will be predictive if delivering faster-than-real-time (FTRT) simulations. Considering the large number of physical behaviors interacting with or affecting wildfires, a complete review of all these physical interactions would be impossible and unnecessary; thus, only the most significant ones are presented here. In Sec. 2.1, representative physical processes concerning fuels, ignition, heat transfer, turbulence and fire whirls, which exist in all types of wildfires (except ground fires), are reviewed. In Sec. 2.2, a discussion of the current existing wildfire modeling approaches is first provided, followed by overviews of RANS and LES modeling that are employed in current CFD-based wildfire models. Summary and conclusions are provided in Sec. 2.3.

2.1. Wildfire spread physics

The physical processes of fire spread were described as a series of piloted ignitions by Fons [25] as early as the 1940s. Any sustained combustion requires that sufficient heat should be liberated by the chemical reaction and then transferred to the unburned fuel to cause subsequent ignition. Weber [26] described the physical processes which are integral to fire spread in three steps:

- (1) an ignition source causes release of reactive gases locally, and results in flames

within and above the fuel bed;

- (2) the heat produced is transferred, a part of which reaches unburnt fuel;
- (3) the unburnt fuel absorbs energy and releases fresh reactive gases, and the subsequent combustion corresponds to fire spread.

Hence, there are three main physical problems concerned with wildfire spread: fuel, ignition, and heat transfer. None of these, however, is sufficiently understood in the context of a forest fire. These three aspects are further explained in Sec. 2.1.1, Sec. 2.1.2, and Sec. 2.1.3, respectively. Moreover, interactions of wildfires with the atmosphere (e.g., turbulent gusting wind, humidity) and topography also play important roles in fire spread. Clark et al. [27] found that fire creates its own weather. This also contributes to the discovery by Finney et al. [28] [14] and Adam [29] that forest fires are inherently dynamic. Wildland fires, particularly when they interact with the wind, exhibit time-dependent flame behaviors like flickering, pulsing, and vortex shedding, but the sources and mechanisms of the dynamic nature are not clearly understood. Dynamic interaction between the flame, the fuel, and the flow field remains one of the most challenging problems faced by combustion scientists. Thus, turbulence and fire whirls, which are of significance in the process of ignition and heating of unburned fuels, are discussed in Sec. 2.1.4.

2.1.1 Fuel

A fuel bed is a load of an extensive variety of combustible, organic wildland fuel, each with its own composition and material properties, in a metastable (usually, the fuels decompose very slowly) state [26]. For instance, in a temperate deciduous forest, tree types include oak, beech, maple, elm, chestnut, hickory, basswood, linden, etc. While in a temperate coniferous forest, mostly fir, pine, and spruce trees exist. Natural fuel beds can also be homogeneous, such as drying grassland and forest litter. The Texas Department of Agriculture [30] in its manual for prescribed burns, has provided a

detailed description of wildland fuels. Fuel can be classified as live or dead and divided into three broad groups as aerial, surface, or ground fuels. Aerial fuels are materials located in the upper forest canopy including tree branches, crowns and high brush. Surface fuels are all materials lying on or immediately above the ground including needles or leaves, grass, small dead wood, low brush, and reproduction. Ground fuels are all combustible materials lying beneath the surface including deep duff, roots, rotten buried logs, and other woody fuels. While far from the only fuel burning in wildland fires, most studies focus on wood as the fuel even while exploring other aspects of fire behavior. Wood is comprised of lignin, cellulose, hemicellulose, and extractives in varying amounts, depending on tree species [29]. Actually, all fuels, living and dead, contain fiber that is known as cellulose. Fuels also contain chemicals and minerals that can enhance or retard combustion. Chemical contents include the presence of volatile substances such as oils, resins, wax, and pitch, which can contribute to fast ignition, high fire intensities and rapid rates of fire spread. These may also explain why some live fuels burn more strongly than dead fuels.

A more detailed study of individual fuel components can give us an indication of potential fire behavior within a fuels complex. For a homogeneous fuel bed with only one type of fuel, the principal characteristics of fuel components that affect fire behaviors are [30] [26]:

- **Fuel loadings:** the oven dry weight of fuels in a given area; they are generally separated by different sizes of live and dead fuel particles.
- **Surface-area-to-volume ratio:** the ratio of the surface area of a fuel to its volume (SAV) using the same unit of measurement. The higher the ratio the finer the fuel (e.g., grass); the lower the ratio the larger the fuel (e.g., logs).
- **Compactness:** the spacing between fuel particles; the closeness and physical arrangement of fuel particles affect both ignition and combustion.

- **Fuel bed depth:** average height of surface fuel that is contained in the combustion zone of a spreading fire front.
- **Moisture content:** the amount of water in a fuel expressed as a percent of the oven-dry weight of that fuel.

For non-homogeneous fuel beds, fuel characteristics of horizontal continuity and vertical arrangement also need to be considered since they are especially important to the spread of surface and crown fires.

Thermal characteristics of conductivity and heat capacity comprise the minimum set of variables needed and are considered sufficient for heat transfer models for fuels. If any chemical processes are to be modeled, kinetic data are required to determine at least the heat of reaction, the reaction rate constant and the activation energy [26]. For mathematical models, inputs always include these fuel properties, and within each fuel model these fuel bed inputs serve for a particular fire behavior or fire effects model.

2.1.2 Ignition

According to Finney et al. [14], ignition criteria of wildland fuels are determined by only the crudest approximations; and this limits development of a theoretical basis for fire spread. Thus, the state of ignition, or sufficient condition for ignition, needs to be defined. Vermesi et al. [31] summarized the four criteria that have been used for piloted ignition: the critical energy, critical temperature, critical mass flux, and time-energy squared—all of which are empirical but based on combustion theories of different degrees of development. Among these, ignition temperature is the most commonly used, as was reviewed by Babrauskas [32], where wood is mostly used to study ignition. The live California chaparral leaves are also studied by Engstrom et al. [33]. It was found that time to ignition was significantly influenced by shape effects,

whereas ignition temperature, which was estimated to be 584 K (oak), was more dependent on chemical composition. Although the ignition temperature assumption is satisfactory in some situations, it is not consistent with the actual physical process and thus not considered quite reliable for future fire spread modeling for several reasons. First, ignition temperature is usually obtained from solid surfaces while ignition actually occurs in the gas phase. Also, in most of the experiments, e.g., Kuznetsov and Filkov [34], different species are heated only by radiant energy, which is not the case in a real forest fire. The most recent experiment done by Vermesi et al. [31] uses transient irradiation, which is still not completely realistic. Finney et al. [14] and Adam [29] suggested not using temperature as an indicator of ignition, but rather visible flames. A better ignition model would be a coupling of solid and gas phases. It was found recently that ignition depends on a critical rate of converting solid mass to combustible gas similar to other substances, such as plastic, and that ignition depends on both heat flux and wind flow. Lyon and Quintiere [35] provided the critical mass flux and heat release rate for piloted ignitions as $1 \text{ g/m}^2\text{s}$ and 24 kW/m^2 , respectively, which are independent of the materials. Thus, an ignition modeling that accounts for both temperature and heat flux should be considered.

Understanding ignition processes at the particle scale is important for developing fire spread models [14]. The physical process of ignition is thoroughly discussed by Torero [36], based on which, Finney et al. [14] described a physically consistent process whereby ignition of fuel particles occurs after the solids are heated at a rate high enough to produce a sufficient quantity of pyrolysis gases. These gases, when mixed with air, can ignite and burn with a heat release rate greater than the heat loss rate to the surroundings. As a material undergoes degradation prior to ignition induced by an external source of heat, both solid and gas phases are involved [36].

Solid phase. Under the action of the intense heat flux coming from the flaming zone, decomposition of vegetation can be summarized using the three following steps according to Morvan et al. [37], Torero [36] and Adam [29]:

- **Drying:** also expressed as evaporation of moisture or water. It is an endothermic phase change that can have a significant effect on the temperature distribution in the solid. Phase changes are generally incorporated into the energy equation as heat sinks where some rate function is created to describe the conversion from one phase to another. It is evident that any predictive tool for ignition should attempt to quantify the impact of phase change on ignition.
- **Pyrolysis:** thermal decomposition of materials in the absence of oxygen, or when significantly less oxygen is present than is required for complete combustion. Solid transforms into gas phase fuel and generally implies the breakdown of the molecules into different, typically smaller, molecules. It tends to be an endothermic process generally controlled by many chemical reactions (sometimes hundreds) which are a strong function of temperature. Most pyrolysis reaction rates tend to be described by Arrhenius type functions of the temperature. The local and total mass production per unit area at the surface can thus be obtained from this rate.
- **Charring:** results from pyrolysis of charring materials, in which case pyrolysis leads to the production of gaseous fuel and a residual solid phase char. The char is mainly a carbonaceous solid that could be further decomposed. The secondary decomposition can be complete, leading to an inert ash or to a secondary char that can be further decomposed in one or multiple steps. It is common to see large voids and cracks in the char region, and a permeability model is needed to account for this.

Gas phase. Once the pyrolysis gas is released, the emerging fuel will encounter the ambient oxidizer and eventually produce a flammable mixture. The sequence of events leads to the ignition of a gas phase flame. In auto-ignition there is no hot spot that will serve as an initiation point for the reaction; thus, the mixture must absorb enough energy to reach ignition. It is clear that auto-ignition is a complex process that fully involves interactions of the solid and gas phases. The process of auto-ignition is extremely difficult to describe in a quantitative manner, even under simple experimental configurations [36]. A mechanism to simplify the process is to include a pilot flame or a hot spot. Currently, all standard test methods that attempt to describe the ignitability of solids use some form of a pilot [36]. In the gas phase, the Semenov theory could be used for the critical temperature (ignition temperature).

2.1.3 Heat transfer

Heat transfer represents the movement of energy between media or within a medium due to the presence of a temperature gradient. To understand the mechanisms governing wildland fire spread, a fundamental understanding of heat transfer processes is required. For wildland fires, all three modes of heat transfer: conduction, convection, and radiation contribute to the combustion process, but in different ways. Conduction usually exists in the condensed phase and controls the fuel pyrolysis process in such a way that the interior of a heating or burning fuel particle acts as a heat sink and pulls heat away from the surface thus reducing production of pyrolysates and the potential for continued combustion [29]. However, conduction is generally assumed to be negligible in the gas phase due to the lack of contact between most discrete fuel particles. For spreading fires, radiation and convection play more critical roles in the heating and burning of unburned fuels. Generally, radiation in wildland fire scenarios describes the process by which the fuel receives energy that sustains the pyrolysis reaction and the burning flame. Convection supplies the energy required to

bring the fuel ahead of the flame front to its ignition point and thus contributes new fuel to the fire. However, radiation and convection are not always limited to those exclusive roles.

In the past, most research assumed radiation was the controlling mechanism of heat transfer in wildland fire spread. For example, Albini [38] [39] suggested that intense radiation from the flame front contributed to fuel preheating and thus fire spread, and it was assumed that radiation is the principal mechanism for fire spread in the crown fire spread model of Butler et al. [40]. Others, however, have questioned the sufficiency of radiation in heating fuels to ignition [14]. Baines [41] and Weber [26] examined the previous research results and found that modeled radiation heat transfer cannot reasonably represent fuel particle temperatures in advance of a flame zone. Baines [41] found that a model that includes convective cooling can produce temperatures similar to measured fuel temperatures. Currently, the mechanisms responsible for ignition, and thus fire spread, have not been explicitly determined at this scale. Moreover, the balance between (and more importantly the interaction between) the contributions of radiation and convection in wildland fires is still not well understood.

Furthermore, it was discovered that convection may play a dominant role in a wildland fire spread. Finney et al. [42] drew this conclusion based on experiments of fire spread through rods spun with excelsior. It was clearly seen that no pyrolysates (smoke) occur before bathing the rods in flames, indicating the importance of convection. Emori and Saito [43] extended the convective-driven and radiative-driven heat transfer regimes to wildland fire scenarios. They examined fire spreading through uniform fuel beds of different fuel arrangements on horizontal or upward slopes. Convection-dominated fires and radiation-dominated fires abide by different power law relationships between the fires' mean flame length, and the rate of fire spread. These power laws differentiated two regimes. Adam [29] continued this work, further developing the equations describing convection driven spread and illustrating

four steps towards ignition for this kind of spread: 1) flaming is near; 2) the fire front is in close proximity and bathes the particle in flames infrequently—this means that the particle temperature does not immediately and rapidly rise because the time that elapses between the first and infrequent flame bathing events allows the particle to cool; 3) when the fire is near, flames bathe the particle regularly, and the time between these events is shorter and not sufficient to enable the particle to cool—as a result, the particle temperature increases dramatically, and the fuel particle enters a pyrolysis stage so that pyrolysates begin to accumulate surrounding the leeward side of the tines (e.g., branches); 4) the particles’ pyrolysates ignite. In most cases, ignition occurs when the pyrolysates reach a critical concentration and the fire bathes the tine location in a flame. This lends credence to the idea that prior to ignition, convective heat transfer, either from direct flame impingement or natural convective heating from buoyancy driven circulation, is significant and may play a more substantial role in the spreading of wildland fires than previously believed.

2.1.4 Turbulence and fire whirls

As implied earlier at the beginning of Sec. 2.1, turbulent transport processes within the fuel bed are significant, and including effects of turbulence on fire spread can improve the accuracy of operational models. In their findings, Pagnini and Mas-sidda [44] concluded that turbulence is of paramount importance in wildland fire propagation since it randomly transports the hot air mass that can preheat and then ignite the area ahead of the fire. According to Heilman and Bian [45], atmospheric boundary layer (ABL) turbulence or wind gustiness can increase the erratic behavior of fires. In addition, Clements et al. [46] found that wildland fires radically modify the ABL by inducing strong fire-atmosphere interactions. The ABL is forced by both the fire-atmosphere coupling and the fire-induced flow close to the fire front, and these interactions lead to increased turbulence intensity. It was observed that measured

turbulence generated by fires was five times greater than turbulence in the ambient environment [46]. However, spatial (horizontal and vertical) scales affected by turbulence range from 1 to 10^3 meters, which makes modeling rather difficult. Turbulence, in its own standing, remains difficult to be studied. The current understanding of turbulence is briefly explained in the next paragraphs.

Turbulence, as well as the physics of all fluid flows (within the confines of the continuum hypothesis), is universally believed to be embodied in the Navier–Stokes (N.–S.) equation introduced by Navier and Stokes in the early to mid 19th century. A simple form of the N.–S. equations for incompressible flow is presented as:

$$\nabla \cdot \mathbf{U} = 0 , \tag{2.1a}$$

$$\mathbf{U}_t + \nabla \cdot \mathbf{U}^2 = -\nabla p + \nu \Delta \mathbf{U} , \tag{2.1b}$$

where $\mathbf{U} = (U, V, W)^T$ represents a velocity field dependent on three spatial coordinates (x, y, z) and time t ; p is the kinematic (divided by constant density) pressure, and ν is the kinematic viscosity; ∇ , Δ , and $\nabla \cdot$ are, respectively, the gradient, Laplace and divergence operators in the particular coordinate system being used. Equations. (2.1) are nonlinear and difficult to solve. From the standpoint of dynamical systems, Strodtbeck [47], in his dissertation, states that a turbulent flow is an evolution in time of the N.–S. equations as a chaotic dynamical system, driven by the conservative, non-linear interactions of the entire spectrum, and controlled by the dissipative, linear terms in the energy and momentum equations.

The notable difference between turbulence and other fluid flows is its wide range of length and time scales, as seen in forest fires. Basically, there are four main sets of scales associated with a turbulent flow: 1) large scale; 2) integral scale; 3) Taylor microscale and 4) dissipation scale. A brief description of these length scales is given here; fuller discussion including derivations can be found in standard works on turbulence, such as Tennekes and Lumley [48].

- **Large scale** L : based on the problem domain geometry.
- **Integral scale** l : is an $\mathcal{O}(1)$ fraction, often taken to be ~ 0.2 of the large scale. It is the largest length scale l associated with the coherent turbulent structure and has maximum turbulence energy. The Reynolds number is $Re_l = U_{rms}l/\nu$, with U_{rms} as the square root of the turbulence kinetic energy.
- **Taylor microscale** λ : an intermediate scale, basically corresponding to relatively high wavenumbers within Kolmogorov inertial subrange. Length scale is estimated by

$$\lambda = lRe_l^{-1/2} . \quad (2.2)$$

- **Kolmogorov (dissipation) scale** η : the smallest of turbulence scales. Length scale is given by

$$\eta = lRe_l^{-3/4} . \quad (2.3)$$

It is known that turbulence enhances dissipative properties of the flow, but since turbulence is due to non-linear interactions, its mathematical characteristics are substantially different from true, linear dissipation. Numerical experiments of three-dimensional spectrally truncated incompressible Euler turbulence by Bos and Bertoglio [49] and the direct numerical simulation (DNS) results for incompressible turbulent flows as early as those presented by Piomelli et al. [50], exhibit substantial inverse transfer of energy from small to large scales, which is known as “backscatter.” They showed that inviscid turbulence exhibits a transient inertial subrange with approximately $k^{-5/3}$ scaling, thus confirming that the inertial subrange in turbulence is due to the conservative non-linear terms and is largely independent of dissipation. It is claimed that in the $k^{-5/3}$ energy spectrum, the transfer of energy from low- k to high- k wavenumbers is in balance with the backscatter [47].

Fire whirls are vertically oriented, intensely rotating columns of gas found in or near fires. Dynamically they are closely related to other swirling atmospheric phe-

nomena such as dust devils, water spouts, and tornadoes [5]. A fire whirl includes those whirls caused by the buoyancy of a fire but with no inner core of flame. Fire whirls range in size from less than 1 m in diameter and velocities less than 10 m/s up to possibly 3 km in diameter and winds greater than 50 m/s, according to Goens [51]. In the wildland fire context, there are many possible sources of ambient vorticity that could contribute to fire whirls. Morton [52] discussed that one important source may be the shear layer that develops when ambient wind flows over the ground surface, producing horizontally oriented vorticity. The primary vorticity-concentrating mechanism in fire whirls appears to be vortex stretching owing to vertically accelerating flow in the whirl core, according to Snegirev et al. [53]. The vertical acceleration is due to buoyant forces from hot gases in the core of the fire whirl. This acceleration causes a reduction in the diameter of a horizontal area enclosed by a chain of fluid particles (horizontal convergence), thereby increasing non-zero vorticity at any location on the horizontal area, Jenkins et al. [54]. This is analogous to a reduction in the moment of inertia of a rotating solid, causing increased rotation rate to conserve angular momentum. For complicated phenomena such as fire whirls including, chemical kinetics models other than dissipative ones are needed to capture the interactions with other physics.

2.2. Wildfire spread modeling

A quite comprehensive review of wildfire spread models before 1990 was provided by Weber [26], in which the models were described as physical (accounted for different modes of heat transfer), empirical (made no differentiation between modes of heat transfer) or statistical (involved no physics at all). Since 1990, the field of spatial data analysis, such as geographic information systems and remote sensing, has developed rapidly; therefore, the reviews after 1990 often included simulation models that made use of this earlier technology. However, nomenclature of model classifications varies.

Grishin [55] divided models into two classes, deterministic or stochastic-statistical. Pastor et al. [56] proposed the descriptions theoretical, empirical and semi-empirical, depending on whether the model was based on pure physics, or of a statistical nature, or a combination of both. Also, in [56], models are categorized according to ground, surface, crown and spotting fires; spotting fires are more comprehensively reviewed by Koo et al. [57], and to be discussed in a subsequent chapter. Perry [58] and Morvan et al. [59] discuss models according to physical, semi-physical/semi-empirical or empirical classifications. The most recent comprehensive review is provided by Sullivan [60] [61] [62], in which a series of models dating from 1990 to 2007 are divided into three broad categories: physical and quasi-physical models; empirical and quasi-empirical models; and simulation and mathematical analogue models.

It is seen that all modeling approaches range from purely physical (based on fundamental understanding of the physics and chemistry involved in a wildland fire) to purely empirical (based on a phenomenological description or statistical regression of observed fire behavior), as is shown in the upper light-grey part of Fig. 2.1, using nomenclature found in [60] [61]. Moreover, mathematical analogue models, simulation

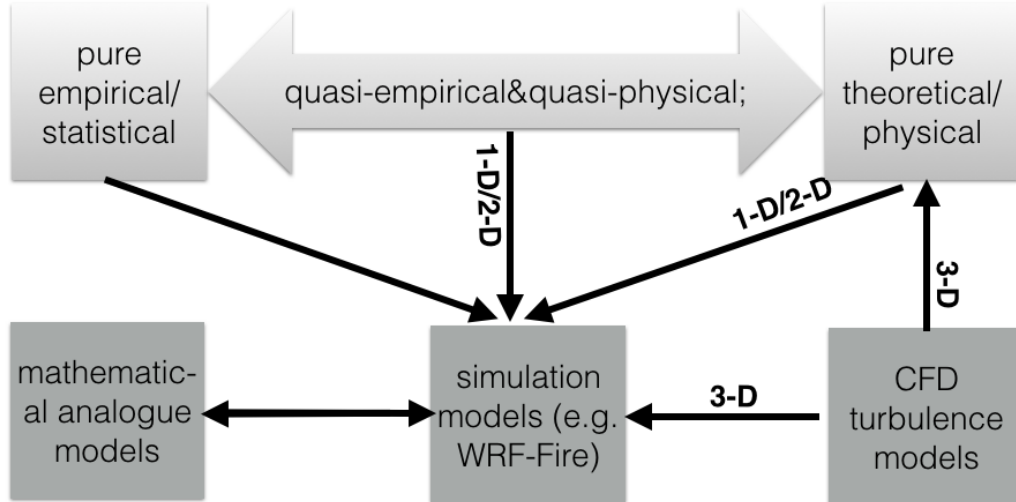


Figure 2.1: Classification of current existing wildfire models.

models, and CFD-based models also exist. The literature on wildfire modeling after 2007 and to the present is mostly an extensive study of previous existing models with quite active developing research on these three aspects, as shown in the lower deep-grey part in Fig. 2.1. These models are connected with each other in one way or another to provide better wildfire modeling. For instance, all lower dimensional (1D/2D) fire spread models can feed into simulation models. Also, CFD contributes to both simulation models and complicated physical models in 3D due to the increasing power of computation. CFD can inherently consider terrain geometry, heat transfer, time varying fire strength, fire chemistry and variations in weather phenomena.

Apart from this, Mell et al. [63] provided a brief overview of physical models and proposed a scheme in which models were defined by the component on which the model was focused: fuel, atmosphere or fire. As seen in Fig. 2.2, five regions are defined to categorize current models. Empirically-based models like FARSITE

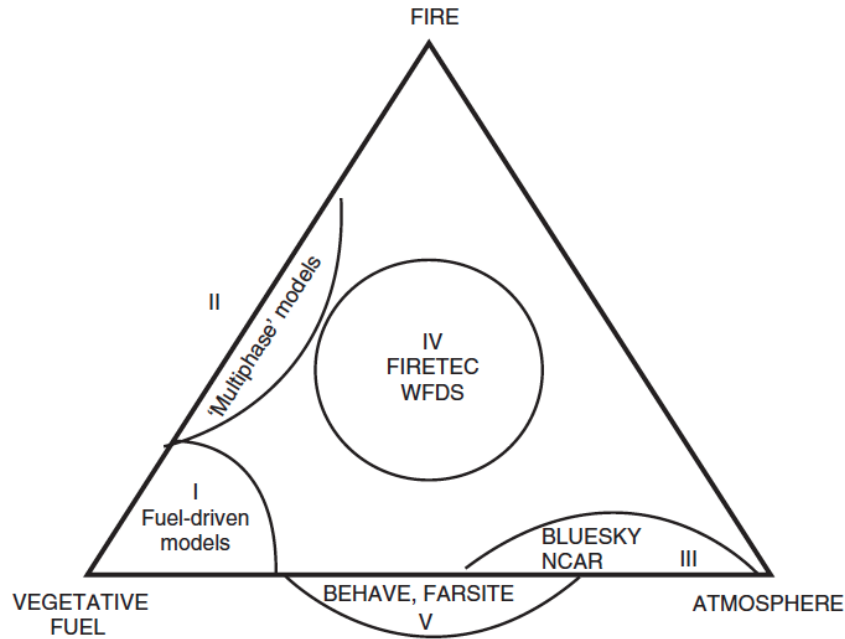


Figure 2.2: Summary of current existing wildfire models according to relation with fuel, atmosphere or fire [63]. Used with permission.

and BEHAVE lie in region V. These are not physics-based fire models and require

only inputs describing the vegetative fuel, terrain, and wind. Other regions that reside within the triangle are quasi-physical or physical models. For approaches in region I, the fire-atmosphere interaction is not modeled. Relevant flame properties, such as temperature and flame geometry, and therefore the heat flux from the fire, are fixed; and relevant models are mostly reviewed in [26]. Region II corresponds to multiphase models computed by CFD methods. Region III represents what are defined as simulation models in Fig. 2.1, which are based on weather research software such as NCAR (National Center for Atmosphere Research) and BLUESKY by Clark et al. [64] [65]. Region IV represents fully three-dimensional simulators such as WFDS (Fire Dynamic Simulator) [20] and FIRETEC [21], which lies in the purely physical mode or CFD turbulence models in Fig. 2.1. It is summarized that models from region II to IV employ CFD methods.

In this section, an introduction to purely empirical, combined empirical and physical, and purely physical models is first presented in Sec. 2.2.1–2.2.4, respectively. The nomenclature used is approximately that used by Sullivan [61] [60] and by Mell et al. [63], since semi-empirical or semi-physical provides no indication as to which half is empirical or physical. For intermediate models, quasi-empirical and quasi-physical, or fuel-driven, models are discussed. For physical models, both multiphase and fire-fuel-atmospheric models are analyzed. In Sec. 2.2.5, simulation and mathematical analogue models are briefly reviewed. Only typical models in each category are introduced; a comprehensive review is provided by Sullivan [61] [60] [62]. Lastly, since CFD models are used widely in physical models such as RANS-based FIRETEC, RNG $k-\varepsilon$ or LES-based WFDS, and LES-based WRF-Fire, the basics of turbulence modeling employing RANS methods and LES is discussed in Sec. 2.2.6 and Sec. 2.2.7, respectively.

2.2.1 Empirical modeling

Empirical modeling is basically derived from statistical correlations of a given experimental dataset without any inclusion of physical mechanism that drives the fire process. Usually, it is an algebraic law defining the rate of fire spread. For example, the mathematical relationship for the simplest McArthur meter, the Mark 3 grassland fire danger meter derived by Nobel et al. [66] is:

$$F_{fdi} = 2 \exp \left(- 23.6 + 5.01 \ln C_{dc} + 0.0281 T_a - 0.226 H_r^{1/2} + 0.663 U_{10}^{1/2} \right) , \quad (2.4a)$$

$$V_{fsr} = 0.13 F_{fdi} , \quad (2.4b)$$

where, C_{dc} is degree of curing, T_a = air temperature, H_r = relative humidity, U_{10} = wind velocity at 10m height, V_{fsr} is fire spread rate, and F_{fdi} is fire danger index. These empirical equations are used to test simulation software for wildland fire under simple test conditions. This meter has been replaced by the Mark 5 version which has more complicated formulas but with the same statistical nature.

The McArthur fire-danger meters for grasslands and forests are widely used in Australia for fire danger forecasting, as described by McArthur [67] and Nobel et al. [66]. The use of McArthur meter has been successful in conditions similar to those under which they were calibrated. It performs very well in predicting similar fires to the test fires. For fires different from the test conditions or more complicated fire behaviors, it is less successful and must be used cautiously. Later models developed by Cheney et al. [68] such as the CSIRO Grass, were based on data from experimental fires but required a number of logical assumptions to predict fire spread beyond the range of the data.

2.2.2 Quasi-empirical modeling

These models (often called semi-empirical models) are based on energy conservation but they usually do not distinguish between the different modes of heat transfer

(conductive, convective, radiative). One of the famous models is the Rothermel fire spread rate formula [16], which was developed from a theoretical base supplied by Williams [69] and Frandsen [70] who applied the conservation of energy principle to a unit volume of fuel ahead of an advancing fire in a homogeneous porous fuel bed. The generic form is given by

$$V_{fsr} = \frac{I_p(1 + \phi_w + \phi_s)}{\rho_b \epsilon_h Q_{ig}} . \quad (2.5)$$

In Eq. (2.5), I_p is net propagating flux transported across the surface of fire inception; it is determined empirically as a function of the reaction intensity I_R as

$$I_p = I_R(192 + 7.894r_{sv})^{-1} \exp \left[(0.792 + 3.760r_{sv}^{0.5})(\beta_{fs} + 0.1) \right] ,$$

where r_{sv} = surface area to volume ratio (cm^{-1}) and β_{fs} = ratio of fuel bed density to solid fuel density. The reaction intensity I_R is related to the fuel mass loss rate per unit area in the fire front and to heat content of the fuel. The oven-dry bulk density ρ_b represents the amount of fuel per unit volume of the fuel bed raised to ignition ahead of the advancing fire, and ϵ_h is the effective heating number calculated from SAV (surface to volume ratio). The heat of pre-ignition Q_{ig} is the heat required to bring a unit weight of fuel to ignition and is calculated empirically based on fuel particle moisture content. Lastly, ϕ_w and ϕ_s are wind and slope correction factors that are determined experimentally.

Although it is empirical in nature, the Rothermel model is derived from experiments conducted with a wide range of fuel parameters and external conditions and has succeeded when applied to many different fuels under diverse meteorological conditions. Also, based on these formulas, well-known software like BehavePlus by Andrews [71] and FARSITE by Finney [72] have been developed as tactical operational fire predicting tools. These packages run faster than real time on personal computers, and can predict simple forest fire spread reasonably well; however, it is difficult to

predict complicated phenomena such as fire whirls and turbulence from these models partly because they are only 2D.

2.2.3 Quasi-physical modeling

These are different from quasi-empirical models in that they account for all forms of heat transfer. Physical modeling is focused on heat transfer within the fuel. For example, consider the equation:

$$\rho c_s \frac{\partial T}{\partial t} = D_{dif} \frac{\partial^2 T}{\partial x^2} + A_{rad} f(x, R_f(t)) - r_{sv} h_{conv} T . \quad (2.6)$$

The left-hand side (LHS) represents the rate of the rise in temperature per unit volume of fuel ahead of the fire front, with ρ the density of the fuel and c_s the heat capacity of the fuel. On the right-hand side (RHS), from left to right are the diffusion term, the radiation term, and the convection term. This is a one-dimensional equation with two independent variables, x and t . The function $T(x, t)$ represents the temperature of the fuel and $R_f(t)$ is the position of the fire front. In Weber [26], the problem of fire spread is interpreted as wave propagation, and Eq. (2.6) is solved analytically using the method of variation of parameters. The representative models are those of Albini [38], Butler et al. [40] and Balbi et al. [73] etc.

Fuel-driven models in Mell et al. [63] are categorized within these quasi-physical models. Many physics models only account for radiative heating as the driving physics [38]. The basis of most of these models is that steady flame spread rate is determined by how long it takes solid fuel ahead of the flame to reach an ignition temperature at an idealized two-dimensional ignition interface. Such models are useful for exploring relative contributions of the different modes of heat transfer, and they can achieve FTRT predictions [73]—but only for conditions appropriate for steady flame spread where net wind speed and direction, fuel properties, terrain, etc., are all constant. The combustion process is usually assumed to be known. It contains no chemistry and relies on the transfer of a prescribed heat release (viz., flame geometry and

temperature are generally assumed) [63] [60], Sullivan et al. [74]. Relevant flame properties, such as the temperature and flame geometry, and therefore the heat flux from the fire, are fixed. Fire-atmosphere interaction is not modeled.

2.2.4 Detailed physical and multiphase modeling

These models attempt to solve (in some approximation) the equations governing fluid dynamics, combustion, and heat transfer. The inclusion of chemical kinetics of combustion into the physics models by Grishin [75] was a major advance at that time according to Weber [26], but the model was only one-dimensional. For massive fires, Williams [76] provided a set of differential equations for conservation of mass, momentum, energy and chemical species concentration. Although processes such as heat conduction and finite-rate chemical kinetics occur in condensed phases in large fires, the processes occurring in the gas phase are of paramount importance, and therefore gas dynamics is the most relevant. The corresponding dimensional differential conservation equations are as follows:

$$\rho_t + \nabla \cdot (\rho \mathbf{U}) = 0 , \quad (2.7a)$$

$$\rho(\mathbf{U}_t + \mathbf{U} \cdot \nabla \mathbf{U}) = -\nabla p + \rho \mathbf{g} + \nabla \cdot \boldsymbol{\tau} , \quad (2.7b)$$

$$\rho \frac{D}{D_t} \left(h + \frac{\mathbf{U}^2}{2} \right) = p_t - \nabla \cdot \mathbf{q} + \nabla \cdot (\mathbf{U} \cdot \boldsymbol{\tau}) + \mathbf{U} \cdot \mathbf{g} + \sum_{i=1}^N Y_i \mathbf{V}_i \cdot \mathbf{g} , \quad (2.7c)$$

$$\frac{D(\rho Y_i)}{D_t} = w_i - \nabla \cdot (\rho Y_i \mathbf{V}_i) , \quad i = 1, \dots, N \quad (2.7d)$$

where $\mathbf{U} = (U, V, W)^T$ is velocity vector; ρ is fluid (gas mixture) density; h is enthalpy per unit mass for the gas mixture; Y_i is mass fraction of chemical species i in the gas; \mathbf{V}_i is diffusion velocity of species i ; w_i is mass rate of production of species i by chemical reactions; D/D_t is the substantial derivative. The stress tensor $\boldsymbol{\tau}$ and heat transfer \mathbf{q}_T are expressed as

$$\boldsymbol{\tau} = \mu(\nabla \mathbf{U} + (\nabla \mathbf{U})^T - \frac{2}{3}(\nabla \cdot \mathbf{U})\delta_{i,j}) + \boldsymbol{\tau}_T , \quad (2.8a)$$

$$\mathbf{q} = \lambda \nabla T + \rho \sum_{i=1}^N h_i Y_i \mathbf{V}_i + \mathbf{q}_T + \mathbf{q}_R, \quad (2.8b)$$

where \mathbf{q}_T and \mathbf{q}_R are due to turbulent effects; \mathbf{q}_R is due to radiation, which is calculated using a transport equation. It is almost impossible to solve such partial differential equations (PDEs) without employing approximations.

Scaling laws have contributed to an improved understanding of physics of wildland fire. Williams [76] identified twenty-nine dimensionless groups required to simulate large fires based on normalization of the governing equations. A subset of seven was designated as critical for even partial simulation: (1) buoyancy, (2) convection (Reynolds number), (3) two radiation groups, (4) gas-phase heat release, (5) fuel gasification energy, and (6) fuel burning rate group. According to experiments [28], buoyancy is very important in modeling forest fire behavior. Quintierre [77] provided a variety of examples of how scaling laws had been used to model various aspects of fires including simple fire plumes, burning (pyrolysis) rate and flame spread. Scaling laws of crib and pool fires, and fire whirls were investigated by Emori and Saito [43], and Soma and Saito [78] in the past decade via the rules of modeling provided by Spalding [79]. Recent research gave a scaling law between Froude number Fr and Strouhal number St to account for the dynamic flame behavior [29].

Among the wide variety of physical models reviewed by Sullivan [60], only IUSTI (Larini et al. [80], Porterie et al. [81]), FIRESTAR (Morvan and Dupuy [82]), FIRETEC and WFDS are discussed here, as listed in Table 2.1. This is justified by the fact that these have been applied to large-scale landscape-type domains; moreover, they remain the main models to which relatively active research is still devoted.

FIRESTAR and IUSTI, both of which commenced as 2-D formulations at the laboratory scale, have progressed (or are progressing) to full 3-D versions and larger computational domains. They solve the full multiphase problem (both solid and gas), but they are far from FTRT deliveries and are constrained to small computational domains. IUSTI is based on macroscopic conservation equations obtained from local

Table 2.1: Fire models. Information extracted from [60].

Model	Discretization method	Dimensions	Minimum resolution ($\delta x, \delta t$)	Turbulence model
IUSTI	Non-uniform FV	2	0.3, 0.025	RNG $k-\varepsilon$
FIRESTAR	FV	2(3)	0.025, 1	RNG $k-\varepsilon$
FIRETEC	FE	3	2, 0.002	RANS
WFDS	FV	3	1.5, $-$	LES

instantaneous forms using an averaging method. The latest work on wildfires using this model is by Porterie et al. [81] in 2007. IUSTI also provided the framework for the development of a related model, FIRESTAR, in an attempt to simplify IUSTI, according to Morvan and Dupuy [82]. FIRESTAR remains a 2-D model but is presently being converted to a 3-D form (Meradji et al. [83]).

In FIRESTAR, moisture evaporation and pyrolysis are modeled with simplified temperature-dependent mass loss rates [82]. Arrhenius kinetics are used for char oxidation. Gas-phase combustion kinetics are assumed to be infinitely fast relative to the mixing of reactants, and the eddy dissipation model is used to determine gas-phase reaction rates. Morvan et al. [84] use FIRESTAR to provide the basis for the formulation of a complete model for flame propagation through forest fuels. It particularly describes how the usual equations of continuum mechanics can be transformed into equations well-suited to a multiphase medium.

FIRETEC and WFDS are relatively unique in that they were originally formulated for full 3-D simulation of fire spread at the landscape scale. Compared to the multiphase model, which more directly solves the governing equations on more highly resolved two-dimensional computational grids, physical models like FIRETEC rely more on heuristic, physically motivated assumptions, such as a prescribed sub-grid probability distribution of the temperature in a grid cell and a rule for partitioning the energy release rate into the gas and solid phases. Many of these assumptions are driven by the limitations on spatial resolution in FIRETEC. FIRETEC provides a

set of differential equations which composes a thorough RANS model, but it is very expensive (in terms of execution time) and thus far from FTRT simulations.

Although LES has been widely used in meteorology and canopy flows, e.g., Patton [85] and Duman et al. [86], its applications in simulating forest fires are quite recent endeavors. One of the most well-known LES-based models is the WFDS developed at NIST. WFDS solves conservation equations based on a low-Mach number approximation and uses eddy-viscosity (e.g., Smagorinsky [87]) models, including wall functions, for turbulence modeling; combustion and chemical reactions are calculated from lumped-species approximations. The model can only simulate small fires with the run time much longer than the real time. Both WFDS and FIRETEC models have been assessed to some extent for grassfire and crown fire predictions (see, e.g., Mell et al. [88], Hoffman et al. [89]); in particular, 86% of the spread rate values estimated from both models fell within the 95% prediction interval of the empirical data, but the available empirical data is quite scarce [89].

2.2.5 Simulation and mathematical analogue modeling

Simulation models are those that implement a fire behavior model (often of low spatial dimensionality) in a landscape spread application and thus address a different set of computation-related problems. WRF-Fire is one example (Clark et al. [65], Clark et al. [64], Coen et al. [19]). It mainly adds a fire model to the original weather research and forecasting model, which often employs LES methods. Input from the fire model is heat flux density computed from fuel fraction and ignition time using a proposed level-set function. The level-set function is based on the spread rate calculation from the Rothermel semi-empirical model, and thus the ignitions are defined through the fire spread rate formula. Several cases have yielded quite reasonable results with this software; see Coen [90], Coen and Riggan [17]. A randomized level-set method is also proposed by Pagnini and Massidda [44].

Mathematically analogous models are those that utilize a mathematical precept, rather than a physical one, for modeling the spread of wildland fire. Mathematically analogue models do not consider physics, but use mathematical equations to model fire spread lines. One such model is based on cellular automata (CA), see Achtemeier [91]. CA is a formal mathematical idealization of physical systems in which space and time are discretized and physical quantities take on a finite set of values. What has changed significantly with regard to CA modeling is the access to more detailed geographic data and, correspondingly, the level of complexity that can be undertaken computationally. This area is very closely related to the simulation models in that the key methods can be found in both approaches, such as CA for fire propagation. The mathematically-aid models might be FTRT, but they are not based on physics and thus have limitations.

2.2.6 RANS modeling—overview

Statistical descriptions of turbulence are natural for the analysis of experimental data, as it is relatively simple to compute statistics for large data sets. RANS modeling is based on the Reynolds decomposition

$$U(\mathbf{x}, t) = \bar{U}(\mathbf{x}) + U'(\mathbf{x}, t) , \quad (2.9)$$

where $U(\mathbf{x}, t)$ is one component of the velocity vector and is well defined in a domain $\Omega \in \mathbb{R}^d$, $d = 1, 2, 3$, for $t \in [0, t_f]$; $U'(\mathbf{x}, t)$ is termed the “fluctuating part” that often needs to be modeled, and $\bar{U}(\mathbf{x})$ is the time-averaged velocity given by

$$\bar{U}(\mathbf{x}) \equiv \lim_{T \rightarrow \infty} \frac{1}{T} \int_0^T U(\mathbf{x}, t) dt . \quad (2.10)$$

The velocity $U(\mathbf{x}, t)$ can be expressed as the Fourier series

$$U(\mathbf{x}, t) = \sum_{\mathbf{k}}^{\infty} a_{\mathbf{k}}(t) \varphi_{\mathbf{k}}(\mathbf{x}) . \quad (2.11)$$

Substituting Eq. (2.11) into Eq. (2.10) yields

$$\overline{U}(\mathbf{x}) = \lim_{T \rightarrow \infty} \frac{1}{T} \int_0^T \sum_{\mathbf{k}} a_{\mathbf{k}}(t) \varphi_{\mathbf{k}}(\mathbf{x}) dt = \sum_{\mathbf{k}} \overline{a}_{\mathbf{k}} \varphi_{\mathbf{k}}(\mathbf{x}) , \quad (2.12)$$

which leads to

$$U'(\mathbf{x}, t) = \sum_{\mathbf{k}} (a_{\mathbf{k}}(t) - \overline{a}_{\mathbf{k}}) \varphi_{\mathbf{k}}(\mathbf{x}) , \quad (2.13)$$

from Eq. (2.12) and Eq. (2.9). It is seen from Eq. (2.13) that $U'(\mathbf{x}, t)$ contains all other (temporal) modes of the Fourier representation except the zeroth mode, and contains all spatial wavenumbers. This implies that $U'(\mathbf{x}, t)$ is difficult to model since it represents essentially the entire solution. A RANS model must capture the effects of fluctuations on every scale from the integral scale down to the dissipation scale (see Sec. 2.1.4).

As discussed previously, RANS modeling attempts to predict only time-averaged flow quantities. This is achieved by solving the RANS equations and does not require resolution of different scales of turbulent flow structures. The conventional RANS equation for incompressible flow is obtained by substituting Eq. (2.9) into the original N.-S. equation, Eq. (2.1), and applying the averaging properties of $\overline{\overline{U}} = \overline{U}$ and $\overline{U'} = 0$; this gives

$$\nabla \cdot \overline{U} = 0 , \quad (2.14a)$$

$$\overline{U}_t + \nabla \cdot \overline{U^2} = -\nabla \bar{p} + \nu \Delta \overline{U} - \nabla \cdot \overline{U'^2} . \quad (2.14b)$$

Since a time-averaged, static analysis could not accurately predict ignition or fire spread, in essentially all modern practical formulations of the RANS equations, the time-derivative term \overline{U}_t is included, despite the fact that $\overline{U} = \overline{U}(\mathbf{x})$ is independent of time. Probably the most commonly-used justification for retaining the time-derivative operator in the RANS equations comes from arguments associated with multiple time scales. The ergodic hypothesis implies “time averaging is equal to ensemble averaging.” There are several precise statements of this, and the reader is referred to Frisch [92] for more details.

The Reynolds stress tensor (RST), $\overline{U'^2}$, needs modeling. Thus, there is no instantaneous interaction between the fluctuating flow field and chemical kinetics. So it is clear that no useful details of a chemically reacting turbulent flow can be obtained from a RANS calculation unless the overall physics is such as to remain very close to the mean values of all variables at all times, which is rare in reaction chemistry. Even in this case an extreme amount of difficult modeling is necessary.

In order to model $\overline{U'^2}$, the Boussinesq hypothesis is often used as a means to relate turbulent shear stress to the mean flow strain rate. Note that this is different from the Boussinesq approximation associated with buoyancy mentioned earlier. The RST is proportional to the deviatoric stress tensor, leading to the relation:

$$-\overline{U'V'} = \nu_T \left(\frac{\partial \overline{U}}{\partial y} + \frac{\partial \overline{V}}{\partial x} \right), \quad (2.15)$$

where ν_T is the eddy viscosity. Note that eddy viscosity is actually a tensor, making it rather difficult to estimate. To simplify this, Prandtl drew on the kinetic theory of gases, which had recently been applied with much success to molecular viscosity. By substituting turbulent eddies for gas molecules and a mixing length for the mean free path, a scalar eddy viscosity is proposed. An immediate weakness apparent in this approach is that, unlike molecules and mean free paths, neither eddies nor mixing lengths are well-defined in a turbulent flow. Wilcox [93] provides a fairly detailed discussion of the Boussinesq hypothesis, emphasizing its shortcomings, in order to justify consideration of more sophisticated approximations to the Reynolds stress tensor.

Other more complex RANS modeling includes the $k-\varepsilon$ and $k-\omega$ models, which perform quite well in today's commercial software. Various extensions of these models exist such as the renormalizing group (RNG) $k-\varepsilon$ by Yaghoti and Orszag [94], and the adaptive control $k-\omega$ method by Li et al. [95]. The $k-\varepsilon$ model includes transport equations for both turbulent kinetic energy k ($1/2(\overline{U'^2} + \overline{V'^2} + \overline{W'^2})$ (different from wavenumber though the same symbol is used) and dissipation rate ε . Several closure

parameters are needed to complete all such models. A set of the simplest equations is

$$k_t + \overline{\mathbf{U}} \cdot \nabla k = \mathcal{P} - \varepsilon + \nabla \cdot [(\nu + \nu_T/\sigma_k)\nabla k] , \quad (2.16a)$$

$$\varepsilon_t + \overline{\mathbf{U}} \cdot \nabla \varepsilon = C_{\varepsilon 1} \frac{\varepsilon}{k} \mathcal{P} - C_{\varepsilon 2} \frac{\varepsilon^2}{k} + \nabla \cdot [(\nu + \nu_T/\sigma_\varepsilon)\nabla \varepsilon] . \quad (2.16b)$$

They are solved together with Eq. (2.14). In Eq. (2.16), \mathcal{P} is production and is related to RST and strain rate. The constants $C_{\varepsilon 1}$, $C_{\varepsilon 2}$, σ_k , σ_ε , C_v are given “standard” values (see, e.g., [93]). For RNG $k-\varepsilon$ these constants are derived explicitly in the RNG procedure. The RNG approach, which is a mathematical technique that can be used to derive a turbulence model similar to the $k-\varepsilon$, results in a modified form of the ε equation which attempts to account for the different scales of motion through changes to the production term.

2.2.7 Large-eddy simulation—overview

LES was first proposed by Smagorinsky [87] in 1963 and Deardorff [96] in 1970. Unlike the Reynolds decomposition where temporal averaging is employed, the LES decomposition, as introduced by Deardorff [96], is constructed by applying a local spatial filter to all appropriate variables, and is written as

$$U(\mathbf{x}, t) = \tilde{U}(\mathbf{x}, t) + U^*(\mathbf{x}, t) , \quad (2.17)$$

where $U(\mathbf{x}, t) \in L^2(\Omega) \times C^1(0, t_f)$; $U^*(\mathbf{x}, t)$ is called the small-scale or subgrid-scale or unresolved part; \tilde{U} is the large-scale or resolved-scale part of the solution expressed as

$$\tilde{U}(\mathbf{x}, t) = \int_{\Omega_i} G(\mathbf{x}|\xi) U(\xi, t) d\xi . \quad (2.18)$$

In Eq. (2.18), $G(\mathbf{x}|\xi)$ represents a filter kernel that is often taken to be a Gaussian. The filter width is chosen to be a few multiples of h in length, with h being the discrete step size of the numerical approximation; Ω_i is a subdomain of the solution domain Ω such that the volume of Ω_i is approximately h^3 .

By using the Fourier representation, the LES decomposition can also be interpreted as the Hilbert space decomposition

$$U(x, t) = \sum_{|k| > 0}^{k_c} a_k(t) \varphi_k(x) + \sum_{|k| = k_c + 1}^{\infty} a_k(t) \varphi_k(x) . \quad (2.19)$$

In Eq. (2.19), k_c is the cutoff wavenumber induced by discretization of the governing equations. This clearly demonstrates that only high-wavenumber parts of the solution need to be modeled, rather than the whole spectrum, as in a RANS form. LES requires modeling of part of the inertial subrange and into the beginning of the dissipation scales. The amount of required modeling is set by the amount of resolution that can be afforded. The arithmetic for LES is often less than $\mathcal{O}(Re^2)$ (which can be derived from Eq. (2.2)), provided the SGS model evaluation is independent of Re , which is usually the case. On one hand, it is more efficient than DNS (direct numerical simulation), which directly calculates deep into the Kolmogorov scale that is usually on the order of one millimeter in fire scenarios and requires arithmetic of $\mathcal{O}(Re^3)$ (which can be derived from Eq. (2.3)). On the other hand, it is more accurate than RANS methods, which were developed as a time-averaged approximation and essentially models everything and may lose significant features of turbulence.

Substitution of Eq. (2.17) into the N.-S. equation and applying the properties of $\widetilde{\widetilde{U}} \neq \widetilde{U}$ and $\widetilde{U}^* \neq 0$ leads to the classical and well-known LES form

$$\nabla \cdot \widetilde{U} = 0 \quad (2.20a)$$

$$\widetilde{U}_t + \nabla \cdot (\widetilde{U}\widetilde{U}) = -\nabla \widetilde{p} + \nu \Delta \widetilde{U} - \nabla \cdot \boldsymbol{\tau}_{SGS} , \quad (2.20b)$$

with

$$\begin{aligned} \boldsymbol{\tau}_{SGS} &= \widetilde{\widetilde{U}\widetilde{U}} - \widetilde{U}\widetilde{U} = L_{i,j} + C_{i,j} + R_{i,j} , \\ L_{i,j} &\equiv \widetilde{\widetilde{U}_i\widetilde{U}_j} - \widetilde{U}_i\widetilde{U}_j, \quad C_{i,j} \equiv \widetilde{\widetilde{U}_i\widetilde{U}_j^*} + \widetilde{\widetilde{U}_j\widetilde{U}_i^*}, \quad R_{i,j} \equiv \widetilde{\widetilde{U}_i^*\widetilde{U}_j^*} . \end{aligned}$$

$L_{i,j}$, $C_{i,j}$, $R_{i,j}$ are Leonard, cross and Reynolds stress, respectively. In particular, neither $L_{i,j}$ or $C_{i,j}$ are Galilean invariant, but their sum is; hence, the complete SGS

stress is Galilean invariant. Usually, models of τ_{SGS} have, from the beginning, been constructed such that $\tau_{SGS} \rightarrow 0$ as $h \rightarrow 0$ (or $k_c \rightarrow \infty$). Thus, it is clear that Eq. (2.20) converges to the N.-S. equations in this limit for such models, and as mentioned previously, $LES \rightarrow DNS$. It is worth noting that presence of the term τ_{SGS} is analogous to the artificial dissipation schemes widely employed for shock capturing in compressible flow simulations.

Subgrid-scale stress τ_{SGS} generally needs to be modeled. The traditional models fall into three general categories: eddy-viscosity models, similarity models, and so-called mixed models, as summarized by Domaradzki and Saiki [97]. Eddy-viscosity models use a generic form based on the Boussinesq hypothesis, as extensively applied in RANS models, and are written as

$$\boldsymbol{\tau}_{SGS} = -2\nu_{SGS}\tilde{\boldsymbol{S}} \, , \quad (2.21)$$

where $\tilde{\boldsymbol{S}}$ is the usual large-scale strain-rate tensor; $\boldsymbol{\tau}_{SGS}$ is the subgrid-scale stress tensor; and ν_{SGS} is the eddy viscosity. Among the eddy-viscosity models, the Smagorinsky model [87] is the oldest and most universally used one, in which the eddy viscosity is usually constructed from the filter width, “Smagorinsky” constant and $\tilde{\boldsymbol{S}}$, analogous to the mixing length formulation of RANS methods. The Smagorinsky model and its various forms perform well for flow far from solid boundaries, and could properly account for global subgrid-scale dissipation, which results in good predictions of important turbulent quantities such as mean velocities and root-mean-square (rms) velocity fluctuations. However, it has the issue that dissipation can only be used to model energy transfer strictly from large scales to small scales; hence, the phenomenon of “backscatter” (see Sec. 2.1.4) is not captured. The more recent models such as the dynamical model by Basu and Porte-Agel [98], is derived from the Germano identity (Germano [99]), and can model backscatter. However, its creation of negative viscosities results in a mathematically ill-posed problem, and it is allowing aliasing to supply the backscatter—negative eddy viscosities actually amplify alias-

ing. It is remarked that the eddy-viscosity models, as used in WFDS (e.g., Thurston et al. [100]) and other commercial software are most widely used.

Similarity models deal with backscatter in a natural way (see, e.g., Bardina et al. [101], Liu et al. [102]). These models assume that the unknown subgrid-scale stress tensor can be approximated by a stress tensor calculated from the resolved field by employing an additional filtering, with the filter width equal to or larger than the one used to obtain the originally resolved field. However, there appears a mismatch in the characteristic length scales for the modeled and the exact SGS fields. Also, the model of Bardina et al. [101] significantly under-predicts net SGS dissipation and, consequently, it cannot be used to reliably predict mean and rms quantities in actual large-eddy simulations. Mixed models (e.g., Piomelli et al. [103]) attempt to combine eddy viscosity and similarity expressions. The good dissipative features of eddy viscosity models and the good predictive capabilities of similarity models for correlations are thought to be complementary. However, because the results do not dramatically improve, and the dependence of the models on a filter introduces an additional complication, mixed models have found only limited acceptance.

Beyond the “classical” approaches mentioned above, many different approaches have been attempted. Fureby and Grinstein [104] proposed an approach termed “implicit” LES (ILES). It simply solves the governing equation with numerical methods that are strongly dissipative and thus replaces physical dissipation (and SGS dissipation) with numerical dissipation. Usually, the computational grid together with the low pass characteristics of the discrete differencing operators act as a filter. Stolz and Adams [105] used an alternative approach to large-eddy simulation based on approximate deconvolution, where the non-filtered field is approximated by truncated series expansion of the inverse filter operator. Deconvolution is similar to the scale-similarity method, but is more stable. The advanced ILES method which combines scale similarity (the behavior at the lowest wavenumbers of the unresolved part is

“similar” to that of the highest wavenumbers of the resolved scale) and deconvolution was also attempted.

Another set of approaches attempts to directly estimate the subgrid-scale variables, as reviewed in detail by Sagaut [106], and Domaradzki and Adams [107]. These include the linear-eddy models (LEMs) and one-dimensional turbulence (ODT) models by Kerstein [108], Echehki et al. [109]. Kerstein’s linear eddy model (LEM) is a synthetic-velocity model that has been extensively developed. LEM simulates SGS fluctuations by combining a one-dimensional heat equation with a stochastic mixing process; thus both dissipation and non-linear interactions are modeled. These models use dissipation primarily to achieve numerical stability; also, they use some kind of model to directly simulate SGS fluctuations. The “estimation” models due to Domaradzki and Saiki [97], and the chaotic map models of McDonough et al. [110] and Hylin [111] are of this type and have achieved quite good results.

It is noted that only eddy-viscosity based classical LES models have been implemented in the current LES form of forest fire modeling; it is intriguing to apply these modern methods for forest fire modeling considering their many advantages in modeling the interaction of turbulence with other physics such as combustion. Also, concerning the computational cost and calculation efficiency, multi-scale methods like synthetic-velocity LES are favored. These methods first remove aliasing using explicit filters, and then model the backscatter through variables directly. A synthetic-velocity model is implemented for the present study and will be discussed in Ch. 3.

2.3. Summary and conclusions

This chapter reviews an abundance of literature on both physics and models associated with wildfire spread, both of which are not yet fully understood. In the physics section (Sec. 2.1), fuel, ignition, and heat transfer are first introduced since they are internally connected within a fire spread. Turbulence and fire whirls are then

discussed to account for the significant effect of turbulence on erratic fire behavior occurring in recent wildfires. In the modeling section (Sec. 2.2), classifications of wildfire models that have been presented in recent reviews are discussed first, followed by a series of topics on specific details of each class of model with a focus on the equation(s) used. One can observe the increasing complexity of equations used (Eq. (2.4)–Eq. (2.7)) from purely empirical to purely physical models. Turbulence approaches of RANS methods and LES are reviewed at the end of the modeling section in an overview fashion. In the LES part, traditional LES methods are first presented, in which filtering the governing equations and reliance on “eddy-viscosity” subgrid-scale (SGS) models are fundamental. Implicit LES (ILES), which relies on built-in numerical dissipation to achieve stability, and structural models, which attempt to reconstruct estimates of SGS quantities in order to return information to the large scale, are also introduced.

From the standpoint of operational tools, the less costly models such as empirical (or semi-empirical) models and mathematical analogues have more advantages since they are able to achieve FTRT speed and produce reasonable results. The physics-based models are devoted to capturing more erratic behaviors of larger fires. Although these models are considered slow at the present time, they are quite promising in the future since they are based on the current understanding of physics, and are continually taking advantage of increasing computational power. Therefore, physics-based CFD models with decent parallelizing features deserve many future studies. Application of turbulence models such as RANS and LES to wildfire spread modeling should draw more attention since they are considered to be pivotally important for modeling extreme fire behaviors that occur frequently in the present era and will likely occur in the future.

Chapter 3: The Wildfire Spread Model

It is almost impossible to include all intricate details of a forest, such as the presence of various plant species along with their complicated combustion chemistry, in any wildfire spread models with fast execution. However, there are several aspects that should be considered in order for a physical model to be potentially predictive. First is the effect of fuel beds on air/combustion gas flow behavior, since the dynamics of fire growth is strongly influenced by the kinematics of flow through porous vegetation, according to Meroney [112]. A fuel bed can be regarded as a porous medium with high porosity in order to account for decreased flow speed and more complicated flow behavior, as was done for forests in Garzon et al. [113] and by Séro-Guillaume and Margerit [114], but a general permeability model is preferred. Second is turbulent gusting wind, which largely contributes to the formation of extreme fire behaviors such as fire whirls. In the interest of modeling, the interaction of subgrid-scale phenomena with the turbulent buoyant thermal plume created by the fires should be captured. Third, heat release rates resulting from combustion need to be estimated reasonably according to fuel properties, porosity, etc. Fourth, ignition is significantly important for studying fire spread, but its physical mechanism is not fully understood [14]. It is expected that moisture content and humidity will have non-negligible effects on the onset of ignition. Fifth is the phenomenon of fire spotting. The multiple ignitions beyond the zone of the main fire caused by firebrands are threats to any firefighting force. Fire spotting is highly dependent on firebrand trajectory, heat transfer and physical properties (size, shape, number) of firebrands.

Current work employs a forest fire model similar to the one proposed in [24], but its submodels incorporate more physical and rigorous characteristics. At present, all five aspects discussed above have been explained in detail and implemented in

simulations. The rest of this chapter describes models employed for each of these in this study and is organized as follows. In Sec. 3.1, governing equations employed in this study are first introduced, and the underlying assumptions are briefly discussed. Then, detailed descriptions of submodels associated with turbulence, porosity, heat release rate, ignition and firebrands are presented, respectively, from Sec. 3.2 to Sec. 3.6. Finally, summary and conclusions for this chapter are provided in Sec. 3.7.

3.1. Governing equations and model features

In the current work, the generalized N.–S. equation with Darcy and Forchheimer terms is employed with regards to flow through porous fuel beds because it is widely used and found in the literature for modeling flow in porous media, e.g., Nithiarasu [115], Nield [116], Nield and Bejan [117]. Also, only gas phase equations are utilized here, similar to the formulas (Eqs. (2.7)) provided by Williams [76]. These equations are further simplified by the Boussinesq approximation, and the effects of chemical reactions are incorporated into the source term in the energy equation. Therefore, the governing equations expressing conservation of mass and balance of momentum and energy are

$$\nabla \cdot \mathbf{u} = 0 , \quad (3.1a)$$

$$\frac{\rho}{\phi} \left(\frac{\partial \mathbf{u}}{\partial t} + \frac{1}{\phi} \mathbf{u} \cdot \nabla \mathbf{u} \right) = -\frac{1}{\phi} \nabla(p_f \phi) + \mu_e \Delta \mathbf{u} + (\rho - \rho_{ref}) \mathbf{g} - D , \quad (3.1b)$$

$$(\rho c_p)_f \left(\frac{\partial T}{\partial t} + \frac{1}{\phi} \mathbf{u} \cdot \nabla T \right) = k_f \Delta T + q_f''' . \quad (3.1c)$$

It is assumed that appropriate boundary and initial conditions are provided so as to constitute a well-posed problem on some domain $\Omega \subseteq \mathbb{R}^3$ with $(\mathbf{x}, t) \in \Omega \times (t_0, t_f]$. The continuity equation shown in Eq. (3.1a) is identical in form to the one for clear fluid flow (Eq. (2.1a)), except that the velocity vector $\mathbf{u} = (u, v, w)^T$ here represents superficial (seepage) velocity that can be related to the intrinsic (or pore) velocity

$\mathbf{U} = (U, V, W)^T$ through the Dupuit–Forchheimer relationship

$$\mathbf{u} = \phi \mathbf{U} .$$

The porosity ϕ is a measure of the void spaces in a porous medium, with values in $[0, 1]$.

In the momentum equation (Eq. (3.1b)), ρ and p_f are fluid density and pressure, respectively. The Brinkman [118] term $\mu_e \Delta \mathbf{u}$ on the RHS mainly accounts for viscous effects from the wall [117]. The effective viscosity μ_e , which is largely dependent on the geometry of a porous medium, is introduced in place of the viscosity of the fluid. For an isotropic porous medium, $\mu_e/\mu = 1/\phi H_{tor}$ is obtained from a detailed averaging process and measurement by Bear and Bachmat [119], where H_{tor} is the tortuosity of the medium. For a simple situation where the tortuosity is assumed to be one, the effective viscosity is thus approximated as μ/ϕ . Moreover, based on the Boussinesq approximation (Spiegel and Veronis [120], Gray and Giorgini [121]), the buoyancy force term on the RHS can be expressed in terms of temperature differences as

$$(\rho - \rho_{ref})\mathbf{g} = \mathbf{g}\beta_e\rho(T_0 - T) ,$$

where ρ_{ref} is a reference density; β_e represents thermal expansion coefficient and T_0 is a reference temperature. The conversion of the density differential to the temperature differential is affected by using the isobaric approximation, $\rho - \rho_{ref}/\rho \approx (T_0 - T)/T$, which is not restricted to small temperature or density differences, as illustrated by Law [122]. The drag D due to porous media is expressed as

$$D = \frac{\mu}{K}\mathbf{u} + c_F K^{-\frac{1}{2}}\rho|\mathbf{u}|\mathbf{u} . \quad (3.2)$$

due to porous media. The Darcy term $-\mu\mathbf{u}/K$ models the retardation effect of a porous medium in low-speed flows, as suggested by Darcy’s law [123], which in its original form is expressed as $\partial p/\partial x = -\mu u/K$ in 1D. In the above expression, μ is the dynamic viscosity of the fluid, and K is the permeability, which is usually

obtained from an empirical equation. A theoretical permeability model that can, in principle, apply to general situations, has also been developed recently by Tang and McDonough [124]. Typically, the Darcy equation holds when the pore Reynolds number (Re_p) is small. As Re_p increases (no need to be turbulent), however, the linearity of Darcy’s law breaks down; hence, the quadratic drag as the Forchheimer term $c_F K^{-1/2} \rho |\mathbf{u}| \mathbf{u}$ is added, according to Joseph et al. [125]. Here, $|\mathbf{u}|$ represents the velocity magnitude, and c_F is a friction factor commonly known as the Ergun [126] coefficient.

In the thermal energy equation, Eq. (3.1c), the subscript f represents fluid phase; T is temperature, and c_p is specific heat at constant pressure. If mass transfer must be considered, thermal conductivity k_f can be replaced by mass diffusivity. In the case of isotropic media, it is a scalar; for an anisotropic medium, \mathbf{k}_f will be a second-rank tensor. The heat source term q''' represents heat generation or heat release rate (HRR) from combustion and radiation heat transfer. The estimation of HRR will be presented in detail in Sec. 3.4. Radiation can be calculated based on the Stefan–Boltzmann law or simply approximated as one-third of the heat source [35]. As discussed in Sec. 2.1.3, radiation is not considered to be as significant as is convection in massive fire spread; thus a relatively crude model is assumed to suffice for the radiative effects in the overall wildfire model. This also avoids the considerable arithmetic required for solving the radiation transport equation, as is done in FDS, which is a tradeoff for the time of simulation.

Finally, it is recognized that Eqs. (3.1) are controversial in some respects. For example, some argue that the advective inertial term in the momentum equation should be omitted since inertial effects are already included in the quadratic drag term; however, considering that the advective inertial term is related to the modeling of turbulence, it should remain [116]. Also, Hooman et al. [127], based on a series of scale analyses, argue that the viscous dissipation terms coming from the drag force

terms should not be neglected in the energy equation. Nevertheless, these terms are neglected in Eq. (3.1c) since incompressible flow with low velocities is dealt with here. In addition, Eqs. (3.1) can also be deduced from the rigorously derived VAT (volume averaging theory) equations, according to Whitaker [128] and Sbutega [129]. The VAT method takes advantage of length scale disparities to describe pore scale and representative elementary volume scale effects. Variables are decomposed into averaged and fluctuation parts to account for the two scales. The derivation procedure resembles RANS (Reynolds-averaged N.-S.) treatments in turbulence modeling, but it uses different assumptions. This results in an equation with fluctuation and integral terms that need closures. Although it is possible to model flow in porous media without employing permeability based on the VAT method (Travkin and Catton [130]), the accuracy of the model is strongly dependent on the closure length scale of a drag coefficient, which has a direct correlation with the commonly used permeability tensor. Also, note that the theoretical techniques employed here for calculating permeability could possibly be applied to close the VAT method.

3.2. Synthetic-velocity large-eddy simulation

Synthetic-velocity LES can be regarded as a heterogeneous multi-scale method [22]—a general methodology for the efficient numerical computation of problems with multi-scales and multiphysics on multigrids (Weinan and Engquist [131]). Different forms of synthetic-velocity LES were introduced in Ch. 2, Sec. 2.2.7. Among these forms, the chaotic-map SGS model, first proposed by McDonough et al. [110], and later studied by Hylin and McDonough [132], is employed in the present study. This SGS model is different from any eddy-viscosity based methods where the Boussinesq hypothesis is being used, and it is anticipated to work well, especially when interacting with other physics. Moreover, it requires minimal arithmetic since only algebraic equations are used. The chaotic-map SGS model was also applied to turbulence-chemical kinetics

interactions by McDonough [133], to a swirling buoyant plume by McDonough and Yang [134], and to a combustion process by Zeng [135]. Such methods differ from traditional LES in three main aspects (see McDonough [136]): 1) solutions are filtered rather than the equations of motion; 2) SGS physical variables are modeled; 3) subgrid-scale results are directly added to those from the resolved scales based on the LES decomposition written as

$$q(\mathbf{x}, t) = \tilde{q}(\mathbf{x}, t) + q^*(\mathbf{x}, t) , \quad (3.3)$$

where \tilde{q} represents filtered variables and q^* the high-wavenumber parts. There are numerous advantages arising from such an approach, and each of the three aspects will be discussed in the subsequent sections.

3.2.1 Explicit filtering

The process of explicit filtering (filtering solutions) allows modeling physical variables directly, rather than having to model SGS stresses (statistics) that are often related to filtering equations (or implicit filtering). Since implicit filtering is not sufficient to remove all aliasing effects due to under-resolution, the artificial dissipation (typically provided by highly-dissipative, eddy-viscosity based turbulence models) is always needed to damp the spurious oscillations associated with aliasing. On the other hand, explicit filtering can remove unnecessary high-wavenumber content to stabilize solution of the N.-S. equations without using SGS stress models. Furthermore, in generalized coordinates, filtering equations is formally difficult because of commutation errors arising from commuting differentiation and the filtering operator when it is applied to the differential equations [137]; however, generalized coordinates have no effect on filtering solutions. Filtering solutions, however, can give rise to additional errors, especially in the context of generalized coordinates, and the errors must be controlled. Filtering solutions also suggests a direct numerical application of mollification, as done theoretically in modern analytical partial differential equation

(PDE) theory. Mollification is convolution of the PDE solution with a C^∞ function to smooth a not very regular solution to a point permitting classical analysis. Mollification is applied to solutions in conjunction with the solution operator. The mollified variables are constructed as [136]

$$u_\epsilon(\mathbf{x}, t) = \int_{-\epsilon}^{\epsilon} u(\xi, t) \delta_\epsilon(x - \xi) d\xi, \quad (3.4)$$

where δ_ϵ is a normalized C^∞ function with compact support in $[-\epsilon, \epsilon]$, and is given by

$$\delta_\epsilon = C_\epsilon e^{-1/(\epsilon^2 - x^2)},$$

with C_ϵ being a normalization constant. Equation (3.4) corresponds to a filter with kernel δ_ϵ ; it is similar, but not identical, to the Gaussian filter that is widely used in LES of turbulence. Based on this, the numerical mollification process that can be composed with discrete solution operators is constructed to provide additional dissipation needed to damp aliasing effects.

One such filter is that of Shuman [138] filter, originally given only in 1D, but which can be extended to 3D as

$$\tilde{u}_{i,j,k} = \frac{u_{i-1,j,k} + u_{i,j-1,k} + u_{i,j,k-1} + \beta_f u_{i,j,k} + u_{i+1,j,k} + u_{i,j+1,k} + u_{i,j,k+1}}{6 + \beta_f}, \quad (3.5)$$

with β_f the filter parameter. This shows that Shuman filter is a weighted average of the nearest-neighbor solution values. It is clear that as $\beta_f \rightarrow \infty$, $\tilde{u}_{i,j,k} = u_{i,j,k}$, indicating no filtering is being done. Expanding, $u_{i-1,j,k}$, $u_{i,j-1,k}$, \dots , etc., in Taylor series, and substituting them into Eq. (3.5) yields

$$\tilde{u}_{i,j,k} = u_{i,j,k} + \frac{h^2}{6 + \beta_f} (u_{xx} + u_{yy} + u_{zz})|_{i,j,k} + \mathcal{O}(h^4). \quad (3.6)$$

This shows that the dominant truncation error is diffusive, and the actual amount of added diffusion is controllable through the filter parameter and the grid spacing h ; the $\mathcal{O}(h^4)$ term is anti-diffusive, leading to some cancellation of the effects of second order.

In addition, the wavenumber response shows that for small values of β_f , the high-wavenumber content of the Fourier representation is almost completely removed; however, it should not be too small since it would also remove some useful high-wavenumber information. As β_f increases, less of the original Fourier coefficients are removed by the filter. If the filter parameter is infinitely large, it does not filter any high-wavenumber parts. Moreover, as noted above, the error caused by filtering can also be controlled with the parameter β_f , and it has been found that this is adequate to guarantee the robust behavior of this treatment of aliasing. Therefore, an appropriate value of this parameter that could remove the correct amount of aliasing, as well as stabilize the algorithm, should be used, and currently, it must be found from numerical experiments. Another filter that is available in the current solver is the Padé filter introduced by Liu et al. [139]. The optimized high accuracy and maximum resolution (HAMR) scheme as an asymptotically stable Padé filter featuring low dispersion is discussed and used in [139].

Specifically, two explicit filtering processes are required in the current solution procedure for turbulent flows. The first one is a low-pass filter applied to the solution before projecting the velocity field to a divergence-free subspace, in order to treat the cell- Re problem and remove aliasing as discussed above. The second is to high-pass filter the large-scale solution, for the purpose of approximating SGS variables based on what is termed “scale similarity” [140] (an assumption that the behavior at the lowest wavenumber part of the unresolved part is similar to that of the highest wavenumbers of the resolved scale). It is natural to consider that the cut-off wavenumber for the second filter should be smaller than the corresponding wavenumber for the first filter. Both Shuman and Padé filters can be used in the two filtering processes. For the case of Shuman filter, the filter parameter β_f for the second filtering should be smaller than that of the first filtering, and both filter parameter values need to be found through trial and error. Padé filters have been used for both low-pass and a high-pass filtering

for compressible turbulent flow, with different sets of filter coefficients, as done by Strodtbeck [47], and for incompressible turbulent flows, as done by Liu [141]. In the present study, only Shuman filters are employed.

3.2.2 Small-scale calculations

As stated previously, the small-scale variables are calculated directly, permitting modeling interactions of flow physics with other phenomena on sub-grid scales. It is essentially impossible to obtain these interactions when employing techniques based on statistical correlations as in typical LES and RANS methods. Although direct modeling of SGS physical variables is considered very difficult to implement, it should improve accuracy, and be computationally efficient—if good models are constructed. In the present study, the construction modified by McDonough [142] from the original form in [110] is utilized. The small-scale flow variable q_i^* (see Eq. (3.3)) is expressed as

$$q_i^* = A_i M_i, \quad i = 1, \dots, N_v, \quad (3.7)$$

where N_v is the total number of small-scale dependent variables; A_i is the amplitude of the i^{th} variable. The chaotic map M_i can exhibit bifurcations leading to a strange attractor, thus producing small-scale turbulent temporal fluctuations; it is scaled to be in the range of $[-1, 1]$. After obtaining q_i^* at all resolved scale grid points, this portion of the solution vector should also be projected onto a divergence-free subspace—as is the case for velocity components computed from essentially any form of Eqs. (2.1) or Eqs. (3.1) on any scale. The projection procedure is the same as used on the large scale, as will be discussed in detail in the next chapter. Calculations of amplitude factor and the fluctuation are presented in the following subsections.

Amplitude factor. Amplitude factor is computed, for each i^{th} dependent variable on each grid point, based on the generalized Kolmogorov power laws, as described

by McDonough and Holloway [143]. Firstly, the formula for the amplitude factor, related to energy $E_i(k_i)$, can be expressed as

$$A_i = \left[\sum_{k=k_T}^{k_T+N} E_i(k_i) \right]^{1/2}$$

by using information from the high-wavenumber part of the large-scale variables and structure functions. Here, $E(k) = C_s \langle \varepsilon \rangle^{\beta_s} k^{-(\beta_s+1)}$. The coefficient C_s and exponent β_s are calculated from a least-squares minimization of the difference between the structure functions. Statistical averages are needed to calculate the structure function of energy. Specifically, the second-order structure functions are expressed as

$$S_2(q_i^{**}, r) \simeq \langle (q_i^{**}(\mathbf{x} + \mathbf{r}) - q_i^{**}(\mathbf{x}))^2 \rangle, \quad i = 1, \dots, N_v,$$

where q_i^{**} is high-pass filtered dependent variable computed as $\tilde{q}_i - \tilde{\tilde{q}}_i$. The average $\langle \cdot \rangle$ is taken over all discrete points of the large-scale finite-difference grid at a distance r from the current point $x_{i,j,k}$ in a 3-D cube containing 27 grid points with $x_{i,j,k}$ at the center; thus there are only four possible values of r .

Wavenumber k_T is calculated from the Taylor microscale length in each resolved-scale grid cell as

$$k_T = \left[\sum_{i=1}^3 \left(\frac{1}{\lambda_i} \right)^2 \right]^{1/2}, \quad \text{with} \quad \lambda_i \simeq \left[\frac{\nu \langle u_i^{**} \rangle}{\langle \varepsilon \rangle} \right]^{1/2}.$$

Here, u^{**} is the high-pass filtered i^{th} velocity component, and $\varepsilon = 2\nu ||\mathbf{S}^{**}||^2$ with ν being the viscosity and $||\mathbf{S}^{**}||$ being the magnitude of the high-pass filtered velocity strain rate. N is prescribed, usually as 10. As seen, the calculation of amplitude factor requires considerable formulas and arithmetic. A possible alternative would be the use of only amplitudes of high-pass filtered variables since these already represent the largest energy contribution of the small-scale part.

Temporal fluctuations. The temporally fluctuating part of small-scale velocity can be modeled using a discrete dynamical system (DDS). The DDS employed here

is called the “poor man’s Navier–Stokes (PMNS) equation”, and was originally described as a simple quadratic map, $x^{(n+1)} = 1 - 2x^{(n)}$, by Frisch [92]. The analysis was based on comparing terms of a rearrangement of the map with those of the Navier–Stokes (N.–S.) equations, which indicated a direct connection of such logistic maps with N.–S. turbulence. McDonough and Huang [144] then derived the PMNS equations through a Galerkin procedure and obtained the following 2-D system of coupled logistic maps,

$$a^{(n+1)} = \beta_1 a^{(n)}(1 - a^{(n)}) - \gamma_1 a^{(n)}b^{(n)} , \quad (3.8a)$$

$$b^{(n+1)} = \beta_2 b^{(n)}(1 - b^{(n)}) - \gamma_2 a^{(n)}b^{(n)} . \quad (3.8b)$$

It has been found that this discrete map may produce essentially any temporal behavior observed either experimentally or computationally in incompressible N.–S. flows, as the bifurcation parameters β s and γ s in Eqs. (3.8) are varied. Bible and McDonough [145] investigated the effects of changing initial conditions on the system basins of attraction and observed fractal basins associated with “strange attractors.” A discussion regarding the connection of such DDSs with the physics of turbulence is presented by McDonough et al. [146], along with results from anisotropic cases. Polly [147], Polly and McDonough [148] extended the system to 3-D, with a more complicated structure and more bifurcation parameters, and discovered that the system behavior is at least slightly different from that of the 2-D system. It has been shown by McDonough [149] that the 3-D system can lead to scaling for the turbulence kinetic energy spectrum in accord with Kolmogorov’s K41 theory (see, e.g., [92]). Moreover, the compressible 3-D poor man’s Navier–Stokes equations have been studied by Strodtbeck et al. [150], who show that a full range of dynamical behavior associated with physical turbulence from low subsonic to fully supersonic Mach numbers is exhibited. Strodtbeck [47] also provides derivation of, and results for, a “synthetic-velocity” model based on the compressible PMNS equations. Specific details of PMNS equations in porous media will be discussed in Ch. 5.

After obtaining the PMNS equations for different flow situations, the set of equations (e.g., Eqs. (3.8)) is iterated a number of times during each resolved-scale time step. This number is set by using a small-scale time scale calculated as $\tau = 1/||\mathbf{S}^{**}||$. The results of integrating this DDS across the large-scale time step are associated with the M_i s in Eq. (3.7) as (take 2-D PMNS Eqs. (3.8), as an example)

$$M_1 = a, \quad M_2 = b ,$$

and these components require rescalings, since the restriction of $|M_i| \leq 1$ is required to make the use of amplitude factors A_i s reasonable.

3.2.3 The complete solution

Since a poor model (and/or its incorrect implementation) could lead to inaccurate results (and/or destabilization of numerical methods employed), rigorous mathematical analyses are important. Therefore, a multi-scale mathematical formalism is required to produce the complete solution [131]. From the preceding treatment, both $\tilde{q}(\mathbf{x}, t)$ and $q^*(\mathbf{x}, t)$, separately, have been constructed to be consistent with the corresponding Hilbert subspace quantities. Recall from the LES decomposition in Eq. (3.3), that the large-scale variable is obtained from solving the unfiltered N.-S. equation on a relatively coarse grid as

$$(\tilde{\mathbf{u}} + \mathbf{u}^*)_t + (\tilde{\mathbf{u}} + \mathbf{u}^*) \cdot \nabla (\tilde{\mathbf{u}} + \mathbf{u}^*) = \nabla (\tilde{p} + p^*) + \nu (\tilde{\mathbf{u}} + \mathbf{u}^*) , \quad (3.9a)$$

$$\nabla \cdot (\tilde{\mathbf{u}} + \mathbf{u}^*) = 0 , \quad (3.9b)$$

similar to the ILES method or under-resolved DNS; but $q^*(\mathbf{x}, t)$ —here identified with u^* is computed separately, as given in the preceding analyses. The same treatment is also applied to any additional physical quantities, e.g., temperature. It is seen that if a consistent discretization (time and space) is applied to Eqs. (3.9), then $\mathbf{u}^*, \mathbf{p}^* \rightarrow 0$ as $dt, h \rightarrow 0$, which implies that the synthetic-velocity approach satisfies the numerical-analytical consistency. Nevertheless, consistency does not imply stability, and it is

often observed that small-scale perturbations arising in multi-scale algorithms lead to destabilization of the underlying numerical method.

In the current solver, the q s are required to satisfy the same discrete equations as do the \tilde{q} s. However, the q^* s are produced with a completely separate algorithm from that of the \tilde{q} s, leading to the conclusion that the time-derivative information is needed for the q^* s. Specifically, the numerical scheme for the large-scale part of the solution is expressed as

$$\tilde{q}^{n+1} = \tilde{q}^n + \Delta t \tilde{F}(\tilde{q}^n), \quad (3.10)$$

where \tilde{F} represents the discrete solution operator for the large-scale solution. For the complete solution operator, synthetic-velocity LES, or other similar heterogeneous multiscale methods (HMM), takes the form

$$q^{n+1} = q^n + \Delta t F^\varepsilon(q^n), \quad (3.11)$$

where F^ε is the discrete solution operator for the complete solution. Subtracting Eq. (3.10) from Eq. (3.11) yields

$$q^{n+1} - \tilde{q}^{n+1} = q^n - \tilde{q}^n + \Delta t [\tilde{F}(q^n) - \tilde{F}(\tilde{q}^n)] + \Delta t [F^\varepsilon(q^n) - \tilde{F}(q^n)]. \quad (3.12)$$

It is suggested [131] that \tilde{F} should be chosen so that it is stable and the difference $F^\varepsilon - \tilde{F}$ should be minimized. Recalling Eq. (3.3), the following temporal difference must hold:

$$q^{n+1} - q^n = \tilde{q}^{n+1} - \tilde{q}^n + dq^* \quad (3.13)$$

in order to obtain consistency for the complete solution operator. Namely, during the actual numerical procedure, the large-scale part of the solution at the new time step is calculated as (using trapezoidal integration for Eqs. (3.9))

$$\tilde{q}^{n+1} = q^n + \Delta t \tilde{F}(q^n) - dq^*, \quad (3.14)$$

where dq^* is time integration of small-scale parts. Here, F^ε is taken to be the same as the one for the large-scale part \tilde{F} , as was done in [137]. Thus, the last

term in Eq. (3.12) is zero, and by comparing Eq. (3.12) and Eq. (3.13), $d\mathbf{q}^* = \Delta t [\tilde{F}(\mathbf{q}^n) - \tilde{F}(\tilde{\mathbf{q}}^n)]$ is obtained. Moreover, the term $\Delta t F^\varepsilon(\mathbf{q}^n)$ in Eq. (3.11) equals $\Delta t \tilde{F}(\mathbf{q}^n)$ in Eq. (3.14), and by substituting the RHS of Eq. (3.11) into Eq. (3.14), the following form is acquired,

$$\mathbf{q}^{n+1} = \tilde{\mathbf{q}}^{n+1} + d\mathbf{q}^* . \quad (3.15)$$

Therefore, a consistent time evolution is obtained by employing Eq. (3.15), and the stability problem that otherwise would occur is remedied.

3.3. Porosity of fuel beds

A forest is often represented as a porous medium with three levels of inhomogeneity in the vertical direction to account for undergrowth (shrubs, grasses, etc.), tree trunks, and crown canopies, respectively, as shown in Fig. 3.1. Each of these regions has very high, but different, porosity. Garzon et al. [113] postulated that the porosity is quite

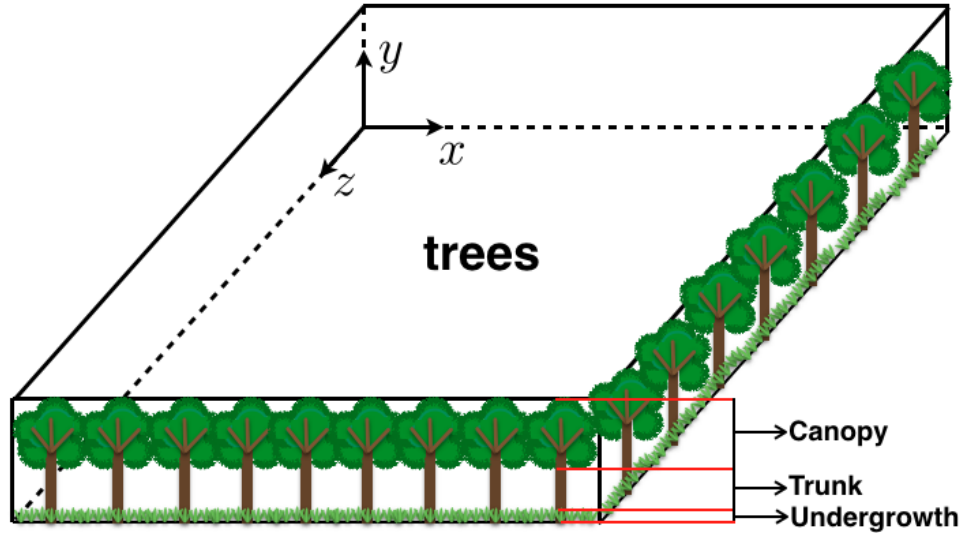


Figure 3.1: Description of a typical forest model.

high near the ground, but generally less so than in the intermediate heights where there are mainly only tree trunks. The porosity at the upper leafy crown level can be

expected to be the lowest of the three regions, but still high. Since porosity for trees is very complex to deal with, it is assumed to be similar to the porosity of fur (on mammals) [113], which ranges from 0.95 to 0.99 (see Table 1.1, Bejan [151]). These values are much larger than the areal porosities (of shelterbelts or forests), which are defined as the area of void per hectare at a given height in a two-dimensional context, rather than volume. Usually, they are estimated by pixels via remote sensing (Perkin and Macfarlane [152] and Dubrasich et al. [153], etc.). As computer power increases, more sophisticated porous medium models with different porosities, both horizontally and vertically, should be considered with proper permeability to account for more physics of flow in forests. In the present study the porosity of each part, which is defined as the ratio of pore space to the total space occupied by tree components, is estimated using typical forest and botanical data available in the literature. The calculated values are expected to be within a reasonable range considering variations of tree types, leaf area index (LAI), canopy height, etc.

Two representative forests are analyzed: the temperate coniferous forest and the temperate deciduous forest. Only simple stands with one dominant species are considered here. The complex stands, e.g., stand A in Table 1 of [153] with a mixing of deciduous and coniferous trees, will be studied in the future. Stand descriptions of both coniferous (Douglas-fir) and deciduous (ash) forests used in the present study are displayed in Table 3.1, as given by Eriksson et al. [154] and by Dubrasich et al. [153]. In Table 3.1, dbh denotes diameter measured at breast height; basal area is the total cross-sectional area of trees at breast height. The stand densities (for both forests) used here are much larger than those from the original source [154] [153], but still reasonable, in order to simulate forests with higher possibilities of wildfire occurrences. LAI is defined as one-sided green leaf area per unit ground surface area. For ash tree forests, 3.6 is a reasonable value of the canopy LAI [154]; for Douglas-fir dominated coniferous forests, Thomas and Winner [155] estimated that LAI is 6 for

the tree crowns, and 1.2 contributed from the undergrowth part.

Table 3.1: Stand descriptions of typical forests.

Stand description	Symbol	Deciduous	Coniferous
Tree species	—	Ash	Douglas-fir
Tree height (m)	H	15	38
dbh (cm)	d_b	20	23
Stand density (trees/ha ^a)	ρ_{std}	2400	2400
Basal area (m ² /ha)	A_b	75.36	99.66
Crown diameter (m)	d_c	4.3	3.15 ^b
Crown depth (m)	H_c	5.2	20 ^c
Crown LAI	a_c	3.6	6

^a1 ha = 10000 m²

^bCorresponding crown area is 8000 m²/ha (see Fig. 1(f) of [153]).

^cHeight for $\leq 90\%$ mean areal porosity (see Fig. 3(f) of [153]).

Trunk. Porosity of the intermediate level—trunks—is firstly estimated because of its relative simplicity in shape and composition compared with the crown and undergrowth. Assuming tree trunks to be cylinders, the volume of each trunk can be calculated by multiplying trunk height times cross-sectional area. Thus, the porosity is obtained as

$$\phi_t = \frac{AH_T - A_b H_T}{AH_T} = 1 - \frac{A_b}{A} ,$$

where A_b is basal area, which can be calculated from dbh as $A_b = (d_b/2)^2 \pi N$; A is the total area of one hectare; $H_T = H - H_c$ is trunk height. Observe that H_T can be canceled out in this formulation and ϕ_t is only dependent on the basal area.

Canopy. Both leaf (or needles for coniferous trees) and branch volume are considered for estimating porosity in the crown canopy. Usually, only the inter- or between-crown porosity is obtained by assuming crowns to be solid [153]. Here, the total voids in both the inter- and within- crowns are considered. The total volume of leaves V_{cl} is represented as

$$V_{cl} = a_c A_{cl} \delta_t \rho_{std} .$$

The crown area A_{cl} is the area beneath the crown of a tree, and can be expressed as $A_{cl} = (\text{average maximum crown spread})^2 \times CF \times \pi/4$, with CF being the “crown form” calculated from the crown shape ratio. Here, CF is taken as 0.480 for Douglas-fir trees that are in “columnar” form, and as 0.549 for ash trees that have shapes from “elongate spade” to “rounded and oval”, according to Frank [156]. The average maximum crown spread is taken to be the crown diameter d_c . The leaf thickness δ_t for both ash and Douglas-fir trees are estimated to be similar to those of peppermint willow (*Agonis flexuosa*), which are around 700 μm (see Table 4 of Witkowski and Lamont [157]); ρ_{std} is stand density, as shown in Table 3.1.

Next, volume of branches is calculated using the general information of branch order, length, and number. The bifurcation ratio of tree branches is found to be analogous to that of river branches, as studied by Leopold [158]; both deciduous (ash) and coniferous (fir) trees were investigated. In Table 3.2, branch orders from one to five denote different generations of tree branches. For instance, branch of order five ($i = 5$) is actually the trunk with number n_{b5} of 1 and diameter d_{b1} of dbh. The number of branches n_{bi} at each order can be obtained using the bifurcation ratio b_r . The branch length l_{bi} at each order is calculated from the length ratio l_r . For deciduous trees, $b_r = 6.5$, and $l_r = 3.4$; for coniferous trees, $b_r = 4.8$, and $l_r = 2.7$ [158]. The branch diameter d_{bi} in each order is calculated through the log ratio relation provided by Niklas [159] using the formula:

$$\log_{10} \left(\frac{l}{L} \right) \sim c_b \log_{10} \left(\frac{d}{D} \right) ,$$

where c_b is a geometry-related coefficient usually taken to be 1 or 3/2, according to [159]. Table 3.2 shows the diameter values calculated from both $c_b = 1$ (d_{bi}) and $c_b = 3/2$ (d_{bi}^*).

Assume branches are cylindrical with cross-sectional diameter d_{bi} ; the branches

volume in one hectare is calculated as

$$V_{cb} = \sum_{i=1}^5 (d_{bi}/2)^2 \pi l_{bi} n_{bi} \rho_{std} ,$$

with i representing order one to five. Recall that at the canopy height H_c , the porosity is given as

$$\phi_c = \frac{AH_c - V_{cl} - V_{cb}}{AH_c} .$$

Table 3.2: Branch information for deciduous and coniferous trees.

Forests	Order	n_{bi}	$l_{bi}(m)$	$d_{bi}(cm)$	$d_{bi}^*(cm)$
Deciduous	5	1	15	20	20
	4	6.5	4.4	5.86	8.83
	3	42	1.3	1.73	3.92
	2	274	0.38	0.5	1.73
	1	1785	0.11	0.147	0.75
Coniferous	5	1	38	23	23
	4	4.8	14	8.48	11.82
	3	23	5.2	3.15	6.11
	2	110	1.93	1.15	3.15
	1	531	0.715	0.43	1.63

Undergrowth. The porosity of undergrowth is determined by calculating volumes of leaves and grass stems. The volume of woody species ($dbh < 5$ cm) may be neglected since its density (trees/ha) is not as large. The total leaf volume is

$$V_{gl} = a_{gl} A_{gl} \delta_t ,$$

where a_{gl} is LAI for the grassland with a typical value of 1.2; A_{gl} is the area of the grassland. It is found that the LAI of undergrowth depends on that of the canopy, and the total leaf area in forest ecosystems with deciduous trees is approximately constant (see Satoo and Madgwick [160]). For the sake of simplicity, only one dominant type of grass is considered here for both deciduous and coniferous woodlands, in spite of the

fact that a diversity of species exist in the undergrowth, and that their developments are dependent on the canopy growths. Biomass properties of other fuel types can also be input into the current solver. Assume “rough horsetail” (*Equisetum hyemale*) is the dominant grass; it is 0.3 cm in diameter, and 55 cm in height, as measured by Niklas [161]. The grass stem density ρ_{grs} is estimated to be 2000 stems/m², which is within the values of around 1380–2680 stems/m² for different soil types and grass species, as provided by Dokken and Hulbert [162]. The stem volume is calculated as

$$V_{gs} = (d_{gs}/2)^2 \pi H_g \rho_{grs} .$$

The average height of undergrowth H_g is the same as the “rough horsetail” grass, so the porosity is expressed as

$$\phi_g = \frac{AH_g - V_{gl} - V_{gs}}{AH_g} .$$

A summary of properties and porosities used for computation to be presented here is shown in Table 3.3. It is seen that these values are very high and are approximately the ones used by Garzon et al. [113]. Porosity of coniferous forests has slightly smaller values than that of deciduous forests, but this is not a unique case. Also, the leaf volume of coniferous trees is smaller than that of the deciduous trees, even though their LAI is larger, because the crown diameter for Douglas-fir trees is smaller. Once porosities are obtained, permeabilities are obtained automatically through a general relationship with porosities, as proposed by Tang and McDonough [124] (which will be presented in Ch. 6), rather than employing “guessed” constant values or empirical equations as is often tried [113].

3.4. Heat release rate

One of the techniques to estimate heat release rate (HRR) per unit volume (S_c), as suggested by Biteau et al. [163], is to use the expression

$$S_c = \Delta H_c \dot{m} , \tag{3.16}$$

Table 3.3: Summary of estimates.

Stand description	Symbol	Deciduous	Coniferous
Undergrowth (m)	—	0~0.3	0~0.3
Trunk (m)	—	0.3~9.8	0.3~18
Canopy (m)	—	9.8~15	18~38
Canopy height (m)	H_c	5.2	20
Canopy leave volume (m ³ /ha)	V_{cl}	48.2	37.69
Canopy branch volume (m ³ /ha)	V_{cb}	1049	5190
Grass height (m)	H_g	0.55	0.55
Grass leave volume (m ³ /ha)	V_{gl}	8.4	8.4
Grass stem volume (m ³ /ha)	V_{gs}	77.7	77.7
Porosity undergrowth	ϕ_g	98.43%	98.43%
Porosity trunk	ϕ_t	99.25%	99.00%
Porosity canopy	ϕ_c	97.89%	97.39%

where ΔH_c (kJ/kg) is the heat of combustion of the material, and \dot{m} (g/s) represents the burning rate. However, neither the biomaterial nor the burning rate is fully understood in the context of wildfire spread although numerous studies have been conducted on burning rates of wood cribs and match sticks, e.g., McAllister and Finney [164]. Since burning rates are found to be affected by multiple factors such as porosity, heat flux, and wind speed, a completely accurate estimation is almost impossible. One of the proposed equations to estimate burning rates of porous wood cribs is

$$\frac{\dot{m}}{A_s b_s^{-0.5}} = f(\phi^*) , \quad (3.17)$$

with A_s being the exposed surface area of the sticks, and b_s as the stick thickness. The RHS f denotes a function of “porosity” ϕ^* (not dimensionless) defined by Heskestad [165] as

$$\phi^* = \left(\frac{A_v}{A_s} \right) s^{1/2} b^{1/2} , \quad (3.18)$$

where s is the spacing between sticks, and A_v represents the vent or open area of the crib shafts.

For a loosely-packed porous medium, $f(\phi^*)$ is approximated by unity; thus the burning rate per unit surface area \dot{m}'' is estimated as

$$\dot{m}'' \sim b^{-n}, \quad (3.19)$$

where n is an empirical exponent with values 0.5 or 0.6 [165]. For under-ventilated cases, the following equation [164] [165]

$$\frac{10^3 \dot{m}}{A_s b^{-0.5}} = 1 - \exp[-50\phi^*] \quad (3.20)$$

is employed. Note that both well-ventilated and under-ventilated cases exist in forested regions. In what follows, properties of the burning rate per unit area, mass loss rate, heat release rate, and burning time for each level (trunk, canopy, and undergrowth) are calculated using Eqs. (3.16), (3.18)–(3.20). Here only oven-dry materials are considered; the treatment of moisture will be discussed in Sec. 3.5 for ignition modeling.

Trunk. In Table 3.4, the density and low heating value (LHV) of the wood for both deciduous/hardwood (black ash tree) and coniferous/softwood trees (Douglas-fir) are given, according to the documented values provided by Phyllis2 [166]. Using Douglas-fir as an example, the trunk diameter is 23 cm, as shown in Table 3.1. Since the spacing between trunks is relatively large compared to their diameter, Eq. (3.19) is used, resulting in burning rate per unit surface area given as $\dot{m}'' = 0.23^{-0.5} = 2.085$ g/s·m². This value is of the same order of magnitude as those given by Tran and White [167], where \dot{m}'' s are somewhat larger owing to smaller thicknesses of the materials considered.

The following calculation is based on one typical fuel in a grid cell in the trunk region. The volume is $dx dy dz = 4 \times 1 \times 4 = 16$ m³ with dx , dy , dz representing the grid spacing in each direction (see Cartesian coordinates of Fig. 3.1). According to the stand density (trees/ha) given in Table 3.1, there are 3.84 trees in one grid cell.

The surface area of trunks (in one grid cell) is calculated as $0.23\pi dy \times 3.84 = 2.77 \text{ m}^2$, resulting in a mass loss rate of $2.77 \times 2.085 = 5.78 \text{ g/s}$. Also, by multiplying the volume by the density, the total mass is calculated as $(0.23/2)^2 \pi dy \times 3.84 \times 530 = 84.5 \text{ kg}$, and the burn time is $84.5/5.78 \approx 4.06 \text{ h}$. Substituting the heat of combustion and burning rate into Eq. (3.16), the heat release rate per unit volume is estimated to be $19 \times 5.78/16 = 6.9 \text{ kW/m}^3$. This value is rather small compared with the value of 1200 kW/m^3 estimated from scaling analyses of pool fires [168], and is used in the FDS [20]. Nevertheless, it appears to be reasonable considering the sizes of trunks and the stand's porosity. Also, crown and surface fires play more important roles in wildfire spread since they burn more rapidly. Properties for deciduous forests are also obtained through the same calculation procedure, and the results are provided in Table 3.4.

Table 3.4: Properties of a typical trunk fuel grid cell.

Stand description	Deciduous	Coniferous
Density (kg/m^3)	540	530
Low heating value (MJ/kg)	17.82	19
Surface area (m^2)	2.4	2.77
Mass (kg)	65	84.5
Burning rate ($\text{g/s}\cdot\text{m}^2$)	2.24	2.085
Mass loss rate (g/s)	5.38	5.78
Heat release rate (kW/m^3)	6	6.9
Burning time (h)	3.6	4.06

Canopy. For the sake of simplicity, the same density and heat of combustion are used for branches and leaves as that of the trunk wood, since all of these are mainly composed of cellulose, lignin, and hemicellulose [157]. Similar to the previous treatment for trunks, Douglas fir and a canopy grid cell (with the same size of the trunk cell) are used as examples for the calculation. First, its surface area of leaves (two-sided) is calculated from the LAI and the crown area as $6 \times A_{crown} \times 2 \times 3.84 \times dy/H_c =$

8.6 m²; the mass of leaves is $8.6/2 \times 0.0007 \times 530 = 1.6$ kg. Although LAI of coniferous woods is larger than that of deciduous forests, its surface area of leaves in one grid cell is much smaller, as shown in Table 3.5. The reason is that the canopy height of deciduous trees is much smaller, indicating more leaves appear in one layer (or one grid cell) with fixed LAI. Leaves are assumed to have the same \dot{m}'' as branches for simplicity since they are both biomaterials in the canopy.

Next, burning rate of branches is calculated. Take the branch number as 110 (for example see Table 3.2); the spacing between branches is between $4/(110 \times 3.84) = 0.947$ cm and $4/\sqrt{110 \times 3.84} = 19.46$ cm. The ratio A_v/A_s is assumed to be 0.01, which is within the range of [0.004, 0.06] obtained from similar stick spacings in [164]. For $s = 0.947$ cm, the branches are considered as under-ventilated, and the Heskestad porosity ϕ^* is calculated as $3.15^{0.5} \times 0.95^{0.5} \times 0.01 = 0.0173$ cm. Therefore, the corresponding burning rate is $\{1 - \exp[-50 \times 0.0173]\} \times 0.0315^{-0.5} = 3.26$ g/s·m² by employing Eqs. (3.18) (3.20). For $s = 19.46$ cm, $f(\phi^*)$ is 0.98, indicating that the branches are well-ventilated, and the burning rate is 5.52 g/s·m² using Eq. (3.20); Eq. (3.19) can also be used in this case. Then, the average value of $(3.26 + 5.63)/2 = 4.4$ g/s·m² is adopted as the burning rate for $n_{b2} = 110$ (Table 3.2). Similarly, for the branch number 531, an average burning rate of 4.3 g/s·m² is obtained. The overall burning rate for the branches is obtained from averaging over burning rates of all branch orders using their surface area as weighting factors. By employing the same calculation procedure as that for the trunks, the mass loss rate, burn time, and heat release rate of the canopy are obtained and provided in Table 3.5. It is seen that for coniferous forests, the heat release rate decreases from 903.7 to 860.8 kW/m³ after 44.3 sec. For deciduous woods, the heat release rate decreases from 1356.6 to 1160 kW/m³ after 44.8 sec. These values are close to the value used by Himoto and Tanaka [169], and in [168], [20], as discussed previously.

Table 3.5: Properties of a typical canopy fuel grid cell.

Stand description	Deciduous	Coniferous
Leaves/needles surface area (m ²)	42	8.6
Leaves/needles mass (kg)	7.9	1.6
Leaves/needles burning rate (g/s·m ²)	4.2	4.2
Leaves/needles mass loss rate (g/s)	176.4	36.1
Leaves/needles heat release rate (kW/m ³)	196.5	42.9
Leaves/needles burning time (s)	44.8	44.3
Branch surface area (m ²)	248	172.6
Branch mass (kg)	550	728
Branch burning rate (g/s·m ²)	4.2	4.2
Branch mass loss rate (g/s)	1041.6	724.9
Branch heat release rate (kW/m ³)	1160.1	860.8
Branch burning time (min)	8.8	16.7

Undergrowth. The heat of combustion for grasses is estimated to be 16.9–17.3 MJ/kg, and the density of general grass leaves is around 427–628 kg/m³, according to Phyllis2 [166]; here values of 17 MJ/kg and 500 kg/m³ are used, as presented in Table 3.6. Leaves and stems are assumed to have the same biomass properties because of their similar composition. The following calculation is based on a typical grass grid cell with a volume of $4 \times 4 \times 0.55 = 8.8$ m³. Since LAI is 1.2 (see Sec. 3.3), the surface area of grass leaves (two-sided) is calculated as $1.2 \times 2 \times 4 \times 4 = 38.4$ m²; the surface area of stems is estimated to be $0.003 \pi \times 0.55 \rho_{grs} \times 16 = 165.8$ m². Burning rate per unit area is estimated from Eqs. (3.18)–(3.20); here A_v/A_s is assumed to be 0.01. Considering $\rho_{grs} = 2000$ stems/m², the stem spacing (cm) is within values of [0.05, 2.2]. Also, given that the stem thickness is 0.3 cm, the Heskestad porosity (cm) is within values of [0.00122, 0.008], and the burning rate is in the range [1.08, 6.09] (g/s·m²). The overall burning rate is 3.6 g/s·m² using the average value. Other properties are calculated in the same way as for the canopy and trunk, and the values are shown in Table 3.6. It is seen that the heat release rates per unit volume in the grassland are close to the values of the canopy level of a forest.

Also, grass leaves burn as fast as those of the forest crown, while branches burn much more slowly.

Table 3.6: Properties of a typical grass fuel grid cell.

Properties	Grass
Density (kg/m^3)	500
Low heating value (MJ/kg)	17
Grass leaves surface area (m^2)	38.4
Grass leaves mass (kg)	6.7
Grass leaves burning rate ($\text{g/s}\cdot\text{m}^2$)	3.6
Grass leaves mass loss rate (g/s)	138.2
Grass leaves heat release rate (kW/m^3)	267
Grass leaves burning time (s)	48.5
Grass stem surface area (m^2)	165.8
Grass stem mass (kg)	62.2
Grass stem burning rate ($\text{g/s}\cdot\text{m}^2$)	3.6
Grass stem mass loss rate (g/s)	596.9
Grass stem heat release rate (kW/m^3)	1153
Grass stem burning time (s)	104.2

3.5. Ignition modeling

For all types of combustion, fuel ignition requires the fuel temperature to reach some minimum level by the application of heat. In addition, the heat must also be applied long enough to raise the temperature of a deeper fuel layer sufficiently to permit pyrolysis to become self-sustaining; simply put, some quantity of heat is required for ignition, according to Countryman [170]. More specifically, if the heat flux is equal to or greater than the activation energy of the fuel particle, then the chemical reaction starts. Pyrolysis gas is emitted from the fuel and combined with oxygen in the air to react and release heat. A portion of the heat is lost to the surroundings, which are at ambient temperature, by convection and radiation, and a portion of it accumulates in the reaction volume that raises the temperature of the fuel–air mixture, and in turn

increases the pyrolysis rate. Once the pyrolysis rate or mass loss rate reaches a critical value, the fuel is assumed to be ignited. This ignition criterion is physics-based, as discussed in Ch. 2, Sec. 2.1.2; however, it is difficult to implement in the current model since only gas phase equations are solved. Considering that both temperature and heat flux should be included in the threshold of ignition, the following three steps are employed in the present study for the determination of ignition:

- (1) moisture or water is evaporated in the fuel;
- (2) temperature is greater than the ignition temperature;
- (3) heat flux is applied long enough to reach the critical energy density.

First, moisture (water) in the fuel material should be evaporated before the onset of flaming ignition. The initial mass of water m_0 can be calculated from the fuel loading and the moisture content (see its definition in Sec. 2.1.1). The evaporation process is expressed as

$$\frac{dm_{H_2O}}{dt} = -\dot{w}_{vap} , \quad (3.21)$$

with conditions of $m(t_0) = m_0$ and $m(t_f) = 0$ with t_0 and t_f , respectively, denoting the initial and final time of the evaporation; \dot{w}_{vap} is the evaporation rate (kg/s) calculated as

$$\dot{w}_{vap} = \frac{q''}{h_{H_2O}} , \quad (3.22)$$

where q'' is the heat provided from radiation and convection; h_{H_2O} is the heat of evaporation for water with the value 2257 kJ/kg. The differential equation can be solved using a simple forward-Euler method. Integrating Eq. (3.21) and substituting Eq. (3.22) into Eq. (3.21) leads to

$$\int_{t_0}^{t_f} \frac{dm_{H_2O}}{dt} dt = -m_0 = - \int_{t_0}^{t_f} \frac{q''}{h_{H_2O}} dt = - \frac{1}{h_{H_2O}} \int_{t_0}^{t_f} q'' dt .$$

Therefore, the total amount of heat required to dry the fuel materials is

$$\int_{t_0}^{t_f} q'' dt = m_0 h_{H_2O} .$$

In addition, humidity in the atmosphere can change the moisture content of the fuel (and evaporation rates), and thus affect the wildfire occurrence and spread rate. For instance, high relative humidity slows the drying process of the fuel and thus postpones ignition and subsequent combustion. Furthermore, if the moisture is combustible fluid other than water discussed above, flaming would depend on both fuel pyrolysis and mixture fraction of evaporated moisture; the evaporation heat depends on the detailed chemical composition of the moisture and the heat flux.

Second, ignition temperature is employed since it is the simplest and the most commonly-used criterion for numerical modeling of ignition. There exists an abundant resource of its values; for example, Engstrom et al. [33] estimated from a series of experiments that the ignition temperature of oak ranges from 436 K to 732 K with an average value of 584 K. For combustible moisture, the ignition temperature is reduced to the gaseous ignition temperature. It is noted that such a simple model is sufficient to qualitatively capture large-scale wildfire behavior, especially when prediction time is an important factor. However, in order to incorporate more physics into the model, other factors, in addition to ignition temperature, should be considered for the reasons stated in Ch. 2, Sec. 2.1.2. Once the ignition temperature is reached, the outer surface of the fuel particle is assumed to produce pyrolysis gas and to react with the oxygen in the air, but in order to sustain this process, sufficient heat must be provided.

Third, a critical energy power density of gas phase combustion may be used in addition to ignition temperature. It is well established that the lower flammability limit in air (LFL), for hydrocarbons, corresponds to a constant combustion energy density of $2050 \pm 150 \text{ kJ/m}^3$. This critical value has been related to a critical flame temperature at ignition on a condensed-phase fuel. Lyon and Quintiere [35] propose using 1.9 MJ/m^3 , which describes the LFL of fuel vapor-air mixture to predict the onset of piloted ignition of combustible polymers. Therefore,

$$\int_{t_f}^{t_i} \dot{q}'' dt \geq 1900 \text{ kJ/m}^3$$

is used, with q'' being the heat flux provided by convection, radiation, and the heat release from the chemical reaction of the initial pyrolysis gas and the oxygen. The heat release rate is thoroughly discussed in Sec. 3.4. Here t_f denotes the time when the surface temperature has reached the critical ignition temperature, and t_i is the time at which ignition occurs.

In addition, Fig. 3.2 shows a sketch of grid cells used in wildfire simulations. The large-scale or atmospheric grid has a grid spacing (m) (in horizontal x and in transversal z direction) of approximately $\mathcal{O}(10)$ or $\mathcal{O}(10^2)$, and it is resolved by the LES flow solver. The sub-grid or fuel grid cells, with a grid spacing of $\mathcal{O}(1)$ m, are utilized

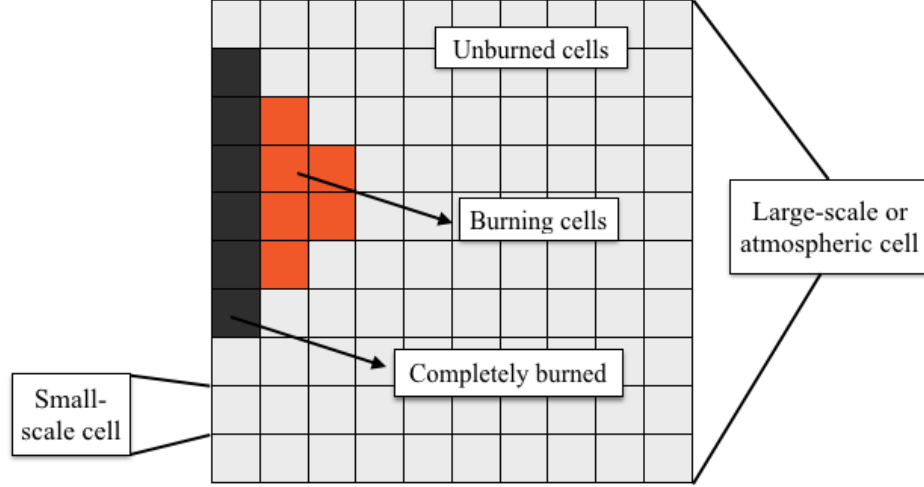


Figure 3.2: Description of cells in one large-scale grid cell.

for better modeling of ignition. Three main states exist for typical cells containing fuel during the calculation: unburned, burning, and completely combusted; they are colored in gray, orange, and deep charcoal, respectively, as illustrated in Fig. 3.2. Unburned fuel grid cells are loaded with fuels, calculated from porosity, as described in Sec. 3.3. Burning cells represent fuels that are ignited, but not yet completely burned; their fuel loading decreases according to the burning rate estimated in Sec. 3.4, and thus the porosity increases. Completely combusted cells have neither any combustible biomass nor heat release; the porosity is assumed to be one. Once the unburned fuel

is ignited, it becomes part of the heat source until it is extinguished, due either to the consumption of the fuel mass or to other factors such as precipitation. Therefore, the source term in Eq. (3.1c) is time dependent.

A description of the solver module of ignition is provided in Figure 3.3. The calculated large-scale variables are input into the module for determination of ignition. Ignitions occurring both at the large cell interface and within the large cell

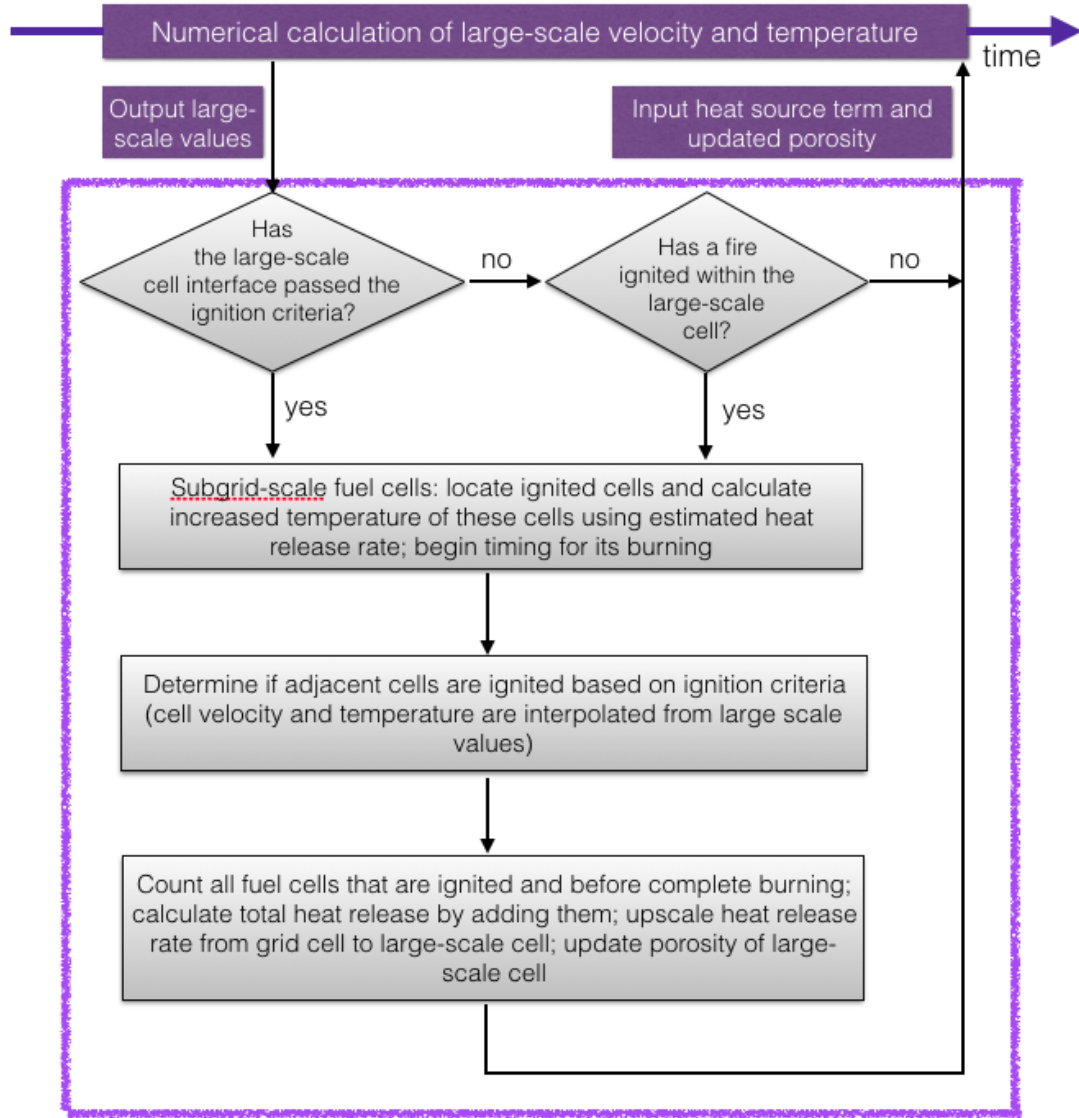


Figure 3.3: Flow chart of the ignition module.

(e.g., landing firebrands) can trigger calculations in subgrid cells. First, positions of

grid cells with ignited fuel are located using a different index notation from that of the large-scale grid cell. Also, the temperature of the ignited cell is updated due to heat release (Sec. 3.4); at the same time, the burn time is recorded until it reaches the maximum value (see Table 3.4–3.6). Second, velocity in cells containing fuel and temperature, are obtained by interpolation from large-scale values. These interpolated values are used to determine whether adjacent cells are ignited, based on the same ignition criteria as those for the large-scale cells. Third, the total heat release is calculated by adding the heat release from all ignited fuel cells; also, the overall porosity of the corresponding large-scale grid is recalculated. Lastly, the total heat release and the updated porosity are input into the calculation of the large-scale grids and affect the overall behavior of fire spread.

3.6. Firebrands

Firebrands are flaming or glowing pieces of fuel, such as cones, leaves, twigs, or bark, that are transported ahead of a fire by fluid motion, fire plumes or fire whirls. The spotting phenomenon has been studied since the 1960s, and a thorough review of research until 2007 was provided by Koo et al. [57]. In massive forest fires, the spot fires caused by firebrands occur frequently and affect fire spread significantly. The determination of a firebrand trajectory is, however, highly probabilistic and not readily amenable to a purely deterministic description. Different shapes of firebrands such as spheres, disks, and cylinders, have been studied in detail. Ellis [171] studied aerodynamics and combustion characteristics of eucalypt bark. Himoto and Tanaka [169] investigated the transport of disk-shaped firebrands in a turbulent boundary layer, but the numerical experiments were conducted on a small computational domain, viz., $2.48 \text{ m} \times 1 \text{ m} \times 1 \text{ m}$. Sardoy et al. [172] investigated firebrands from burning trees using a physics-based wildfire model. A detailed statistical characterization of the size and shape of firebrands was presented by Tohidi et al. [173]; firebrand gen-

eration from burning vegetation was studied by Manzello et al. [174,175] focusing on firebrand sizes and mass using different types and heights of trees.

Firebrand models are roughly divided into two categories: 1) decoupling of lofting and propagation phases, or use of simple combinations of fire plumes and ambient winds; 2) modeling firebrand behaviors in coupled wildfire-atmosphere wind fields. In the first category, the fires are often idealized as being stationary, and the plume is described as a steady vertical velocity field. Such models have been used by fire behavior analysts in the U. S. to predict so-called “worst-case” scenarios; however, none of these models consider the interaction between the fire and the atmosphere, especially with some rendition of turbulence [176]. In the latter category, Garzon et al. [113], and McDonough et al. [23] calculated the complex velocity fields of wildland fires. Garzon et al. [113] focused on a physical, but limited, forest fire model using a RANS-based method. McDonough et al. [23] modeled turbulence through an additive turbulent decomposition (ATD)/chaotic-map procedure (as discussed previously). The parallel efficiency of the numerical methods used in solving the corresponding equations was also investigated. In their studies, firebrands do not change in size, shape, or mass during lofting and transport; the two-dimensional results were exploratory and not subjected to direct testing. The studies of Koo et al. [177] and Bhutia et al. [176] are examples of extending the numerical solutions of firebrand simulations—in more realistic velocity fields—to 3-D, which led to a more accurate rendition of fire/atmosphere turbulence.

The behavior of firebrands can be considered as a series of three stages: (1) generation or release; (2) lofting and transport; (3) deposition and subsequent ignition (or not) of unburned fuels. The current study mainly focuses on the latter two, even though the proposed forest fire model can potentially deal with all three stages. First, randomly generated firebrands from both canopies and undergrowth are utilized. A more physical method is to evaluate the weight of the firebrands and the lifting by

the flow field: when the lift is equal to or greater than the weight, the firebrand is assumed to be released from the original tree structure. The second stage employs the equations of motion and firebrand combustion provided by Stephen and Fernandez-Pello [178], and Bhutia et al. [176]. Third, the temperature and the state of combustion of the firebrands are evaluated at their landing, and subsequent ignition is determined using the ignition criterion specified in Sec. 3.5.

3.6.1 Firebrand trajectories

In the current work, firebrand particles are assumed to be spherical in shape, albeit they are most likely cylindrical. Since a sphere is symmetrical, the net force on it tends to produce drag in the direction of the free stream velocity, hence there is no lift per se. In order to compute firebrand trajectories, one-way coupling is assumed; or in other words, the firebrands have no effect on the ambient fluid flow during their flight since they are too small to produce a non-trivial effect. However, the fluid flow has a significant effect on the firebrands. A firebrand receives the prevailing effect of the buoyant plume near the heat source that elevates and transports it downwind.

The firebrand trajectories are computed based on Newton's second law of motion and the fact that the firebrands are acted upon by the surrounding fluid (drag) and gravity. Velocity and position for each firebrand are calculated using the following initial value problem:

$$m_{fb} \frac{d\mathbf{U}_{fb}}{dt} = \mathbf{F}_D + \mathbf{F}_g , \quad (3.23)$$

$$\frac{d\mathbf{X}_{fb}}{dt} = \mathbf{U}_{fb} , \quad (3.24)$$

with appropriate initial conditions. In the above m_{fb} , \mathbf{U}_{fb} , \mathbf{X}_{fb} represent firebrand mass, velocity, and position, respectively; \mathbf{F}_g is the gravitational force expressed as

$$\mathbf{F}_g = m_{fb} g \mathbf{e}_3 , \quad (3.25)$$

with g being gravitational acceleration, and \mathbf{e}_3 being a unit vector in the (local) “vertical” direction. The drag force \mathbf{F}_D is expressed as

$$\mathbf{F}_D = \frac{1}{2} C_D \rho_{air} A_{fb} |\mathbf{u}_f - \mathbf{U}_{fb}| (\mathbf{u}_f - \mathbf{U}_{fb}) , \quad (3.26)$$

In Eq. (3.26), $\mathbf{u}_f - \mathbf{U}_{fb}$ is the relative velocity between the particle and the air; \mathbf{u}_f represents the wind that interacts with wildfires and can be obtained from interpolation of \mathbf{u} being calculated using Eq. (3.1b); $|\cdot|$ denotes the velocity difference magnitude; A_{fb} is the projected cross-sectional area of the particle; ρ_{air} is density of the ambient air. The drag coefficient C_D is a function of the Reynolds number expressed as $Re = |\mathbf{u}_f - \mathbf{U}_{fb}| \cdot d_{fb} / \nu_{air}$, where d_{fb} is the diameter of the particle, and ν_{air} is the kinematic viscosity of the air surrounding the particle. Due to combustion, the mass m_{fb} and diameter d_{fb} of the particles are expected to decrease with time (to be discussed below). Properties of ν_{air} and ρ_{air} are evaluated at average conditions of ambient pressure and the arithmetic mean of the particle temperature and the ambient temperature [178]. A good approximation of C_D is 0.45 for $5 \times 10^4 < Re < 2.6 \times 10^5$, as suggested in [176] [178], and by Haider and Levenspiel [179] and Kundu [180]. The initial value problem shown in Eqs. (3.23) (3.24) can thus be solved numerically using simple backward or forward Euler method. It should be noted that the accuracy of given data does not support using any higher-order accuracy for numerical simulations.

3.6.2 Firebrand heat transfer and combustion

Firebrand particles cool by convection and radiation as they are carried away by the wind. Assuming lumped capacitance for a particle, its temperature T_{fb} is given by the solution of the transient energy equation [178] [176]:

$$(\rho V c)_{fb} \frac{DT_{fb}}{Dt} = -S_{fb}(\mathbf{q}_{conv}'' + \mathbf{q}_{rad}'') + \dot{Q}''' . \quad (3.27)$$

Here, ρ_{fb} , V_{fb} , and c_{fb} are, respectively, density, volume, and specific heat capacity of the particle; S_{fb} is the surface area of the particle; \mathbf{q}_{conv}'' and \mathbf{q}_{rad}'' are, respectively, the convective and radiative heat fluxes lost by the firebrand particle to the surroundings; \dot{Q}''' is heat release rate from combustion if a flaming firebrand is considered.

The convective heat flux \mathbf{q}_{conv}'' can be represented by Newton's law of cooling as

$$\mathbf{q}_{conv}'' = \bar{h}(T_{fb} - T_{\infty}) , \quad (3.28)$$

where T_{fb} and T_{∞} are the temperatures of the firebrand particle and the ambient air, respectively. The average convection heat transfer coefficient \bar{h} is calculated using the Nusselt number expressed as $\overline{Nu} = \bar{h} d_{fb}/k_{air}$, with d_{fb} being the diameter of firebrand particle, and k_{air} being the thermal conductivity of the air. An approximated value of $2.6 \times 10^{-2} \text{Wm}^{-1} \text{K}^{-1}$ measured at a temperature of 300 K is used for k_{air} (Montgomery [181]). For convective heat transfer relating to a solid sphere, the average Nusselt number is

$$\overline{Nu} = 2 + 0.6Re^{1/2}Pr^{1/3} ,$$

where Pr is the Prandtl number approximated with a typical value of 0.70 for burning wood in air [181].

The net radiative heat flux \mathbf{q}_{rad}'' lost by a hot particle to its surroundings is given by the Stefan-Boltzmann law

$$\mathbf{q}_{rad}'' = \sigma\epsilon_e(T_{fb}^4 - T_{\infty}^4) , \quad (3.29)$$

where σ is the Stefan-Boltzmann constant ($5.67 \times 10^{-8} \text{kg s}^{-3} \text{K}^{-4}$), and ϵ_e is emissivity of the firebrand particle. Substitution of Eqs. (3.28) and (3.29) into Eq. (3.27) leads to the time rate of change of temperature for a spherical firebrand particle as

$$\frac{dT_{fb}}{dt} = -\frac{6}{(\rho c)_{fb}d_{fb}} [\bar{h}(T_{fb} - T_{\infty}) + \sigma\epsilon_e(T_{fb}^4 - T_{\infty}^4)] + \frac{\dot{Q}'''}{(\rho V c)_{fb}} .$$

The effect of combustion is represented by changes in the mass and diameter of the spherical firebrand, and it is calculated in a transient flow field. The particle surface

chemical reactions, as did in other particle (not just firebrands) trajectory studies (Davuluri et al. [182]), are not considered at present. Here, Tse and Fernandez-Pello's [178] simple combustion model is adopted for the burning of spherical wood firebrands. The pyrolysis front of a firebrand is simulated by an effective mass diameter d_{eff} . The Frössling [183] relation is used, where d_{eff} regresses in a d square-law fashion as

$$\frac{d(d_{\text{eff}}^2)}{dt} = -\beta_c ,$$

with β_c being a modified burning constant for a firebrand particle burning in forced convection, expressed as

$$\beta_c = \beta^0(1 + 0.276Re^{1/2}S_c^{1/3}) ,$$

where β^0 is an average burning rate constant estimated to be $4.8 \times 10^{-7} \text{m}^2\text{s}^{-1}$ [183]; Sc is the Schmidt number defined as the ratio of the kinematic to molecular diffusivities, and S_c is 0.7 for air (at ambient temperature). The mass of the particle m_{fb} is then approximated by

$$m_{fb} = \frac{\rho_{p,0}\pi d_{\text{eff}}^3}{6} .$$

Using the above, and the heat of combustion for a given biomaterial, heat release rate \dot{Q}''' during the flight of a flaming firebrand can also be calculated; it is zero if the firebrand is extinguished. In this study, it is assumed that the density of firebrands is constant throughout the flight.

The actual diameter d_{fb} of the particle is obtained by matching results of the Tarifa et al. [184] size regression data and using the same burning rate constant β^0 for the mass burning rate (Stephen and Fernandez-Pello [178]). The regressing of actual diameter d_{fb} in differential form is expressed as

$$\frac{d(d_{fb}^4)}{dt} = -2\sqrt{3}\beta_c^2 t$$

for the best data fit. Moreover, it is assumed that heterogeneous combustion extinction occurs when $m_{fb}/m_{p,0} = 0.24$ [178] [176]. Upon extinction, the firebrand cools

from an initial temperature of ~ 993 K since the burning firebrand temperature of 993 K is used for smoldering wood in forced air flow [176].

3.7. Summary and conclusions

In this chapter, the employed wildfire model is described in detail. A typical forest fire problem with a wind speed of approximately tens of meters per second (even for fire whirls, Mach numbers < 0.3) can always be viewed as an incompressible flow problem even though the air is compressible. Therefore, the governing equations (including porous medium models) are the generalized Navier–Stokes equation of incompressible flow, based on the Boussinesq approximation for buoyant convection, plus a thermal energy equation. Effects of combustion are incorporated in the source term of the thermal energy equation, rather than being computed from transport equations for different (essentially unknown) chemical species. The latter is quite expensive with respect to computational resources and slows the solution process. Most models accounting for the chemistry of forest fires are still formulated in 2D, which is inappropriate for turbulence simulation. Simulators, such as WFDS, use lumped species; but they still cannot achieve real-time solutions [20]. Eventually, details of chemistry and combustion on both large and small scales should be considered. The current code in use is structured to permit inclusion of any of these additional transport equations.

Several submodels with novel features are embedded in order to develop a physics-based wildland fire model that is potentially predictive and eventually operational. These submodels are developed separately for research purposes. First, the synthetic-velocity LES with the derived DDS is employed, which is able to capture the interaction between turbulence and other physical phenomena such as the fire. Second, porosity in each part of the forest is estimated through available botanical data, and the results are within a reasonable range of values. The porosity of grasslands can

also be calculated in the same way as employed for forests. A general permeability model is also used. Third, heat release rate is calculated via fuel burning rate (which depends on porosity), surface area, and heat of combustion. The estimated values are also within the range of documented values. Fourth, both heat flux and temperature are considered for the onset of ignition; sub-grid cells are used to predict ignition. Finally, firebrand equations are discussed in relation to both heat transfer and combustion, rather than only trajectories. It is postulated that such an approach with physics-based sub-models has the potential to simulate complicated forest fires more accurately. Note, finally, that currently few, if any, existing wildfire models include all of these physical aspects.

Chapter 4: The Solver

The CFD research code adopted here was originally developed by McDonough et al. [185] with Fortran 77/90, and has become more developed over the years, presenting its credibility and potential in simulating more complicated forest fire problems. It solves the incompressible Navier–Stokes equation via a projection method for both laminar and turbulent flows in generalized coordinates on structured, staggered grids. Plot3D format is used for both grid and solution files. Furthermore, this solver was originally designed to be parallelized. Parallelization of the code with MPI (Message Passing Interface) was attempted with early versions on shared hardware where each processor contained only a single core. Parallelization with any MPI message-passing model tends to result in very complex algorithms and require tight optimization of communication exchanges, according to Bessonov et al. [186]. Modern shared-memory and distributed-shared-memory platforms have promoted the use of another parallel programming paradigm—OpenMP [187]. The current work aims to parallelize the overall code using OpenMP on distributed-memory systems only, and a hybrid of MPI and OpenMP will be studied in the future.

Section 4.1 presents the analytical form and solution procedure of the projection method employed here. Section 4.2 provides a discussion of grid generation in the context of generalized coordinates. In Sec. 4.3, the procedure of obtaining the auxiliary solution by solving the Burger’s equation (momentum equation without pressure-gradient term) is discussed in detail. In Sec. 4.4, parallelization of the pressure Poisson equation (PPE), which consumes a large portion of the total arithmetic for large problems, is investigated. The performance of parallelizing the overall code, including the PPE and the momentum equation, is presented in Sec. 4.5. Finally, Sec. 4.6 provides summary and conclusions associated with this portion of the study.

4.1. Projection methods

Projection methods are mainly used to treat pressure-velocity coupling in the momentum equation. They can be regarded as a class of Navier–Stokes equation solution procedures originally in the work of Leray [188]. The numerical implementation of projection methods was first introduced by Chorin [189]. There have been numerous versions of projection methods after Chorin’s work, but here this section mainly presents a fairly detailed description of a modern approach in a form somewhat similar to the one used by Kim and Moin [190]. In particular, Gresho *projection-1* method [191], which was first proposed by Fortin et al. [192], is employed in the current solver. A second-order method was also published by Bell et al. [193].

Recall Eqs. (3.1a)–(3.1b). First, as in most basic (low-order) projection methods, one solves the momentum equations without pressure gradient terms. Then one solves a simple equation associated with pressure. These can be expressed as

$$\frac{\partial \hat{\mathbf{u}}}{\partial t} + \frac{1}{\phi} \nabla \cdot (\hat{\mathbf{u}}^2) = \nu \Delta \hat{\mathbf{u}} + \frac{\phi}{\rho} (\hat{B} - \hat{D}) , \quad (4.1a)$$

$$\mathbf{u}_t = -\nabla \Phi . \quad (4.1b)$$

Formally, this is a fractional-step procedure, as studied extensively by Yanenko [194]. Equation (4.1a) is in the form of a vector system of Burgers equations, and $\hat{\mathbf{u}}$ denotes an “auxiliary velocity,” which is not divergence free. The auxiliary velocity is relatively easy to obtain by solving Eq. (4.1a), assuming that such difficulties as the cell-*Re* problem and aliasing can be handled (as discussed in Sec. 3.2.1 in the previous chapter). Here, \hat{B} and \hat{D} are forcing terms denoting body and drag forces, respectively. The second equation is converted to a pressure Poisson equation, whose solution leads to the construction of the Leray projector needed to obtain the required divergence-free solution. Note that this is not the true pressure obtained from the original N.–S. equation; thus, the notation Φ is introduced as the “pseudo pressure” in place of the physical pressure p .

First, taking the divergence for both sides in Eq. (4.1b) leads to

$$(\nabla \cdot \mathbf{u})_t = -\Delta\Phi ,$$

and the LHS is approximated as

$$(\nabla \cdot \mathbf{u})_t \simeq \frac{(\nabla \cdot \mathbf{u})^{n+1} - (\nabla \cdot \hat{\mathbf{u}})}{dt} ,$$

where dt is the same time-step size used to numerically solve Eq. (4.1a). Next, $(\nabla \cdot \mathbf{u})^{n+1}$ is taken to be zero in order to enforce the divergence-free condition at the advanced time level, as was probably first done in the marker-and-cell (MAC) method of Harlow and Welch [195]. This leads to

$$\Delta\Phi = \frac{\nabla \cdot \hat{\mathbf{u}}}{dt} , \tag{4.2}$$

which implies that if Φ satisfies Eq. (4.2) for any $\hat{\mathbf{u}}$, then \mathbf{u}^{n+1} can be constructed as

$$\mathbf{u}^{n+1} = \hat{\mathbf{u}} - dt\nabla\Phi , \tag{4.3}$$

so that $(\nabla \cdot \mathbf{u})^{n+1} = 0$ is satisfied, as required. Equation (4.3) is the Leray projector with the factor dt . For the Gresho *projection-1* method [191], the approximation of

$$p^{n+1} = \Phi$$

is set. Observe that the error in using Φ in place of physical pressure corresponds to

$$p = \Phi + \mathcal{O}(dt/Re) , \tag{4.4}$$

as given by Kim and Moin [190].

After the Leray projection, the true pressure Poisson equation (PPE) for physical pressure could be calculated using the usual numerical approximations, since the velocity field is now divergence-free. For both pseudo and true PPE problems, Neumann conditions are always imposed on solid boundaries; however, in order to increase the convergence rate for the linear solver, a scheme is used in the current

study to transform Neumann conditions to Dirichlet conditions by assigning pressure values of the previous time step to the current time step. This method would cause a first-order error for time-dependent problems, but the overall projection method is still first-order accurate in any case (to be discussed). Note that solving the true or additional PPE can be quite computationally expensive. However, this step is not required for problems that do not need a high-order accuracy of pressure. Namely, Eq. (4.4) shows that if Re is large, and/or the time step dt is small, which is the case for the wildfire simulations performed in the present study, then the difference between physical and pseudo pressure is small. The basic steps for computation are outlined as (see McDonough [196]):

1. solve the “Burgers’ equation” form of the momentum equations;
2. filter solution \hat{u} obtained from Burgers’ equation;
3. perform Leray projection to obtain divergence-free advanced time level solution;
4. prepare results for output to post-processing software such as FieldView, Tecplot, etc.

The order of accuracy of this projection method is approximately $\mathcal{O}(k)$, which is independent of the time integration/evolution procedure due to its fractional-step construction. Take the explicit forward Euler time integration method as an example. The semi-discrete form of Eq. (4.1a) is expressed as

$$\hat{\mathbf{u}} = \mathbf{u}^n + dt \left[\nu \Delta \mathbf{u}^n - \frac{1}{\phi} \nabla \cdot (\mathbf{u}^n)^2 \right]. \quad (4.5)$$

Then the substitution of $\hat{\mathbf{u}} = \mathbf{u}^{n+1} + dt \nabla \Phi$ (obtained from Eq. (4.3)) into Eq. (4.5) yields

$$\mathbf{u}^{n+1} = \mathbf{u}^n + dt \left[\nu \Delta \mathbf{u}^n - \frac{1}{\phi} \nabla \cdot (\mathbf{u}^n)^2 - \nabla \Phi \right]. \quad (4.6)$$

Since Φ and p differ by $\mathcal{O}(dt)$, substitution of Eq. (4.4) results in a local $\mathcal{O}(dt^2)$ leading error, which corresponds to a global error of $\mathcal{O}(dt)$. This error comes from

the fractional-steps operator splitting, so it cannot be removed by simply increasing the order of accuracy of the integration scheme. The overall projection scheme constructed in this way, however, is first order in time; but it is typically found to be an acceptable practical approach. Compared with other predictor-corrector methods, this modern projection method needs less computation and is able to achieve the same order of accuracy. A second- (or higher-) order (in time) projection method has also been attempted in numerous studies, such as those of Gresho [191], and Shen [197], which is to be implemented in the current solver in the future.

4.2. Grid generation

The non-uniform gridding due to arbitrary terrain and the forest area requires more treatment (refinement) via grid generation, especially in the context of the structured-grid approach being used here. It requires generalized-coordinate transformation of the PDEs and boundary conditions, resulting in a generally more complicated mathematical structure of the discretized equations. Nevertheless, it is extremely convenient to perform all computations with standard numerical models in the transformed space, where the grid mesh is uniform and Cartesian. Information regarding the original physical grids is usually obtained from either external coding or grid generation software, e.g., Pointwise [198]. However, the transformation relations between generalized/curvilinear and orthogonal coordinate systems are not trivial, and will be presented below, based on the book of Thompson et al. [199].

First, for mapping the physical domain to the computational domain, the transformation \mathbf{T} and the Jacobian matrix of the transformation $\mathbf{J}(\mathbf{T})$ are, respectively,

$$\mathbf{T} : \begin{pmatrix} x \\ y \\ z \end{pmatrix} \longrightarrow \begin{pmatrix} \xi(x, y, z) \\ \eta(x, y, z) \\ \zeta(x, y, z) \end{pmatrix}, \quad \mathbf{J}(\mathbf{T}) = \begin{bmatrix} \xi_x & \xi_y & \xi_z \\ \eta_x & \eta_y & \eta_z \\ \zeta_x & \zeta_y & \zeta_z \end{bmatrix}.$$

As seen from above, the individual terms of $\mathbf{J}(\mathbf{T})$ utilize the physical coordinates as independent variables; this is contrary to our intention to perform all computations in the transformed coordinate system where the independent variables are (ξ, η, ζ) . Consequently, it is more natural to work with the inverse transform and corresponding Jacobian matrix, written as

$$\mathbf{T}^{-1} : \begin{pmatrix} \xi \\ \eta \\ \zeta \end{pmatrix} \longrightarrow \begin{pmatrix} x(\xi, \eta, \zeta) \\ y(\xi, \eta, \zeta) \\ z(\xi, \eta, \zeta) \end{pmatrix}, \quad \mathbf{J}(\mathbf{T}^{-1}) = \begin{bmatrix} x_\xi & x_\eta & x_\zeta \\ y_\xi & y_\eta & y_\zeta \\ z_\xi & z_\eta & z_\zeta \end{bmatrix}.$$

For this to be of use, relationships between elements of $\mathbf{J}(\mathbf{T})$ and those of its inverse need to be found. For the generalized or curvilinear coordinates, the covariant basis vectors are tangent to the curvilinear coordinates, while the contravariant basis vectors are orthogonal. Associated with the covariant basis vectors are covariant components of the metric tensor, which are used to represent differential increments of arc length, surface area, and volume. The components of the 3×3 symmetric metric tensor

$$g = \begin{bmatrix} g_{11} & g_{12} & g_{13} \\ g_{21} & g_{22} & g_{23} \\ g_{31} & g_{32} & g_{33} \end{bmatrix}$$

are given by

$$g_{11} = x_\xi^2 + y_\xi^2 + z_\xi^2, \quad g_{13} = g_{31} = x_\xi x_\zeta + y_\xi y_\zeta + z_\xi z_\zeta, \quad (4.7a)$$

$$g_{22} = x_\eta^2 + y_\eta^2 + z_\eta^2, \quad g_{23} = g_{32} = x_\eta x_\zeta + y_\eta y_\zeta + z_\eta z_\zeta, \quad (4.7b)$$

$$g_{33} = x_\zeta^2 + y_\zeta^2 + z_\zeta^2, \quad g_{12} = g_{21} = x_\xi x_\eta + y_\xi y_\eta + z_\xi z_\eta. \quad (4.7c)$$

It is evident that the Jacobian matrix of the transformation is related to the determinant of the inverse Jacobian matrix as

$$\sqrt{g} = \sqrt{\det[\mathbf{g}]} = \det[\mathbf{J}(\mathbf{T}^{-1})]. \quad (4.8)$$

Furthermore, by using the relations between contravariant and covariant basis vectors, the elements of the Jacobian matrix (in which x , y , and z are independent variables) can be related to those of its inverse as

$$\xi_x = \frac{y_\eta z_\zeta - y_\zeta z_\eta}{\sqrt{g}}, \quad \xi_y = -\frac{x_\eta z_\zeta - z_\eta x_\zeta}{\sqrt{g}}, \quad \xi_z = \frac{x_\eta y_\zeta - y_\eta x_\zeta}{\sqrt{g}}, \quad (4.9a)$$

$$\eta_x = -\frac{y_\xi z_\zeta - y_\zeta z_\xi}{\sqrt{g}}, \quad \eta_y = \frac{x_\xi z_\zeta - z_\xi x_\zeta}{\sqrt{g}}, \quad \eta_z = -\frac{x_\xi y_\zeta - y_\xi x_\zeta}{\sqrt{g}}, \quad (4.9b)$$

$$\zeta_x = \frac{y_\xi z_\eta - z_\xi y_\eta}{\sqrt{g}}, \quad \zeta_y = -\frac{x_\xi z_\eta - x_\eta z_\xi}{\sqrt{g}}, \quad \zeta_z = \frac{x_\xi y_\eta - x_\eta y_\xi}{\sqrt{g}}. \quad (4.9c)$$

In the physical domain, the first derivative operator in one direction can be expressed (via the chain rule) as

$$\frac{\partial}{\partial x} = \xi_x \frac{\partial}{\partial \xi} + \eta_x \frac{\partial}{\partial \eta} + \zeta_x \frac{\partial}{\partial \zeta}.$$

Since finite-difference discretization of these geometrical differentials are trivial in the uniform grid-spacing computational domain (ξ, η, ζ) , elements of \mathbf{J}^{-1} for these coefficients can be easily and accurately constructed using second-order centered differencing. Second derivatives are treated in the same way, except that more coefficients occur; they result in the more complicated form, e.g.,

$$\frac{\partial^2}{\partial x^2} = \left(\xi_x \frac{\partial}{\partial \xi} + \eta_x \frac{\partial}{\partial \eta} + \zeta_x \frac{\partial}{\partial \zeta} \right) \left(\xi_x \frac{\partial}{\partial \xi} + \eta_x \frac{\partial}{\partial \eta} + \zeta_x \frac{\partial}{\partial \zeta} \right).$$

Note that these coefficients (ξ_x , η_x , etc., computed from physical grid-point locations via Eqs. (4.9a)) need be calculated only once during problem setup, and then stored, unless the physical grid is time dependent. They will not be recalculated during construction of partial derivatives, thus saving arithmetic operations. Different transformation coefficients must be implemented for each of u , v , w , and center cells since staggered grids (to be discussed) are used.

4.3. Solution and parallelization of the momentum equations

Staggered-grid formulations require the use of four separate, but overlapping, control volumes in 3D, as colored in blue, red, green, and black in Fig. 4.1. Since the one-

half indexing is very inconvenient for coding and implementation, “cell” notation and storage are employed in the current solver [200]. Figure 4.1 also shows the notation of grid indexing and the staggered dependent variables associated with the grid cells (i, j, k) . This cell index corresponds to that of the natural finite-difference grid point in the upper right-hand corner of the cell, as denoted by a yellow star.

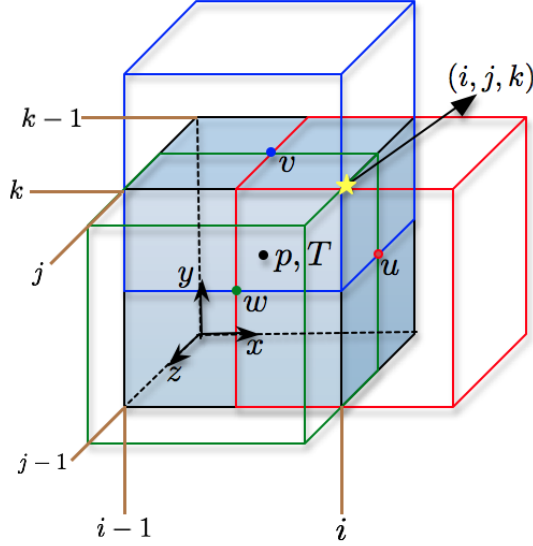


Figure 4.1: Sketch of 3-D staggered gridding.

The staggered-grid finite-volume momentum equations are thus derived from control volumes in correspondence to the dependent variables and are presented (in 2D) as

$$u_t + (\bar{u}^2)_x + (\tilde{u}\bar{v})_y = \nu \Delta u , \quad (4.10a)$$

$$v_t + (\tilde{u}\bar{v})_x + (\tilde{v}^2)_y = \nu \Delta v , \quad (4.10b)$$

where “ \sim ” and “ $-$ ” represent vertical and horizontal averages, respectively, which are given by

$$\bar{u}_{i,j} = \frac{1}{2}(u_{i,j} + u_{i-1,j}) , \quad \bar{v}_{i,j} = \frac{1}{2}(v_{i,j} + v_{i+1,j}) , \quad (4.11a)$$

$$\tilde{u}_{i,j} = \frac{1}{2}(u_{i,j} + u_{i,j+1}) , \quad \tilde{v}_{i,j} = \frac{1}{2}(v_{i,j} + v_{i,j-1}) . \quad (4.11b)$$

Equations (4.10) are also called the Burger’s equations since the pressure term is not included due to the use of the projection method, as discussed above. Thus, u , v in Equations (4.10) are actually auxiliary velocity components, but to simplify notation, “ \wedge ”, as used in Eqs. (4.1), is suppressed. Also, the source terms implemented as forcing terms (at cell centers) are not presented, for simplicity.

Time integration of Eq. (4.10) is performed with the “generalized” trapezoidal method; for the x -momentum equation, it is written as

$$u^{n+1} = u^n + \theta dt [\nu \Delta u - (\bar{u}^2)_x - (\tilde{u}\bar{v})_y]^{n+1} + (1 - \theta) dt [\nu \Delta u - (\bar{u}^2)_x - (\tilde{u}\bar{v})_y]^n , \quad (4.12)$$

where θ is a weighting factor of the integration scheme and is provided by the user. For $\theta = 0$, the explicit forward-Euler method occurs; for $\theta = 0.5$, trapezoidal integration is recovered; and for $\theta = 1$, the backward-Euler integration scheme is produced. With regard to time accuracy, forward and backward-Euler methods are first-order accurate, while trapezoidal integration is second-order accurate. The backward-Euler scheme is usually somewhat more stable for non-linear problems than is the trapezoidal method; thus larger step sizes dt may be employed.

4.3.1 δ -form quasilinearization

Nonlinearities in the N.-S. equation are handled with the δ -form Newton–Kantorovich (quasi-linearization) approach—see, e.g., Ames [201], Kantorovich and Akilov [202]. First, define

$$\delta u = u - u^{(m)} , \quad (4.13)$$

where the superscript (m) denotes an iteration counter, as in ordinary Newton iteration procedures. Since a staggered grid is being used, the velocity field needs to be averaged to construct the control-volume implementation of this method; the resulting forms for the non-linear terms (in the x -momentum equation) are, respectively,

$$\begin{aligned}
(\bar{u}^{(m)2})_x|_i &= \frac{1}{h}(\bar{u}_{i+1}^{(m)2} - \bar{u}_i^{(m)2}) + \frac{1}{h}(\bar{u}_{i+1}^{(m)}\delta u_i - \bar{u}_i^{(m)}\delta u_{i-1}) \\
&\quad + \frac{1}{h}(\bar{u}_{i+1}^{(m)}\delta u_{i+1} - \bar{u}_i^{(m)}\delta u_i) ,
\end{aligned} \tag{4.14}$$

$$\begin{aligned}
(\tilde{u}\bar{v})_y|_j &= \frac{1}{h}(\tilde{u}_j\bar{v}_j - \tilde{u}_{j-1}\bar{v}_{j-1})^{(m)} + \frac{1}{2h}(\bar{v}_j^{(m)}\delta u_j - \bar{v}_{j-1}^{(m)}\delta u_{j-1}) \\
&\quad + \frac{1}{2h}(\bar{v}_j^{(m)}\delta u_{j+1} - \bar{v}_{j-1}^{(m)}\delta u_j) ,
\end{aligned} \tag{4.15}$$

with “ \sim ” and “ $-$ ” quantities defined in Eqs. (4.11). The remaining linear diffusive term is treated by simply substituting the definition of δu into the term as

$$\Delta u = \Delta(u^{(m)} + \delta u) , \tag{4.16}$$

and no averages are required in this case, which is much easier to handle.

By substituting Eqs. (4.13)–(4.16) into Eq. (4.12), the complete δ form of the momentum equation is written as

$$\begin{aligned}
\left\{ I - \theta dt \left[\nu \Delta(\cdot) - (\bar{u}^{(m)}\cdot)_x - (\bar{v}^{(m)}\cdot)_y \right] \right\} \delta u &= u^n - u^{(m)} \\
&\quad + \theta dt \left[\nu (\Delta u^{(m)} - (\bar{u}^{(m)2})_x - (\tilde{u}^{(m)}\bar{v}^{(m)})_y) \right] \\
&\quad + (1 - \theta) dt \left[\nu \Delta u^n - (\bar{u}^n)_x - (\tilde{u}^n\bar{v}^n)_y \right] .
\end{aligned} \tag{4.17}$$

Expressions such as $(\bar{u}^{(m)}\cdot)_x$ in the above equation denote an appropriately averaged value of δu that is to be inserted into the slot indicated by the “ \cdot ”. These expressions are discretized by a chosen method consistent with the procedure resulting in Eq. (4.14) and (4.19). As seen in Eq. (4.17), when $m \rightarrow \infty$, implying $u^{(n+1)} = u^{(m)}$ and $\delta u = 0$, the RHS becomes the complete original equation (Eq. (4.12)). Also, the RHS can be evaluated at any iteration m . The LHS is equivalent to the Jacobian matrix of a typical Newton’s method. Analogous equations hold for δv and δw for solving the y - and z -momentum equations.

4.3.2 Spatial discretization

Further discretization of Eq. (4.17) is straightforward but not trivial. For concise notation, Eq. (4.17) is written in the form

$$J(\mathcal{F}_x)\delta u = -\mathcal{F}_x, \quad (4.18)$$

where $-\mathcal{F}_x$ is the RHS part that includes both n and $n+1$ time step information; $J(\mathcal{F}_x)$ is the Jacobian matrix required for implementing a Newton iteration procedure. The former should be discretized to gain as much accuracy as possible, and the latter should be approximated so as to obtain maximum numerical stability. First, spatial derivatives in the RHS terms are approximated using a 2nd-order, centered finite-volume discretization with staggered indexing, so that the discretized form of $\mathcal{F}_x^{(n+1)}$ is given as

$$\begin{aligned} \mathcal{F}_x^{n+1} = & -u_{i,j}^{(m)} + \theta dt \left\{ \nu \left[\frac{1}{h_x^2} (u_{i-1,j} - 2u_{i,j} + u_{i+1,j})^{(m)} + \frac{1}{h_y^2} (u_{i,j-1} \right. \right. \\ & \left. \left. - 2u_{i,j} + u_{i,j+1}) \right] - \frac{1}{4h_x} \left[u_{i+1,j}^2 + 2(u_{i+1,j} - u_{i-1,j})u_{i,j} - u_{i-1,j}^2 \right]^{(m)} \right. \\ & \left. - \frac{1}{2h_y} \left[(u_{i,j} + u_{i,j+1})\bar{v}_{i,j} - (u_{i,j-1} + u_{i,j})\bar{v}_{i,j-1} \right]^{(m)} \right\}. \end{aligned} \quad (4.19)$$

Also, \mathcal{F}_x^n has completely analogous terms as in Eq. (4.19). At each time step, iteration is required until $\mathcal{F}_x = \mathcal{F}_x^n + \mathcal{F}_x^{n+1} = 0$, to within a specified tolerance.

Usually, $J(\mathcal{F}_x)$ is obtained by differentiating the RHSs of Eq. (4.19)—the $n+1$ time level of \mathcal{F}_x —with respect to each of the five entries of u and v (or seven entries in 3-D cases) for every grid point. Two-dimensional cases with five-band discrete matrices are analyzed here, because first, the 3-D solver is extended from a 2-D code; second, the Douglas–Gunn time splitting method is used (to be discussed) and its form is essentially independent of spatial dimension. Therefore, the elements of

Jacobian matrix (for the x -momentum equation) are precisely

$$\frac{\partial \mathcal{F}_x^{n+1}}{\partial u_{i-1,j}} = -\frac{\theta dt \nu}{h_x^2} - \frac{1}{2h_x}(u_{i,j} + u_{i-1,j}) , \quad (4.20a)$$

$$\frac{\partial \mathcal{F}_x^{n+1}}{\partial u_{i,j-1}} = -\frac{\theta dt \nu}{h_y^2} , \quad (4.20b)$$

$$\frac{\partial \mathcal{F}_x^{n+1}}{\partial u_{i,j}} = 1 - 2\theta dt \nu \left(\frac{1}{h_x^2} + \frac{1}{h_x^2} \right) + \frac{1}{2h_x}(u_{i+1,j} - u_{i-1,j}) + \frac{1}{2h_y}(\bar{v}_{i,j} - \bar{v}_{i,j-1}) , \quad (4.20c)$$

$$\frac{\partial \mathcal{F}_x^{n+1}}{\partial u_{i,j+1}} = -\frac{\theta dt \nu}{h_y^2} , \quad (4.20d)$$

$$\frac{\partial \mathcal{F}_x^{n+1}}{\partial u_{i+1,j}} = -\frac{\theta dt \nu}{h_x^2} - \frac{1}{2h_x}(u_{i+1,j} + u_{i,j}) . \quad (4.20e)$$

In order to improve stability of the overall algorithm, as well as to satisfy the discrete maximum principle for equations of δu and δv , the first-order upwinding scheme is employed here. Also, the use of upwinding for the LHS advective terms is quite common practice. For porous media flow, the Darcy term is also included in the LHS Jacobian matrix to enhance implicitness of the numerical scheme since cases with very small permeabilities can result in computational instabilities. Other momentum source terms are treated as forcing functions. The basic form of the first-order upwind-difference formula is given by

$$\left(\bar{u}_{i,j}^{(m)} \cdot \right)_x \simeq D_{\mp} \left(\bar{u}_{i,j}^{(m)} \cdot \right) \equiv \begin{cases} D_- \left(\bar{u}_{i,j}^{(m)} \cdot \right) , & \bar{u}_{i,j}^{(m)} > 0 , \\ D_+ \left(\bar{u}_{i,j}^{(m)} \cdot \right) , & \bar{u}_{i,j}^{(m)} < 0 , \end{cases} \quad (4.21)$$

with D_- , D_+ , representing backward and forward finite differencing, respectively. Furthermore, the use of upwinding preserves tridiagonality of system matrices, which will be particularly important for implementation of efficient time-splitting solution procedures (herein, D-G). Also, the Jacobian matrix elements, which are produced from first-order upwinding, are somewhat simpler than those given in Eqs. (4.20). Although the approximate Jacobian matrix is used, it produces no serious side effects other than slightly slowed convergence of quasilinear iterations [196]. With D_0 denoting the centered finite difference, the complete discretized Burger's equation in,

e.g., the x direction, can be expressed as

$$\begin{aligned} \left\{ I - \theta dt \left[\nu(D_{0,x}^2 + D_{0,y}^2)(\cdot) - D_{\mp,x}(\bar{u}^{(m)}\cdot) - D_{\mp,y}(\bar{v}^{(m)}\cdot) \right] \right\} \delta u = u^n - u^{(m)} \\ + \theta dt \left[\nu(D_{0,x}^2 + D_{0,y}^2)u^{(m)} - D_{+,x}(\bar{u}^{(m)2}) - D_{-,y}(\tilde{u}^{(m)}\bar{v}^{(m)}) \right] \quad (4.22) \\ + (1 - \theta)dt \left[\nu(D_{0,x}^2 + D_{0,y}^2)u^n - D_{+,x}(\bar{u}^{n2}) - D_{-,y}(\tilde{u}^n\bar{v}^n) \right]. \end{aligned}$$

Here, a simplified form of upwind differencing is used for LHS; the usual centered approximations are employed in the RHS. Note that D_- , D_+ , used on RHS are actually centered since they represent differences taken across grid cells. However, these notations on the LHS are not centered, because the dependent-variable increments δu appear at the staggered-grid points, rather than in the cell center.

4.3.3 Douglas and Gunn time-splitting

In the present study, Douglas and Gunn time-splitting [203] is applied to efficiently solve large matrix systems arising from discretization of the N.-S. and thermal energy equations, e.g., Eq. (4.22), provided that the system matrix corresponding to the complete multi-dimensional system is sparse and banded with very regular band structure. For notational simplicity, Eq. (4.22) is written as

$$(\mathbf{I} + \mathbf{A}^{n+1})\delta u = s^n, \quad (4.23)$$

where the superscripts n and $n + 1$ denote time levels. Both s^n and \mathbf{A}^{n+1} contain iteration m information. Here, δu is the difference of dependent variables between successive quasi-linearization iterations; namely, it is updated to $\delta u^{(m+1)}$ such that $u^{(m+1)} - u^{(m)} = \delta u^{(m+1)}$. Next, the matrix \mathbf{A} can be written as a sum of matrices,

$$\mathbf{A} = \sum_{i=1}^3 \mathbf{A}_i = \mathbf{A}_x + \mathbf{A}_y + \mathbf{A}_z.$$

Each \mathbf{A}_i is a matrix associated with discretization in a specific spatial direction, thus implying parallelization possibilities, at least in principle. Application of the D-G

procedure to Eq. (4.23) yields

$$(\mathbf{I} + \mathbf{A}_x)\delta u^{(1)} = s^n , \quad (4.24a)$$

$$(\mathbf{I} + \mathbf{A}_y)\delta u^{(2)} = \delta u^{(1)} , \quad (4.24b)$$

$$(\mathbf{I} + \mathbf{A}_z)\delta u^{(3)} = \delta u^{(2)} . \quad (4.24c)$$

Thus,

$$\delta u^{(m+1)} = \delta u^{(3)} .$$

Observe that since matrices \mathbf{A}_x , \mathbf{A}_y , and \mathbf{A}_z are tridiagonal, each of the (1-D) Eqs. (4.24) can be easily solved by the direct LU decomposition method. Since multi-dimensional problems are decomposed into sequences of 1-D problems via this approach, only $\mathcal{O}(N)$ ($N = N_x \times N_y \times N_z$) arithmetic operations are performed per time step, and this cannot be easily achieved with any common iterative method. Explicit methods may be as efficient as time splitting, but for multi-dimensional problems they require (usually) unacceptably small time steps to maintain stability.

The numerical properties of consistency, accuracy, and stability of this split scheme are discussed in detail in [136]. First, the fact that the RHS of Eq. (4.24a) is the complete original unsplit equation implies that each split step is consistent with the unsplit difference equation. Second, spatial and temporal accuracy of the split scheme is formally of the same order as that of the unsplit scheme. Third, stability of the split scheme is at least as robust as that of the unsplit scheme. Furthermore, D-G makes it easier to extend a 2-D CFD code to a 3-D one, as was done by McDonough and Dong [204]. Considering this configuration, the parallelization is implemented in such a way that planar 2-D equations are solved at the same time.

Finally, it is remarked that although only momentum equations are discussed here, the energy equation is solved in a similar way. In this solver, the thermal energy equation is coupled with the momentum equation by the Boussinesq buoyancy term; namely, it is in the outer “*do loop*” of the “*do loop*” of quasi-linearization of

the momentum equation. Once the advanced-time velocity is obtained from the momentum equation, it is substituted into the energy equation, which therefore will not have non-linear advection terms. The energy equation is also solved by the D–G time splitting method, and thus can be parallelized in the same way.

4.4. Solution and parallelization of the pressure Poisson equation

As is well known, it is of great importance to efficiently solve the pressure Poisson equation (PPE) of incompressible CFD when using essentially any primitive-variable formulation. Since arithmetic required for this task is sometimes as much as 80% of the total arithmetic for a CFD problem, PPE solvers should be parallelized in order to improve the speed of a complete CFD code. Jacobi iteration and successive overrelaxation (SOR) methods (which include Gauss–Seidel) are common algorithms used in solving elliptic equations (see, e.g., Young [205]), albeit there has been considerable emphasis on Krylov subspace methods in recent years (Axelsson [206] or Saad [207])—for example, GMRES and BiCG-Stab. However, the latter methods are relatively complex and require significantly more storage than Jacobi or SOR approaches. Hence, they are less well suited for use in modern computer architectures which employ many cores with limited RAM per core. Moreover, their required arithmetic per iteration greatly exceeds that of Jacobi and SOR algorithms. Our purpose in the current study is to parallelize Jacobi and SOR codes and explore their speedups, efficiencies, etc., within the framework of common higher-level programming languages.

In particular, both serial and parallel performance of the three widely-used programming languages Fortran (McCracken [208]), C, and C++ (Stroustrup [209]), are considered. Fortran is typically used for numerical calculations associated with sci-

The material contained in this section (Sec. 4.4) has been published as [Procedia Engineering, **61**, 2013, 136–143] [10.1016/j.proeng.2013.07.106] © [copyright Elsevier] [<https://www.journals.elsevier.com/procedia-engineering>]

entific programming, but the latter two are becoming more and more widely used and are involved in GPU calculations. GPUs might be the future for powerful parallelization; therefore, knowing the fastest language with an interface to GPUs and parallelization is important for future scientific calculations. Hence, it is intriguing to compare details of the speed differences between the three languages and investigate their performance in both serial and parallel computations. The analysis section opens with a well-posed mathematical problem corresponding to the PPE of incompressible CFD along with its discretization. It also includes the descriptions of computing tools and parallel strategies. Details of timers and compilers employed for the three programming languages are then given. In the results section, the parallelization results from Jacobi, point-SOR and red-black ordered SOR iterations, are presented; an overall rating of these methods is summarized in the conclusion section.

4.4.1 Analysis

The problem. The PPE problem studied here takes the form

$$\Delta p = f(x, y, z) , \quad (x, y, z) \in \Omega \subset \mathbb{R}^3 , \quad (4.25)$$

with Dirichlet boundary conditions $u(x, y, z) = \text{const.}$ on all boundaries ($\partial\Omega$). Here, p is the pressure and f a forcing function; Δ is the usual Laplace operator. The problem is simplified in the following respects: set the forcing function to zero; use unity Dirichlet boundary conditions on all of $\partial\Omega$, and let solution domain Ω be the unit cube. Hence, the exact solution is $u \equiv 1$ everywhere permitting easy detection of rounding and iteration errors since there is no truncation error for any consistent discretization.

Equation (4.25) is discretized by second-order centered differencing resulting in a linear system of equations to be solved using Jacobi and SOR iteration. The uniform grid spacings (e.g., $h_x = 1/(N_x - 1)$) are canceled from the difference equation, due

to the homogeneity of Eq. (4.25), resulting in

$$u_{i,j,k}^{(n+1)} = a_x \left(u_{i-1,j,k}^{(n)} + u_{i+1,j,k}^{(n)} \right) + a_y \left(u_{i,j-1,k}^{(n)} + u_{i,j+1,k}^{(n)} \right) + a_z \left(u_{i,j,k-1}^{(n)} + u_{i,j,k+1}^{(n)} \right), \quad (4.26)$$

with $i, j, k = 1, 2, \dots, N_x, N_y, N_z$; a_x , a_y and a_z are coefficients resulting from the discretization, and (n) is the iteration counter. N_x , N_y etc., are the numbers of grid points in each spatial direction.

Parallelization. The parallelization strategy used here for all three iterative methods consists of parallelizing only the outer loop of the three nested loops of a 3-D problem. This defines planes via the two inner indices and sends different planes to different cores—a very simple form of domain decomposition [136]. Note that each plane is currently treated serially within each core. Furthermore, since there are only 16 cores per node, cores must be used repeatedly in processing x - y planes of the 3-D problem. This parallelization mechanism has undergone only initial investigation, but current results show reasonable speedups. As a point of interest, it has also been demonstrated that parallelizing the inner loop is even much slower than the serial case, a not entirely unexpected result. A similar strategy is to send each plane to different nodes, and parallelize the plane in each node. This should be faster, but needs more cores and MPI to cross the nodes. Future work within the framework of a complete large-eddy simulation code may include this approach.

The hardware. All codes were run on the high-performance computer, DLX, a Dell, Inc., cluster, at the University of Kentucky, consisting of 256 basic compute nodes, each of which has 64GB RAM of 1600 MHz and dual 2.6 GHz Intel E5-2670 processors with 8 cores (Sandy Bridge) in each processor. Thus, there are 16 cores available without accessing other nodes. However, the RAM per core is only 4 GB, which implies that numerical algorithms should be relatively simple in order to avoid requiring excessive storage. In light of this, Jacobi iteration seems to be a reasonable

choice of solution method (despite its deficiencies) because it can be easily parallelized on the DLX using OpenMP, Dagum and Menon [187]. This will be done in the present study for both Jacobi and SOR methods since OpenMP is believed to be better for parallelizing across cores, and it is much simpler than MPI. MPI could be used across nodes—and across processors—very well, but it is more difficult to implement.

Programming languages. Codes to solve this linear system of equations using Jacobi, point SOR and red-black ordered SOR iterative methods are written in three different programming languages: Fortran, C, and C++, as noted earlier. To permit valid comparisons of these languages, factors such as parallelization strategy, algorithm, and code structure are made the same across the languages for each iterative method. One can refer to Appendices A and B for specific code examples of point SOR in Fortran and C; codings for other algorithms are similar, and the C++ programs are very much like those in C. It should be noted that some intrinsic parts embedded in each language, e.g., ways of extending stack size for large problems, are written in different ways; also for codes written in C and C++, do-loops are used to set the initial conditions of pressure rather than employing vector code assignments that are used in Fortran; the manner in which results are written to files is also not perfectly identical across the three languages. However, this will not affect recorded timing results because wall-clock timings begin with the lines of code that immediately follow initializations and end before writing results to files.

Timing and compilation. A very important factor that can potentially affect run-time results of any numerical experiment is the timer. In the context of parallelization, the elapsed time, or wall-clock time, is commonly used rather than the total CPU time accumulated by all processors (or cores). The directive `omp_get_wtime` in OpenMP is employed to monitor run time. This is the same for all three languages in the parallel computing environment; the same timer can also be used for serial cases when the

number of threads is set to one. The timers specific to C/C++ and Fortran in the serial case outside the parallel computing environment are also tested. The run times showed little difference between using them and the common timer, so all reported results were obtained using the OpenMP directive. It should be noted that measured results often varied somewhat on a run-to-run basis; as much as 10% run-to-run differences were observed. This is mainly due to the state of the computer (including a number of other users) at the time a job begins execution. Thus, averaging timing data over several runs might be reasonable, but instead the direct data of a single execution by running jobs for all three languages simultaneously is used. Clearly, this sacrifices absolute run times, but for purposes of comparisons across programming languages this is adequate for mitigating the “initial machine state” problem.

In addition, compilation can also be a reason for run-time differences. `gfortran` is employed to compile Fortran; `g++` and `gcc` compilers were used for C++ and C, respectively. The Intel compiler, `ifort`, was also used for some cases of Fortran code, and it could sometimes provide up to 20% faster execution speed than `gfortran`. However, it did not seem to perform stably if more than three cores were employed—it even produced different numbers of iterations for unknown reasons. Hence, mostly `gfortran` is used as Fortran compilations. Moreover, the codes were all compiled at the `-O3` optimization level. It is found that executables produced with `-O1` were slower than those obtained with `-O2`, `-O3` and `-O4` in both serial and parallel cases. The latter three optimization levels showed very little difference in calculation speeds. The performance of `-O2` was slightly faster than that of the other two in serial cases, and `-O3` was slightly faster in parallel cases. Here, the `-O3` optimization is used to perform all reported numerical experiments.

4.4.2 Jacobi iteration method

In this section, the main results from parallelization of different linear iterative methods using three programming languages are presented and discussed in detail. Several cases of Eq. (4.26) have been run for Jacobi, point SOR and red-black ordered SOR methods (using an iteration convergence tolerance $\epsilon_t = 10^{-10}$ applied to the max-norm of the iteration error). For each of the three languages, grid-point problems of 51^3 , 101^3 , 151^3 and 201^3 are solved, and each was run using core number ranging from one to sixteen, the maximum number of cores in one node. Since problem size of millions of grid points is often employed in many industrial problems, and much of the data yield similar information, the cases of 101^3 grid-point problem are mainly considered using both Jacobi and SOR methods for observable comparisons. The 201^3 grid-point problem is also discussed for both point and red-black ordered SOR methods in the interest of showing more information about their performance for even larger problems.

In Jacobi iteration, calculation of each grid-point value is independent since it is calculated from its neighborhood points of the preceding iteration as indicated in Eq. (4.26), which implies that all points within the 3-D nested do-loop could be parallelized. However, as indicated earlier, only x - y planes are calculated in parallel to speed up the overall calculation by parallelizing the outer loop and to guarantee that compute times exceed those for communication. Each plane is assigned to different cores at the same time, but the values within each plane are still calculated serially by the chosen core (thread). Different parallelization methods have also been attempted to allow all points, rather than just some points, to be parallelized in the context of Jacobi iteration, but did not improve performance over that of the plane-wise strategy. This is likely due to a large amount of information required to be exchanged between different cores and consequent increased communication, leading to increases in run time.

Figure 4.2 shows the relationship between number of cores used and the corresponding speedups for each language solving the 101^3 grid-point problem via Jacobi iteration. It is clearly seen that there is a near-linear relationship (with slope somewhat less than one) between speedups and the number of cores used for all three languages when less than eight cores are assigned, and there is little difference in speedups amongst the three languages. However, the speedup increases much more

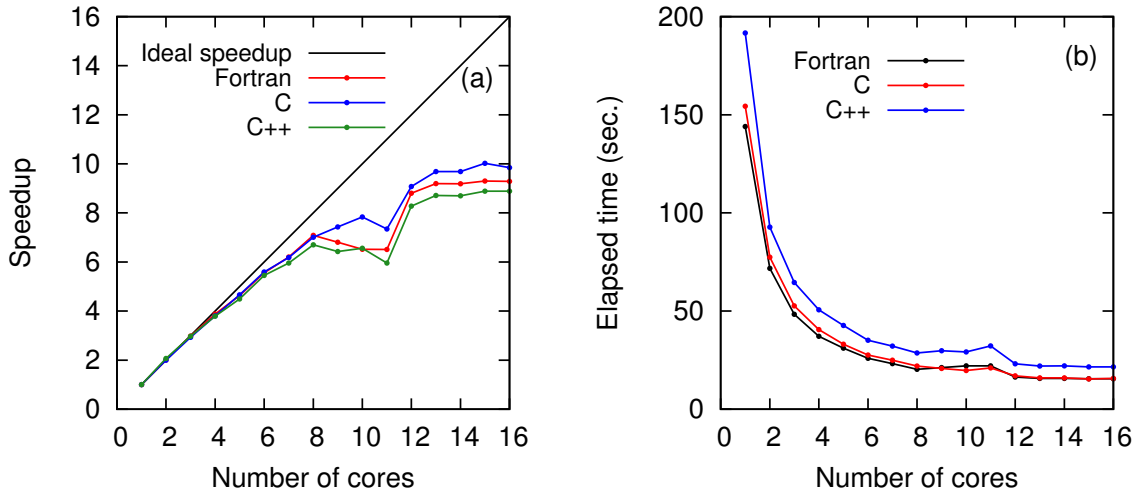


Figure 4.2: Jacobi iteration for 101^3 grid-point problem: number of cores vs. (a) speedup; (b) elapsed time.

slowly when more than eight cores are used, and there is even a decrease in speedups for cores between eight and twelve. Also, the difference in speedups of the three languages becomes somewhat more evident; C has an at most 10% higher speedup over Fortran, and Fortran exhibits at most a 5% higher speedup over C++. The discrepancy from eight cores to twelve may be explained by remembering that the DLX nodes contain two processors, and each has eight cores. In addition, OpenMP works best across cores rather than between processors; hence, the observations for greater than eight cores are not completely unexpected—except for the noticeable decrease in speed at eleven cores for all programming languages. This possibly represents a communication problem, but exact details will require further investigation.

It is emphasized that speeding up the PPE code is our primary objective; hence elapsed time provides the most direct information in this regard, and this is shown in Figure 4.2(b). As is true for Fig. 4.2(a), these results correspond to the 101^3 grid-point problem. Clearly, the parallelized code has greatly decreased the calculation time compared with the serial case. As the number of cores increases, elapsed time decreases accordingly. Moreover, the figure shows that Fortran is slightly faster than the other two languages. It does not differ much from C but is approximately 10% faster than C++ in a parallel environment. Furthermore, Fig. 4.2(b) shows that for C and Fortran, run times decrease from approximately 150 sec. to about 15 sec. in going from a single core to sixteen.

Figure 4.3 displays the relationship between the problem size and parallel efficiency, given as

$$\text{efficiency} = \frac{S_P}{P} . \quad (4.27)$$

Only Fortran results are shown, but similar results are found for C and C++. Here, S_P is speedup with P cores. From this figure, it is clear that OpenMP parallel

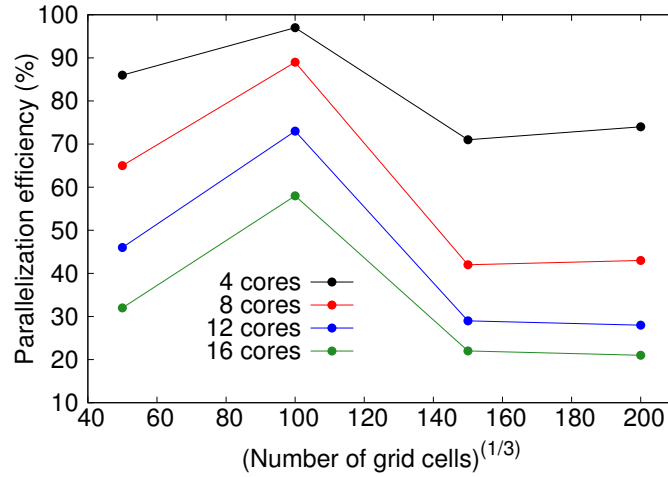


Figure 4.3: Jacobi iteration in Fortran: problem size vs. efficiency with different number of cores.

performance of Jacobi iteration is best for the 101^3 grid-point problem. For the 51^3 grid-point problem however, the highest speedup achieved for sixteen cores is just

around six, while for both 151^3 and 201^3 grid-point problems, the speedups for sixteen cores are only about three, which are even worse. Hence, problem size is also a factor that influences parallel performance; and it is generally expected that efficiency should increase as problem size increases since this typically implies improved balancing of computation and communication times. This agrees with results shown in the figure for problems with up to 101^3 grid points, but efficiency generally decreases as problem size increases beyond this. This may be due to the increased time needed to read from RAM on a different core if RAM for each core is not quite sufficient for the problem. Also, it is easily seen that for a particular grid-point problem, as the number of cores increases, efficiency decreases—consistent with Fig. 4.2(a).

4.4.3 Point SOR and red-black SOR iteration methods

In this subsection, results from both point and red-black ordered SOR methods are provided and discussed. It is shown that although SOR would seem to be more difficult to parallelize, its performance is not degraded when simple OpenMP parallelization, completely analogous to that used for Jacobi iteration, is employed. In particular, theoretical optimal convergence rates are still observed.

Unlike Jacobi iteration, point SOR iteration seems difficult to parallelize since calculation of values at the new iteration needs information from the same iteration level. Indeed, the dependence on evolved values makes it un-parallelizable for all points in the 3-D nested loop. However, this problem is avoided by ignoring the fact that calculation of any particular grid-function value depends on other values at the same iteration which in parallel computation may, or may not, have been updated. This approach performs quite well through using OpenMP in the same way as done for Jacobi iteration. This is not hard to explain by observing that only x - y planes are calculated in parallel, so the SOR iteration method is still effective within each plane, where values in x and y directions of the new iteration level are always available.

For values in z -direction, information from the preceding iteration is still used to guarantee parallelization, and this partially parallelized point SOR proves to work decently.

Comparatively, red-black ordered SOR [205] seems to be much easier to parallelize because the black-point values from a previous iteration are the only information needed to calculate red points in the current new iteration level, and vice versa. Hence, parallelization can be performed within each set of the red and black points. The two 3-D nested do-loops are both parallelized by implementing OpenMP on the outer loops, a very straightforward parallelization. These loops are similar to the Jacobi iteration do-loop since every point can ideally be calculated in parallel, but the best performance is achieved by parallelizing the outer loops since this leads to less information exchange and thus shorter run time.

For optimal SOR, the total arithmetic scales as $\mathcal{O}(N^{1.333\dots})$, where N is the total number of grid points in a 3-D discrete approximation, rather than $\mathcal{O}(N^2)$ required by Jacobi iterations. The optimal iteration parameters for both point and red-black ordered SOR are given by (see, e.g., [205])

$$\omega_b = \frac{2}{1 + \sqrt{1 - \cos \pi h}} \quad (4.28)$$

for uniform grid spacing h in all directions and Dirichlet boundary conditions on all of $\partial\Omega$.

The 101^3 grid-point problem. Figure 4.4 displays speedups of point SOR (part (a)) and red-black ordered SOR (part (b)) analogous to results given in Fig. 4.2(a) for Jacobi iteration. It is apparent that nearly linear speedup (with slope slightly less than unity) is observed in Fig. 4.4(a) through, roughly, six to eight cores for all three programming languages; performance degrades somewhat thereafter, and the difference between different languages becomes larger, with Fortran staying closest to ideal speedup (except for 16 cores). However, a comparison of Fig. 4.4(a) with Fig.

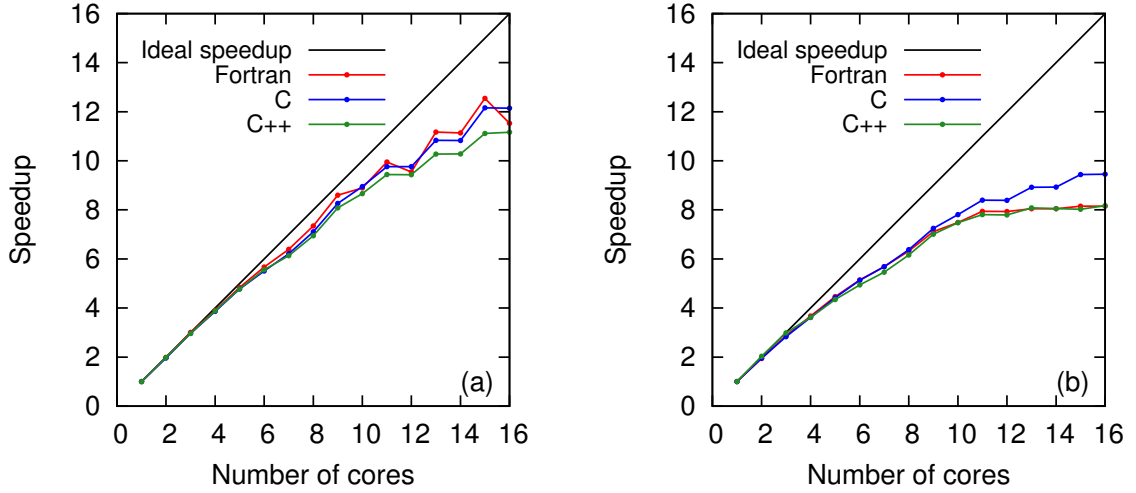


Figure 4.4: Number of cores vs. speedup for 101^3 grid-point problem: (a) point SOR; (b) red-black ordered SOR.

4.2(a) shows that point SOR parallel performance is noticeably better than that of Jacobi iterations, especially for more than eight cores, this is not the case with red-black ordered SOR shown in Fig. 4.4(b) though. Sub-linear speedups are observed after only four cores. The highest speedup achieved for this method is only eight for sixteen cores. The performance of C++ and Fortran is similar, while C is noticeably better despite inferior to the point SOR case. It seems that this method cannot go any farther for more than eight cores, which is even worse than Jacobi iteration in Fig. 4.2(a). This indicates that parallelizing the outer loop might not be a promising strategy for red-black ordering for large number of cores. A possible explanation is that if more cores are assigned, more threads are working at the same time with different efficiencies and speeds; but the black points can only be calculated if all the red points are finished, and vice versa, which implies that there is a wait time for the slower threads to finish the previous task.

Although the red-black ordered SOR method does not perform as well as point SOR and Jacobi iteration with respect to parallelization, it does exhibit reduced time of calculation. Run times for both SOR methods are presented in Fig. 4.5.

The first thing observed is that run times for both methods are far less than for Jacobi iteration—by more than an order of magnitude (ranging from slightly over 4 sec. to less than 0.4 sec.)—because the numbers of iterations are far fewer for both methods and parallelization was more effective (only for point SOR). Also, it is clearly seen that red-black ordered SOR has as much as 60% reduced time in the serial case compared with point SOR because of even fewer required iterations, and it can achieve the same computation time as point SOR using less than eight cores, which is relatively fast and actually resource saving.

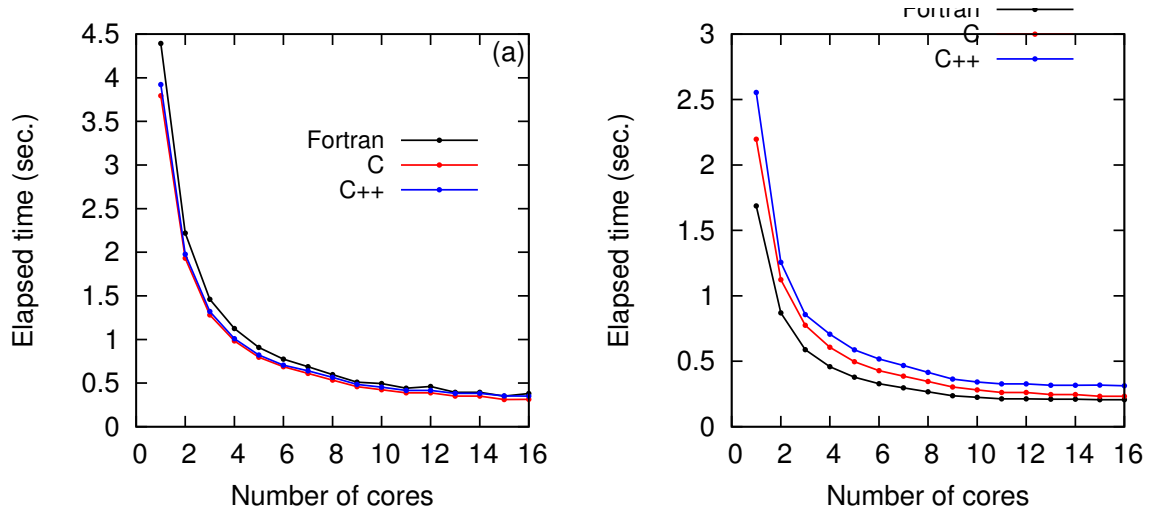


Figure 4.5: Number of cores vs. elapsed time for 101^3 grid-point problem: (a) point SOR; (b) red-black ordered SOR.

It is then reasonable to ask whether SOR is performing as theoretically predicted (see [205]) despite not always having available the most recent iterates. Namely, Figs. 4.4 and 4.5 correspond to only a single (rather moderate) problem size, so one must question whether this performance will persist for both larger and smaller problems. It is easily shown, as noted earlier, that total arithmetic scales as $\mathcal{O}(N^{1.333\dots})$, and this implies that required number of iterations at a fixed convergence tolerance must be proportional to $N^{0.333\dots}$. Figure 4.6 shows that this is precisely true for the parallelized algorithm of point SOR; red-black ordered SOR should have similar results.

In particular, the required number of iterations grows rather slowly for optimal SOR permitting solution of quite large problems when only moderate parallelization is employed (eight cores for results in Fig. 4.6).

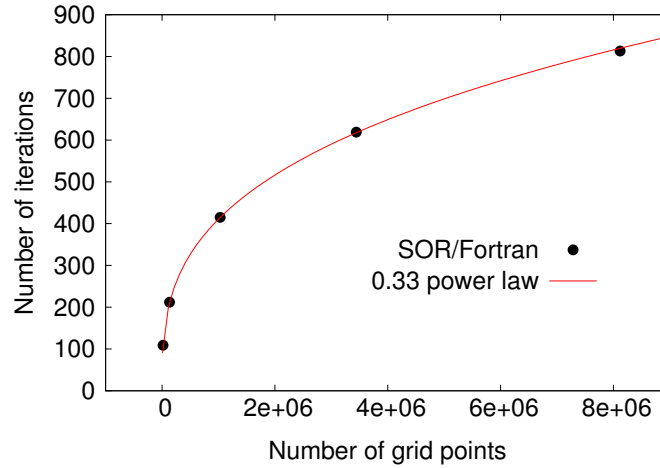


Figure 4.6: Required iterations vs. problem size for optimal SOR.

The 201³ grid-point problem. It is also interesting to consider performance of SOR iterations for a 201³ grid-point problem since this magnitude of problem is closer to current practical applications, and the performance of Jacobi iteration parallelization, as stated earlier, simply cannot satisfy the current needs. As seen in Fig. 4.7(a), point SOR in Fortran provides almost linear speedup with number of cores ranging from one to sixteen; it has nearly ideal linear speedups for less than eight cores, which is the best result at present. C and C++ also perform quite well for less than eight cores; however, beyond eight cores their speedup deteriorates, even decreasing slightly with 12 or more cores. It is roughly concluded that C and C++ do not parallelize as effectively as Fortran for larger problems, but run time (ranging from about 5 sec. to 70 sec. for corresponding cores) for the three languages is almost the same and far less (two to three order of magnitudes) than what Jacobi iteration needs, as observed from part (b) of Fig. 4.7. C and C++ seem to require somewhat less run time than Fortran in serial computing, but Fortran provides better OpenMP parallelization.

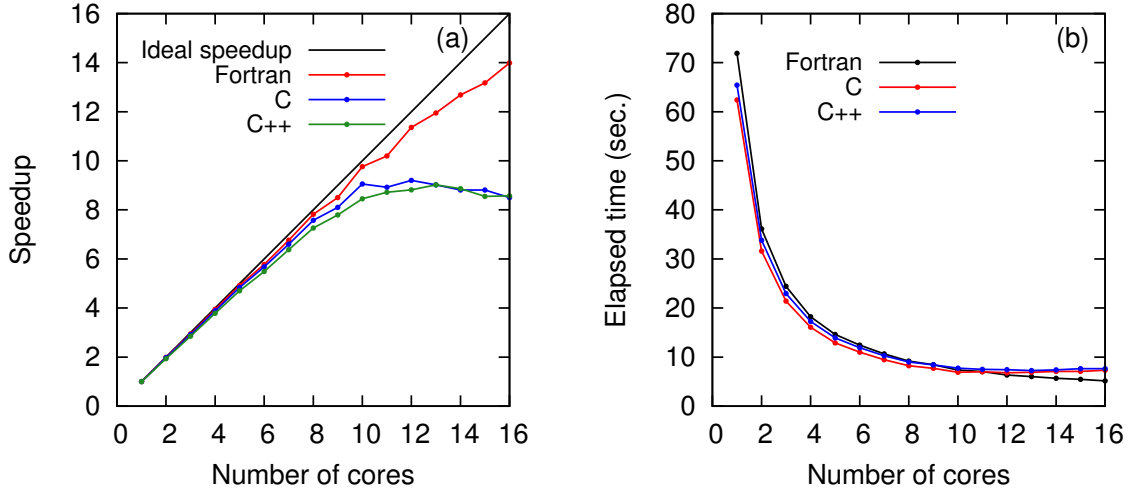


Figure 4.7: Point-SOR for 201^3 grid-point problem: number of cores vs. (a) speedup; (b) elapsed time.

Red-black ordered SOR for larger problems, however, is somewhat similar to the performance of Jacobi iteration with respect to parallelization, as shown in Fig. 4.8(a). Increase of speedup almost stops beginning from four cores for C and C++ and from six cores for Fortran. The method simply does not parallelize with OpenMP after

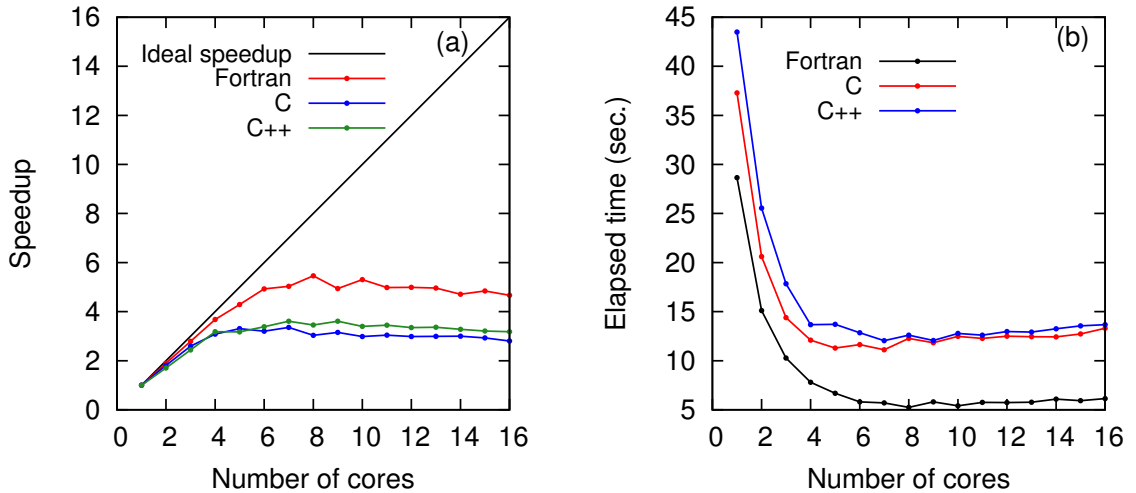


Figure 4.8: Red-black ordering SOR for 201^3 grid-point problem: number of cores vs. (a) speedup; (b) elapsed time.

that point. However, the elapsed time figure in part (b) shows that red-black ordered SOR used in Fortran can actually achieve 5 sec. run times using only eight cores,

which is already the least time that point SOR could achieve for maximum cores in one node; C and C++ could only achieve run times around 14 sec. at best. Thus, no matter whether point SOR or red-black ordering are used for parallelization, Fortran seems to be a better choice of programming language for large problems.

Lastly, the efficiencies of the two SOR methods are presented in Fig. 4.9 analogous to Jacobi iteration. Part (a) shows that parallelization efficiency continues to increase as the problem size increases (except for a slight, unexplained, decrease in efficiency for the case with 16 cores) even when over 150^3 grid points are used, which is generally expected. However, red-black ordered SOR in Fig. 4.9(b) shows decreasing efficiency after problem size exceeds 151^3 grid-points for all cases, similar to Jacobi iteration, and which again reflects only fair performance in parallelization with OpenMP. Also, for a set grid size, as the number of cores increases, efficiency decreases, which corresponds to previous results. It is found that point SOR is best for parallelization within the current OpenMP strategy compared with the other two methods shown in Figs. 4.3 and 4.9(b).

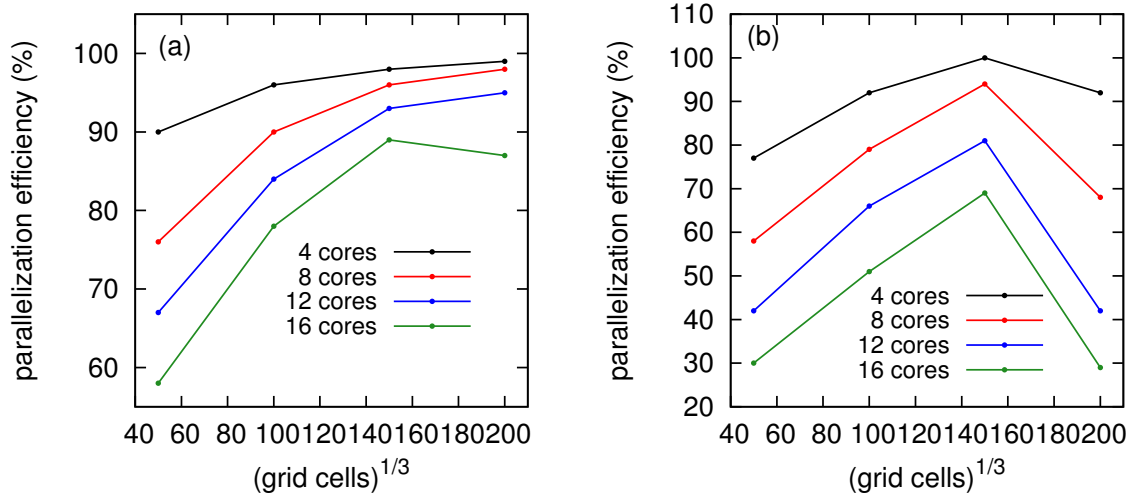


Figure 4.9: Problem size vs. efficiency with different number of cores in Fortran: (a) point SOR; (b) red-black ordered SOR.

Some concluding remarks. In this section results for parallelized Jacobi and SOR iterations applied to solving a simplified PPE, in order to decrease total run-time expenditure, are presented. Codes written in Fortran, C, and C++ were run for both serial and parallel cases employing OpenMP with up to, and including, 16 cores. Care was exercised to guarantee these comparisons are valid in terms of algorithm/code structure, optimization levels and timers, across the three languages.

In this OpenMP structure, it is concluded that parallelization of Jacobi iteration has greatly decreased the time for calculation, but that it is still not competitive with optimal point SOR in either parallel performance or reduced run time. Indeed, for the baseline 101^3 grid-point problem, the run time for parallelized Jacobi iterations employing 16 cores was nearly four times longer than that for SOR run on a single core—and SOR shows better parallel efficiency than does Jacobi iteration; for the 201^3 grid-point problem, Jacobi iteration performs even worse and could hardly achieve the results from point SOR in Fortran. In addition, for Jacobi iterations, it is found that the speedup somewhat anomalously decreases as the number of cores used increases in a certain range of number of cores; this was not observed for either of the SOR methods. On the other hand, red-black ordered SOR is not as effective as point SOR in parallelization but could achieve the same run time with fewer cores; also both SOR methods show that Fortran produces noticeably better results than C and C++, while the difference is not very obvious in Jacobi iteration.

Furthermore, some unsatisfactory results reveal limitations of OpenMP—again, mainly for Jacobi iterations—although it is simpler to implement. The structure of the DLX, and typical machines like it, may be more suitable for MPI (or combinations of MPI and OpenMP). Moreover, it is also found that Fortran is approximately 10% faster than C, and C is approximately 10% faster than C++ for serial cases in Jacobi iteration and red-black ordered SOR, although this is not the case for point SOR; for parallel cases, Fortran is slightly faster than C, and still approximately 10% faster

than C++ in Jacobi iteration; in red-black ordered SOR, Fortran is 10% faster than C, and C is approximately 10% faster than C++ for the baseline 101^3 grid-point problem, but for larger problems, Fortran is as much as 50% faster than C; for point SOR, Fortran is faster than C and C++ for larger numbers of cores. It is remarked that for large problems in which Fortran can execute up to 50% faster than C, this can be the difference between “overnight turnaround,” or not; and this can be crucial in industrial scenarios. In addition, it should be noted that using optimal iteration parameter in SOR is of crucial importance. Without these, SOR performance would be only marginally better than that of Jacobi iterations, and this highlights the need to seek optimal parameters in the context of more general (than Dirichlet) boundary conditions, or to find an efficient, invertible mapping of general boundary conditions to Dirichlet conditions.

4.5. Parallel performance of the solver with OpenMP

The code being used is well structured for parallelization. There are at least three levels at which this can be done [185]. The most obvious one is due to the reinterpretation of Douglas & Gunn time splitting to permit 2-D planar solves within a 3-D domain, allowing planes to be solved in parallel. Second, further parallelization is possible within each planar solve. Third, the “enhanced” ILES is implemented in such a way that the large and small scales of the solution can be computed simultaneously during each time step, thus allowing further parallelization. In addition, the PPE solvers can be parallelized [210], as described in the previous section.

First, as shown in the LHS of Fig. 4.10, parallelization of the PPE solver for generalized coordinates presents results almost as good as those obtained for a simple SOR code [210]. Speedup of 11 could be achieved for 14 cores with an almost linear speedup for up to more than 8 cores. The results come from an $81 \times 101 \times 81$ gridding of the cubical LDC problem.

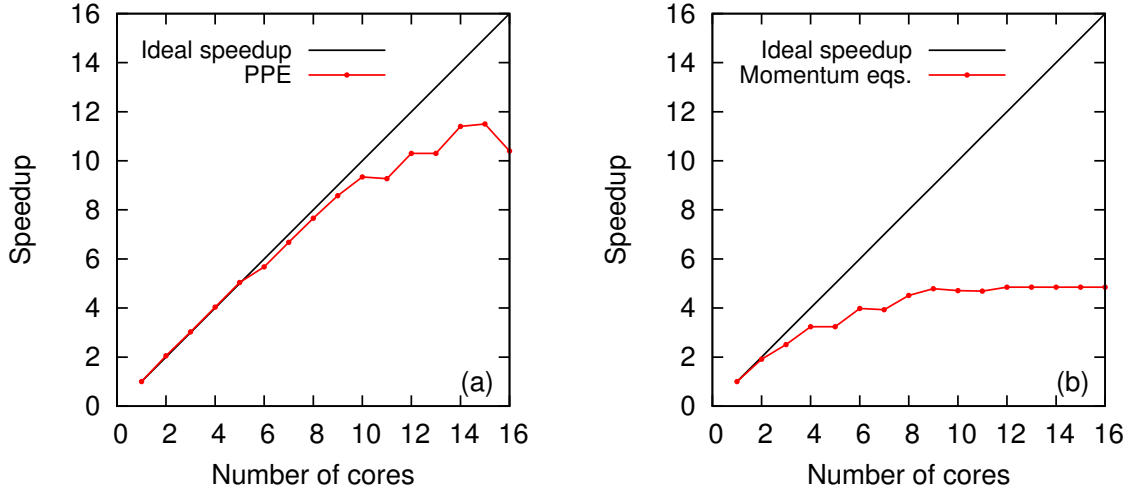


Figure 4.10: Parallel Performance of (a) PPE solver and (b) momentum equation

Second, parallel performance of the momentum equation solved with Douglas–Gunn time splitting is shown in the RHS of Fig. 4.10. As is seen, speedup of a maximum of 4.85 is obtained for 16 cores; linear speedup is lost after only two cores, and the speed increases very slowly after that. This is due to the fact that time and memory are required for each thread to copy all the 2-D variables for each independent calculation. These once-shared 2-D variables are made thread-private through OpenMP to allow each 2-D planar solve be sent to each core. As the number of cores increases, more copies of variables are made by threads, and more run time is needed. If this does not offset decreased time by parallelizing each planar solve, speed is lowered. Also, it is seen that the speed does not increase at all after eight cores. Since one socket has only eight cores, this may be due to what is called non-uniform memory access (NuMA), which indicates that remote accesses become much slower than local ones for every processor [211]. Another way to treat the momentum equation is to parallelize each line solve within each 2-D planar solve, the results of which are not as good as the present treatment of the momentum equation, although some speedup of around four for 16 cores could be achieved. It is also intriguing to consider using both MPI and OpenMP, since 2-D planar solves could be sent to different nodes by MPI, and they could be parallelized within each node using

OpenMP. This, however, still needs much investigation, as it is found that hybrid methods are even slower than pure MPI methods in some situations.

Parallel performance of the overall code is also tested. For laminar flow LDC problems using a large number of grid points, factors of approximately six in speedup could be achieved for 16 cores. For turbulent flow computed with the enhanced ILES method, the tested speedup is around 4.5. This speedup could also be roughly estimated by using the percentage of the arithmetic operations for solving the PPE and momentum equations, as well as the speedups shown in Fig. 4.10. For 16 cores, only 1/10 of the serial run time is needed for PPE, and 1/4.85 for the momentum equation.

For the momentum equation solves, the present ILES code has a total arithmetic operation of approximately 800 (not separately counting adds and multiplies) for each grid point, with another 72 operations per grid point for the (algebraic) solution process for each iteration. Thus, there are roughly 900 arithmetic operations per grid point, with the (reasonable) assumption of four (4) quasilinear iterations per time step. Note that this operation count may seem extremely large, but it arises from the fact that this is a generalized-coordinate code.

The same operation counting procedure shows that set-up requires approximately 70 arithmetic operations per grid point for the PPE, and this is done only once per time step. For SOR, in 3-D, if N is the total number of grid points, the required number of iterations needed to significantly reduce iteration error is $C_p N^{0.333\dots}$, where C_p is an $\mathcal{O}(1)$ constant depending only on the convergence tolerance. There are around 30 arithmetic operations per iteration for each grid point. As a result, PPE solves are rather less important for generalized-coordinate codes than for Cartesian coordinates with respect to parallelization, especially with a smaller number of grid points. For instance, if a 51^3 grid-point problem is considered, the total arithmetic count per grid per time step for PPE is around 3000 (C_p is assume to be one), even

less than the number (3600) for momentum equations. The arithmetic of PPE can, however, overrun that of the momentum equation very easily if a somewhat larger C_p and a larger grid size problem are considered.

For a typical CFD grid size of $N = 51^3$, it is estimated that the PPE solver takes around 50% of the total arithmetic, and the momentum equation takes another 50%; thus the speedup is estimated to be approximately

$$\frac{1}{(50\% \times 0.1 + 50\% \times 0.21)} \approx 6.45 ,$$

for the overall code. Note that the speedup would change accordingly if the number of SOR iterations decreases and the number of quasi-linearization iterations increases. For turbulent flow computations, since the PPE must be solved twice in the context of synthetic-velocity LES, it takes as much as 70% of the overall computation; and the momentum equations take around 20%, with 10% of other parts. Thus, the speedup is estimated to be

$$\frac{1}{(80\% \times 0.1 + 20\% \times 0.21 + 10\%)} \approx 4.5 ,$$

which is not far from the tested speedup of 4.7. Further parallelization could be attempted within the small do-loops in the small-scale part. The large scale and small scale are also expected to be calculated in parallel using MPI. However, the tradeoff still needs to be considered since much time is needed for millions of words of data to transport to another node for each time step.

4.6. Summary and conclusions

In this chapter, a detailed presentation of numerical implementation and parallelization is provided for the basic flow solver. First, the Gresho [191] projection method is employed in the current CFD research code. This is quite different from the widely-used commercial CFD codes, such as Fluent or STAR-CD, which are based on different forms of the SIMPLE algorithm (see Patankar [200]). The projection methods

are theoretically more efficient for time-dependent simulations, which are becoming more widely performed. Although the incompressible flow assumption is used, transferring to any of the non-Boussinesq methods (e.g., the low-Mach-number approximation [20]) in the context of this projection code should also be relatively easy. Second, generalized coordinates are implemented in the code for computing problems with irregular geometry (such as terrain) on uniform grids. Third, solution procedures of the momentum equation and the PPE are presented in detail. The 2^{nd} -order centered differencing discretizations in space and 2^{nd} -order discretizations in time are employed. Nonlinearities are handled with the δ -form Newton–Kantorovich (quasilinearization) procedure, which is implemented in a “block-Jacobi” diagonal fashion. Douglas & Gunn [203] time splitting is used for the momentum and energy equations, and optimal point SOR is used for the (pseudo) pressure Poisson equation (PPE). Explicit solution filtering is performed with a modified 3-D Shuman filter [138].

OpenMP parallelization of the ILES code mainly focuses on two parts: the momentum equations, and the PPE. The momentum equations are parallelized based on the D–G time splitting methods employed in independent directions. The Jacobi and successive overrelaxation (SOR) iterations (both point SOR and red-black ordered SOR) are used to solve a simple problem that mimics the 3-D PPE, utilizing Fortran, C, and C++. It is found that point SOR programmed in Fortran performs best in parallelization with regard to nearly-perfect linear speedups with increasing number of cores, especially for a large problem size. Comparisons are made in the context of having the same algorithm, code structure, and optimization level in compilation. The overall performance is tested by employing the canonical lid-driven cavity (LDC) problem. Since OpenMP does not require explicit information exchanges within the shared-memory architecture, it is found to be simpler and more efficient than MPI across cores. Only 16 cores (maximum cores in current available processors) are being used here; thus, scalability of the model needs to be improved for implementation

using hundreds, or thousands, of cores. Hybrid OpenMP and MPI could be a solution to further increase the speed, but OpenMP needs an extra operation to work on distributed memory systems, as illustrated by Basumallik et al. [212].

Chapter 5: The Poor Man's Navier–Stokes Equations in Porous Media

In recent years, numerous studies have been conducted to numerically simulate turbulent flow through porous media. Hutter et al. [214] used dynamic large-eddy simulation (LES) to explore flow in materials with low porosity and have obtained quite good comparisons with experimental results. Kazerooni and Hannani [215] proposed using the $v2f$ model, which is similar to large-eddy simulation and exhibits superior accuracy with respect to the conventional $k-\varepsilon$ two-equation Reynolds averaged N.–S. (RANS) model. Kuwahara et al. [216] employed renormalization group to derive a subgrid-scale (SGS) model and have shown that the Forchheimer-extended Darcy's law holds for turbulent flow in porous media. However, most of this work has been done using LES with different forms of eddy viscosity based SGS models, the limitations of which have been discussed in Ch. 2, Sec. 2.2.7. This suggests modeling the SGS velocity of turbulent flow through porous media directly, using a synthetic velocity—no eddy-viscosity approach. The synthetic-velocity form of LES, which, instead of modeling sub-grid stresses, models SGS velocities, which may, or may not, be used to directly calculate the stresses. As discussed in Ch. 3, Sec. 3.2, the form of Eq. (3.7) is employed with the amplitude factor being calculated from the high-pass filtered velocity. The temporal fluctuations, however, should be obtained from the generalized Navier–Stokes equation with an addition of forcing terms accounting for linear and non-linear drag forces of the medium—Darcy and Forchheimer terms.

The generalized Navier–Stokes equation for incompressible flow in porous media,

The material contained in this chapter has been published [213] as [International Journal of Bifurcation and Chaos, **26**, 05, 2016, 1650086] [10.1142/S0218127416500863] © [copyright World Scientific Publishing Company] [<http://www.worldscientific.com/worldscinet/ijbc>]

as used by Nithiarasu et al. [115], takes a form similar to that of the original N.–S. equations. It can be viewed as a non-linear dynamical system exhibiting “strange attractors,” which indicates temporally chaotic behavior associated with physical turbulence. Thus, the current work aims to develop a DDS from this equation and investigate bifurcation behaviors of this system. Generally, such chaotic maps are expected to be infused into a self-contained model of subgrid-scale velocity fluctuations in the context of a synthetic-velocity form of large-eddy simulation (LES), as mentioned above. In Sec. 5.1, analysis of the problem is provided. In Sec. 5.2 and 5.3, the characteristic behaviors of the system are explored in terms of regime maps, power spectra, time series and phase portraits. Finally, summary and conclusions are provided in Sec. 5.4.

5.1. Analysis

In this section, the governing equations employed in this study are first introduced. Then a detailed derivation of the poor man’s Navier–Stokes equation with Darcy and Forchheimer terms is presented; the assumptions embedded therein are also briefly discussed.

5.1.1 Flow regime analysis

The generalized model for 3-D incompressible flow through porous media is described in detail in Ch. 3. The Darcy and Forchheimer terms appearing in Eq. (3.1b) are also proposed by Ward [217] and Ahmed and Sunada [218], assuming that the linear coefficient $-\mu/K$ depends on fluid properties only, and the non-linear coefficient $c_F K^{-1/2} \rho$ depends on geometric properties of the media only. In the Forchheimer term, c_F is known as the Ergun coefficient; based on experiments [126], it is related

to the geometry of a porous medium and can be expressed as

$$c_F = \frac{1.75}{\sqrt{150\phi^3}}. \quad (5.1)$$

Venkataraman [219] developed curves relating the friction factor and Reynolds number theoretically and demonstrated regimes ranging from Darcian, to transitional, to turbulent flow, as is shown in Fig. 5.1. The friction factor f_k , Reynolds number

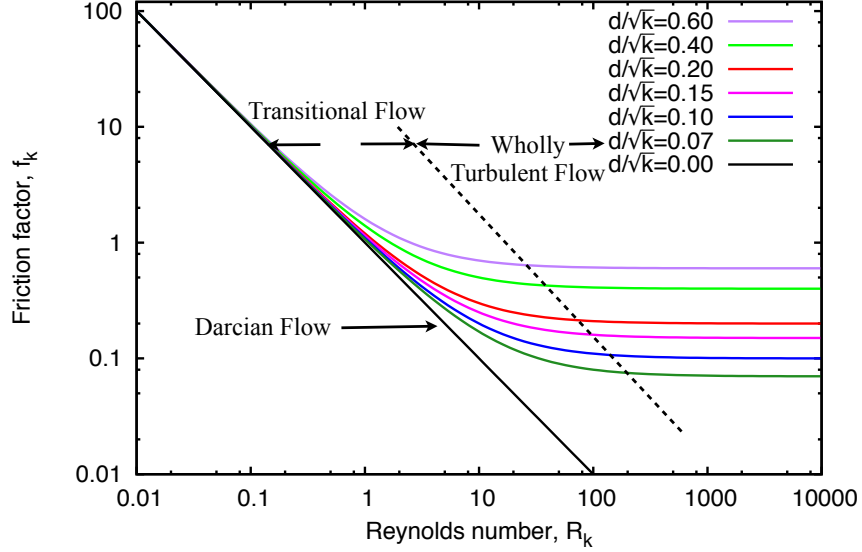


Figure 5.1: Relationship between friction factor and Reynolds number [219].

R_k , and the parameter d are respectively expressed as [217]

$$f_k = \frac{1}{R_k} + \frac{d}{\sqrt{k_p}}, \quad R_k = \frac{\mathbf{u}\sqrt{k_p}}{\nu}, \quad d = c_F\sqrt{k_p}. \quad (5.2)$$

The intrinsic permeability k_p in Eqs. (5.2) equals the permeability K since only one-phase fluid is considered. Figure 5.1 shows only the theoretical curves for reference in later discussion, below; verification of these with available experimental data was also provided (see Fig. 3 in [219]). As is seen, different flow regimes depend on any two of the three parameters f_k , R_k , and d/\sqrt{K} , with d/\sqrt{K} related to c_F according to its expression in Eqs. (5.2). Thus, turbulent flow may exist in porous media even at small R_k if f_k or c_F is large enough; also Darcian or transitional flow may occur at large R_k if f_k or c_F is sufficiently small.

5.1.2 Derivation

Mathematical analysis of Eqs. (3.1) often begins with a Leray projection to a divergence-free subspace of the Sobolev space of solutions, thus eliminating the pressure gradient from Eq. (3.1b). Also, the effective velocity in the momentum equation is replaced with the actual velocity since the actual (pore) velocity contains more local information than the macroscopic effective velocity, and the PMNS equations mainly account for behaviors on sub-grid scales that are local in space and time. This results in x -momentum and thermal energy equations expressed as

$$U_t + UU_x + VU_y + WU_z = \frac{\mu_e}{\rho} \phi \Delta U - \frac{\mu \phi}{K \rho} U - c_F K^{-\frac{1}{2}} \phi^2 U \sqrt{U^2 + V^2 + W^2} - g_x \beta_e \rho (T - T_0) , \quad (5.3)$$

$$T_t + UT_x + VT_y + WT_z = \frac{k_f}{(\rho c)_f} \Delta T + \frac{q_f'''}{(\rho c)_f} . \quad (5.4)$$

The y -momentum and z -momentum equations are obtained in an analogous way; g_y is the gravity acceleration; g_x and g_z are zero. Typical scalings are applied to the dependent and independent variables in Eq. (5.3) and (5.4) using velocity scale U_* , length scale L_* , time scale L_*/U_* , and temperature scale $(T_1 - T_0) = \delta T$, for instance,

$$U_{**} = \frac{U}{U_*}, \quad x_{**} = \frac{x}{L_*}, \quad t_{**} = \frac{t}{L_*/U_*}, \quad T_{**} = \frac{T - T_0}{T_1 - T_0} = \frac{T - T_0}{\delta T} ,$$

where T_1 and T_0 are reference temperatures (often corresponding to boundary temperatures). Therefore, the dimensionless form of Eq. (5.3) and (5.4) can be written as

$$U_t + UU_x + VU_y + WU_z = \frac{1}{Re} \Delta U - \frac{\mu \phi L_*}{K \rho U_*} U - c_F K^{-\frac{1}{2}} \phi^2 L_* U \sqrt{U^2 + V^2 + W^2} - \frac{Gr}{Re^2} T , \quad (5.5)$$

$$T_t + UT_x + VT_y + WT_z = \frac{1}{Pe} \Delta T + S , \quad (5.6)$$

where the non-dimensional numbers are

$$Re = \frac{\rho U_* L_*}{\phi \mu_e}, \quad Pe = \frac{U_* L_* (\rho c)_f}{k_f}, \quad Gr = \frac{g \beta_e \delta T L_*^3}{\nu^2} ,$$

and the source term becomes

$$S = \frac{q_f''' L_*}{(\rho c)_f U_* \delta T} .$$

For simplicity, the same notations for variables are used. Coordinate subscripts indicate partial differentiation. The form of nonlinearity in Eq. (5.5) is somewhat different from that of the usual N.-S. equations; hence, a somewhat more complicated bifurcation behavior should be anticipated.

The following derivation procedure is in a manner similar to that provided in [144]. A Galerkin procedure is employed with velocity and temperature components expressed in Fourier representations as

$$U(\mathbf{x}, t) = \sum_{\mathbf{k}=-\infty}^{\infty} a_{\mathbf{k}}(t) \varphi_{\mathbf{k}}(\mathbf{x}) , \quad V(\mathbf{x}, t) = \sum_{\mathbf{k}=-\infty}^{\infty} b_{\mathbf{k}}(t) \varphi_{\mathbf{k}}(\mathbf{x}) , \quad (5.7a)$$

$$W(\mathbf{x}, t) = \sum_{\mathbf{k}=-\infty}^{\infty} c_{\mathbf{k}}(t) \varphi_{\mathbf{k}}(\mathbf{x}) , \quad T(\mathbf{x}, t) = \sum_{\mathbf{k}=-\infty}^{\infty} d_{\mathbf{k}}(t) \varphi_{\mathbf{k}}(\mathbf{x}) . \quad (5.7b)$$

Here, $\mathbf{k} \equiv (k_1, k_2, k_3)^T$ is a 3-D wavevector, $\mathbf{x} = (x, y, z)^T$, and $\{\varphi_{\mathbf{k}}\}$ is an unspecified, countable, orthonormal set of basis functions, which is assumed to be complete in L^2 and possess differentiation properties analogous to complex exponentials. It is realized that constructing such a basis set for computational purposes could be difficult, but this is not necessary for the present analysis. The elements of $\{\varphi_{\mathbf{k}}\}$ have the following wave-like properties:

$$\partial_i \varphi_{\mathbf{k}} = k_i \tilde{\varphi}_{\mathbf{k}} , \quad \partial_i \partial_j \varphi_{\mathbf{k}} = -k_i k_j \varphi_{\mathbf{k}} , \quad C_{\mathbf{k}} \tilde{\varphi}_{\mathbf{k}} \in \{\varphi_{\mathbf{k}}(\mathbf{x})\} , \quad (5.8)$$

where $C_{\mathbf{k}}$ is a normalization constant.

Details for the x -momentum equation are given; treatment of momentum equations in other directions is identical. First, substituting Eqs. (5.7) into Eq. (5.5) and (5.6), and applying the wave-like property of the basis functions shown in Eqs. (5.8)

to first and second-order spatial derivatives in the equations leads to

$$\begin{aligned}
& \sum_l \dot{a}_l \varphi_l + \sum_{l,m} m_1 a_l a_m \varphi_l \tilde{\varphi}_m + \sum_{l,m} m_2 b_l a_m \varphi_l \tilde{\varphi}_m + \sum_{l,m} m_3 c_l a_m \varphi_l \tilde{\varphi}_m \\
&= -\frac{C|\mathbf{k}|^2}{Re} \sum_l a_l \varphi_l - \frac{\mu\phi L}{K\rho U} \sum_l a_l \varphi_l - \frac{Gr}{Re^2} \sum_l d_l \varphi_l \\
& - \sum_l \left(c_F K^{-\frac{1}{2}} \phi^2 L \sqrt{\left(\sum_m a_m \varphi_m \right)^2 + \left(\sum_m b_m \varphi_m \right)^2 + \left(\sum_m c_m \varphi_m \right)^2} \right) a_l \varphi_l .
\end{aligned} \tag{5.9}$$

Similarly, the energy equation becomes

$$\begin{aligned}
& \sum_l \dot{d}_l \varphi_l + \sum_{l,m} m_1 a_l d_m \varphi_l \tilde{\varphi}_m + \sum_{l,m} m_2 b_l d_m \varphi_l \tilde{\varphi}_m + \sum_{l,m} m_3 c_l d_m \varphi_l \tilde{\varphi}_m \\
&= -\frac{C|\mathbf{k}|^2}{Pe} \sum_l d_l \varphi_l + S .
\end{aligned} \tag{5.10}$$

In Eq. (5.9) (5.10), “ $\dot{\cdot}$ ” indicates differentiation with respect to time. The appearance of the normalization constant C in the dissipation term is due to the assumption that the derivatives are also orthogonal, but with possibly different normalizations. Next, construct the inner product of each term in Eq. (5.9) and (5.10) with orthonormal $\varphi_{\mathbf{k}}$ for each \mathbf{k} ; this leads to

$$\begin{aligned}
& \dot{a}_{\mathbf{k}} + \sum_{l,m} m_1 a_l a_m \int_{\Omega} \varphi_{\mathbf{k}} \varphi_l \tilde{\varphi}_m + \sum_{l,m} m_2 b_l a_m \int_{\Omega} \varphi_{\mathbf{k}} \varphi_l \tilde{\varphi}_m \\
& + \sum_{l,m} m_3 c_l a_m \int_{\Omega} \varphi_{\mathbf{k}} \varphi_l \tilde{\varphi}_m = -\frac{C|\mathbf{k}|^2}{Re} a_{\mathbf{k}} - \frac{\mu\phi L}{K\rho U} a_{\mathbf{k}} - \frac{Gr}{Re^2} d_{\mathbf{k}} \\
& - c_F K^{-\frac{1}{2}} \phi^2 L \sum_l a_l \int_{\Omega} \varphi_{\mathbf{k}} \varphi_l \sqrt{\left(\sum_m a_m \varphi_m \right)^2 + \left(\sum_m b_m \varphi_m \right)^2 + \left(\sum_m c_m \varphi_m \right)^2} ,
\end{aligned} \tag{5.11}$$

and

$$\begin{aligned}
& \dot{d}_{\mathbf{k}} + \sum_{l,m} m_1 a_l d_m \int_{\Omega} \varphi_{\mathbf{k}} \varphi_l \tilde{\varphi}_m + \sum_{l,m} m_2 b_l d_m \int_{\Omega} \varphi_{\mathbf{k}} \varphi_l \tilde{\varphi}_m \\
& + \sum_{l,m} m_3 c_l d_m \int_{\Omega} \varphi_{\mathbf{k}} \varphi_l \tilde{\varphi}_m = -\frac{C|\mathbf{k}|^2}{Pe} d_{\mathbf{k}} + S_{\mathbf{k}} ,
\end{aligned} \tag{5.12}$$

for all \mathbf{k} . As seen, the last (Forchheimer) term in Eq. (5.11) contains more complicated nonlinearities requiring careful treatment. In Eq. (5.12), $S_{\mathbf{k}} = \langle S, \varphi_{\mathbf{k}} \rangle$. However,

after truncating the infinite system of ordinary differential equations (ODEs) to a single arbitrary wavenumber \mathbf{k} , the resulting form is largely simplified as follows

$$\begin{aligned} \dot{a}_{\mathbf{k}} + A^{(1)}a_{\mathbf{k}}a_{\mathbf{k}} + A^{(2)}b_{\mathbf{k}}a_{\mathbf{k}} + A^{(3)}c_{\mathbf{k}}a_{\mathbf{k}} \\ = \left(-\frac{C|\mathbf{k}|^2}{Re} - \frac{\mu\phi L}{K\rho U} - c_F K^{-\frac{1}{2}}\phi^2 L\mathcal{N}\sqrt{(a_{\mathbf{k}})^2+(b_{\mathbf{k}})^2+(c_{\mathbf{k}})^2} \right) a_{\mathbf{k}} - \frac{Gr}{Re^2}d_{\mathbf{k}}, \end{aligned} \quad (5.13)$$

and

$$\dot{d}_{\mathbf{k}} + D^{(1)}a_{\mathbf{k}}d_{\mathbf{k}} + D^{(2)}b_{\mathbf{k}}d_{\mathbf{k}} + D^{(3)}c_{\mathbf{k}}d_{\mathbf{k}} = -\frac{C|\mathbf{k}|^2}{Pe}d_{\mathbf{k}} + S_{\mathbf{k}}, \quad (5.14)$$

with $A^{(i)} = k_i \int_{\Omega} \varphi_{\mathbf{k}}^2 \tilde{\varphi}_{\mathbf{k}}$ and $\mathcal{N} = \int_{\Omega} \varphi_{\mathbf{k}}^2 |\varphi_{\mathbf{k}}|$, $i = 1, 2, 3$. In order to obtain a discrete equation, a simple forward-Euler explicit time-integration procedure is employed to obtain

$$\begin{aligned} a^{(n+1)} = a^{(n)} - \tau \left(A^{(1)} (a^{(n)})^2 + A^{(2)} a^{(n)} b^{(n)} + A^{(3)} a^{(n)} c^{(n)} + \frac{C|\mathbf{k}|^2}{Re} a^{(n)} \right. \\ \left. + \frac{\mu\phi L}{K\rho U} a^{(n)} + c_F K^{-\frac{1}{2}} \phi^2 L\mathcal{N} a^{(n)} \sqrt{(a^{(n)})^2 + (b^{(n)})^2 + (c^{(n)})^2} + \frac{Gr}{Re^2} d^{(n)} \right). \end{aligned} \quad (5.15)$$

Note that wavenumber notation is suppressed for simplicity; (n) represents time steps. The energy equation is integrated using backward Euler for the diffusion term because if $|\mathbf{k}| > Pe$, the differential equation will be stiff, thus

$$d^{(n+1)} = d^{(n)} - \tau \left(D^{(1)} d^{(n)} a^{(n)} + D^{(2)} d^{(n)} b^{(n)} + D^{(3)} d^{(n)} c^{(n)} + \frac{C|\mathbf{k}|^2}{Pe} d^{(n+1)} - S_{\mathbf{k}} \right). \quad (5.16)$$

The arbitrary discrete time step parameter τ can be calculated from physics when constructing a model but will be included in bifurcation parameter definitions in the present study. Rearranging terms yields

$$\begin{aligned} a^{(n+1)} = \tau A^{(1)} a^{(n)} \left(\frac{1 - C\tau|\mathbf{k}|^2/Re}{\tau A^{(1)}} - a^{(n)} \right) - \tau A^{(2)} a^{(n)} b^{(n)} - \tau A^{(3)} a^{(n)} c^{(n)} \\ - \tau \frac{\mu\phi L}{K\rho U} a^{(n)} - \tau c_F K^{-\frac{1}{2}} \phi^2 L\mathcal{N} a^{(n)} \sqrt{(a^{(n)})^2 + (b^{(n)})^2 + (c^{(n)})^2} - \tau \frac{Gr}{Re^2} d^{(n)}. \end{aligned} \quad (5.17)$$

and

$$d^{(n+1)} = (1 - \tau D^{(1)} a^{(n)} - \tau D^{(2)} b^{(n)} - \tau D^{(3)} c^{(n)}) d^{(n)} / (1 + \beta_T) + \tau S / (1 + \beta_T). \quad (5.18)$$

Assuming $1 - C\tau|\mathbf{k}|^2/Re = \tau A^{(1)}$, as was done in [144], the core expression of the logistic map is recovered. This is viewed as a quadratic map transformation; it was not employed in [150], but similar equations resulted. Through further rearrangements and analogous derivations in other directions, the 3-D poor man's Navier–Stokes equations with Darcy and Forchheimer terms and a thermal energy equation are obtained as

$$a^{(n+1)} = \beta_1 a^{(n)}(1 - a^{(n)}) - \gamma_{12} a^{(n)} b^{(n)} - \gamma_{13} a^{(n)} c^{(n)} - \lambda_1 a^{(n)} - \mu_1 a^{(n)} \sqrt{(a^{(n)})^2 + (b^{(n)})^2 + (c^{(n)})^2}, \quad (5.19a)$$

$$b^{(n+1)} = \beta_2 b^{(n)}(1 - b^{(n)}) - \gamma_{21} a^{(n)} b^{(n)} - \gamma_{23} b^{(n)} c^{(n)} - \lambda_2 b^{(n)} - \mu_2 b^{(n)} \sqrt{(a^{(n)})^2 + (b^{(n)})^2 + (c^{(n)})^2} + \alpha_T d^{(n)}, \quad (5.19b)$$

$$c^{(n+1)} = \beta_3 c^{(n)}(1 - c^{(n)}) - \gamma_{31} a^{(n)} c^{(n)} - \gamma_{32} b^{(n)} c^{(n)} - \lambda_3 c^{(n)} - \mu_3 c^{(n)} \sqrt{(a^{(n)})^2 + (b^{(n)})^2 + (c^{(n)})^2}, \quad (5.19c)$$

$$d^{n+1} = (1 - \gamma_{uT} a^{(n)} - \gamma_{vT} b^{(n)} - \gamma_{wT} c^{(n)}) d^{(n)} / (1 + \beta_T) + d_0. \quad (5.19d)$$

In these equations, β_i s, $\gamma_{i,j}$ s, λ_i s and μ_i s, $i, j = 1, 2, 3, i \neq j$, are bifurcation parameters. Evaluation of such a large number (15) of parameters seems difficult, but they are all directly related to physical variables and can be calculated from the high-pass filtered large-scale solutions in the context of LES subgrid-scale turbulence modeling. Hence, this does not pose a turbulence “closure” problem.

First, β_i s are calculated from

$$\beta_i = D^* (1 - \frac{C}{Re_i} \tau |\mathbf{k}|^2), \quad Re_i \equiv \frac{h^2 |\partial u_i^{**} / \partial x_i|}{\nu_e \phi}, \quad (5.20)$$

where the Re_i are small-scale component (cell) Reynolds numbers for each velocity component; h is the discretization step size for the large-scale numerical approximation; u^{**} is the high-pass filtered i^{th} velocity component, and ν_e is the effective

kinematic viscosity. Although Re here, and R_k in Eq. (5.2), use different characteristic lengths, they represent the same flow behaviors and can be used for qualitative analysis, as is done in following sections. The coefficient D^* is usually taken to be four as analyzed in [144] following the scaling originally used by May [220] for the logistic map which appears as the first term in each of Eqs. (5.19) except Eq. (5.19d). The single retained wavevector \mathbf{k} can be calculated from the reciprocal of Taylor micro-scale length in LES SGS constructions. The $\gamma_{i,j}$ s in the x -momentum equation are expressed as

$$\gamma_{12} = \tau A^{(2)} = \tau \frac{\partial u}{\partial y}, \quad \gamma_{13} = \tau A^{(3)} = \tau \frac{\partial u}{\partial z}, \quad (5.21)$$

with similar descriptions in other directions. These consist of the small-scale time step size and the Galerkin triple products corresponding to the selected wavevector. The latter of these carries information associated with the velocity gradients or strain rates, and they can be evaluated with high-pass filtered resolved-scale data on the computational grid of LES. Use of Eqs. (5.21) precludes use of Galerkin triple products.

From the form of Eq. (5.19d), coefficient of β_T and α_T can be expressed as

$$\beta_T = \frac{C}{Pe} \tau |\mathbf{k}|^2, \quad \alpha_T = -\tau \frac{Gr}{Re^2}. \quad (5.22)$$

It is seen that as $Pe \rightarrow 0$, $\beta_T \rightarrow \infty$. In Eq. (5.6), it is also clear that as Pe increases, the effects of diffusion become small, and vis versa for the advection and source term S . This is consistent with what is shown in Eq. (5.19d), where $d_0 = \tau S / (1 + \beta_T)$, and is set by the high-pass filtered temperature so that the SGS behavior fluctuates about it. Also, if $\beta_T \rightarrow \infty$, $d^{n+1} \rightarrow 0$, indicating no turbulent behavior for the temperature.

Bifurcation parameters associated with Darcy and Forchheimer terms are expressed as

$$\lambda_i = \tau \frac{\mu \phi L}{K \rho U} \sim \frac{\phi}{K}, \quad \mu_i = \tau c_F K^{-\frac{1}{2}} \phi^2 L \mathcal{N} \sim \frac{\phi^2}{\sqrt{K}}, \quad i = 1, 2, 3. \quad (5.23)$$

It is clearly seen that these parameters are related to porosity and permeability in each direction, and thus are positive values. For isotropic porous media, they are the same in all directions, in contrast to the anisotropic case. Also, porosity and permeability have the constraints that as $\phi \rightarrow 0$, $K \rightarrow 0$, and as $\phi \rightarrow 1$, $K \rightarrow \infty$. Here, $\phi, K \neq 0$ must hold because fluid is not a solid phase. Note that $\phi = 1$ corresponds to clear fluid flow, indicating values of both λ and μ are zero; this is consistent with the derived DDS. On the other hand, bifurcation parameter values (λ and μ) reflect values of porosity and permeability. For instance, smaller values indicate relatively high-porosity media flow (large permeability), and vice versa.

If values of permeability and porosity are known, these parameters can be evaluated for constructing a model. Usually, porosity can be estimated through measurement, and permeability can be calculated in terms of porosity from an appropriate empirical equation. A recently derived general permeability model calculated from porosity, strain rate and effective viscosity (which are related to specific details of the geometry like tortuosity, etc.), Tang and McDonough [124], can also be used. Since the dynamic viscosity of air is $\mu \sim 10^{-5} \text{Kg/m s}$, the time step size is usually taken to be $\tau \sim 10^{-3} \text{ s}$, and L, U, ρ_0 are order of magnitude one; λ can be estimated as $10^{-8} \times \phi/K$, and μ is approximately $10^{-4} \times \phi^2/\sqrt{K}$, according to Eq. (5.23).

Consider a porous medium with porosity of 0.1. Its permeability can be estimated to be around 10^{-6} through the empirical Carman–Kozeny [221] [222] equation, which leads to values of λ and μ approximately 0.001. These parameter values can be initial estimates for the current study of the DDS in the absence of large-scale LES results. By determining valid ranges for the parameters of additional terms, as will be done in the present study, the first step is to construct a mapping of flow physics in porous media turbulence in 3D as was done in [144] for simple incompressible flows—but only in 2D.

5.1.3 Bifurcation analysis

For the sake of simplicity, here, the incompressible flow N.–S. equation without buoyancy and energy equation is investigated. Thus the bifurcation parameters associated with energy and buoyancy are zero in the following calculations and discussions. Among the 15 bifurcation parameters in the DDS of Eq. (5.19), six are from the porous terms. Many numerical investigations have been conducted previously associated with the β and γ parameters [144–147, 150]. Here, the behaviors resulting from the additional parameters λ and μ , and in a rather small subspace of the complete space of possible parameter values, are mainly considered. Both isotropic and anisotropic porous media are considered. Bifurcation behavior of the DDS is discussed in terms of power spectral density (PSD), time series, phase portraits and the so-called “regime maps” (bifurcation diagrams exhibiting a broad view of PSD behaviors for different combinations of parameters).

Calculations of regime maps and basins of attractions reported for this study were performed on the 256-basic-node Dell high-performance computing cluster at the University of Kentucky Computing Center, each basic node of which has two 2.6 GHz Intel E5-2670 eight-core processors and 64 GB of RAM. The initial conditions are $a^{(0)} = 0.3$, $b^{(0)} = 0.95$, $c^{(0)} = 0.2$ for all cases except those investigating sensitivity to initial conditions (SIC). These initial conditions were chosen after numerical experimentation showed that the resulting flow is in the stable regime of the DDS. Individual cases were computed using a desktop computer with a 2.4 GHz Intel Core 2. All results were obtained using double precision (64-bit) Fortran. A typical run consisted of 10^4 iterations of Eqs. (5.19) with the last 5×10^3 subjected to the indicated statistical analysis. In the case of power spectra, a standard radix-2 fast-Fourier transform (FFT) was used, and this was applied to the final 2^{12} (or 4096) points of the time series for $\{a^{(n)}\}$, $\{b^{(n)}\}$, $\{c^{(n)}\}$, which are sufficient to produce stationary results needed to identify the basic solution regimes.

5.2. Bifurcation results for variation of β

As shown previously (Eq. (5.20)), β is determined by Re and chosen wavevector; λ and μ are calculated from porosity and permeability. It is intriguing to see how the DDS behaves for flow through media with different porosities as Re increases. Thus, regime maps for varying β and λ with fixed γ , and varying β and γ with fixed λ (and μ) are presented in this section. Regime maps for μ and β present similar information as those for λ and β , since λ and μ are related, as seen in Eqs. (5.23).

In Fig. 5.2, part (a) is the color table associated with different power spectral density (PSD) behaviors, as employed in [144]. Part (b) shows the regime map of $\beta = \beta_1 = \beta_2 = \beta_3$ and λ_1 with relatively small λ_2 (large porosity in the y -direction) and large λ_3 (small porosity in the z -direction), indicating anisotropic porous media. The chosen value of $\gamma = \gamma_1 = \gamma_2 = \gamma_3 = -0.03$ is somewhat arbitrary, but based

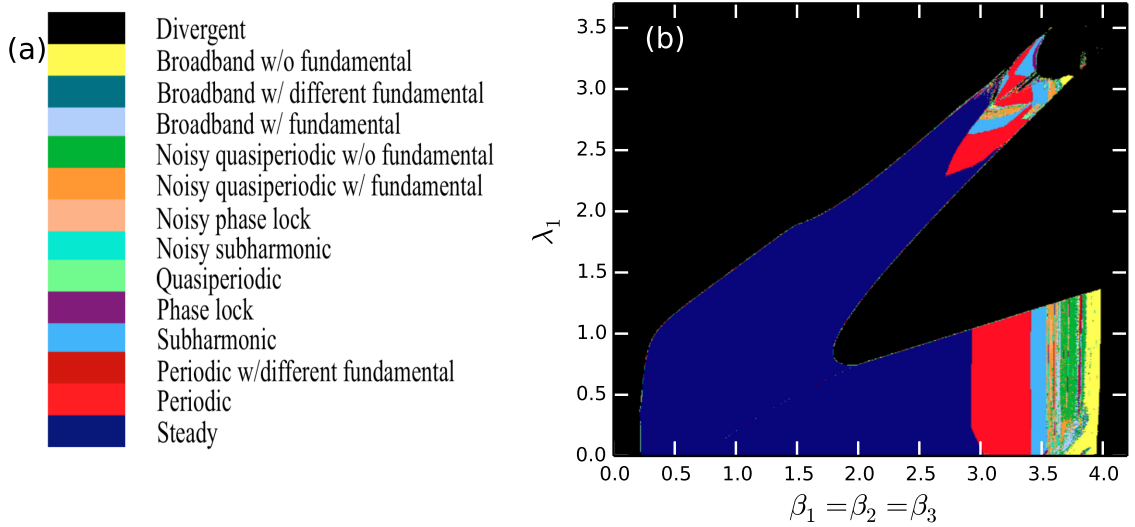


Figure 5.2: Regime map of β vs. λ_1 . (a) color table, (b) $\gamma = -0.03$, $\lambda_1 = \mu_1$, $\lambda_2 = 0.02$, $\mu_2 = 0.01$, $\lambda_3 = 1.2$, $\mu_3 = 1$.

on the conditions that it produces stable results and that it corresponds to various non-trivial (except divergent and steady) behaviors seen in the regime map for clear fluid flow. As is seen, most non-trivial behaviors occur in the region for $\beta > 2.7$ with

$\lambda_1 < 1.4$ or $\lambda_1 > 2.25$. In the region with relatively small λ_1 , as Re increases, the Feigenbaum [223] bifurcation sequence is observed:

$$steady \longrightarrow periodic \longrightarrow subharmonic \longrightarrow chaotic,$$

corresponding to the observed regimes (see Fig. 5.1) as

$$Darcian \longrightarrow nonlinear\ transitional \longrightarrow wholly\ turbulent.$$

In the “chaotic” region, both non-noisy and noisy behaviors are intertwined with each other. There is even a slice of periodicity with different fundamental in the the region of quasiperiodic w/o fundamental, as seen in the map of γ vs. β of [144].

For relatively large λ_1 , as is shown in the zoom in of Fig. 5.3(a), mostly periodic and subharmonic behaviors are present in the central region, surrounded by some chaotic-like behavior, which does not appear in the lower region for $\beta \in [3, 3.6]$. Since

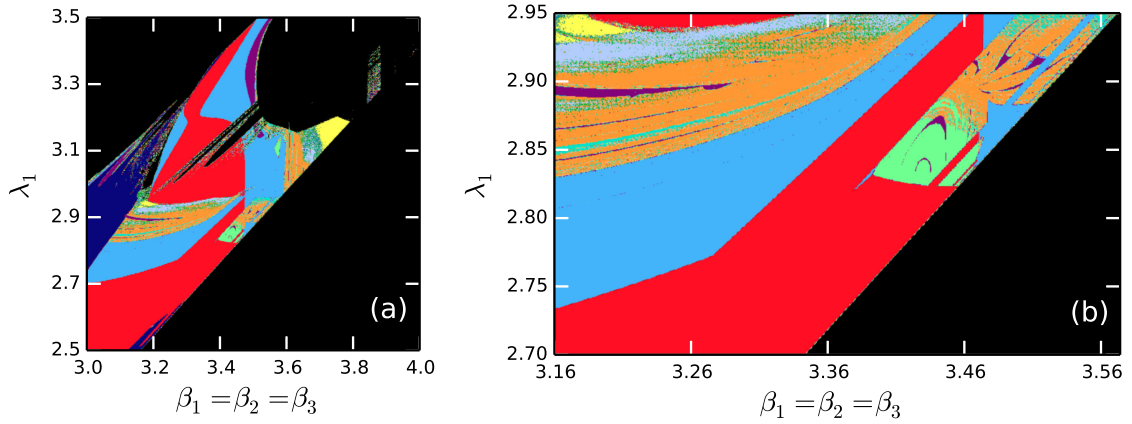


Figure 5.3: Regime map zoom-ins of Figure 5.2(b). (a) $(\beta, \lambda_1) \in [3, 4] \times [2.5, 3.5]$, (b) $(\beta, \lambda_1) \in [3.16, 3.56] \times [2.7, 2.95]$.

porosity in this region is relatively small, which results in larger values of d/\sqrt{K} from Eq. (5.1), the flow transitions to turbulence at smaller Re based on Fig. 5.1. There is an arc-shaped region at the top of this figure due to the “invading” divergent solutions, some of which also protrude far into the non-divergent area in the middle of the arc region, within which Arnol’d “tongues” are imbedded. Part (b) shows an

even smaller region where there is quasiperiodic behavior, within the periodic region, corresponding to a somewhat modified Ruelle and Takens [224] bifurcation sequence similar to that observed by Gollub and Benson [225] in Rayleigh–Bénard convective experiments (in the absence of a porous medium).

Figure 5.4 shows power spectra from a point within each of the regions of Fig. 5.2(b) to demonstrate how each solution behaves. There are 12 types of non-trivial

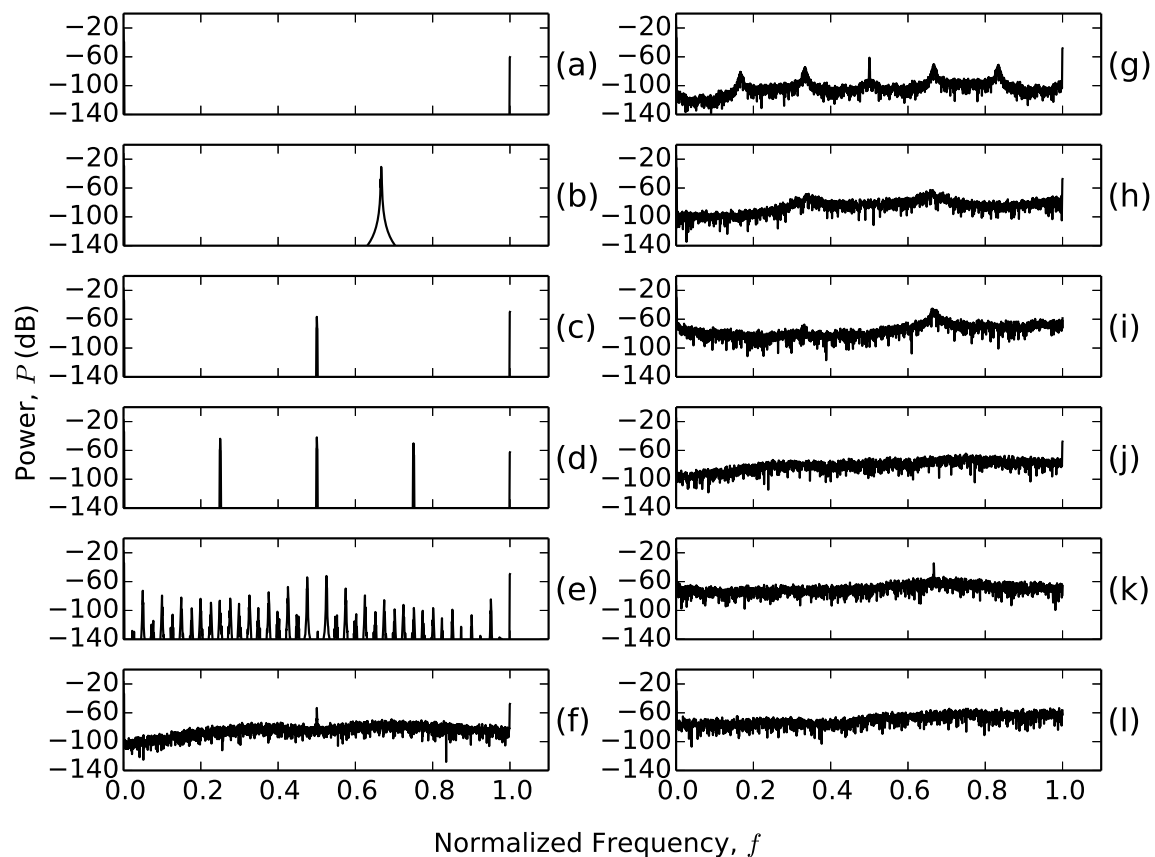


Figure 5.4: Example power spectrum of the 12 non-trivial types of behavior: (a) periodic; (b) periodic w/ different fundamental; (c) subharmonic; (d) phase lock; (e) quasiperiodic; (f) noisy subharmonic; (g) noisy phase lock; (h) noisy quasiperiodic w/ fundamental; (i) noisy quasiperiodic w/o fundamental; (j) broadband w/ fundamental; (k) broadband w/ different fundamental; (l) broadband w/o fundamental.

behavior observed associated with this DDS: (a) periodic, $(\beta, \lambda_1) = (3.2, 0.5)$; (b) periodic with different fundamental, $(\beta, \lambda_1) = (3.8373, 1.0678)$; (c) subharmonic, $(\beta, \lambda_1) = (3.5, 0.5)$; (d) phase lock, $(\beta, \lambda_1) = (3.18898, 2.89167)$; (e) quasiperiodic,

$(\beta, \lambda_1) = (3.4395, 2.8576)$; (f) noisy subharmonic, $(\beta, \lambda_1) = (3.6696, 0.1216)$; (g) noisy phase lock, $(\beta, \lambda_1) = (3.6033, 0.1558)$; (h) noisy quasiperiodic w/ fundamental, $(\beta, \lambda_1) = (3.65, 0.5)$; (i) noisy quasiperiodic w/o fundamental, $(\beta, \lambda_1) = (3.85, 0.5)$; (j) broadband with fundamental, $(\beta, \lambda_1) = (3.68, 0.5)$; (k) broadband with different fundamental, $(\beta, \lambda_1) = (3.8958, 0.0532)$; (l) broadband without fundamental, $(\beta, \lambda_1) = (3.9, 0.5)$. These PSDs are distinguished by noisy or non-noisy behavior and the position and appearance of the fundamental frequency. The criteria to distinguish phase locked and subharmonic behaviors is also discussed in detail in [144]. It seems that they are quite similar, and phase-locked points are usually embedded in the quasiperiodic regions, as is shown in Fig. 5.3(b), often (but not always) as Arnol'd tongues. The frequencies have been normalized because the time increments corresponding to map iterations are arbitrary (which would not be the case for a LES problem).

Figure 5.5 shows the time series corresponding to the power spectra in Fig. 5.4. The time scale used is arbitrary, but the same scale is used in all time series presented herein. It is obviously seen that the velocities have quite different values in $[-1, 1]$ with peak-to-peak amplitude also differing considerably. Parts (d) and (e) have negative values of velocity (and amplitudes are not particularly small). It is of interest to note that negative values of velocity generally lead to divergent behavior in the absence of the additional porosity terms. Since the corresponding points are obtained from the upper region of the regime map, they represent flow through media of quite small porosity. Thus, small velocities are anticipated. As is known, the PMNS equation is employed to construct SGS models, which will be added to the resolved large scale, implying that negative values will make large-scale velocities smaller, thus corresponding to low-porosity flows. The time series of part (k) has relatively large amplitude following from the fact that the value of λ at this point of the regime map is much smaller than for the other cases displayed and thus repre-

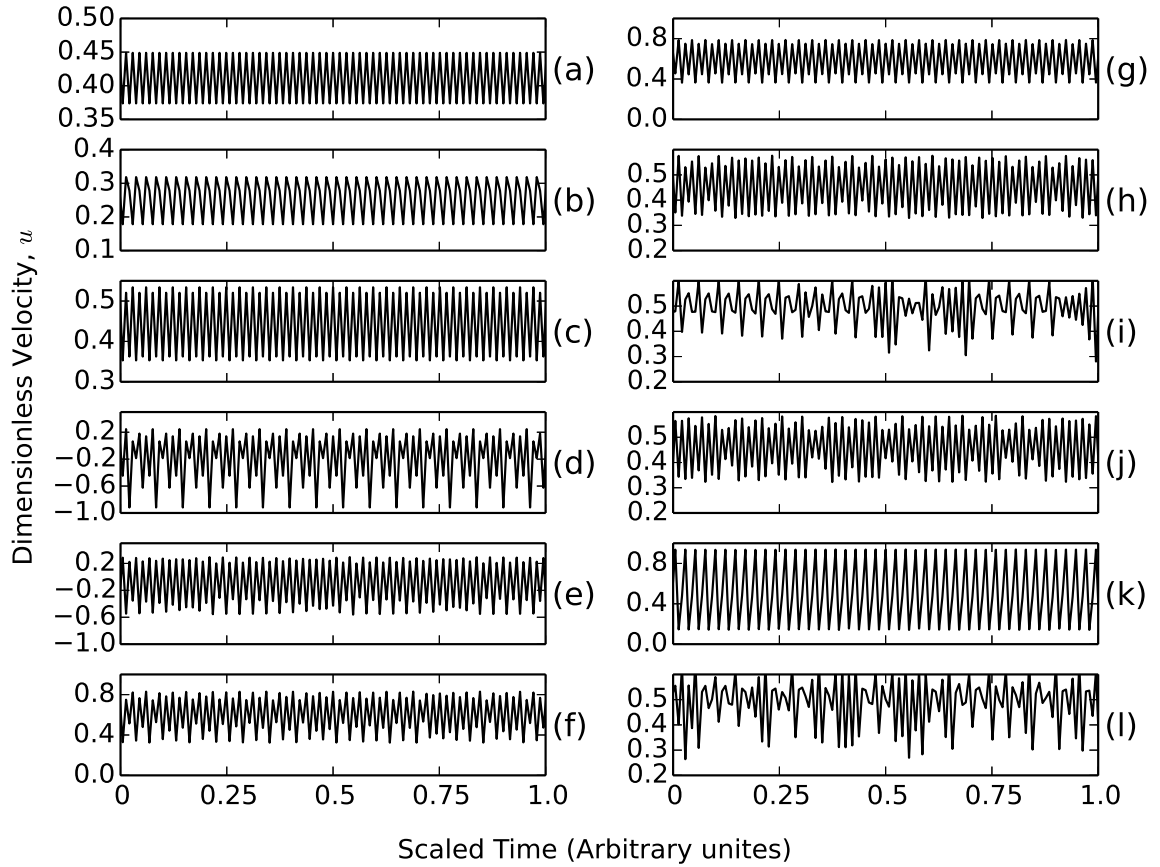


Figure 5.5: Example time series of the 12 non-trivial types of behavior: (a) periodic; (b) periodic w/ different fundamental; (c) subharmonic; (d) phase lock; (e) quasiperiodic; (f) noisy subharmonic; (g) noisy phase lock; (h) noisy quasiperiodic w/ fundamental; (i) noisy quasiperiodic w/o fundamental; (j) broadband w/ fundamental; (k) broadband w/ different fundamental; (l) broadband w/o fundamental.

sents a large-porosity flow. Apart from this, these time series show very interesting distinguishable behaviors. First, (a) and (k) are similar; this is due to the appearance of the fundamentals at the end and in the middle respectively of the frequency domain. However, as the time series is considered over larger ranges of time, it can be clearly seen that the amplitudes of peaks in (k) are not exactly the same, due to the broadband effects, while in (a) they are. In parts (c) and (d), the time series are clearly distinguishable although the corresponding PSDs are similar,. Both (i) and (l) show some intermittency; they correspond to noisy quasiperiodic and broadband

without fundamental, respectively. The fact that their corresponding power spectra do not contain a fundamental is expected to produce this behavior. Part (i) shows type II intermittency [226], which contains aspects of both types I and III intermittencies. Parts (c), (e), (f), (g), (h) and (j) are similar but not exactly the same; they have different amplitudes and numbers of sub-amplitudes. Especially part (j) seems to show type II intermittency.

Another anisotropic possibility is displayed in Fig. 5.6, which shows a regime map of β and λ_1 with larger porosity (small λ or μ) in both y - and z -directions. It is

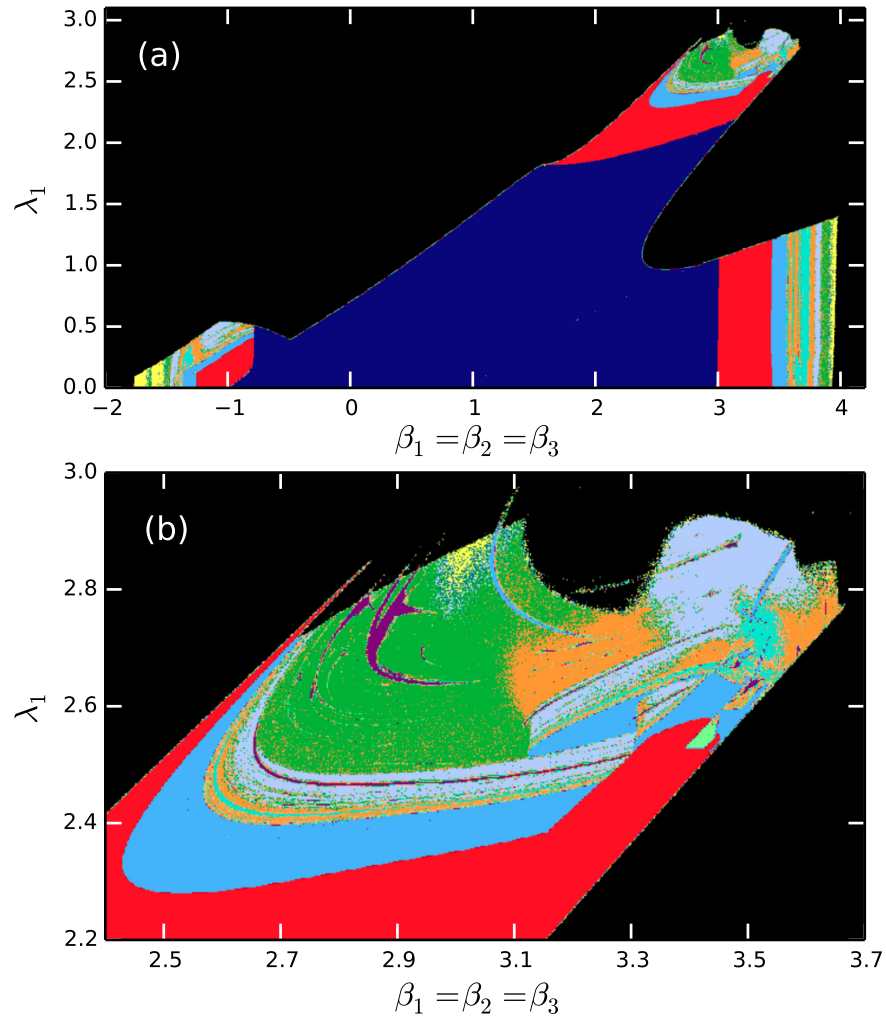


Figure 5.6: Regime map of β vs. λ_1 . (a) $\gamma = -0.03$, $\lambda_1 = \mu_1$, $\lambda_2 = 0.02$, $\mu_2 = 0.002$, $\lambda_3 = 0.2$, $\mu_3 = 0.02$, (b) zoom in for $(\beta, \lambda_1) \in [2.4, 3.7] \times [2.2, 3.0]$.

seen in part (a) that the range of β increases, and more non-trivial behavior appears outside of the steady behavior, especially the additional part for $\beta < 0$. It is remarked that, rather generally, $\beta < 0$ leads to divergence of the DDS for non-porous PMNS equations (but see Bible [227] for some counter examples). Bifurcation sequences similar to those shown in Fig. 5.2(b) are observed in all non-trivial solution regions. In the region $(\beta, \lambda_1) \in [3, 4] \times [0, 1.5]$, a more clearly-defined sequence following the subharmonic solutions is shown: noisy subharmonic is followed by quasiperiodic w/ fundamental, broadband with fundamental, quasiperiodic w/o fundamental and broadband w/o fundamental. The low-porosity (large λ_1) regions $(\beta, \lambda_1) \in [2.4, 3.7] \times [2.2, 3.0]$ present more noisy behaviors than in the previous case (Fig. 5.2(b)) even for a smaller Re number, due to larger porosity in other directions. Also, as noted previously, this indicates that turbulence in porous media may be related to smaller Re since d/\sqrt{K} is large in this low-porosity region, consistent with the physics implied by Fig. 5.1. A zoom-in plot of this region is shown in part (b) of Fig. 5.6. For particular values of β , as λ_1 increases, the same bifurcation sequence is seen (periodic \rightarrow subharmonic \rightarrow chaotic). There also appears a small area of quasiperiodicity at the right-most of the periodic region, as shown in the previous case (Fig. 5.2(b)).

Lastly, effects of forcing (porous) terms on the overall behavior of the original PMNS equations are investigated by comparing regime maps of β and γ with different fixed values of λ and μ , as is shown in Fig. 5.7. By setting both λ and μ to zero, part (a) shows regime map for clear fluid flow, similar to that presented in Plate 1 of [144] for 2-D flow and in Fig. 3.3 of [147] for 3-D flow computed with slightly different initial conditions. Note that behaviors for β less than one are mostly steady and thus are not presented. Parts (b) and (c) show results for non-zero porous terms, with part (c) computed from larger value of μ . It is seen that stable ranges of γ decrease, in comparison with part (a), and their values are less than zero, which is expected from the formula of the DDS because of drag terms. Further observation reveals that

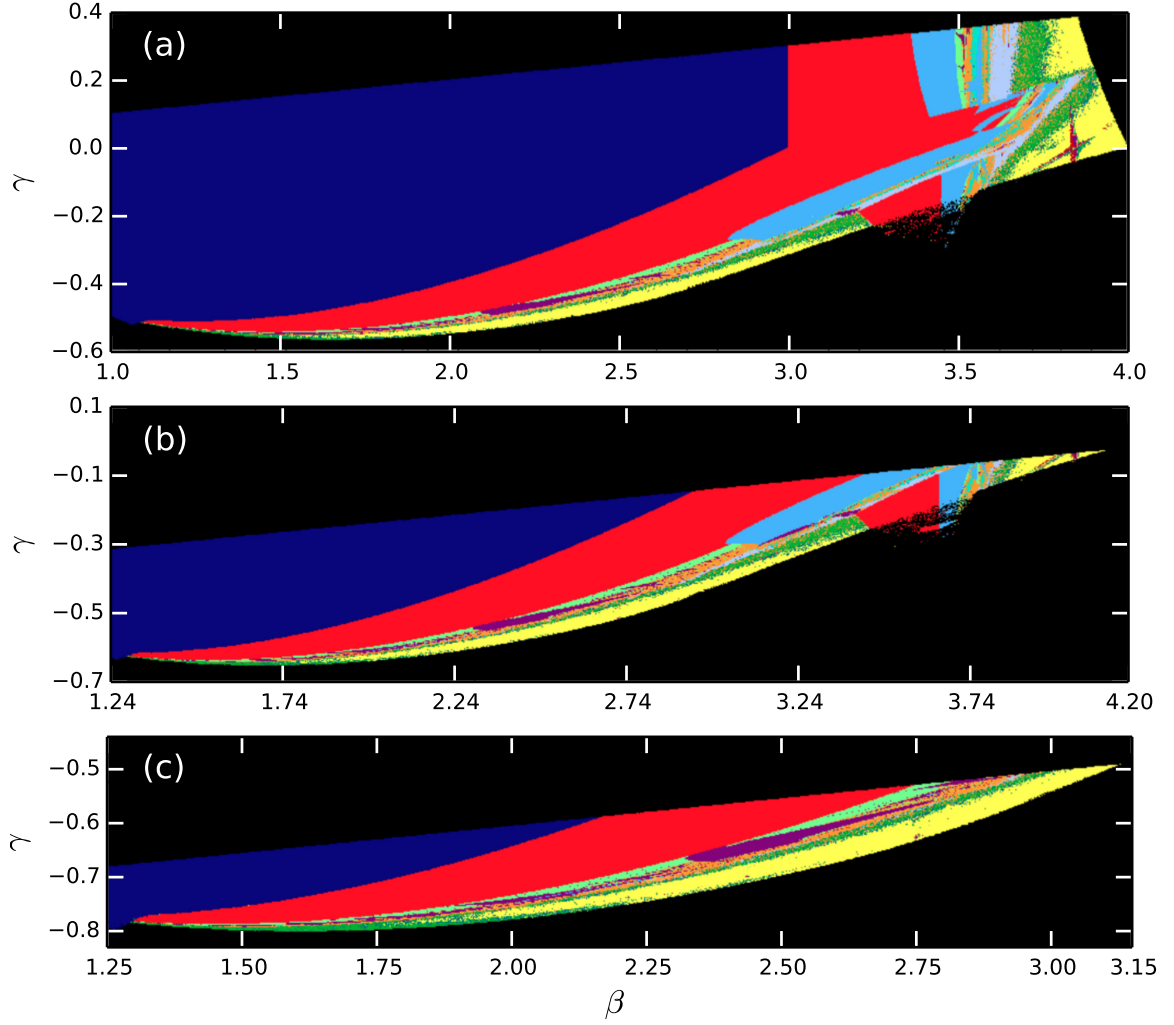


Figure 5.7: Regime map of β vs. γ : (a) $\lambda = \mu = 0$, with $(\Delta\beta, \Delta\lambda_1) = (0.0015, 0.00154)$; (b) $\lambda = 0.2, \mu = 0.02$, with $(\Delta\beta, \Delta\lambda_1) = (0.00148, 0.00133)$; (c) $\lambda = \mu = 0.2$, with $(\Delta\beta, \Delta\lambda_1) = (0.00095, 0.00078)$.

the shape and distribution of PSD behaviors in regime map of part (b) is similar to the lower part of the map in part (a), and part (c) is similar to the even lower part of part (a), but values of corresponding γ and β are not the same. As Re increases, the Feigenbaum sequence is observed in parts (a) and (b), while in part (c), Ruelle and Takens bifurcation sequence appears:

$$steady \longrightarrow periodic \longrightarrow quasiperiodicity \longrightarrow chaotic.$$

In part (c), flow becomes totally (for all γ values) unsteady at around $\beta = 2.13$, and chaotic at about $\beta = 2.75$; both values are smaller than those of part (b). This is because part (c) represents lower porosity flow (larger μ), resulting in larger d/\sqrt{K} than that of part (b); and thus transition to nonlinear, wholly turbulent, flow occurs at lower Re as seen in Fig. 5.1.

5.3. Bifurcation results for variation of λ and μ

In this section, different sets of the original nine fluid dynamic bifurcation parameters (β and γ) are fixed using both isotropic and anisotropic values, also in such a way that the corresponding clear fluid flow presents PSD behaviors corresponding to points in Fig. 5.7(a) at quite different places—usually at the interface of different noisy behaviors—to produce more non-trivial solutions than those lying in the non-turbulent region when varying other parameters. Therefore, characteristics of the DDS exhibited by varying only the bifurcation parameters resulting from the Darcy (λ) and Forchheimer (μ) terms are mainly investigated. Computations were performed with (λ, μ) -resolution using 1001×1001 points in the regime map, corresponding to more than 10^6 cases. Each case was run with 10^4 map iterations of Eqs. (5.19). Both isotropic and anisotropic porous media cases have been studied, followed with investigations of the characteristic of sensitivity to initial conditions.

5.3.1 Isotropic porous media

Figure 5.8 shows λ vs. μ for ideal isotropic porous media (porosity parameters the same in all directions). Part (a) is the same color table given in Fig. 5.2(a), but repeated here for ease of reference. In part (b), bifurcation parameters are set as $\beta_1 = 3.9$, $\beta_2 = 3.87$, $\beta_3 = 3.1$, $\gamma_{12} = \gamma_{13} = \gamma_{21} = \gamma_{23} = 0.3$, $\gamma_{31} = -0.5$, $\gamma_{32} = -0.02$, indicating an anisotropic turbulent flow without porous media. First, it is observed that stable (non-divergent) ranges of both λ and μ are approximately $[0, 0.045]$, con-

sistent with the value estimated previously based on their analytical forms. Second,

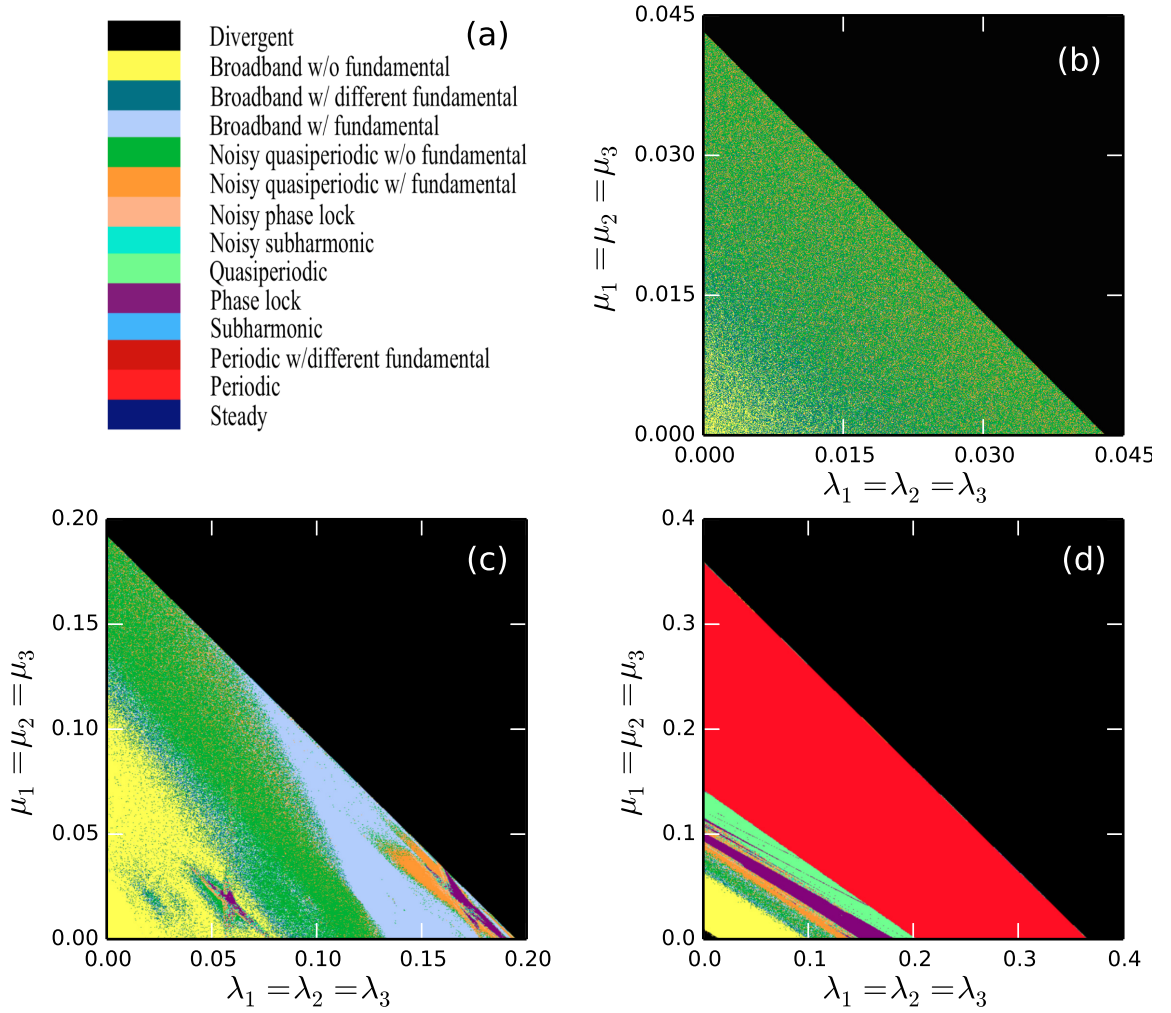


Figure 5.8: Regime maps of λ vs. μ . (a) color table, (b) $\beta_1 = 3.9$, $\beta_2 = 3.87$, $\beta_3 = 3.1$, $\gamma_{12} = \gamma_{13} = \gamma_{21} = \gamma_{23} = 0.3$, $\gamma_{31} = -0.5$, $\gamma_{32} = -0.02$, (c) $\beta = 3.8$, $\gamma = -0.01$, (d) $\beta = 2.5$, $\gamma = -0.48$.

the interface between divergent and non-divergent regions is clear cut, which implies a linear relationship between λ and μ when setting the limiters for calculation of subgrid-scale turbulence, in which case, ranges of values of λ would decrease as μ increases, and vice versa. Third, noisy behaviors from quasiperiodic w/ fundamental to broadband w/o fundamental are shown in the non-divergent region, with different colors intertwined with each other. As values of both parameters approach zero, more

broadband behaviors occur; since the effects from porous terms are very small, the original values of β and γ lead to a more turbulent-like behavior in a clear fluid. As both values get larger, noisy quasiperiodic behaviors become more prevalent. This implies that for certain situations, as effects from the drag terms increase, the flow is less likely to transition to turbulence, in accord with the fact that the velocity, and thus the Re number, would decrease in a porous medium.

In addition, β and γ are made isotropic with different values in parts (c) and (d) for further investigation. In part (c), $\beta_i = 3.8$, $\gamma_{i,j} = -0.01$, for all $i, j = 1, 2, 3$, which is within the chaotic region for the PMNS equation without porous terms (see Fig. 5.7(a)). It is seen that the range of values of λ and μ is much larger than shown in (b) due to the isotropy of β and γ . Since if Re for clear fluid flow is the same in each direction (parts(c) and (d)), larger values of permeability may be permitted consistent with flow in isotropic porous media, resulting in wider ranges of porous media flow and thus parameter values. Also, a relatively large region of broadband behavior with fundamental is shown in part (c). In part (d), $\beta = 2.5$ and $\gamma = -0.48$, which is in a chaotic region that is close to periodic solutions of the regime map for the 3-D case of clear fluid flow. This less chaotic case can result from flow in media of lower porosity (smaller permeabilities); thus the range of parameter values is twice that of part (c). Also, as μ or λ decreases (or the porosity increases), the observed bifurcation sequence is periodic \rightarrow quasiperiodic \rightarrow phase lock \rightarrow chaotic. Note that the small area of divergence shown in the lower-left corner of part (d) (λ and $\mu \rightarrow 0$) is due to the different initial conditions of $c^{(0)} = 0.2$ used in the present case, compared with the case used previously [147].

In all, β and γ have a large influence on the behavior of the DDS for porous terms, since for different Re , flow behaviors would be different even within the same porous medium (see Fig. 5.1). Increasing values of porous terms makes the flow velocity smaller and thus lead to less-turbulent-like behavior. Moreover, in these

cases, the coefficient d/\sqrt{K} increases as bifurcation parameter values increase, and this increases the chance of flow transition to more chaotic behavior, which seems to contradict what has been observed in Sec. 5.2; however, as noted previously, the Re for flow through porous media actually also decreases considering that the characteristic length \sqrt{K} decreases. The observed behavior is mainly due to the effect of decreasing Re outweighing that of increasing the Ergun coefficient or the friction factor.

5.3.2 Anisotropic porous media

More general cases for flow in anisotropic porous media are also considered. Figure 5.9 shows a regime map for varying λ and μ in one direction (x -direction) while fixing different values of these parameters in other directions; β and γ are set as in part (b) of Fig. 5.8. The choice of these parameter values is rather arbitrary, but it prevents uniformly divergent behavior. Part (a) is for a mildly anisotropic case where

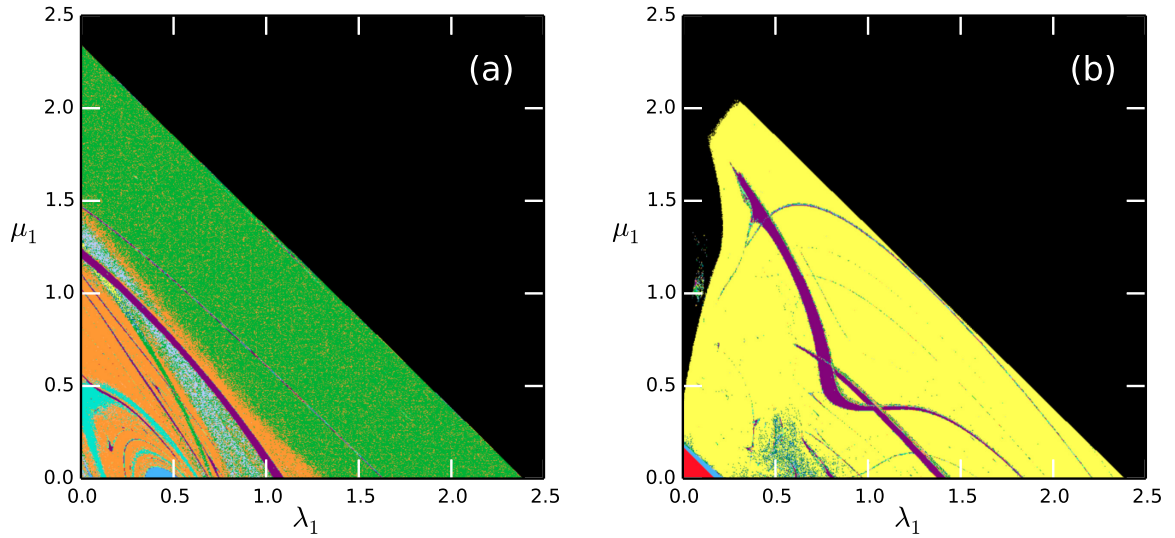


Figure 5.9: Regime maps of λ_1 vs. μ_1 . (a) $\lambda_2 = 0.01$, $\mu_2 = 0.01$, $\lambda_3 = 0.2$, $\mu_3 = 0.3$, (b) $\lambda_2 = 0.02$, $\mu_2 = 0.02$, $\lambda_3 = 1.2$, $\mu_3 = 1.2$.

the difference in parameter values in y and z directions is not very large; part (b) corresponds to larger differences.

First, both (a) and (b) show the ranges of λ_1 and μ_1 nearly covering the interval $[0, 2.5]$, which is almost two orders of magnitude greater than the previous isotropic case (Fig. 5.8(b)). Second, the shape of their cutoffs (lines between divergent and non-divergent areas) is similar to that shown in Fig. 5.8, which provides some information about setting limiters of a SGS model. Note that in part (b) the non-divergent region is not exactly triangular when $0 < \lambda_1 < 0.4$ and $0.5 < \mu_1 < 2$, and it shows considerable divergence but with some small “islands” of non-divergence. Third, parts (a) and (b) present notable differences in the behaviors shown in the non-divergent region. In (a), for $0 < \lambda_1 < 1.2$ and $1 < \mu_1 < 1.5$, mostly noisy quasiperiodicity w/ fundamental occurs; subharmonic and noisy-subharmonic behavior also appears at even lower parameter values. As λ_1 and μ_1 become larger, indicating a porous medium with smaller porosities in the x direction, mostly quasiperiodic w/o fundamental behavior occurs. Part (b) presents mostly broadband without fundamental behavior except for regions of phase lock embedded within the noisy behavior; it also shows some interspersed regions of broadband with different fundamental behavior in the lower and slightly left area; periodic and subharmonic behaviors are observed in the lower-left corner, for large porosities in x direction. Both parts (a) and (b) have shown quite opposite tendencies from those of the previous isotropic cases. It is indicated that if the porosity is small in only one direction, the system behavior is less likely to be chaotic; if porosities in two directions are small, noisy behaviors occur, as seen in parts (a) and (b); if porosities in all three directions are small (as seen in Fig. 5.8(b)), ranges of values remain small, and quite chaotic behaviors occur even though they are not as chaotic as the case when porosities in all three directions are large.

Figure 5.10 displays regime maps of λ_1 vs. λ_3 to account for various combinations of different porosities in two directions with fixed porosity in the third direction. In part (b) of Fig. 5.8, β and γ are set corresponding to anisotropic turbulence in the absence of a porous medium; λ and μ can be made equal as noted previously. In

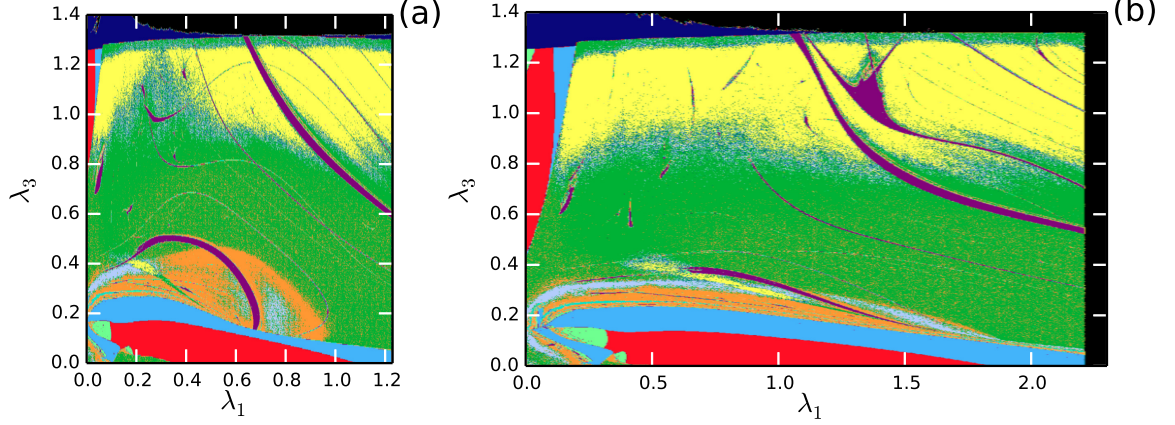


Figure 5.10: Regime maps of λ_1 vs. λ_3 . (a) $\lambda_2 = \mu_2 = 0.02$, $\mu_1 = \lambda_1$, $\mu_3 = \lambda_3$, (b) $\lambda_2 = 0.02$, $\mu_2 = 0.01$, $\mu_1 = 0.1$, $\mu_3 = \lambda_3$.

Fig. 5.10(a), λ and μ are equal in each direction with a small parameter value in the y -direction; part (b) is similar to part (a) except that the x -direction μ value is fixed and there is a slight difference between λ and μ in the y -direction. In this way, parameters are controlled in two directions and can provide more information than does the previous anisotropic case. It is observed that the shape of the non-divergent region in both parts (a) and (b) are essentially rectangular and are different from those of previous regime maps. Thus, it is easier to set the limiters for SGS models since the cutoffs are nearly constant parameters. Also, the range of values of λ_1 in (b) is almost twice that of (a) since it is already fixed by μ_1 , as mentioned above; nevertheless, the general nature and extent of non-trivial behaviors are similar in both plots (a) and (b). For fixed values of λ_1 in the middle of the domain, as λ_3 increases, the same bifurcation sequence occurs: periodic \rightarrow subharmonic \rightarrow quasi-periodic w/ fundamental \rightarrow quasi-periodic w/o fundamental \rightarrow broadband w/o fundamental. Also, as shown in previous maps, slices of phase lock are embedded in the noisy behavior regions. Finally, as noted above, it is clearly seen in both plots that as λ_3 or λ_1 decrease (porosity gets larger in one direction), less chaotic behavior such as periodic and subharmonic occurs. These anisotropic cases demonstrate another

possibility mentioned at the end of Sec. 5.3.1; that is, the effect from increasing friction factor outweighs that of decreasing Re , which gives rise to more chaotic flow as bifurcation parameter values increase.

5.3.3 Sensitivity to initial conditions

The property of sensitivity to initial conditions (SIC) is the hallmark of the strange attractor description of turbulence first put forward by Ruelle and Takens [224]. Investigation of SIC for this DDS is provided in this section. Figures 5.11 and 5.12 present PSD behaviors of noisy quasiperiodic w/o fundamental and broadband w/o fundamental, respectively, in terms of time series and phase portraits. They are

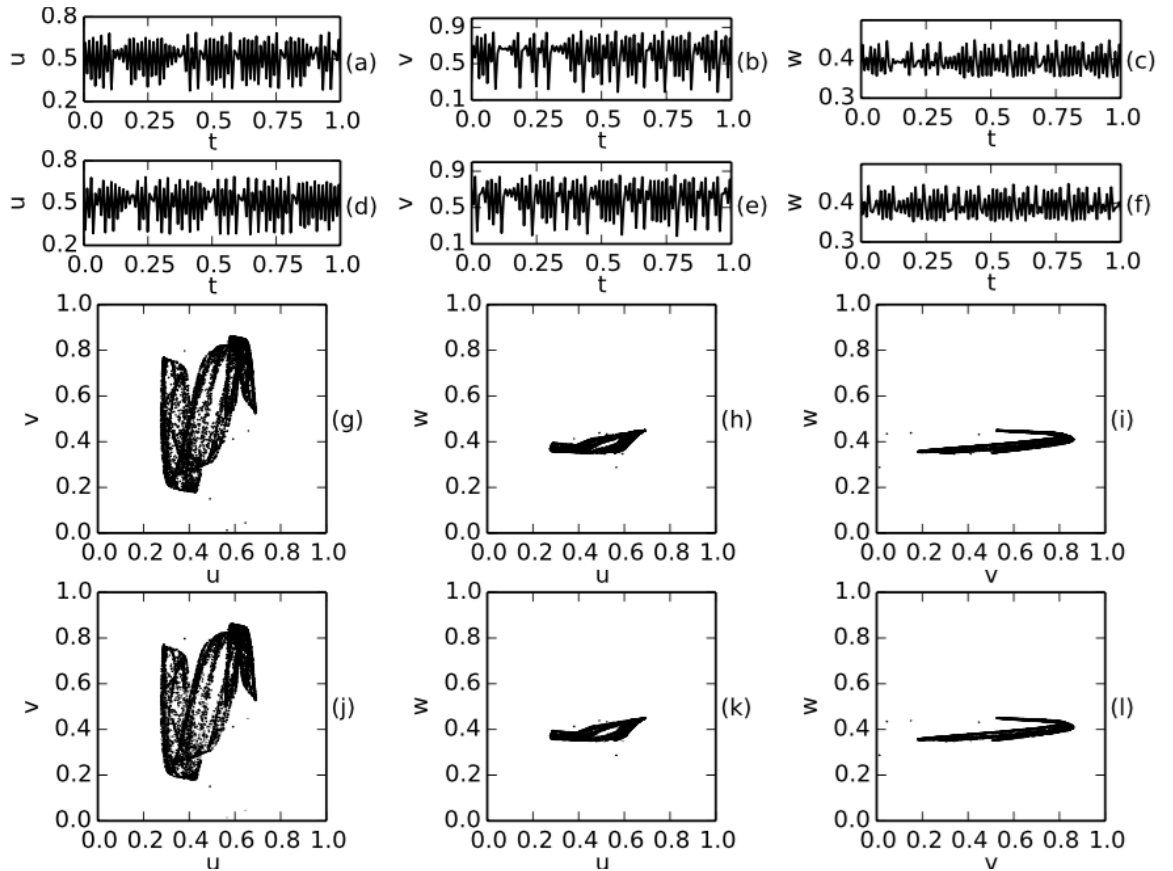


Figure 5.11: Behavior of quasiperiodic w/o fundamental for slightly perturbed initial conditions: (a)–(f) time series; (g) & (l) phase portraits.

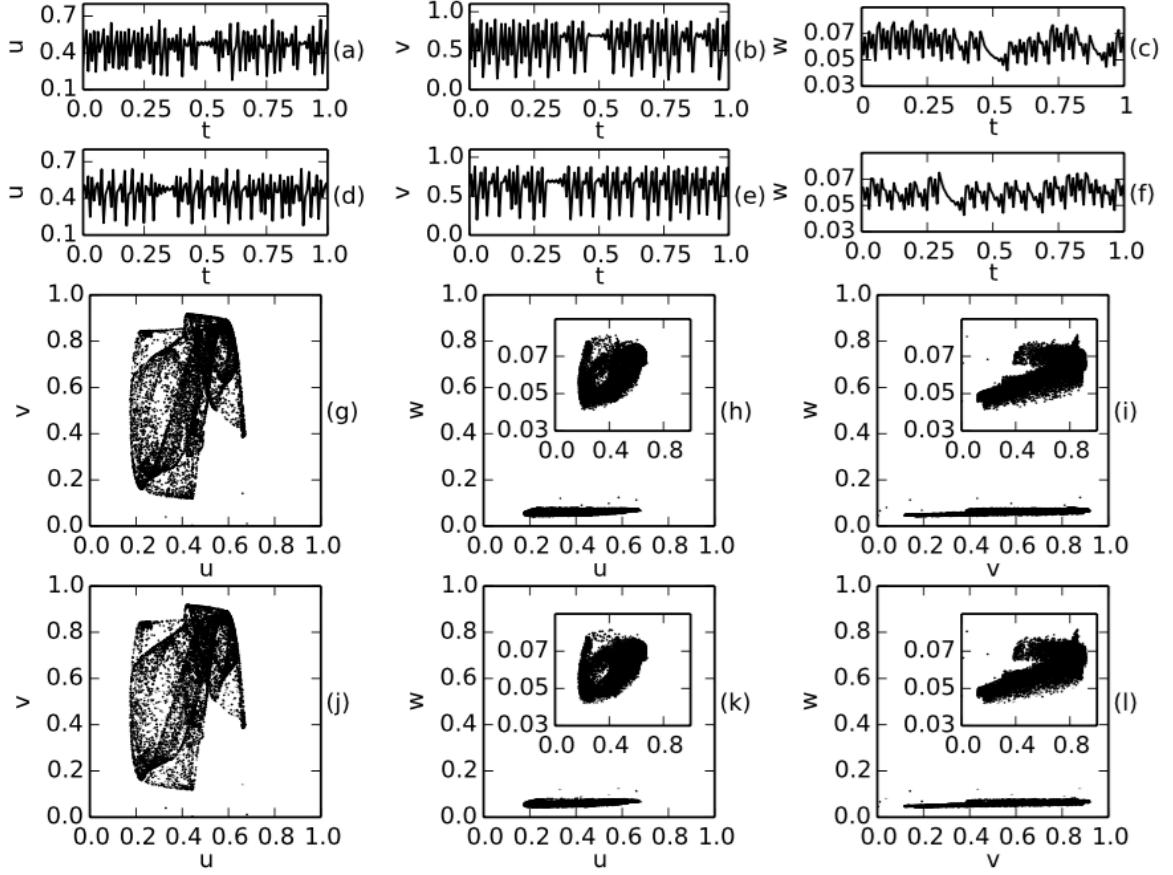


Figure 5.12: Behavior of broadband w/o fundamental for slightly perturbed initial conditions: (a)–(f) time series; (g) & (l) phase portraits.

computed from individual cases in specific regions with indications of stable results. Parts (a), (b), (c), (g), (h), (i) in both figures are computed from the original initial conditions, and all other parts are computed from mildly perturbed conditions: $a^{(0)} = 0.3$, $b^{(0)} = 0.95$, $c^{(0)} = 0.20001$. In Fig. 5.11, bifurcation parameters are obtained from the regime map of Fig. 5.10 with $(\lambda_1, \lambda_3) = (0.4, 0.6)$. As is seen, time series are notably different in each direction for this anisotropic case, resulting in considerably different phase portraits. Comparing parts (g), (h), (i) with (j), (k), (l) for the two different initial conditions, phase portraits in each direction are almost the same, while time series of parts (a), (b), (c) and the corresponding parts (d), (e), (f) are different in detail, presenting SIC. The strong similarity of phase portraits implies

that the original and perturbed cases are evidently on the same attractor.

In Fig. 5.12, bifurcation parameters are obtained from the regime map of Fig. 5.9 with $(\lambda_1, \mu_1) = (0.4, 0.5)$, which is a very stable area for this type of behavior. At the same time, it is clear from the very strong similarity of phase portrait topology for different initial conditions that the solutions lie on the same attractor, as in the previous case. Note the inner plots in parts (h), (i), (k), (l) are zoom-ins of their corresponding phase portraits, with different axis scales, and it is shown that phase portraits in each direction are also significantly different from each other. Also, it is relatively easy to detect both SIC and intermittency from the time series. The notable difference in time series for two initial conditions is that the position of the longest interval of intermittency in each direction moves towards the left, while nearly retaining its original shape. Also, intermittency in the time series has a longer interval of less chaotic behavior than that of the case of noisy quasiperiodicity w/o fundamental (Fig. 5.4(i)). Phase portraits are different from ones in the previous case, and in both cases they are not symmetric, in contrast to what is shown in [144], where the 2-D PMNS equation with only isotropic β and γ was investigated.

Figure 5.13 shows basins of attraction (sets of initial values that asymptote to the same attractor) for the two cases discussed above. The plots use the same procedure (PSD identification of solution type) and color map as in previous regime maps. The initial conditions for u, v, w velocity components are expressed as $a^{(0)}, b^{(0)}, c^{(0)}$, respectively. In Fig. 5.13 (a), intertwined behaviors of noisy quasiperiodic both w/ and w/o fundamental occur; in Fig. 5.13 (b), only broadband w/o fundamental behavior is shown in the non-divergent region. Note that the trivial steady solution is actually obtained at zero initial data for both cases, which is too small to present in current plots. These two cases are from a quite stable region of the bifurcation parameter domain, and thus fractal boundaries between behavior types are not expected.

Moreover, only time series for u -component velocity are shown in Fig. 5.14 since

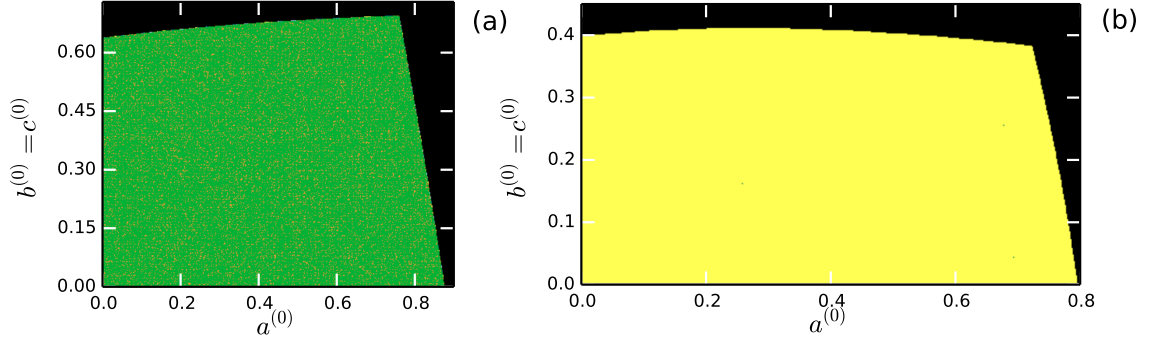


Figure 5.13: Basins of attraction for bifurcation parameters in (a) Figure 5.11, (b) Figure 5.12.

phase portraits do not show much difference for different initial conditions. In Fig. 5.14, the initial conditions $(a^{(0)}, b^{(0)} = c^{(0)})$ are set as (a) (0.4, 0.1), (b) (0.6, 0.2), (c) (0.4, 0.3), (d) (0.6, 0.45). These are relatively large differences between (a) and (b), and between (c) and (d). Nevertheless, (a) and (b) have similar overall structure with type II intermittencies, suggesting a single, very stable attractor. This also holds for the comparison between parts (c) and (d). This indicates that the PMNS equation of the current study can provide chaotic, but deterministic and stable temporal fluctuations in SGS models for synthetic-velocity forms of LES.

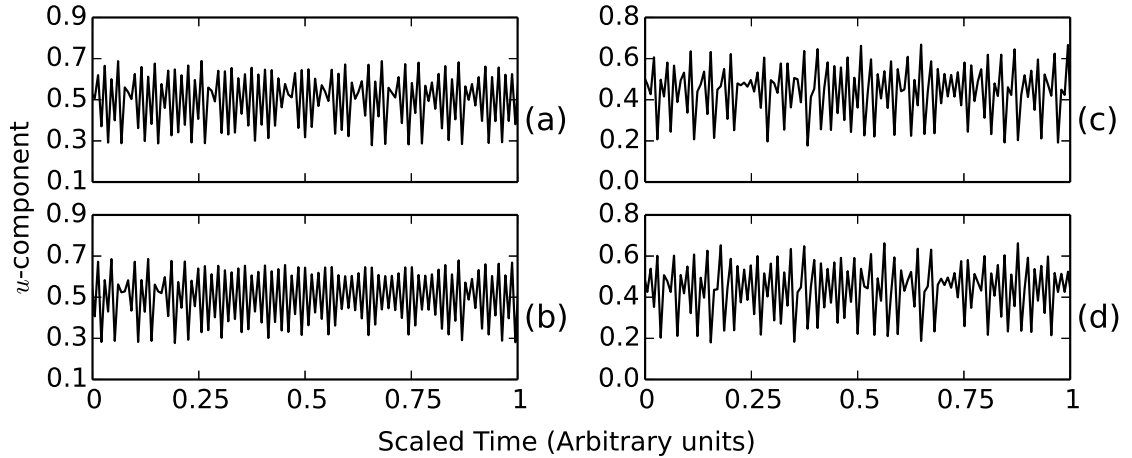


Figure 5.14: Time series for large perturbation of initial conditions. Bifurcation parameter values corresponding to (a) & (b) Figure 5.11, (c)&(d) Figure 5.12.

5.4. Summary and conclusions

In this chapter a 3-D PMNS DDS with Darcy and Forchheimer terms is derived from the generalized Navier–Stokes equations for incompressible flow in porous media through a Galerkin procedure. The current DDS contains six additional bifurcation parameters, beyond those of the original 3-D PMNS, due to the linear and non-linear drag forces and are expected to exhibit somewhat more complicated bifurcation behavior. Unlike usual closure problems of turbulence modeling, these additional parameters are directly related to physical variables and can be calculated from porosity and permeability.

Numerical investigations in terms of regime maps, power spectra, time series, phase portraits and basins of attraction have been carried out to study characteristic behaviors of this system. Results with variation of β produced regime maps considerably different than those associated with free fluid flow. Both Feigenbaum and Ruelle and Takens bifurcation sequences are observed as β increases. It was also shown that chaotic behavior could occur at low Re for large values of friction factor, consistent with the physics shown in [219]. Results with variation of λ and μ are provided for flow in both isotropic and anisotropic porous media. The isotropic cases show that low-porosity flow leads to less chaotic behavior since flow velocity decreases. However, the anisotropic cases show quite the opposite tendency, which arises from combined effects of the decreasing Re and increasing friction factor. Also, the ranges of stable parameter values for anisotropic cases are much larger compared with those of isotropic cases. Lastly, the property of SIC is investigated for two single cases of flow in anisotropic porous media using both mild and relatively large perturbations. The time series show notable qualitative differences for different initial conditions, while similarity of phase portrait topology implies that solutions lie on the same attractor even for large perturbation of initial conditions.

Finally, it is admitted that the DDS with a co-dimension of 15 is so compli-

cated that a thorough investigation of all combinations of parameter values is nearly impossible—and maybe of little value. Also, some behaviors such as dispersion of different noisy regimes in Fig. 5.3 (a) and basin of attraction regime maps (Fig. 5.13(a)) may also be due to the numerical limits set in the selection algorithm rather than entirely due to fundamental mathematical properties of the DDS. Other than this, the observable differences in these system behaviors, including power spectra, time series and phase portraits, are in agreement with experimentally verified physics of fluid flow through porous media (see Fig. 5.1). It is concluded that this DDS has the potential to provide temporal fluctuations of SGS models for synthetic-velocity LES of turbulence through porous media, and its performance along with the large-scale part will be studied in future work. Extension of this DDS to convective buoyant flows will also be considered.

Chapter 6: A Theoretical Model for the Porosity-Permeability Relationship

Phenomena of fluid flow through porous media are widely seen in nature, such as air flow in forest canopies, groundwater in aquifers and oil in reservoir rocks, in engineering, such as pin fin heat sinks for electronic devices and lotus-type porous metals for compact heat transfer applications, and in biology, such as blood flow in choriocapillaris of the human eye and cerebrospinal fluid flow in brain tissue. They have been studied both experimentally and theoretically in the past several decades (e.g., [228] [129] [229]). Several models have been introduced to mathematically describe fluid flows in porous media such as the Darcy, the Brinkman-extended Darcy, the Forchheimer-extended Darcy [117], and the so-called generalized models [115] as presented in Ch. 3. In all of these models, parameters of porosity and permeability are used and are very important in determining flow characteristics. Porosity is often estimated via direct measurements. Common porous materials have porosities ranging from $0.02 \sim 0.99$ (see Table 1.1 of [117]). Permeability is typically determined in the laboratory by application of Darcy's law under steady-state conditions, with values in $[0, \infty)$. It is visualized as an operator that converts hydraulic gradients to velocity (along the x , y , z directions), as discussed by Liakopoulos [230], and is therefore a tensor with an array of nine coefficients written in a form as

$$\mathbf{K} = \begin{bmatrix} K_{xx} & K_{xy} & K_{xz} \\ K_{yx} & K_{yy} & K_{yz} \\ K_{zx} & K_{zy} & K_{zz} \end{bmatrix}.$$

The material contained in this chapter has been published as [International Journal of Heat and Mass Transfer, **103**, 2016, 984-996] [10.1016/j.ijheatmasstransfer.2016.07.095] © [copyright Elsevier] [<https://www.journals.elsevier.com/international-journal-of-heat-and-mass-transfer>]

For the sake of simplicity, in the present study the relation between velocity and hydraulic gradient is only referred to the principle axes; thus all coefficients of the tensor reduce to zero except the diagonal ones. Also, the diagonal values are assumed to be the same under isotropic conditions, indicating a scalar permeability as

$$K = K_{xx} = K_{yy} = K_{zz} .$$

Since permeability is often difficult to estimate, various permeability models are available and have proven to work well for specific kinds of problems. For instance, the classical and well-known semi-empirical Kozeny–Carman (K–C) equation [222] [221] for flow in packed beds of solids is

$$K = \frac{\phi_s D_p^2 \phi^3}{C_0 (1 - \phi)^2} , \quad (6.1)$$

with ϕ_s , ϕ , D_p being sphericity of the particles, porosity, and particle diameter, respectively. The empirical coefficient C_0 is usually taken to be a constant (~ 180) and can be adjusted for different solid constituent geometries. Its various forms include the one obtained after applying the Archie relationship [231], the modified K–C equation based on fractal geometry [232], and one based on experiments with glass and natural fibrous mats [233]. These models all have similar forms with different exponents of porosity in the numerator. Note that permeability calculated from these models is a constant, which only applies to porous media with exactly the same micro-scale structure (e.g., pore fabric, pore throat) everywhere. Otherwise, at least a spatially dependent permeability is expected for a porous medium, even with constant porosity. Although performance of such correlations is satisfactory for certain problems, it is difficult to apply them over broader ranges of situations without changing the empirical information, which has attendant need for potentially costly laboratory experiments. This motivates attempting to find a general formula for the relationship between porosity and permeability to provide convenience for better macroscopic simulation of fluid flow through porous media.

The rest of this chapter is organized as follows. In the analysis section, the generalized model is first introduced. Then a detailed derivation of the functional dependence of permeability in terms of various physical parameters associated with porous media flows is explained. In the third section, numerical results for both lid-driven cavity and convection problems in a cube are presented and discussed. Summary and conclusions are provided in a final section.

6.1. Analysis

As seen in the governing equation provided in Ch. 3, the energy equation applies only to the fluid phase. The more rigorous form combining thermal properties of both the solid matrix and the fluid phase is expressed as (see, e.g., Bejan [151])

$$(\rho c)_m \frac{\partial T}{\partial t} + (\rho c_p)_f \mathbf{u} \cdot \nabla T = k_m \Delta T + q_m''' , \quad (6.2)$$

with

$$(\rho c)_m = (1 - \phi)(\rho c)_s + \phi(\rho c_p)_f , \quad (6.3a)$$

$$k_m = (1 - \phi)k_s + \phi k_f , \quad (6.3b)$$

$$q_m''' = (1 - \phi)q_s''' + \phi q_f''' , \quad (6.3c)$$

where the subscript s corresponds to solid, and the subscript m denotes effective properties incorporating effects of both solid and fluid phases, for instance, k_m is effective thermal conductivity of the porous medium.

According to the stability theory proposed by Prigogine and Glansdorf [234] [235] for general non-equilibrium thermodynamic cases, local thermodynamic equilibrium is still satisfied and has the same form of formulas (e.g., equation(s) of state) as would pertain globally. Thus, the following classical conditions follow:

$$(\delta S)_{eq} = 0 , \quad (equilibrium) \quad (6.4a)$$

$$(\delta^2 S)_{eq} < 0 , \quad (stability) \quad (6.4b)$$

where δS and $\delta^2 S$ are first- and second-order deviations of entropy from equilibrium. Subscript *eq* denotes evaluation at the equilibrium state. For equilibrium thermodynamics, theory states that stability depends only on the sign of the curvature $(\delta^2 S)_{eq}$. Also, the quantity $\delta^2 S$ plays an essential role in the overall theory. For non-equilibrium thermodynamics, the following conditions need to be satisfied at all spatial locations and time t inside the system:

$$\delta^2 S < 0 , \quad (6.5a)$$

$$\partial_t \delta^2 S > 0 . \quad (6.5b)$$

The second condition, Eq. (6.5b), is mainly due to Lyapunov theory [236], required for Eq. (6.5a) to be valid for all time t .

From this, it is concluded that entropy (equilibrium) or entropy production rate (non-equilibrium) should be maximized to achieve a physically stable state. Thus, the underlying approach used here is to take the first derivative of entropy production rate with respect to permeability (assuming that porosity is an invertible function of permeability) and force it to be zero. Then solve the resulting differential equation for porosity in terms of permeability. Also, the second and higher derivatives should be checked to be certain that they are less than zero, thus implying maximization.

6.1.1 Derivation of permeability formula

For fluid flow through porous media in general cases, the volumetric entropy generation (production) rate is given, for example in [237], as

$$\dot{S}_{gen} = \frac{\mu}{KT} \phi^2 \mathbf{U}^2 + \frac{c_F \rho}{\sqrt{KT}} \phi^3 |\mathbf{U}| \mathbf{U}^2 + \frac{\Psi}{T} + \frac{k_m (\nabla T)^2}{T^2} . \quad (6.6)$$

The “dot” used above is notation for D/Dt , the substantial derivative. Assuming that convective effects can be neglected, this simplifies to the local time derivative operator

$\partial/\partial t$ in the following analysis since convective terms are conservative within the N.–S. context. The first and second terms on the RHS are fluid friction irreversibility from Darcy and Forchheimer drag forces, respectively. The third term is entropy production from viscous dissipation Ψ , which is expressed as $2\mu\bar{E}^2$ with \bar{E} being the strain rate tensor Euclidean norm. Viscous dissipation is obtained by subtracting the mechanical energy equation from the total energy equation for fluid flow in porous media. Thus it is expressed in terms of superficial velocity, as is also true in the expressions of drag dissipation. Through the Dupuit–Forchheimer relationship, these terms can all be expressed using pore velocity, as is shown in Eq. (6.6), and the viscous dissipation in 3-D is

$$\begin{aligned} \Psi = 2\mu_e\phi^2 & \left[\left(\frac{\partial U}{\partial x} \right)^2 + \left(\frac{\partial V}{\partial y} \right)^2 + \left(\frac{\partial W}{\partial z} \right)^2 \right] \\ & + \mu_e\phi^2 \left[\left(\frac{\partial V}{\partial x} + \frac{\partial U}{\partial y} \right)^2 + \left(\frac{\partial V}{\partial z} + \frac{\partial W}{\partial y} \right)^2 + \left(\frac{\partial U}{\partial z} + \frac{\partial W}{\partial x} \right)^2 \right], \end{aligned}$$

with $(U, V, W)^T$ being the pore velocity components of \mathbf{U} .

The last term in Eq. (6.6) is heat transfer irreversibility due to heat diffusion in the energy equation [180] [127]. In the present study, for simplicity, the thermal properties of the solid matrix and the fluid have been taken to be identical ($k_s = k_f = k_m$), as was done in [115], despite obvious shortcomings. A more reasonable expression for k_m with respect to porosity will be considered in derivations of subsequent studies. Thus porosity does not appear. Also, this term is not included in the entropy production rate in the following derivation. This is reasonable since porous terms associated with velocity only appear in the momentum equation.

For simplicity, the entropy production rate is expressed as:

$$\dot{S}_{gen} = bK^{-1}\phi^2 + cK^{-1/2}\phi^3 + a\phi^2, \quad (6.7)$$

with

$$a = \frac{\Psi}{\phi^2 T}, \quad b = \frac{\mu}{T} \mathbf{U}^2, \quad c = \frac{c_F \rho}{T} |\mathbf{U}| \mathbf{U}^2. \quad (6.8)$$

The velocity, strain rates, etc., have been lumped into coefficients a, b, c which are considered to be constant in Eq. (6.7) since only local variables are considered. To begin, the first-order differential of entropy should be zero, as $\delta S = 0$, due to the local thermodynamic equilibrium assumption. Although the entropy production rate (time derivative of entropy) is used in Eq. (6.7), it is trivial to obtain $\delta \dot{S} = 0$ since K is independent of the local time. Take the first derivative of the entropy production rate with respect to permeability as follows:

$$\frac{\partial \dot{S}_{gen}}{\partial K} = 2a\phi \frac{d\phi}{dK} + 2bK^{-1}\phi \frac{d\phi}{dK} - b\phi^2 K^{-2} + 3cK^{-1/2}\phi^2 \frac{d\phi}{dK} - \frac{1}{2}c\phi^3 K^{-3/2} = 0 . \quad (6.9)$$

After simple manipulation, Eq. (6.9) leads to the following analytically solvable ordinary differential equation (ODE),

$$\frac{d\phi}{dK} = \frac{b\phi^2 K^{-2} + 1/2c\phi^3 K^{-3/2}}{2a\phi + 2bK^{-1}\phi + 3cK^{-1/2}\phi^2} . \quad (6.10)$$

Set $\phi \equiv y$ and $K^{-1/2} \equiv x$ to express Eq. (6.10) as

$$\frac{dy}{dx} = \frac{-2by^2x - cy^3}{2ay + 2bx^2y + 3cxy^2} , \quad (6.11)$$

and write this as

$$(2bxy^2 + cy^3)dx + (2ay + 2bx^2y + 3cxy^2)dy = 0 . \quad (6.12)$$

Let $P = 2bxy^2 + cy^3$ and $Q = 2ay + 2bx^2y + 3cxy^2$. Since $\partial P/\partial y = \partial Q/\partial x = 2bxy + 2cy^2$, Eq. (6.11) is an exact differential equation, which has a general solution $u(x, y) = C_a$ with C_a an arbitrary constant. Also, $du = P(x, y)dx + Q(x, y)dy$. This leads to

$$u(x, y) = \int_{x_0}^x (2bxy^2 + cy^3)dx + \int_{y_0}^y (2ay + 2bx_0^2y + 3cx_0y^2)dy , \quad (6.13)$$

where (x_0, y_0) is one specific point in the solution domain. Let $(x_0, y_0) = (0, 0)$ be “initial data”, so

$$by^2x^2 + cy^3x + ay^2 = C_a , \quad (6.14)$$

with C_a being the integration constant. Solving the quadratic equation for the unique potentially positive solution yields

$$x = \frac{-cy^3 + \sqrt{c^2y^6 - 4by^2(ay^2 - C_a)}}{2by^2} . \quad (6.15)$$

Substituting this back into the definition of ϕ and K leads to

$$K^{-1/2} = \frac{-c\phi^3 + \sqrt{c^2\phi^6 - 4b\phi^2(a\phi^2 - C_a)}}{2b\phi^2} . \quad (6.16)$$

The integration constant C_a is found to be $C_a = a$ from the condition that as ϕ goes to unity, K goes to ∞ . Further manipulation leads to the final expression for permeability in terms of porosity

$$K = \frac{4b^2\phi^2}{(\sqrt{c^2\phi^4 + 4ab(1 - \phi^2)} - c\phi^2)^2} . \quad (6.17)$$

The argument of the square root is guaranteed to be non-negative since ϕ is always less than or equal to unity, and all coefficients are non-negative.

The remaining question is whether the maximum of entropy production rate is actually obtained. In that case, the second derivative should be less than zero at the critical point (where the first derivative is zero). By simple hand calculation, the second derivative is greater than zero, which seems contradictory to what is required. However, it is the entropy production rate being used here, rather than the entropy. In order to view this in an intuitive way, Fig. 6.1 presents entropy production rate versus permeability.

It is observed that there exists a minimum point for

$$\frac{\partial}{\partial K} \left(\frac{\partial S}{\partial t} \right) = 0 , \quad \frac{\partial^2}{\partial K^2} \left(\frac{\partial S}{\partial t} \right) > 0 , \quad (6.18)$$

with K and t being independent variables, as implied previously. The coefficients a, b, c , fixed at physically reasonable values, are calculated from the permeability model for an arbitrary position and time, and are quite representative. Different values of these coefficients have also been used to calculate the entropy production rate.

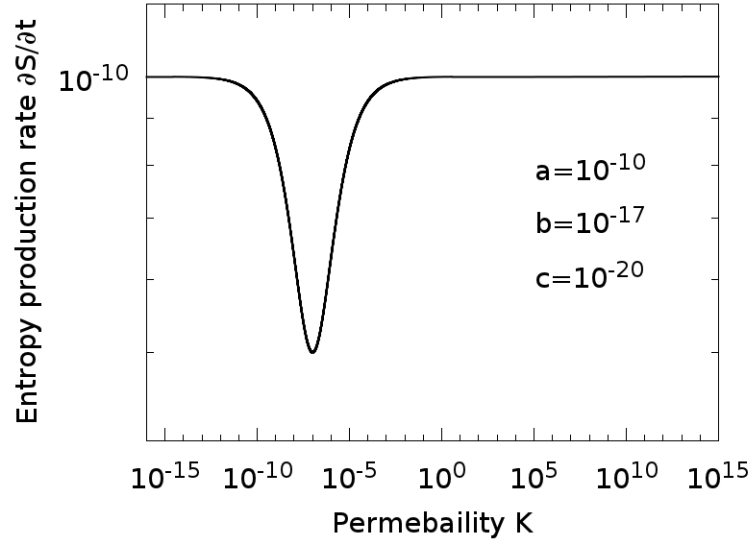


Figure 6.1: Relationship between entropy production rate and permeability.

Their resulting plots show similar tendencies, with minimum points corresponding to different permeability values. According to the Clairaut exchange theorem [238], Eq. (6.18) can be rewritten as

$$\frac{\partial}{\partial t} \left(\frac{\partial S}{\partial K} \right) = 0, \quad \frac{\partial}{\partial t} \left(\frac{\partial^2 S}{\partial K^2} \right) > 0. \quad (6.19)$$

It is seen that the second condition in Eq. (6.19) is identical to Eq. (6.5b) from the non-equilibrium thermodynamic stability theory. Also, Fig. 6.1 shows that as $K \rightarrow \infty$, all derivatives of entropy production rate $\rightarrow 0$, including the second condition in Eq. (6.18). Thus the second condition in Eq. (6.19), $\partial_t(\partial^2 S) \rightarrow 0$, implies asymptotic stability. In this case, since time is always increasing, $\partial^2 S$ must be less than zero to satisfy the condition. Hence, both conditions for non-equilibrium stability stated in [234] are locally satisfied for all values of space and time in the system of concern.

6.1.2 Further discussion

In all, formula (6.1) is expected to be applicable in a wide range of cases since it is derived from a general theory. It is in a form similar to previous empirical equations

in that porosity appears in the numerator (but with a different exponent), and the factor $(1 - \phi)$ occurs in the denominator. It is analogous to Eq. (6.1), but in a more complicated way. For flow with low pore velocity, the value of coefficient c is much smaller than that of a (strain rate); therefore, terms with coefficient c in the denominator can be neglected, and Eq. (6.17) is simplified to

$$K = \frac{b \phi^2}{a(1 - \phi^2)} . \quad (6.20)$$

Substituting a and b (as shown in Eqs. (6.8)) into Eq. (6.20), and using $\mu_e = \mu/\phi$ for Ψ leads to

$$K = \frac{D_y^2 \phi^3}{1 - \phi^2} . \quad (6.21)$$

The coefficient D_y^2 is some length scale related to the strain rate as

$$D_y^2 = \frac{\mathbf{U}^2}{\left[\left(\frac{\partial U}{\partial x} \right)^2 + \left(\frac{\partial V}{\partial y} \right)^2 + \left(\frac{\partial W}{\partial z} \right)^2 \right] + \left[\left(\frac{\partial V}{\partial x} + \frac{\partial U}{\partial y} \right)^2 + \left(\frac{\partial V}{\partial z} + \frac{\partial W}{\partial y} \right)^2 + \left(\frac{\partial U}{\partial z} + \frac{\partial W}{\partial x} \right)^2 \right]} ,$$

which is similar to the square of particle size used in Eq. (6.1). For flow with large pore velocity, the coefficient c is large. If the calculated values of a and b are not sufficiently large, then the denominator of Eq. (6.17) would be close to zero, resulting in unreasonable high permeability. In this case, the flow has high probability to be turbulent with much larger viscous dissipation, and finer computational grids, and or turbulence modeling, are therefore needed. Moreover, one of the notable differences from previous empirical or semi-empirical equations is the absence of empirical parameters in the formula. One may say that c_F and μ_e in the permeability model are also empirical parameters, but they are parameters which already existed in the governing equations. A similar procedure such as that used to treat permeability here may be applicable for c_F and μ_e , but this is beyond the scope of the current work.

Furthermore, Eq. (6.17) has the potential for applicability to problems with inhomogeneous or non-isotropic porous media where variable permeability values are expected. The simplest case is a uniformly-structured (internal) porous medium with

boundaries or interfaces being solid, non-porous, walls. Solid walls can be considered as having zero permeability, and allowing no fluid to pass through. Thus, the permeability is not constant up to, and including, the boundaries. In a more general porous medium with space-dependent micro-structures, permeability would not be the same even if the local porosity (in the representative elementary volume scale [129]) is the same everywhere. In Eq. (6.17), permeability is related to effective viscosity, which is found to be different for different geometries (channel fluid, bluff body, etc. [239]).

Lastly, it is remarked that from the standpoint of computational fluid dynamics (CFD), this model is easily discretized and implemented. Permeability is calculated at the center of each grid cell with centered differencing used to discretize velocity gradients required by the permeability model.

6.2. Lid-driven cavity problem

Lid-driven cavity flow without porous media has been widely used as a benchmark problem for many numerical methods and incompressible codes due to the simple geometry, yet complicated flow behaviors, especially in 3D. Lid-driven cavity flow with porous media has also been studied in recent years. Usually, constant permeabilities in the whole cavity have been used to examine different flow behaviors [240]. However, as was noted previously, fluid flow through porous media with boundaries will result in a different permeability distribution, which is expected to be seen using the current model. The porous medium in the cavity is assumed to be uniformly-structured with tortuosity being unity, and thus the effective viscosity used is μ/ϕ . Effects from inhomogeneity inside the porous medium will be considered in subsequent studies. All computations are performed in parallel mode (using 16 cores) on the high-performance computing cluster as the at the University of Kentucky Computing Center, each basic node of which has two 2.6 GHz Intel E5-2670 eight-core processors and 64 GB of RAM.

The geometrical configuration and boundary conditions are sketched in Fig. 6.2.

No-slip boundary conditions are imposed on all faces of the cube. The lid velocity is U , and the length of each side of the cube is L . The center plane at which much of the data discussed below are obtained is indicated by dashed lines.

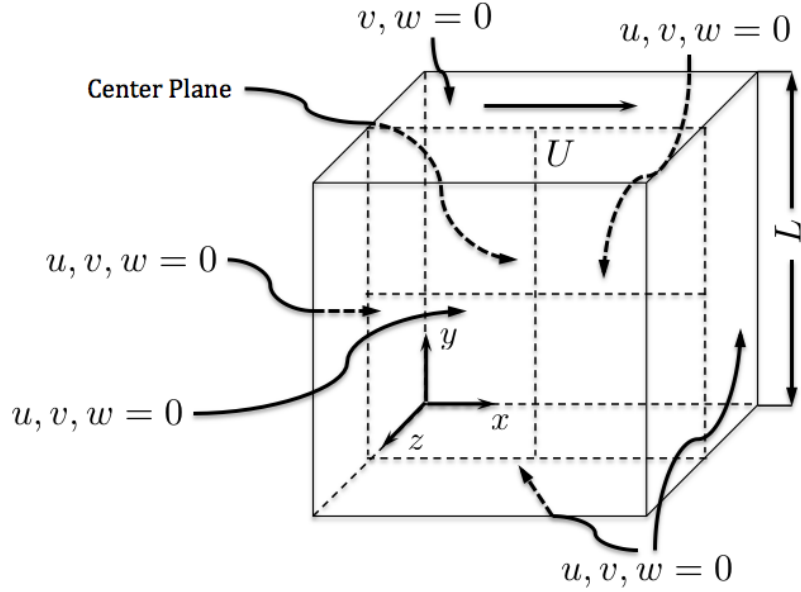


Figure 6.2: Sketch of the 3-D lid-driven cavity problem.

6.2.1 Verification

Verification of the code implemented with the permeability model is first done by setting porosity to unity, since the generalized N.-S. equation reduces to the standard N.-S. equation as $\phi \rightarrow 1$, which has abundant benchmark data for LDC flow. In these calculations, L is 0.01m and U is 0.1m/s. The chosen length scales are somewhat arbitrary but are expected to result in faster convergence to steady state. Grid function convergence tests were performed for Reynolds number, Re , of both 100 and 400 using 41^3 , 81^3 and 161^3 grid points. Table 6.1 presents L^2 norm errors (indicated as $\|\cdot\|_2$) calculated from the differences of two successive grid functions ($f_i^h, f_i^{h/2}$ and $f_i^{h/2}, f_i^{h/4}$ with superscript denoting grid spacing). The ratios indicate at least first-order accuracy, which is consistent with the fact that solutions are nonclassical due to singularities in the upper right-hand corner of the cavity. Figure 6.3 shows u -

Table 6.1: Grid function convergence test

	$\ f_i^h - f_i^{h/2}\ _2$	$\ f_i^{h/2} - f_i^{h/4}\ _2$	Ratio
$Re = 100$	9.06×10^{-4}	3.16×10^{-4}	2.87
$Re = 400$	5.0×10^{-3}	1.87×10^{-3}	2.67

component velocity profiles computed on three different grids; the highlighted square parts are zoomed in for a clearer view of grid convergence. It is clear from these zoom-ins that convergence is essentially second-order away from cavity corners. Moreover, it is seen that 41^3 and 81^3 grids are sufficient to produce reasonably accurate results for this initial investigation, especially for cases with smaller Re numbers. Figure

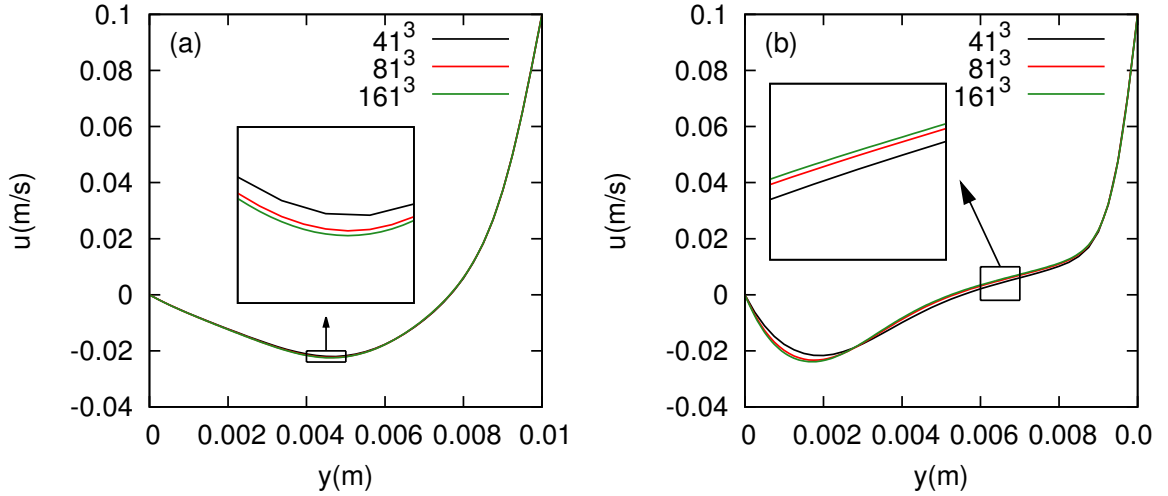


Figure 6.3: Velocity profiles computed with three different grids: (a) $Re = 100$; (b) $Re = 400$.

6.4 shows that solutions computed on the 81^3 grid compare well with the 3-D results from [241]. It is interesting to note that although the flow is steady for both values of Re , there is a significant change in shape of the velocity profiles already when $Re = 400$.

Next, 2-D results from Guo [240] are verified by using constant permeabilities for $Re = 10$ with $\phi = 0.1$ on the same length and velocity scales as adopted previously. In the present study, calculations are performed on a 41^3 uniform grid, and “2-D”

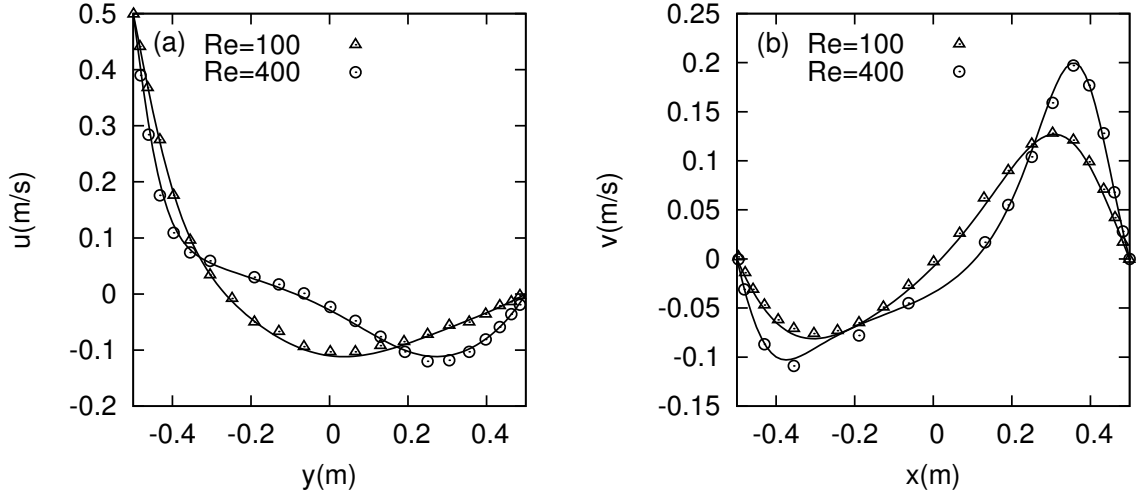


Figure 6.4: Velocity profiles through the cavity center, solid lines are calculated solutions and symbols are benchmark solutions [241]: (a) u component along the vertical center line; (b) v component along the horizontal center line.

solutions are obtained by setting boundary conditions at fore and aft walls to be stress-free. These are not exactly 2-D considering influences from the interfaces of no-slip and stress-free boundaries (corners) on the overall results, but solutions in the center plane may not be affected since it is far away from corners, and results agree quite well with the published solutions (see e.g., Fig. 6.7 in [240]), as demonstrated in solid lines in Fig. 6.5. It should be noted that the Darcy numbers, Da (K/L^2), and the viscosity ratio J (μ_e/μ) used in [240] are not exactly the same as employed here, where Da is lower and J is higher. The agreement of solutions indicates a trade-off between Da and J ; also, higher J means larger viscous dissipation resulting in larger drag forces and smaller permeability (Da). Moreover, the 3-D results (denoted by dashed lines) calculated from the same conditions show some mild deviations from 2-D results for larger Darcy numbers because of the aft and fore wall effects on the advective behavior of the flow; for smaller Da with less advection, this effect is negligible, resulting in 2-D and 3-D solutions being almost indistinguishable. Lastly, it should be clear from analyses of the preceding section that variable permeability may produce quite different results, even when porosity is constant. It is thus important

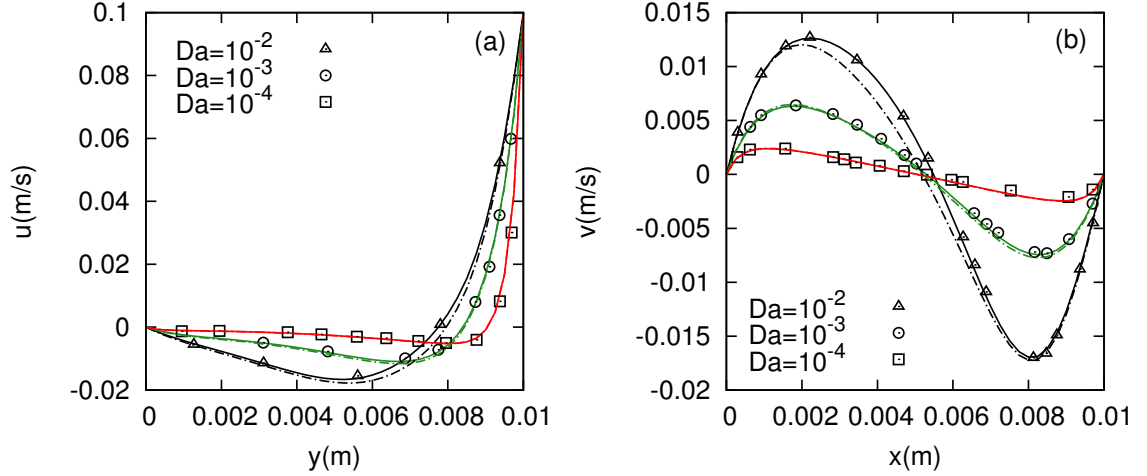


Figure 6.5: Velocity profiles for different constant permeabilities, solid lines are calculated solutions, and symbols are solutions from [240]: (a) u component along the vertical center line; (b) v component along the horizontal center line.

to obtain a permeability distribution to produce physically correct results.

6.2.2 General model results

The current model produces permeability automatically. Computations have been performed with $\phi = 0.1, 0.5, 0.9$ for $Re = 10$. The coefficient c_F in Eq. (3.1b) is calculated using Eq. (5.1) based on experimental investigations of Ergun [126]. It is equal to the value d/\sqrt{K} given in [219], since $d = \beta_k \nu / \alpha_k$, with the non-linear coefficient $\beta_k = c_F \rho / \sqrt{K}$, and the linear coefficient $\alpha_k = \mu / K$ (α_k and β_k correspond to a and b , respectively, in the original paper of [219]). In Table 6.2, $R_k(1)$ and $R_k(2)$ are critical values for flow transition to non-linear and turbulent regimes, respectively, and are calculated as [219]

$$R_k(1) = \frac{0.17}{c_F^{1.1}}, \quad R_k(2) = \frac{10}{c_F}; \quad (6.22)$$

corresponding critical permeability values $K(1)$ and $K(2)$ are calculated via

$$R_k(1) = \frac{\phi U \sqrt{K(1)}}{\nu}, \quad R_k(2) = \frac{\phi U \sqrt{K(2)}}{\nu}.$$

If permeability is less than $K(1)$, Darcy flow usually occurs; if $K(1) < K < K(2)$, flow begins to transition to non-linear behavior as K approaches $K(2)$; if $K > K(2)$, flow becomes unsteady and wholly turbulent. For instance, all three permeability values used for $\phi = 0.1$ in the computations shown in Fig. 6.5 are smaller than $K(2)$, indicating steady flows; also, two permeability values are even smaller than $K(1)$, suggesting that the flow is in the Darcy regime.

Table 6.2: Estimation of flow regimes [219]

Porosity	$c_F(d/\sqrt{K})$	$R_k(1)$	$R_k(2)$	$K(1)$	$K(2)$
0.1	4.52	0.0323	2.21	1.05×10^{-7}	4.90×10^{-4}
0.2	1.60	0.102	2.21	2.58×10^{-7}	9.80×10^{-4}
0.3	0.870	0.198	2.21	4.37×10^{-7}	1.47×10^{-3}
0.4	0.565	0.319	2.21	6.35×10^{-7}	1.96×10^{-3}
0.5	0.404	0.461	24	8.48×10^{-7}	2.45×10^{-3}
0.6	0.307	0.622	24	1.08×10^{-6}	2.94×10^{-3}
0.7	0.244	0.802	24	1.31×10^{-6}	3.43×10^{-3}
0.8	0.200	1.00	24	1.56×10^{-6}	3.92×10^{-3}
0.9	0.167	1.21	59	1.82×10^{-6}	4.41×10^{-3}

Figure 6.6 presents velocity profiles computed from the derived permeability model for LDC flow (Eq. (6.17) with Eqs. (6.8)). As seen, profiles are similar in shape to those shown in Fig. 6.5 although different porosities are used here. For low-porosity flow, the u velocity gradient near the moving wall (lid) is quite steep, as shown in part (a). Also, it is seen in part (b) that vertical velocity magnitude decreases as porosity decreases, as expected. For larger porosity cases, profiles are similar to those for the clear fluid case, but with smaller velocity values and more symmetric velocity distributions since less fluid flow is driven by the moving lid for a cavity with porous media.

Figure 6.7 shows contour plots of u -component velocity in the mid-plane of the 3-D cavity with color bars denoting the range of values for different porous-media flows. Streamlines are shown with white lines. As porosity decreases, it is easily seen

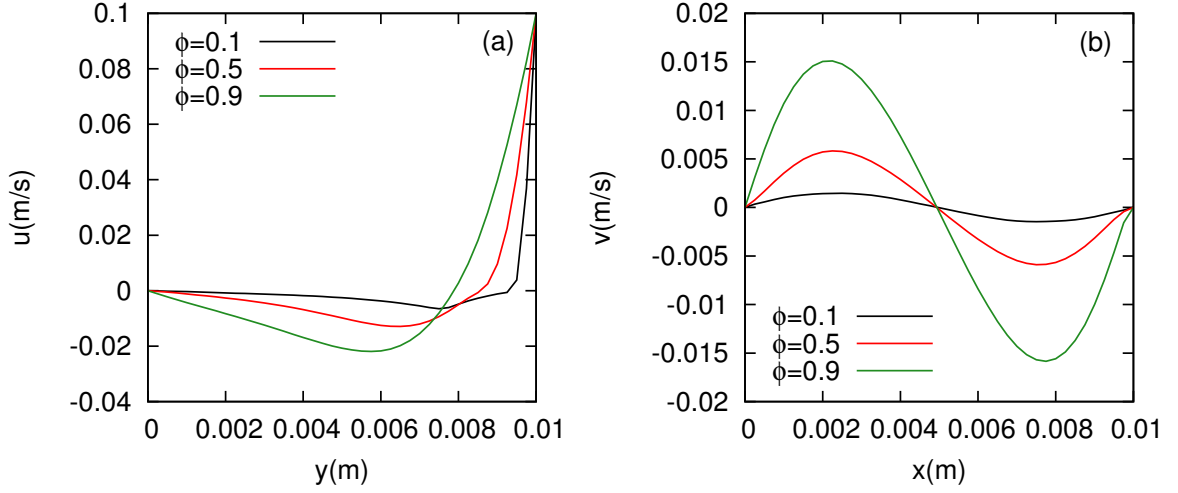


Figure 6.6: Velocity profiles through the cavity center for LDC flow in different porosity media: (a) u component along the vertical line; (b) v component along the horizontal line.

that the overall velocity decreases, especially in the area adjacent to the top lid; also, the vortex core, demonstrated by the streamlines, moves towards the upper center since there is more kinetic energy dissipation lost to the porous medium structure (friction) and thus decreasing of advection effects. In particular, the typical lower corner vortices of higher- Re LDC flow are not present in the porous-media cases.

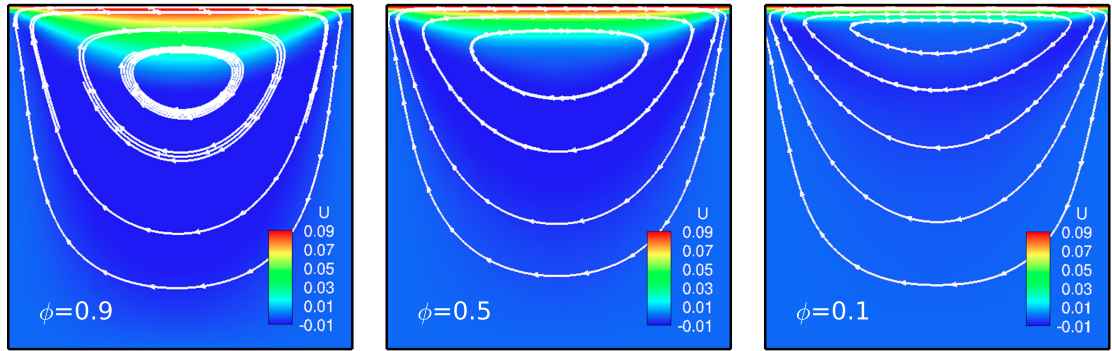


Figure 6.7: Velocity streamlines in the middle x - y plane.

Figure 6.8 shows both permeability and strain rate profiles on the cavity mid plane. It can be estimated from part (a) that the calculated average permeabilities are of order of magnitude 10^{-6} , 10^{-4} , 10^{-2} for porosities of 0.1, 0.5, 0.9, respectively, which

are smaller than the critical values for Darcy flow shown in Table 6.2. Permeabilities

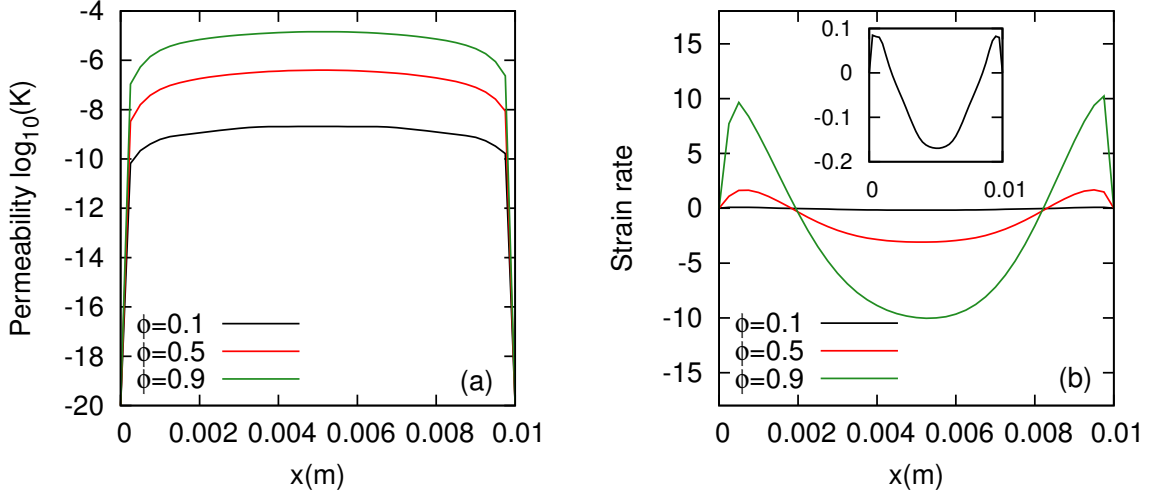


Figure 6.8: Permeability (log-scale) and strain rate through the cavity center computed with permeability model and successively increasing porosity: (a) permeability; (b) strain rate.

in some regions may indicate non-linear flows, but still are far from the turbulent regime. It is seen that permeability increases as porosity increases, and its value near the cavity center is essentially constant for this particular problem. It should be noted that permeability at the impermeable wall boundaries is assigned to be close to zero (10^{-20}), rather than identically zero, to prevent floating-point arithmetic overflows. It is noted that because of Dirichlet boundary conditions are applied to the momentum equations, they are not evaluated on solid boundaries where permeability is zero. Nevertheless, very small values lead to overflows at grid points adjacent to boundaries. Part (b) of Fig. 6.8 shows one component of the off-diagonal strain rate tensor, $u_y + v_x$, since for the LDC problem this component carries the most information. It is seen (by comparing parts (a) and (b) of this figure) for each case that as strain rate increases, permeability decreases, and vice versa, as expected from the permeability model (recall Eqs. (6.8) and (6.17)), which indicates an inverse correlation between strain rate and permeability. Large-porosity flows have larger

absolute strain rates since they exhibit larger velocity.

Figure 6.9 presents contour plots of permeability ($\log K$) distribution in the center plane for three porosity cases. Streamlines are also shown. The range of color scale decreases as porosity decreases to provide more information. Although different color scales are being used, it can still be seen that the overall permeability becomes lower as porosity decreases since the same color represents lower permeability for low porosity cases. In each plot, contours of relatively higher permeability values form a “band” structure in the upper area of the plane, and the “band” moves towards upper lid as porosity decreases. This is consistent with the streamlines as permeability is calculated from the flow field (recall dependence on strain rate).

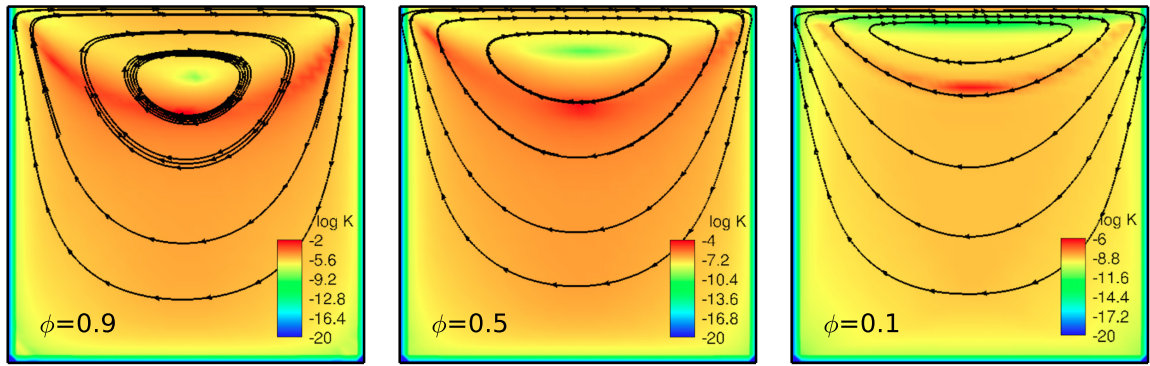


Figure 6.9: Permeability distributions (log-scale) of lid driven cavity flows through different porous media in the middle x - y plane.

Figure 6.10 shows contour plots of strain rate (same component as used in Fig. 6.8(b)) distribution with streamlines also indicated. The same color scales are used for all porosity cases to allow direct comparison. As porosity decreases, the overall value of strain rate decreases because of decreasing velocity. Also, a clear inverse correlation with permeability (Fig. 6.9) is shown. For instance, the area near the top lid has relatively lower permeability for higher strain rates.

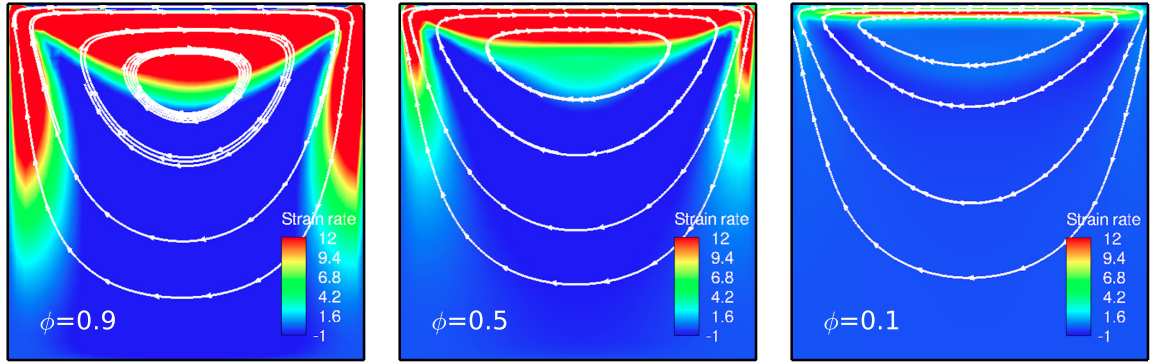


Figure 6.10: Strain rates of lid driven cavity flows through different porous media in the middle x - y plane.

6.3. The natural convection problem

Natural convective flow with the geometrical configuration shown in Fig. 6.11 has long been used for the study of natural convective heat transfer, both without and with porous media in the cavity. No-slip boundary conditions are imposed on all faces of

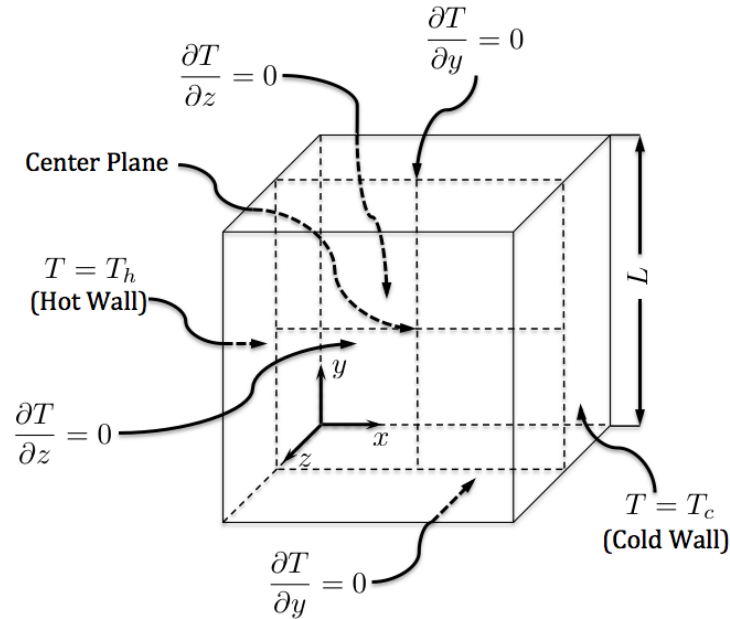


Figure 6.11: Sketch of the cubicle natural convection problem.

the cube, with zero velocities; temperatures are assigned at both the LHS hot wall and

the RHS cold wall; other walls are adiabatic (no heat flux). Usually, only numerical benchmark solutions for flow without porous media are available in literature since it is somewhat more difficult to perfectly satisfy the adiabatic boundary conditions experimentally. For cavity flow through porous media, different constant permeabilities are often used for an investigation of flow field responses. In the present study, variable permeability is automatically computed from the model derived in Sec. 6.1 for different porosities. The length scale of the cube L is 0.01m on each side, to be consistent with the size of the cube in the LDC problem discussed previously.

6.3.1 Verification

Initial validation is performed for the case of constant, unit porosity as in the LDC problem. Since benchmark solutions for flow without porous media exist in the literature and are computed from dimensionless equations [242] [243], scalings of the dimensional variable solutions produced here are required for direct comparison. For the current study, velocity solutions are scaled by κ/L with κ being the thermal diffusivity. Table 6.3 shows computed maximum velocity values (after scaling) for Rayleigh number, Ra , ranging from 10^3 to 10^6 employing 81^3 uniformly spaced grid points. Physical parameters used are as follows: $\nu = 10^{-5} \text{m}^2/\text{s}$, $\beta_e = 3.43 \times 10^{-3}/^\circ\text{C}$, $g = 9.8 \text{m/s}^2$, $Pr = 0.71$, $L = 0.01 \text{m}$. Different wall temperatures are then assigned according to Ra . For instance, if $T_c = -2.095^\circ\text{C}$, $T_h = 2.095^\circ\text{C}$,

$$Ra = \frac{g\beta_e(T_h - T_c)L^3}{\nu\kappa} = 999.9 \simeq 1000 ,$$

for an approximation of $Ra = 10^3$; obviously, a ten times larger temperature difference will result in an increase of Ra of the same magnitude, etc. Define the relative error e_R as $|v_b - v_p|/v_b$, where v_b represents benchmark solutions, and the v_p are present results. For lower Ra such as 10^3 and 10^4 , the relative error is within 1%, which is satisfactory. For larger Ra , the error increases—as summarized in Table 6.3—since a larger number of grid points would be needed to achieve full resolution of the thermal

boundary layers; but errors are still tolerable for initial qualitative studies focusing on permeability effects.

Table 6.3: Comparison of present results with benchmark data from [243]

	Present study	Ref [243]	e_R	Present study	Ref [243]	e_R
	$Ra \approx 10^3$	$Ra = 10^3$		$Ra \approx 10^4$	$Ra = 10^4$	
u_{max}	3.53	3.54	0.28%	16.789	16.719	0.42%
v_{max}	3.52	3.54	0.56%	19.161	18.983	0.94%
w_{max}	0.17	0.17	0	2.17	2.156	0.65%
	$Ra \approx 10^5$	$Ra = 10^5$		$Ra \approx 10^6$	$Ra = 10^6$	
u_{max}	44.996	43.90	2.5%	127	126.97	0.02%
v_{max}	69.63	71.06	2.0%	223.042	236.72	5.8%
w_{max}	9.37	9.69	3.3%	25.06	25.56	1.9%

Figure 6.12 displays patterns of streamlines, velocity components and temperature, for comparison with the patterns shown in 2-D calculations in [244] (see Fig. 6.5 of that reference). It is seen that the flow field changes gradually as Ra increases; in particular, convection effects become more dominant. Also, it is observed that the mid-plane 3-D results shown do not differ noticeably from the 2-D results of [244]. Furthermore, at the highest value of Ra , although the flow and temperature fields are beginning to be more complicated, they are still far from being turbulent, as indicated in [243]. This is in sharp contrast with Rayleigh-Bénard convection between flat plates and arises because of flow confinement in the cavity.

In Fig. 6.13, flow patterns for natural convection with constant permeability are shown, as is done in [115] for 2-D cases, where the effective viscosity is also calculated from μ/ϕ . Part (a) uses the same Da and Ra as in Fig. 6.8(b) of [115]. The values in parentheses represent corresponding non-dimensional values after scaling for ease of comparison with [115]. The flow patterns and the value of v_{max} agree well although here 3-D cases are calculated. In this case with relatively large permeability, the no-slip condition is apparent in the vector plot (see velocity vectors near corners)

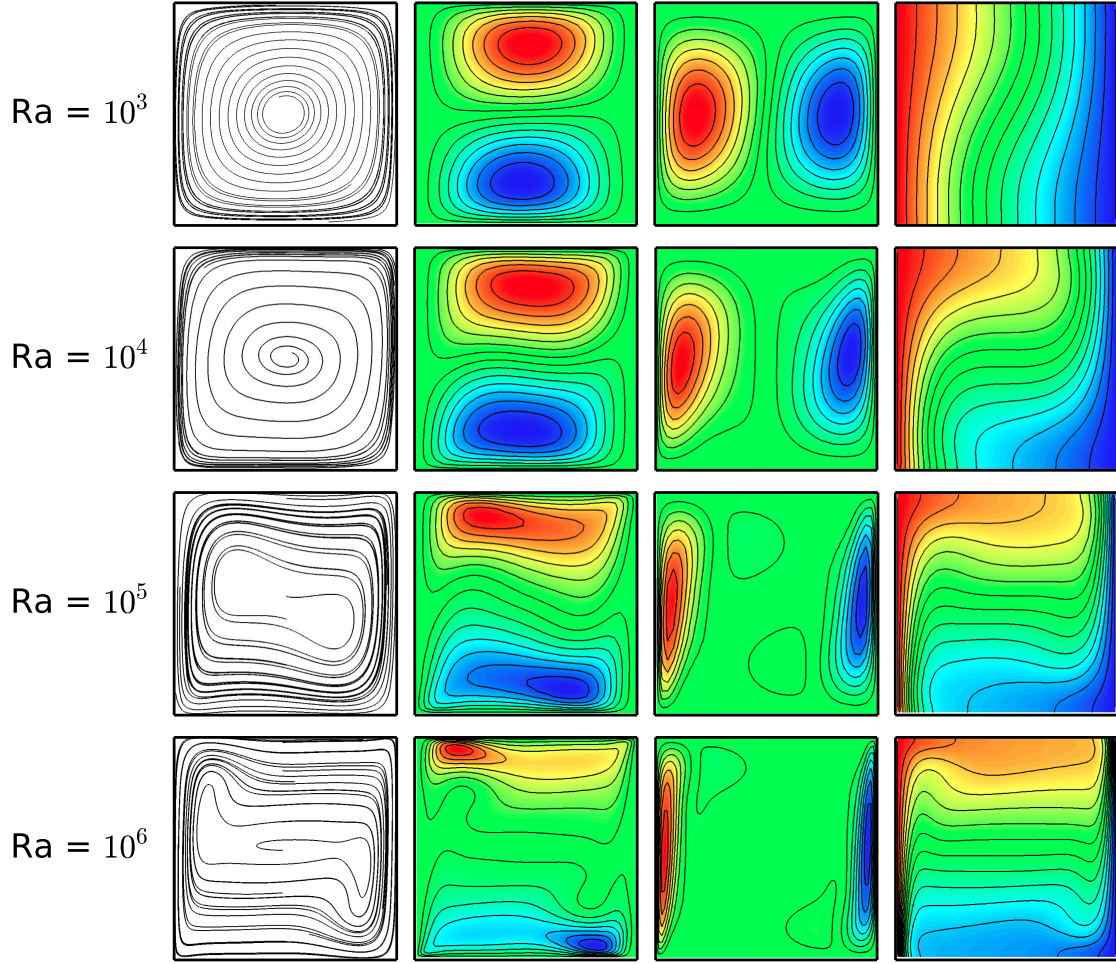
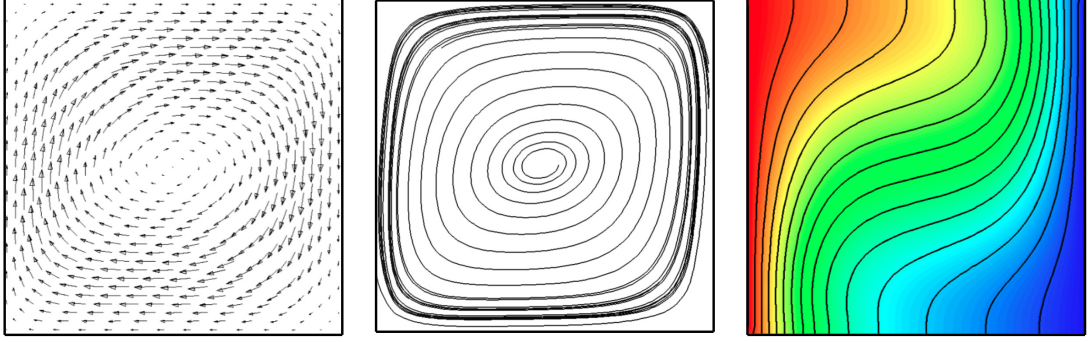


Figure 6.12: Flow patterns for convective flow compared with cite, from left to right: velocity streamlines, u component velocity, v component velocity, temperature.

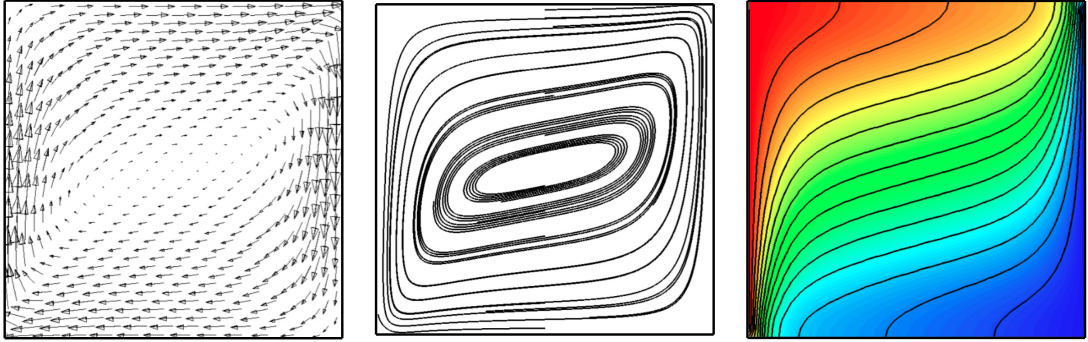
because of the Brinkman and non-Darcy terms, indicating the greater contribution of inertial effects; the streamline and isotherm patterns are also similar to that of the pure fluid case, with a gradual variation of velocity and temperature.

Part (b) is calculated with low permeability, and it is seen in the vector plot that velocity near the walls is large, showing the tendency to seemingly violate the no-slip condition and implying that boundary layers are becoming extremely thin; they are not resolved on the grid being used. Also, similar to what is shown in Fig. 6.8(a) of [115] (not exactly the same condition but with a low Darcy number), the streamlines presented here intensify near the hot and cold walls, also indicating thin

boundary layers near the wall. The isotherms are also similar to those of [115], and, in particular, converge at the bottom corner of the hot wall and the top corner of the cold wall. Moreover, it is important to note that, as summarized in [115], for low Darcy–Rayleigh numbers ($Ra^* = RaDa$), it is the regime of Darcy flow [115]; also, the Darcy flow regime is applicable up to a fairly high Ra for Da less than 10^{-4} .



(a) $Ra = 10^4$, $K = 10^{-6}$ ($Da = 10^{-2}$), $\phi = 0.6$, $u_{max} = 0.011m/s(7.8)$, $v_{max} = 0.013m/s(9.23)$, $w_{max} = 0.00105m/s(0.75)$.



(b) $Ra = 10^6$, $K = 10^{-8}$ ($Da = 10^{-4}$), $\phi = 0.8$, $u_{max} = 0.042m/s(30)$, $v_{max} = 0.076m/s(54)$, $w_{max} = 0.002m/s(1.42)$.

Figure 6.13: Streamline, u -component velocity, v -component velocity, isothermal patterns for different Darcy and Rayleigh numbers.

6.3.2 General model results

Next, results computed using the derived permeability model (see Eq. (6.17)) are presented for flow through three different porous media ($\phi = 0.1, 0.5, 0.9$), with fixed $Ra = 10^4$ obtained by setting temperatures on cold and hot walls, respectively, as $T_c = -20.95^\circ\text{C}$ and $T_h = 20.95^\circ\text{C}$. For Ra as low as 10^4 in the current case, Ra^* is considered to be low and these cases are expected to be non-turbulent if Da is lower than around 10^{-1} . All computations are performed on 41^3 grids.

It is seen in Fig. 6.14(a) that the vertical velocity magnitude decreases noticeably as porosity decreases; for $\phi = 0.1$, the profile is also shown in the zoom-in plot since the magnitude (10^{-5}) is so small that very little variation can be seen through the cavity; for $\phi = 0.5, 0.9$, there is a positive peak near the hot wall and a negative peak near the cold wall as expected. In the central portion of the cavity, the magnitude

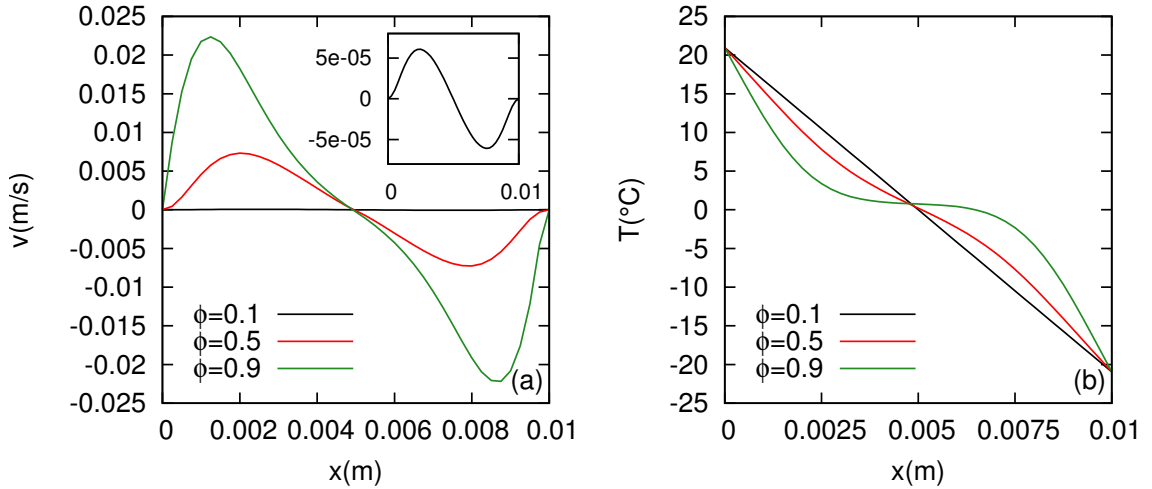


Figure 6.14: (a) Velocity and (b) temperature profiles through the cavity center for convective flow through different porosity media.

gradually changes, rather than being small, as shown in Fig. 6.7(a) of [115], where a higher Ra and constant Da are used. Also, higher velocity gradients are obtained for the larger porosity case. The temperature profiles shown in part (b) are also different from those of [115] (see Fig. 6.7(b)). There are no obvious small values in the central

region of the cavity for the case of $\phi = 0.5$ since smaller permeability values are produced from the model; also, larger temperature gradients occur for larger porosity cases.

Qualitative depiction of flow patterns and temperature profiles are provided in Fig. 6.15 (compare with Fig. 6.12). For low porosity (such as 0.1), velocity is so small that convective flow is insignificant, and heat conduction is dominant; velocities are anti-symmetric. For $\phi = 0.5$, temperature gradients begin to change, showing stronger convective effects. Streamlines for $\phi = 0.9$ begin to be similar to the clear fluid case shown in Fig. 6.12 for $Ra = 10^4$.

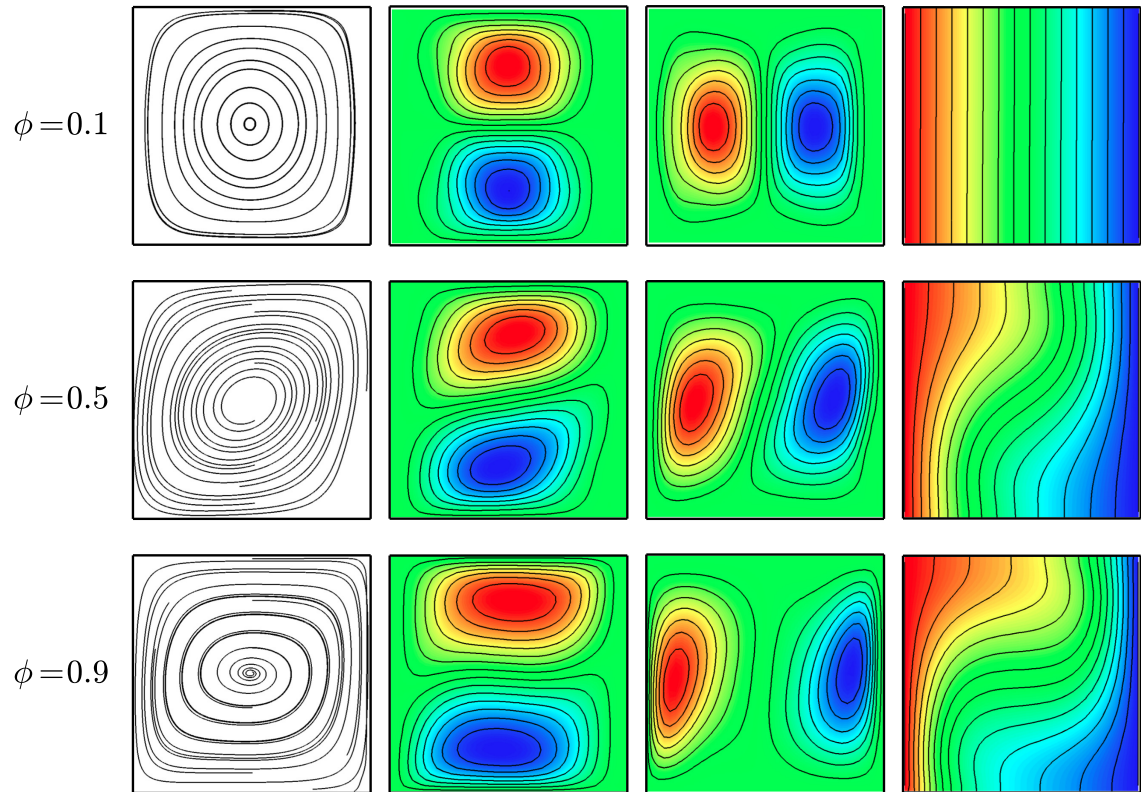


Figure 6.15: Flow patterns for convective flow through different porous media, from left to right: velocity streamline, u -component velocity, v -component velocity, temperature.

In Fig. 6.16 results from automatically calculated variable permeabilities are presented; these vary only with space since steady flow is considered for the present

study. Note that permeability also varies with time if non-steady flow is considered, which is much more complicated. Part (a) shows permeability profiles through the cavity center for different values of porosity. It is shown that as porosity decreases, the averaged value of permeability decreases, as expected. All profile shapes are similar in that they have two peak values with a valley value between them. The peak values move towards the center as porosity decreases. Details of profile shape for different porosity are not exactly the same; but at the same x location, usually permeability increases as porosity becomes larger. This is in correspondence with the strain rate shown in part (b), where permeability is calculated from Eq. (6.17). The zoom in plot is provided for $\phi = 0.1$ after rescaling of y -coordinates since it is nearly a straight line in the original scale. Observe that all strain rate profiles have the opposite tendency as permeability, indicating the inverse relationship emphasized earlier.

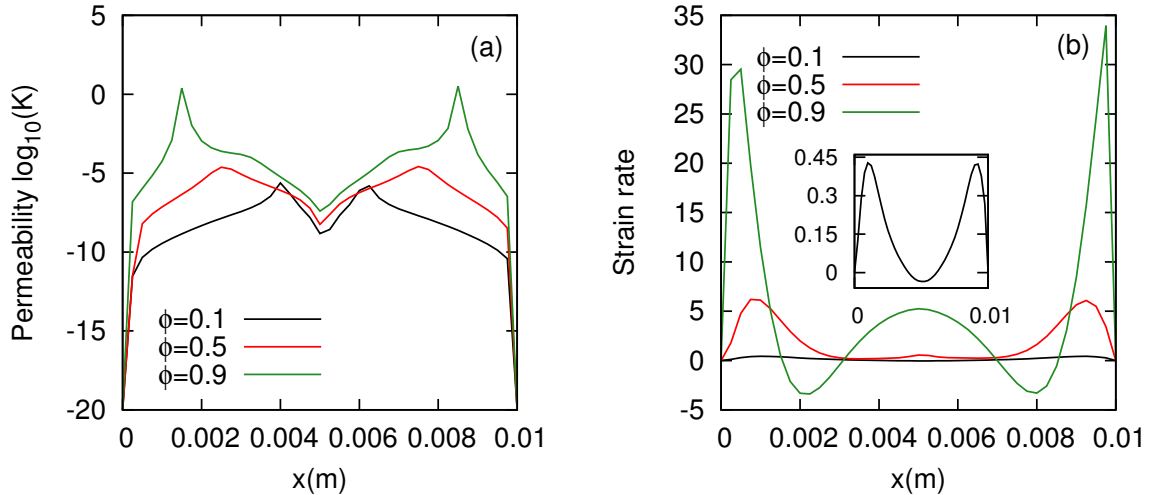


Figure 6.16: (a) Permeability and (b) strain rate through the cavity center for convective flow through different porosity media.

Figure 6.17 provides a more detailed view of the permeability distribution in the center plane of the cavity. Different ranges of color scales have been used for the three cases in order to demonstrate a clearer distribution in each plot at the expense of better quantitative comparisons. First, observe that, as the porosity decreases,

the overall permeability becomes smaller since the range of permeability values, as seen from the color bar, decreases. Second, relatively high permeability values occur away from the walls for all cases, but the shapes of distributions are significantly different for different porosities. In the case of $\phi = 0.9$, four notable contour regions with higher permeability values occur and are connected to each other; for $\phi = 0.5$, two diagonal “bands” appear; and for $\phi = 0.1$, four small round areas occur somewhat symmetrically about the cavity center. Lastly, the notable regions with small permeabilities in the center of these plots appear as “cores” with shapes similar to the cores of the main vortical flow field corresponding to the streamlines. These features correlate, qualitatively, with strain rate shown in the next figure.

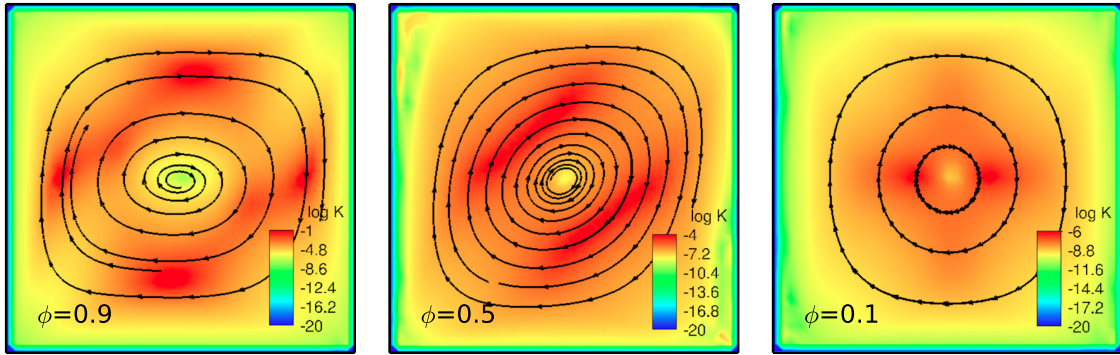


Figure 6.17: Permeability of cubicle convective flow through different porosity media in the middle x - y plane, $Ra = 10^4$.

The strain rate distributions are shown in Fig. 6.18. Since the range of values for the case $\phi = 0.1$ is not close to the same magnitude as in the other cases, a different scale of $[-0.04, 0.04]$ is employed, as shown in the color bar, in order to present more notable information. First, it is seen that the overall absolute strain rate decreases as porosity becomes lower, due to low velocities in lower porosity cases. Second, observe that for $\phi = 0.9$, the magnitude of strain rate is high near the wall, while for $\phi = 0.5, 0.1$, strain rate near the wall is lower than the adjacent area and in this adjacent area decreases gradually into the center. Third, the inverse correlation between Figure

6.17 and 6.18 for each case is also seen, but it is clear that this is significantly more complicated than a simple reciprocal is would be expected by examining Eq. (6.17). For instance, in the case of $\phi = 0.9$, lower values of permeability occur in the center core and the surrounding places near the wall, where absolute values of strain rate are higher. Also, contours shown in Fig. 6.18 tend to be increasingly symmetric as ϕ becomes small, as also shown in the permeability distribution plots. The center area formed by larger strain rate values near the wall decreases as porosity decreases, corresponding to the shrinking permeability “cores” (Fig. 6.17) formed by larger permeability values.

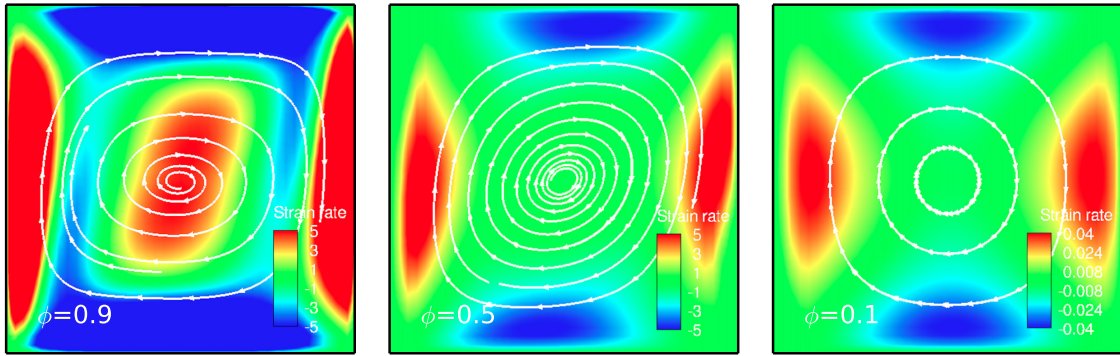


Figure 6.18: Strain rate of cubicle convective flow through different porosity media in the middle x - y plane, $Ra = 10^4$.

6.4. Summary and conclusions

In this chapter a general relationship between porosity and permeability has been derived from maximization of entropy production rate of fluid flow in porous media in order to stabilize the non-equilibrium thermodynamic system. An explicit expression for permeability in terms of porosity is obtained analytically through solving an ODE resulting from taking the first derivative of entropy production rate with respect to permeability. It is observed that stability is asymptotic as $K \rightarrow \infty$. The resulting formula automatically satisfies the constraints relating porosity and permeability (as

$\phi \rightarrow 0$, $K \rightarrow 0$, and as $\phi \rightarrow 1$, $K \rightarrow \infty$). Potentially it can be used in general situations (no additional empirical parameters as appear in various correlations) for flow in both homogeneous and inhomogeneous porous media.

Numerical simulations of cubicle lid-driven cavity and natural convective flows have been carried out for both cold and hot fluid cases, respectively, to provide an initial investigation of performance of this model. It is observed that the present model can produce different permeabilities in the solution domain accounting for influences from solid walls. Computational results for velocity and temperature distributions are noticeably different from those calculated with constant, fixed permeabilities. Results computed with the derived model show consistency with expected flow physics for various porosities.

The results of this study are quite explorative and need to be verified by future experiments, since there are no benchmark experimental results yet for porous media problems with the same configurations employed in this study (technical difficulties in experimental apparatus). The model is applied only to incompressible flows in the present study. The same derivation procedure can be performed to obtain a relationship that is applicable to compressible flows as well. The effects of solid wall boundaries on permeability distribution in a homogeneous porous medium are mainly investigated. Inhomogeneity inside a porous medium will be considered in future studies with an emphasis on the geometry-related effective viscosity. Also effects of different thermal transport properties of liquid and solid materials will be explored.

Chapter 7: Computations of Wildfire Spread

In order to demonstrate the importance and operational potential of the modeling approach thoroughly discussed from Ch. 3 to Ch. 6, four wildfire simulations were performed considering different fuel types (grass and forest), terrain types (flat and mountain), and the influence of firebrands. All computations are performed in parallel mode on the high-performance computing cluster referred to in Ch. 6, Sec. 6.2. In Sec. 7.1, numerical data associated with canopy drag effects, physical domain, grid information, and boundary conditions of all simulations are presented. In Sec. 7.2, computational results of grassland fires on flat (open) terrain are presented and discussed first since grassfires are relatively simple among wildfires and have been studied both experimentally and numerically in a fair amount of literature (e.g. [37] [63] [83]). In Sec. 7.3, simulation results of forest fire spread involving both surface and canopy fires are provided. Also, preliminary results of crown fire spread on meso-scale realistic terrain are given. In Sec. 7.4, firebrand calculations are carried out in the context of both fixed and time-dependent flow field of a forest fire. Lastly, Sec. 7.5 provides summary and conclusions from the computational results.

7.1. Numerical details

Since the estimated porosities (see Sec. 3.3) of a typical three-level (undergrowth, trunk, canopy) forest model are very high (close to unity), they have no significant effects on the inertial term, and possibly the Darcy term (if the porosity-dependent permeability is fairly large) in the governing equation (Eq. (3.1b)). Therefore, the non-linear Forchheimer term is dominant, and is usually the only drag force term in the momentum equation for canopy flows in many studies (see, e.g., Shaw and

Schumann [245], Yamada [246], Aumond et al. [247] and Mueller et al. [228]). The Forchheimer term can be expressed in a way more familiar to the atmospheric modeling community as

$$f_d = c_d a_f \rho |\mathbf{u}| \mathbf{u} , \quad (7.1)$$

where c_d represents a drag coefficient and is regarded as equivalent to the Ergun coefficient c_F in Eq. (3.2); a_f represents leaf area density defined as the one-sided leaf area per unit volume, and is usually a function of height [245]. Drag coefficients in canopies often range between 0.15 and 0.37 on the basis of an analysis of micrometeorological data from a deciduous forest by Shaw et al. [245] [248]. Here, a drag coefficient of $c_F = 0.15$ is used. Inhomogeneity of the porous fuel bed is demonstrated by the distribution of leaf area density. If it is assumed that the projected frontal area of a fuel particle is half of the total surface area, as with flat leaves, then the leaf area density is expressed as $a_f = \sigma_s \beta_p / 2$ [228]. Here, β_p is the solid volume fraction of vegetation, or simply put, the porosity; σ_s is the surface to volume ratio of a fuel particle. Comparing Eq. (7.1) with the Forchheimer term in Eq. (3.2) shows that $K^{-1/2} = a_f$. This provides a good approximation of permeability values used in canopy flows. Also, the theoretical permeability model described in Ch. 6 is dependent on porosity and geometry-related parameters, similar to the expression for a_f stated above.

Figure 7.1 (a) shows a leaf area density distribution estimated from observations in experimental sites (Dupont et al. [249]); part (b) shows the corresponding permeability values within the canopy. For both plots, non-dimensional heights y/h are denoted in the y -axes with h being the tree height. The part of the tree with approximately zero leaf area density is considered as the trunk; the region higher than the tree with approximately zero a_f is regarded as the atmospheric air. As seen in part (b), permeability values range from $\mathcal{O}(10^0)$ to $\mathcal{O}(10^5)$, which are much larger than the values used for the numerical problem treated in Ch. 6. Note that the undergrowth

part is not presented here in both plots, but it is assumed that it has leaf area density and permeability values similar to that of the canopy level in computations.

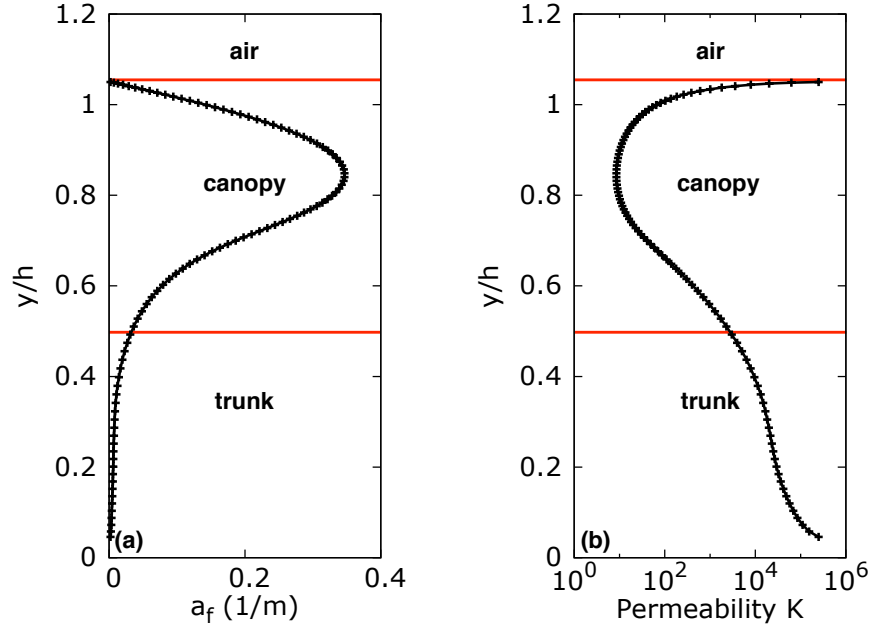


Figure 7.1: Profiles of (a) leaf area density a_f ; (b) corresponding permeability values.

In this study, permeability in a forest is calculated from Eq. (6.17)—the theoretical model described in Ch. 6. The Darcy term is retained in case large flow velocity and small computed permeabilities occur. Porosities estimated in Sec. 3.3 and other geometry-dependent parameters such as tortuosity H_{tor} are utilized. It should be noted that the definition of tortuosity (see Ch. 3) used here is provided by Bear and Bachmat (see Sec. 2.3.6 of [119]). In their study, a value of $\sim 1/3$ is estimated for the tortuosity of a very simple configuration; viz., the void space in a cubical box is made up of straight tubes (parallel to the axes of the box) with a constant cross-section. For cases with any tortuous tubes (tube-length larger than cube-length), $H_{tor} < 1/3$. Since the paths of void spaces in the canopy or undergrowth can be quite tortuous, and much longer than the straight paths parallel to the axis of the canopy or undergrowth, the tortuosity in the canopy and undergrowth is assumed to be much smaller than

1/3. Recall that $\mu_e/\mu = 1/(\phi H_{tor})$; thus, with very small H_{tor} , the effective viscosity μ_e will be large, resulting in large values of the coefficient a appearing in Eq. (6.17) and small permeability values. Therefore, in real computations, the coefficient a is amplified in an empirical way. It is assumed that the ratio of the total horizontal length (of $\sim \mathcal{O}(10^2)$ leaves) to their thickness might be a good approximation of the amplification factor according to the definition of tortuosity in [119]. In this initial investigation, amplification factors of 500, 10, and 1000 are used for undergrowth, trunk, and canopy, respectively, according to the complexity of biomass in each level. In addition, since the resolution used for wildfire simulations is not (or cannot be) sufficiently large for using the general model, especially for turbulent porous flows, as discussed previously (Sec. 6.1.2), it is possible to get undesired infinitely large permeability values from the general model. Consequently, limits of permeabilities are used with reasonable values provided in Figure 7.1 (b).

For each simulation, the terrain is positioned at the bottom of the three-dimensional computational domain. An example of the computational domain and grids used in this study is shown in Fig. 7.2, where x, y, z represents streamwise, vertical, and span-wise direction, respectively. The length in x, y, z directions is, respectively, denoted by $Lx + Lxe$, Ly , and Lx . Note that the computational domain is somewhat larger than the physical domain since an extended computational domain (in streamwise direction with a length of Lxe) is required to satisfy the outlet boundary condition for fully-developed flow. In x and z directions, uniform grids are used in the physical domain, while stretching grids in x direction are used with filtering in the extended domain. In the y direction, non-uniform grids are stretched from the first grid with the smallest grid spacing (usually the height of grass). Thus, relatively refined grids are used in the lower atmospheric region, as seen in the zoom-in plot in Fig. 7.2.

Table 7.1 shows details of the four simulations being performed. As seen, different physical domains are used for each case in order to investigate the effects of terrain.

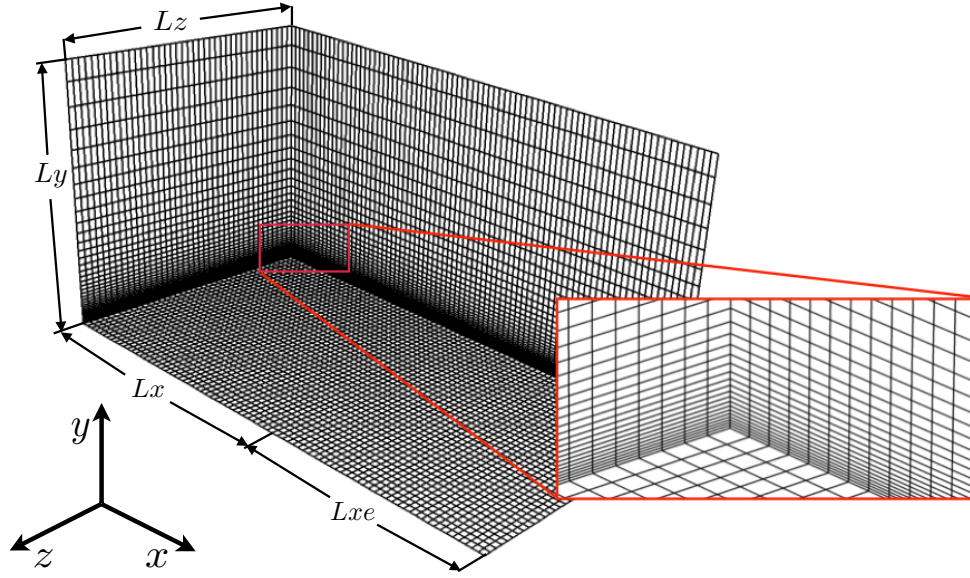


Figure 7.2: Sketch of the computational domain used in this study.

The domain size for simulation 1 is typical for grassland fires. Both horizontal and vertical lengths are increased in simulation 2 for forest fires. A meso-scale terrain is used for simulation 3 for a typical devastating forest fire; the “ \sim ” is used since Ly is not uniform within the domain. Simulation 4 employed an extended length in x direction on the basis of simulation 1, for the sake of firebrand studies. In x and z directions, grid spacing is 5 m for simulation 1, 2, 4, and ~ 50 m for simulation 3. In the y direction, grid spacing ranges between 0.5–16 m for simulation 1, 0.5–28 m for simulation 2, 1.5–167 m for simulation 3, and 0.5–22 m for simulation 4. It is seen

Table 7.1: Summary of the different numerical conditions used for each simulation (Sim.) conducted in this study.

Sim. no.	Fuel type	Physical domain: $Lx(Lxe) \times Ly \times Lz$	Physical grids: $Nx(Nxe) \times Ny \times Nz$
1	Grass	$200(200) \times 200 \times 200 \text{ m}^3$	$41(40) \times 41 \times 41$
2	Forest	$350(50) \times 300 \times 200 \text{ m}^3$	$71(10) \times 51 \times 41$
3	Forest	$2.95(1.8) \times \sim 2 \times 2.29 \text{ km}^3$	$60(35) \times 61 \times 57$
4	Forest	$500(400) \times 200 \times 200 \text{ m}^3$	$101(40) \times 41 \times 41$

that rather coarse grids (especially for simulation 3) are used in these simulations, but rather coarse atmospheric resolution (grid spacing 100–500 m) is found to be capable of qualitatively capturing fire growth and behavior such as surface and crown fire spread [90]. Grid spacings used for simulation 1, 2, 4 are also expected to capture some coherent structure of turbulence using synthetic-velocity LES. Because the size of such structures in the upper canopy of such flows has been found to be on the order of h_c (the canopy height) in the horizontal direction and $h_c/3$ in the vertical direction by Finnigan [250].

The same boundary conditions are utilized for all simulations. The ABL (atmospheric boundary layer) velocity (U component) profile expressed as [251]

$$\frac{U(y)}{U_\tau} = \frac{1}{\kappa} \ln \left(\frac{y}{y_0} \right) \quad (7.2)$$

is prescribed as the upwind streamwise boundary conditions (V and W component velocities are zero). A maximum free-stream wind velocity of 10 m/s is employed. In Eq. (7.2), U_τ is the friction velocity defined as $\sqrt{\tau_w/\rho}$ with τ_w being the wall shear stress; y_0 is the roughness height of terrain; κ is the von Karman constant (~ 0.4). The roughness and estimated ABL depth are, respectively, ~ 0.5 m and 510 m for a typical forest, and are, respectively, ~ 0.05 m and 400 m for bushes or grass (see Figure 1.3 and Table 1.1 of [251]). As mentioned previously, a fully-developed flow is prescribed for the downwind streamwise boundary condition. The no-slip condition with zero velocity is used for the bottom boundary (terrain). Stress-free conditions (velocity normal to the surface and shear stress are zero) are enforced on top, fore and aft (spanwise) boundaries.

Boundary conditions for solving the PPE were discussed in Ch. 4, Sec. 4.1. Neumann conditions of $\partial\Phi/\partial\mathbf{n} = 0$ (Φ is pseudo pressure, $\partial/\partial\mathbf{n}$ is normal derivative) are prescribed on all boundaries except for the outlet (open), where a Dirichlet condition of $\Phi = 0$ is employed. For temperature, an atmospheric temperature of 20 °C is assigned for the upwind (inlet) boundary; adiabatic conditions are employed on all

other boundaries. For combustion effects, heat release rate described in Sec. 3.4 is used. The temperature in wildfire simulations can reach as high as 800 °C–1200 °C. The ignition modeling described in Sec. 3.5 is employed. Ignition temperatures of 230 °C, 330 °C, and 330 °C are used for grass, canopy, and trunk, respectively. The moisture content of the fuel is assumed to be zero for simplicity. Before the onset of ignition, velocity and pressure in the domain are initialized by calculating the cold flow field with a Re number of 10^5 . Also, wildfire spread results will be presented only in the physical domain (i.e., not including the extended region) in the following sections.

7.2. Grassland fire (simulation 1)

Figure 7.3 shows grassfire spread of simulation 1 at four different times: 5 s, 40 s, 60 s, and 130 s after initiation. The grass is assumed to be 0.5 m high and has the same properties as undergrowth discussed in Ch. 3, Sec. 3.3. The initial ignition region lies in the center of the up-wind streamwise boundary of a homogeneous fuel bed, as can be seen in part (a) of Fig. 7.3 since the fire has not yet spread far from the initial line. The region occupies 5 m, 0.5 m, and 50 m in x , y , z directions, respectively. For each plot, six iso-surfaces of temperature are used, viz., 63 °C, 100 °C, 160 °C, 230 °C, 500 °C, 600 °C, with the same legend denoting the color gradient. The interaction between the grassfire and air flow is clearly seen from part (b) to (d). The ABL flow pattern is changed due to the hot buoyancy induced by the fire—leading to formation of fire plumes; at the same time, the fire shape is also noticeably changed by the strong wind blowing from the upstream. As time evolves, more fuel is burning; and these interactions become more intense, resulting in more turbulent behavior. Also, it is seen that relatively lower temperature (less than the ignition temperature of 230 °C) exists in fire plumes, and higher temperature is shown within the burning region, as expected. The iso-surface of ignition temperature displays the

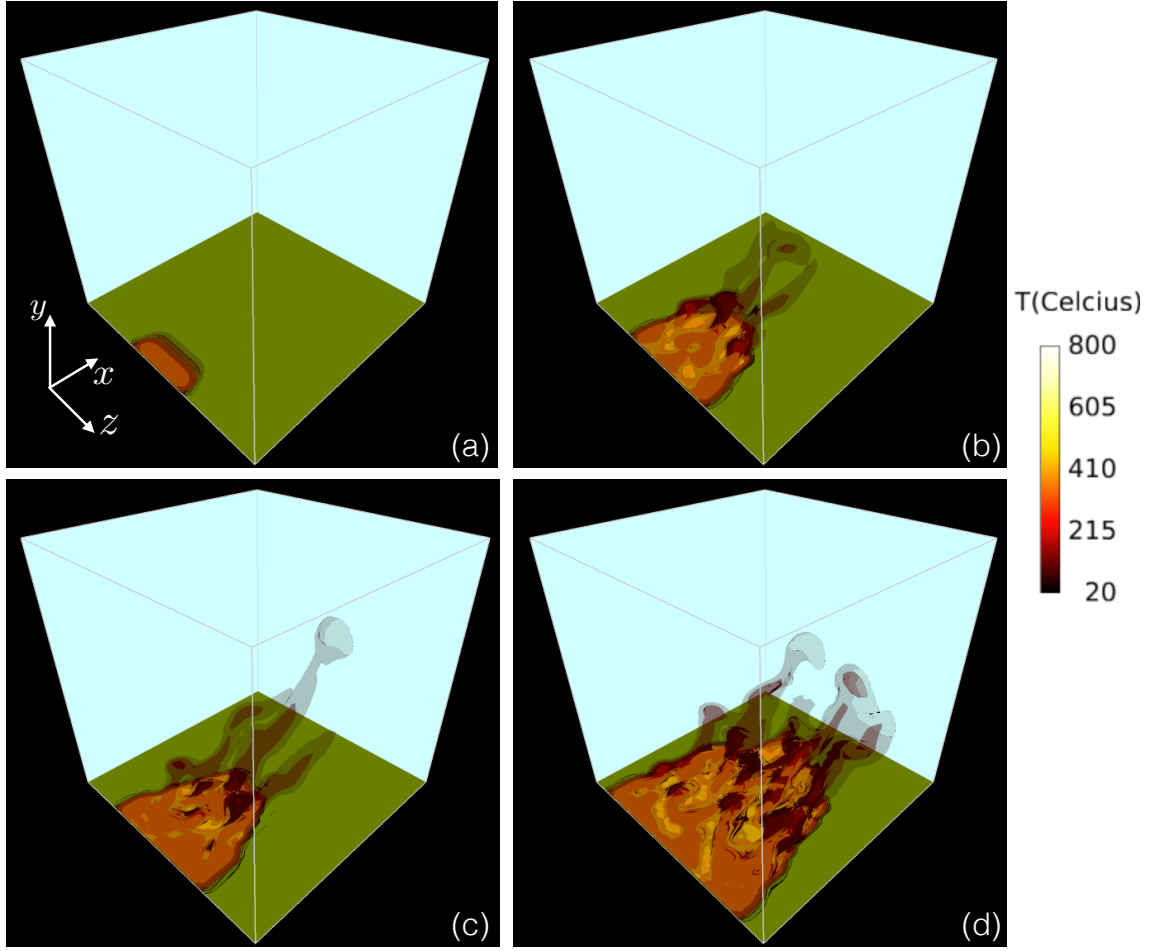


Figure 7.3: Iso-surfaces of temperature (transparency): 63°C (87.5%), 100°C (75%), 160°C (75%), 230°C (62.5%), 500°C (0%), 600°C (0%) for fire burn at (a) 5 seconds; (b) 40 seconds; (c) 60 seconds; (d) 130 seconds.

automatically formed (via the simulation) oval shape of a typical grassfire front line (see the photo of experimental fire F19 in [63]). Since the total burn time of grass is set to be 150 s in this simulation, decreased temperature with depletion of fuels is not present in Fig. 7.3, where the largest burn time is 130 s. It is noted that finer grids of $161 \times 81 \times 81$ points have also been used for the same grassfire problem for the study of grid independence, and the results (not shown here) show similar fire behavior.

Figure 7.4 (a) shows velocity vectors and temperature contours in the middle x - y plane ($z = 100$ m) in the lower portion of Fig. 7.3 (d). Same legend (color gradient) is

used for both vectors and contours. As is seen, only the region adjacent to the bottom

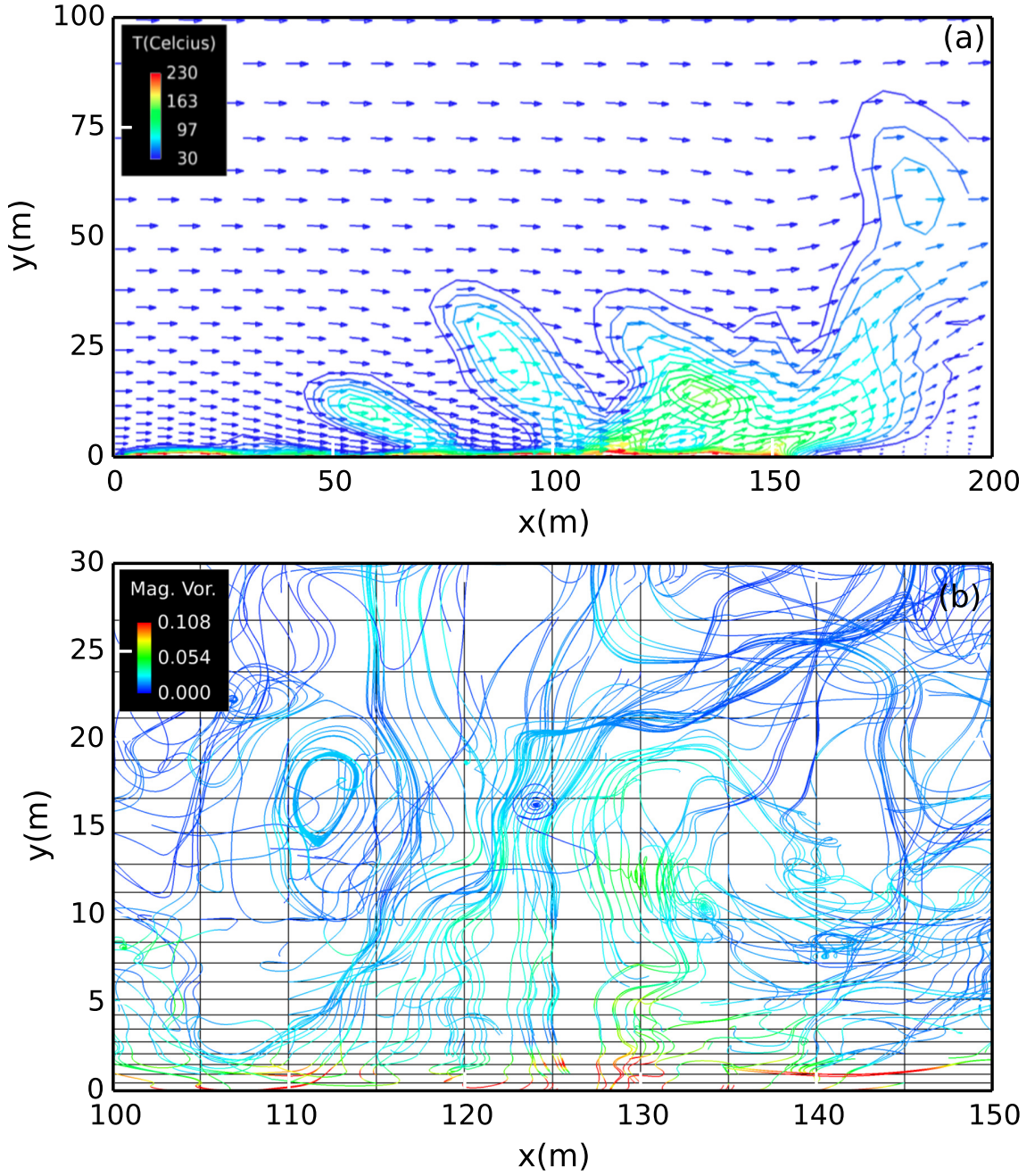


Figure 7.4: Flow field in the $x-y$ plane at $t = 130$ seconds and $z = 100$ m in correspondence of part (d) of Fig. 7.3: (a) Temperature contours and velocity vectors; (b) subgrid-scale streamlines.

is red, since red represents temperature greater than the ignition temperature and mostly burning fuels satisfy this condition. Thus, it is observed that the fire has

spread to ~ 150 m at this time (130 s). Also, the contours show that several puffs are pinched or beginning to pinch off from the main smokey region. The vectors show that the wind field is significantly altered by the buoyant plume. Part (b) shows streamlines of subgrid-scale velocity integrated from the same plane as part (a), but with a smaller overall region. Streamlines are colored with vorticity magnitude as shown in the legend. It is seen that high values exist mainly in the region close to the grass since velocity gradient is relatively large in this area, and vorticity is the anti-symmetric part of the velocity gradient. Apart from this, relatively higher magnitudes also exist for $x \in [120, 130]$; this region contains a small-scale updraft and vortices form beside it. The corresponding region in part (a) also shows that temperature is higher within several small puffs. The temperature in part (a) is obviously affected by the SGS velocities. However, small-scale velocity behavior is not demonstrated in the large scale vectors in part (a) since the grid spacing is too coarse to provide sufficient resolution of small-scale fire behaviors. The streamlines shown in part (b) still resembles the overall shape of the corresponding fire plume in part (a), but it also shows a very irregular flow field with vortices and swirls of various sizes, including some that are smaller than the grid scale. This is possible only with synthetic-velocity SGS models.

Moreover, the effect of different ignition lines on grassfire spread rate are investigated by running two additional simulations similar to simulation 1. Figure 7.5 shows velocity vectors one grid cell above the ground (black) and scalar iso-surface of ignition temperature (yellow) of three simulations at 60 s (left) and 120 s (right), viewed from above. Ignition lines of 25 m, 50 m, and 100 m are employed, as denoted in red. Observe from the vectors that the flow direction is somewhat altered by the fire. The fire-front line and shape are indicated by the iso-surface and are automatically computed (as observed previously). Note that similar fire fronts can be visualized using depletion degree of burning fuels (calculated from burn time). The shape of

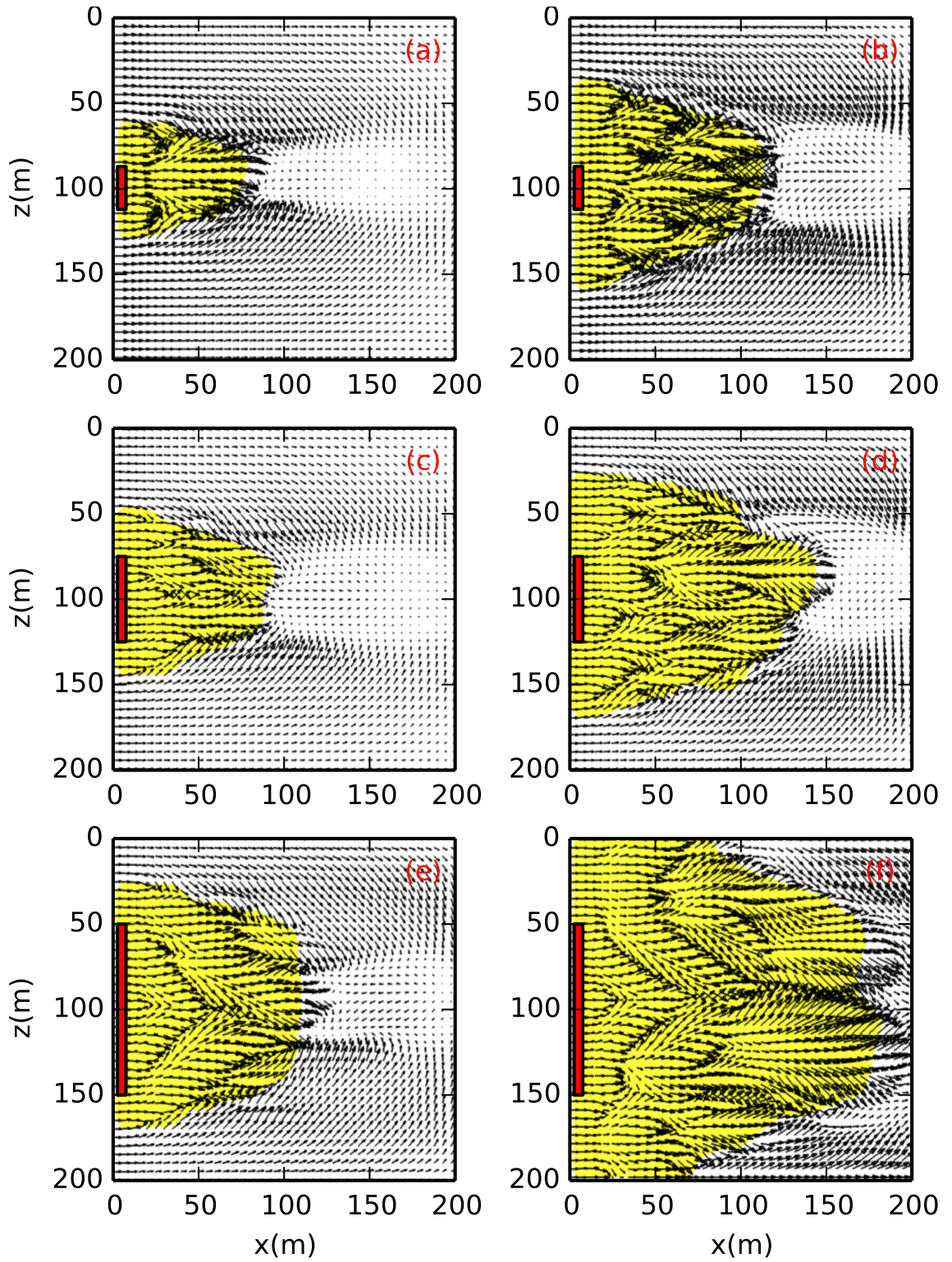


Figure 7.5: Top view of grassfire burn with ignitions lines of (a)(b) 25 m; (c)(d) 50 m; (e)(f) 100 m at 60 seconds (left) and 120 seconds (right).

such fire fronts at different times are similar to those at corresponding times calculated from WFDS (see Fig. 9(b) of [63]) with the same physical domain and ignition configuration (position, depth, length, and size). The spread rate estimated from Fig. 7.5 is as follows: (a) ~ 1.3 m/s; (b) ~ 1.0 m/s; (c) ~ 1.67 m/s; (d) ~ 1.25 m/s; (e) ~ 2.0 m/s; (f) ~ 1.5 m/s. Fire with a longer ignition line spreads faster since more fuel is ignited by the initial line and heat transfer from radiation is larger in the horizontal direction. Also, it is seen that for all cases, fire spreads faster during the first 60 s, and slows down in the next 60 s. The reason for this is that the fire-induced vertical updraft carries heat away from the fire and draws cooler air across the perimeter of the burning region, especially in the middle z region with the fastest spread speed, which slows the spread. The spread rates estimated are slightly slower than those of WFDS, especially at $t = 120$ s; this is because U_2 (ambient wind speed at 2 m above ground) here is 4.03 m/s, which is smaller than 5 m/s used in [63].

7.3. Forest fire

Compared with grassland fire cases, simulations of forest fires are more complicated since more complex fuel materials are involved such as bushes, tree trunks, and canopies (see Fig. 3.1), the drag effects of which are considered non-negligible. In this section, forest fires on both flat and realistic terrains are investigated.

7.3.1 Flat terrain (simulation 2)

Figure 7.6 shows forest fire spread of simulation 2 at four different times: 10 s, 60 s, 120 s, 180 s. The forest is assumed to be ~ 13 m high, and has similar properties to coniferous forests discussed in Ch. 3, Sec. 3.3–3.4. Specifically, in the y direction, the first grid cell represents the undergrowth part (0–0.5 m); the second to the 12th represent the trunk (0.5–6.54 m); the 12th to 18th (6.54–12.66 m) represent the canopy part. The initial ignition region is the same as that of simulation 1 with an ignition

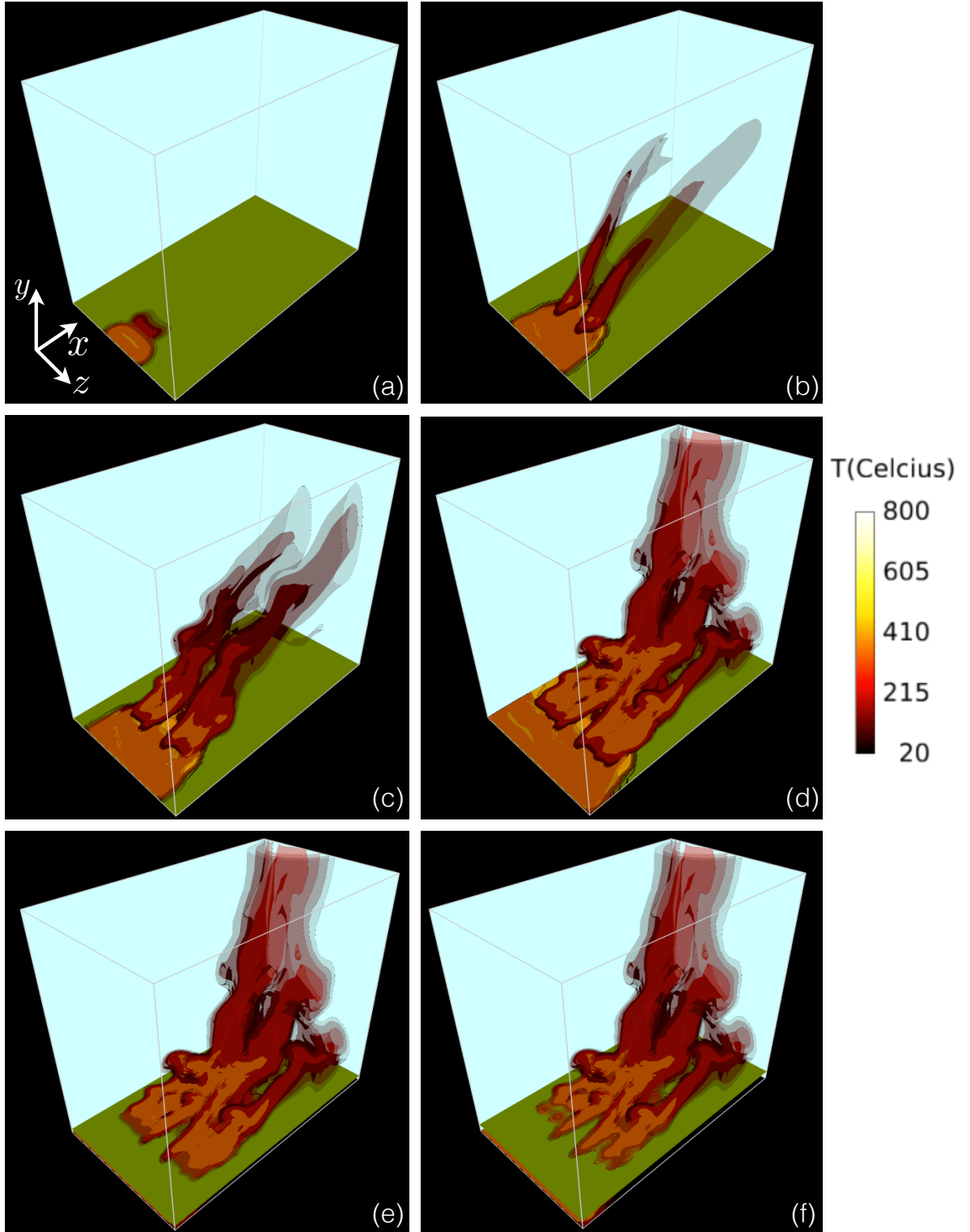


Figure 7.6: Iso-surfaces of temperature (transparency): 63°C (87.5%), 100°C (75%), 160°C (75%), 230°C (62.5%), 500°C (0%), 600°C (0%) for fire burn at (a) 10 seconds; (b) 60 seconds; (c) 120 seconds; (d)–(f) 180 seconds; (e) canopy at $y = 6.54$ m; (f) canopy at $y = 12.66$ m.

line of 50 m. This fire (which is initiated from the undergrowth level) can be regarded as a surface fire and is quite practical since most human-caused fires (e.g., campfires) are surface fires, which may transition to large crown fires through ladder fuels. Part (a) shows the surface fire (crown fire has not yet started) 10 s after fire initiation, with a small puff beginning to form, similar to grassland fire shown previously (Fig. 7.3). For each plot, six iso-surfaces (as denoted in the caption of Fig. 7.6) with the same temperature, transparency, and legend as those of grassland fires are used. Part (b) (60 s) shows two distinct fire plumes (see the black line with lower temperature iso-surface) on top of the surface fire, indicating the beginning of the transition from surface to crown fire. Although the canopy fire is at an early stage, the plume is already much higher than that of the grassland fire. Tree crowns are heated and ignited by the hot buoyant plume from the surface fire. Note that ladder fuels are not provided for this transition. The reason might be that the trunk level is not very high and fire plumes still remain at high temperature as they reach the canopy. Parts (c) and (d) show that more fuels in the canopy are ignited and burning, and that canopy fires are becoming more turbulent with much higher temperature in the higher fire plumes. At 180 s, the plume has reached 300 m height into the atmosphere, and the temperature in a large part of the plume is greater than 230 °C. It is also seen that the canopy fire burns much more intensely with turbulent capricious behaviors and much higher buoyant plumes than in the grassfires shown in Fig. 7.3.

Moreover, observe that the canopy fire in the middle region (z direction) does not burn as intensely as those in the two sides, which is different from the grassfire where fire plumes are much more evenly distributed. This may be because a much larger volume of cold air is drawn in by the buoyant plumes from canopy fires compared with surface fires, which prevents the fire from burning in the middle region. The spread rate of surface fire in Fig. 7.6 is similar to the grassfire. The spread rate of canopy fires is much faster than that of grassfires, which is around 2.5 m/s since

more fuels are contained in the canopy. Parts (e) and (f) show the same fire spread as part (d), but with different planes at the bottom. The bottom and top planes of the canopy are used, respectively, for (e) and (f) in order to observe the shape of canopy fires within the canopy. It is seen that the ignited or burning fuels are decreasing as they are positioned higher in the canopy. The fire at the top of the canopy shows many “holes”, indicating that many fuels are not burned, which is different from the surface fire. From computations, it is also found that surface and crown fires tend to coexist. If only a crown fire exists, the cold air from below and the fire front would suppress its spreading in the absence of firebrands.

Figure 7.7 (a) shows velocity vectors of fluid flow through a forest (roughly in the middle region in x direction) before an initiation of fire (h represents tree height). It is clearly seen that the flow field in the forest is affected by its drag force. The overall velocity is small in the forest compared with open flows, which is different from flow through grass. Within the forest, the velocity in the canopy is slightly smaller than the largest velocity in the trunk space. Note that for flow near the forest edge, the velocity in the trunk space is noticeably larger than that in the canopy, and decreases gradually until the flow reaches further into the forest, as observed in [228]. This may also contribute to a faster speed of canopy fire and the formation of several fire plumes observed in Fig. 7.6. Since the cold air is drawn (inverse flow direction) with lower velocity, the burning fire experiences less cooling. Figure 7.7 (b) to (e) show velocity vectors and temperature contours at $z = 100$ m (top), $z = 50$ m (bottom), and $t = 120$ s (left), $t = 180$ s (right) in correspondence with Fig. 7.6 (c) (d). Velocity vectors are somewhat altered by the fire. Also, more puffs of various sizes are formed compared with grassland fires, indicating more turbulent flow behaviors.

It is clearly seen that the canopy fire development in the central region ($z=100$ m) and that at the two sides are quite different. Part (b) shows canopy ignited at around $x = 100$ m, and the corresponding surface fire spreads this far. However, in part (d),

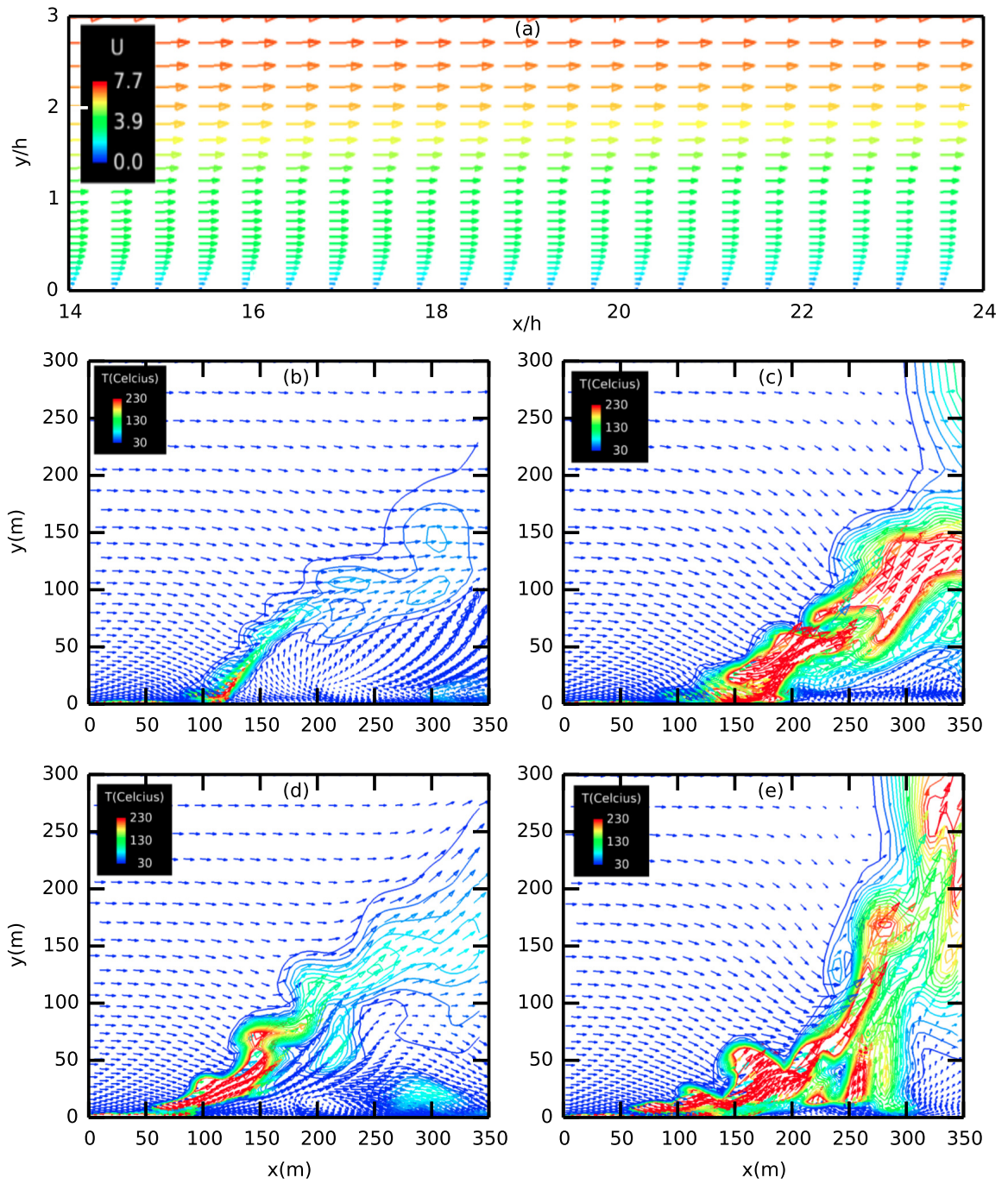


Figure 7.7: (a) Velocity vectors in forest for cold flow. Temperature contours and velocity vectors in the x - y planes of (a)(b) $z = 100$ m (top), (c)(d) $z = 50$ m (bottom) at (a)(c) 120 seconds (left) and (b)(d) 180 seconds (right).

the canopy was ignited at $x=50$ m and has spread to approximately $x=150$ m by this time; the corresponding surface fire is at only $x=75$ m. Fires in (d) are more intense than in (b) as they have been initiated earlier, and have had more time to develop. Also, more consecutive puffs are pinched off from the main fire. The reason might be that, in the middle region, the surface fire spreads faster with a formation of large plumes, causes inverse cold flow, and cools off the burning fuels, which affects the crown fire since it is heated to some extent by the surface fire to ignite. However, along the two sides, not as much buoyancy occurs initially; thus, the fire is cooled somewhat less and can ignite unburned canopy fuels faster. Also, the trunk space, which is not shown in Fig. 7.6, is shown here. Since heat release rate from the trunk is not large (see Table 3.4), its temperature is not as high as the undergrowth and canopy. Third, as hot plumes from surface fire continue to heat the upper crown, more tree crowns are ignited and more intense turbulent behavior occurs, as shown in parts (c) and (e) of the figure. The trunk also has a temperature over 230°C in (c). Part (e) shows even more turbulent fire behavior since more fuels are burning for the reason stated above. The canopy fire reaches the maximum distance of around $x=260\text{m}$ while the surface fire is at ~ 170 m; but the burning fuels are not simply connected with numerous “holes” present.

Figure 7.8 shows small-scale (SGS) behaviors of the lower part of Fig. 7.7 (b) and a zoom-in plot in part (b) of Fig. 7.8. It is seen that the small scale streamlines resemble the large-scale velocity vectors shown in Fig. 7.7 (b), but with more sub-grid scale details. The streamlines are more complicated than those of the grassfire with various sizes of vortices and different vortex structures attached with the main higher updraft or plume. The relatively large magnitude of vorticity appears in the middle of the plume ($x=220$ m), in correspondence with the detachment of a large puff presented in Fig. 7.7 (b), possibly implying existence of fire whirls. Generally, large vorticity magnitude concentrates in regions in or near the forest and fire plumes. It

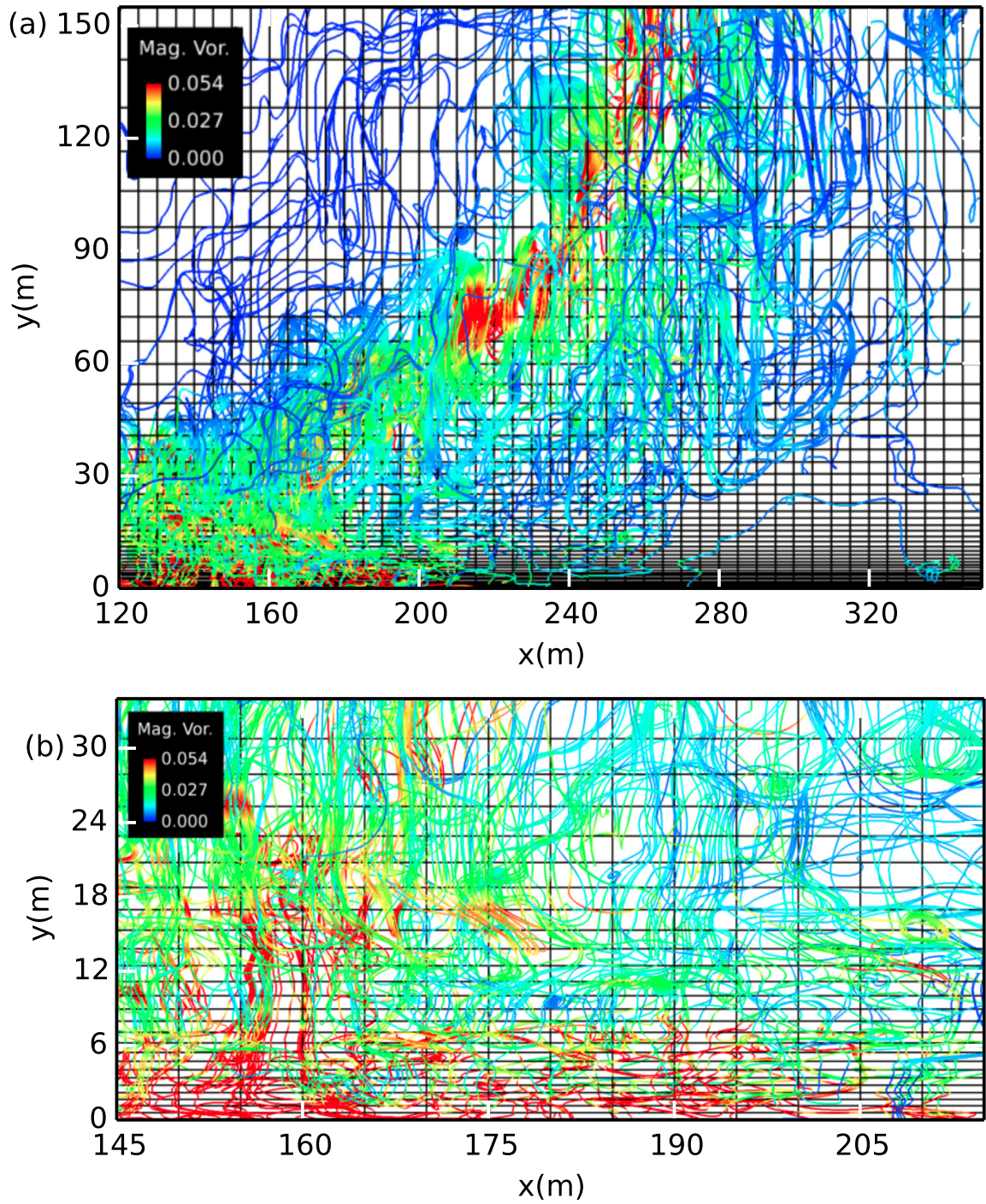


Figure 7.8: (a) Subgrid-scale streamlines at time 180 seconds and $z = 100$ m; (b) zoom-in of (a).

is seen that grid cells in higher regions of the atmosphere ($y = 150$ m) are fairly large, but small-scale behaviors can also be captured via the synthetic-velocity SGS. In addition, the amplitude of small-scale velocity is around $\mathcal{O}(10^0)$, which is even able to lift small firebrands, and it will be intriguing to consider this in subsequent studies. The amplitude of small-scale temperature is around $\mathcal{O}(10^{-1})$ – $\mathcal{O}(10^0)$, depending on positions in the flow field. It is seen that synthetic-velocity LES has the potential for combining resolved-scale and modeled results in a way that does not formally demand scale separation and, in general, provides direct interaction between large- and small-scale physics. It is noted that such details of different vortex structure of enhanced resolution below the large grid scale, which is not provided by most of the eddy-viscosity models or implicit LES (ILES), are available using synthetic-velocity LES.

7.3.2 Realistic terrain (simulation 3)

Figure 7.9 shows the terrain used for simulation 3. This terrain represents a small part of the Buckhorn mountain in Arizona. The elevation data is extracted from the WebGIS (Geographic Information Systems) with a resolution of ~ 30 m. The height of the terrain in the vertical direction is denoted by a color gradient in the legend. This height is transformed from the sea level elevation to the relative height from a chosen original point, for the sake of simplicity for computation. As seen from Fig. 7.9 (a) and (b), the terrain is raised from the lowest region in the corner formed by $x-$ and $z+$, to the highest region in the corner formed by $x+$ and $z-$. A fairly steep slope appears near the $x+$ and $z-$ corner and forms a mountain in a triangle shape with ~ 600 m above the original point. The slope or incline is relatively gentle at the bottom and at the top of the small mountain. For real computation, the elevation file (.dem) is first transformed into Plot3D format (.xyz), and then read into Pointwise (grid generation software [198]) to generate the grids used in simulation 3, with a

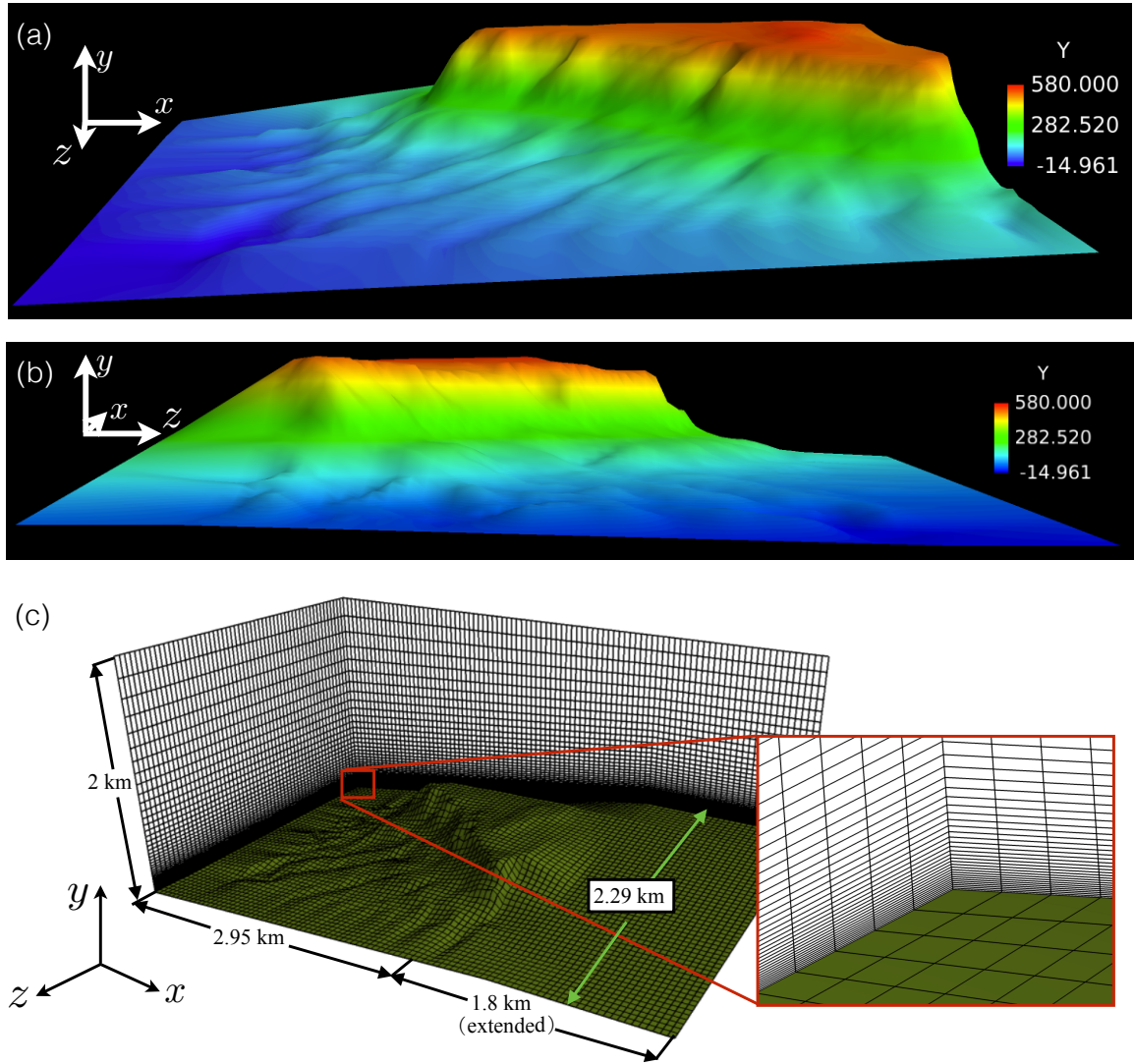


Figure 7.9: (a) Terrain viewed from z +; (b) terrain viewed from x +; (c) computational domain and grids

grid spacing of ~ 50 m, which is larger than the available resolution. Part (c) of Fig. 7.9 shows the computational domain and grids, as previously mentioned in Table 7.1. Undergrowth, tree trunks, and canopy are represented by the first grid cell (~ 1.5 m), second to eighth grids cells (~ 11 m), and eighth to fourteenth grid cells (~ 13 m), in y direction, respectively.

Figure 7.10 shows canopy fire spread at four different times: 6 s, 80 s, 160 s, 220 s. The iso-surfaces are indicated in the caption of Fig. 7.10. The fire is initiated in the canopy (8–14 grid cells) with a perpendicularly projected ignition line of 250 m in the z direction and 50 m in the x direction positioned in the downhill region of the terrain, as can be seen in part (a). The forest-green bottom represents a x - z plane within the canopy at $j = 12$ (12th grid cell in y direction), which still resembles the shape of the terrain. It is seen that fire spreads very rapidly in this case; the overall spread rate based on the fuels covered is estimated to be ~ 6 m/s, which is much greater than the cases of grassfire simulation 1 and a forest fire on flat terrain in simulation 2. However, it is considered qualitatively reasonable due to the fairly large inlet velocity (10 m/s for free stream), the large initial ignition region, and the uphill terrain—all leading to an intensely burning canopy.

Part (b) of Fig. 7.10 shows fire spread in the downhill region that is relatively flat. A fire plume is formed at this time (80 s). Six iso-surfaces of temperature are also seen, with lower temperatures (≤ 230 °C) appearing in the plume and higher temperatures (500 °C and 800 °C) shown in the burning crowns. Part (c) shows fire spread in the direction towards the nearest mountain area. As fire ascends the hill, it spreads even faster due to buoyancy effects. The puffs formed in the downhill region have pinched off from the smoky region and the large fire plume appears in the new fire front on the edge of the mountain. Part (d) shows that the fire has “climbed up” the mountain and further spreads on the top region. The spread rate on top of the mountain is expected to be similar to that in the downhill region since the top is also

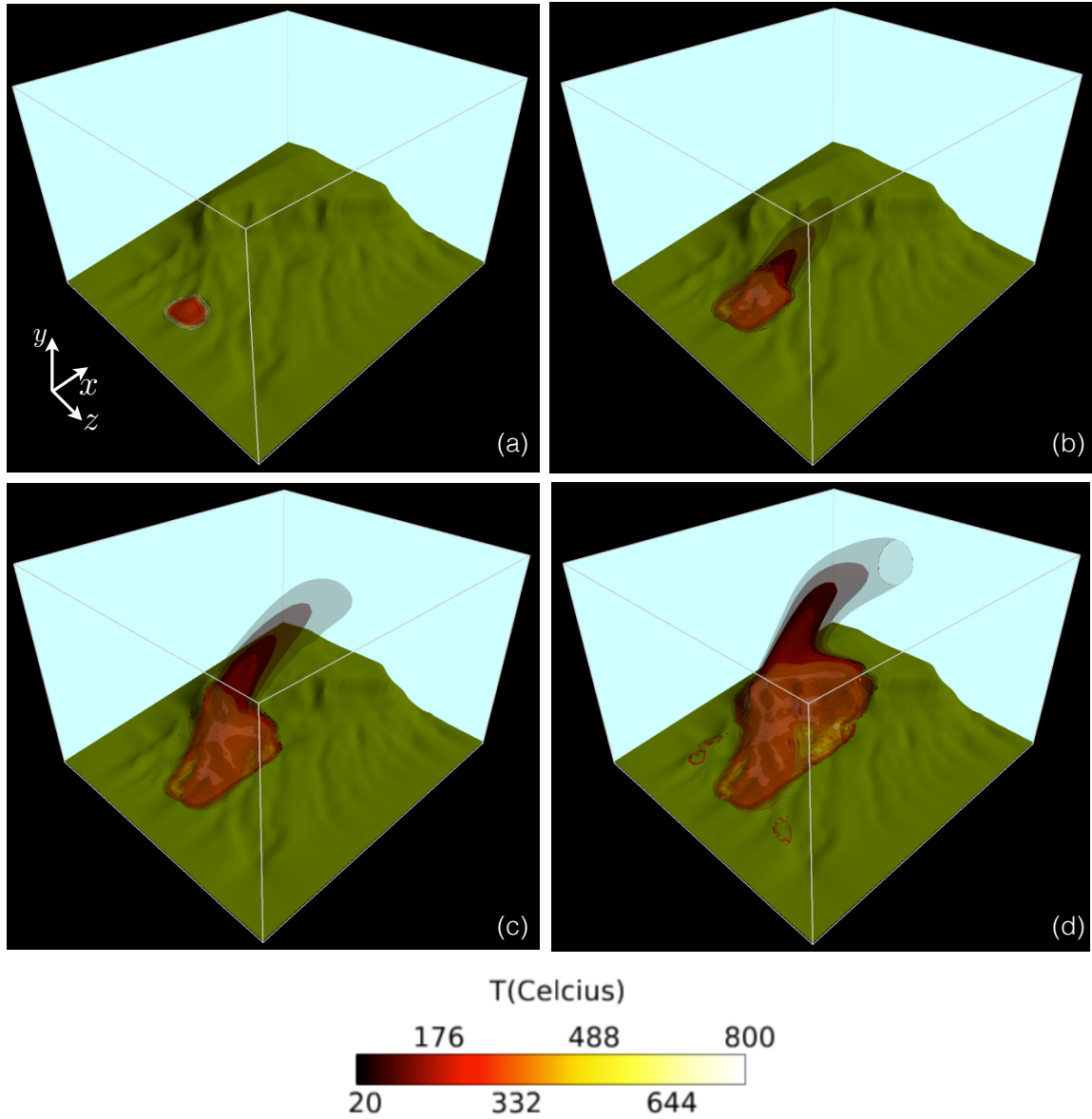


Figure 7.10: Iso-surfaces of temperature (transparency): 63°C (87.5%), 100°C (75%), 160°C (75%), 230°C (62.5%), 500°C (50%), 800°C (0%) for canopy fire burn at times: (a) 6 seconds; (b) 80 seconds; (c) 160 seconds; (d) 220 seconds.

relatively flat. As time evolves, fire plumes are further deformed with greater height and higher temperature. In general, fire plumes in Fig. 7.10 are much higher (~ 1500 m) than plumes shown in previous simulations considering the same lowest iso-surface temperature, indicating a more intensely burning fire on a meso-scale terrain. In addition, an increasing area of yellow-green is also seen (maybe not quite obvious) in the downhill region as time evolves, especially in part (d). This indicates that non-consecutive crown fuels are ignited, similar to the “holes” observed in Fig. 7.6. Since these regions mainly exist in concave areas, fire spreads much slower due to buoyancy. On the other hand, it is seen that the high temperature 800°C mainly exists in areas with bulges, also because of buoyancy. The irregular shape of “holes” and the 800°C temperature iso-surface also indicate some intricate turbulent behaviors within the canopy.

Figure 7.11 shows small-scale behaviors of the mountain fire in correspondence to part (d) of Fig. 7.10, but with a much smaller region on top of the mountain. Note that small-scale temperature values range between $\mathcal{O}(10^0)$ – $\mathcal{O}(10^1)^\circ\text{C}$ although a rather small range of values is used in the legend in Fig. 7.11 (a) in order to demonstrate more noticeable details. This magnitude of temperature fluctuations is expected to influence the large-scale temperature to some extent, but maybe moderately, compared with the forest fire temperature ($\mathcal{O}(10^2)$ – $\mathcal{O}(10^3)^\circ\text{C}$). It is seen in part (a) that temperature fluctuations are quite intense up to $y = 654$ m into the atmosphere, and several stable puffs are present up to a higher region. Part (b) shows streamlines corresponding to part (a). Vortices with various sizes and structures are present with larger vorticity magnitude appearing in the region below $y = 654$ m, which is about the same region in part (a) with intense and chaotic fluctuations. The non-flickering plumes shown in the higher region of Fig. 7.11 (a) is also reflected in the large-scale behavior in Fig. 7.10 (d), but with more irregular details, as seen in Fig. 7.11 (b). Large-scale turbulent behaviors are not demonstrated in fire plumes in

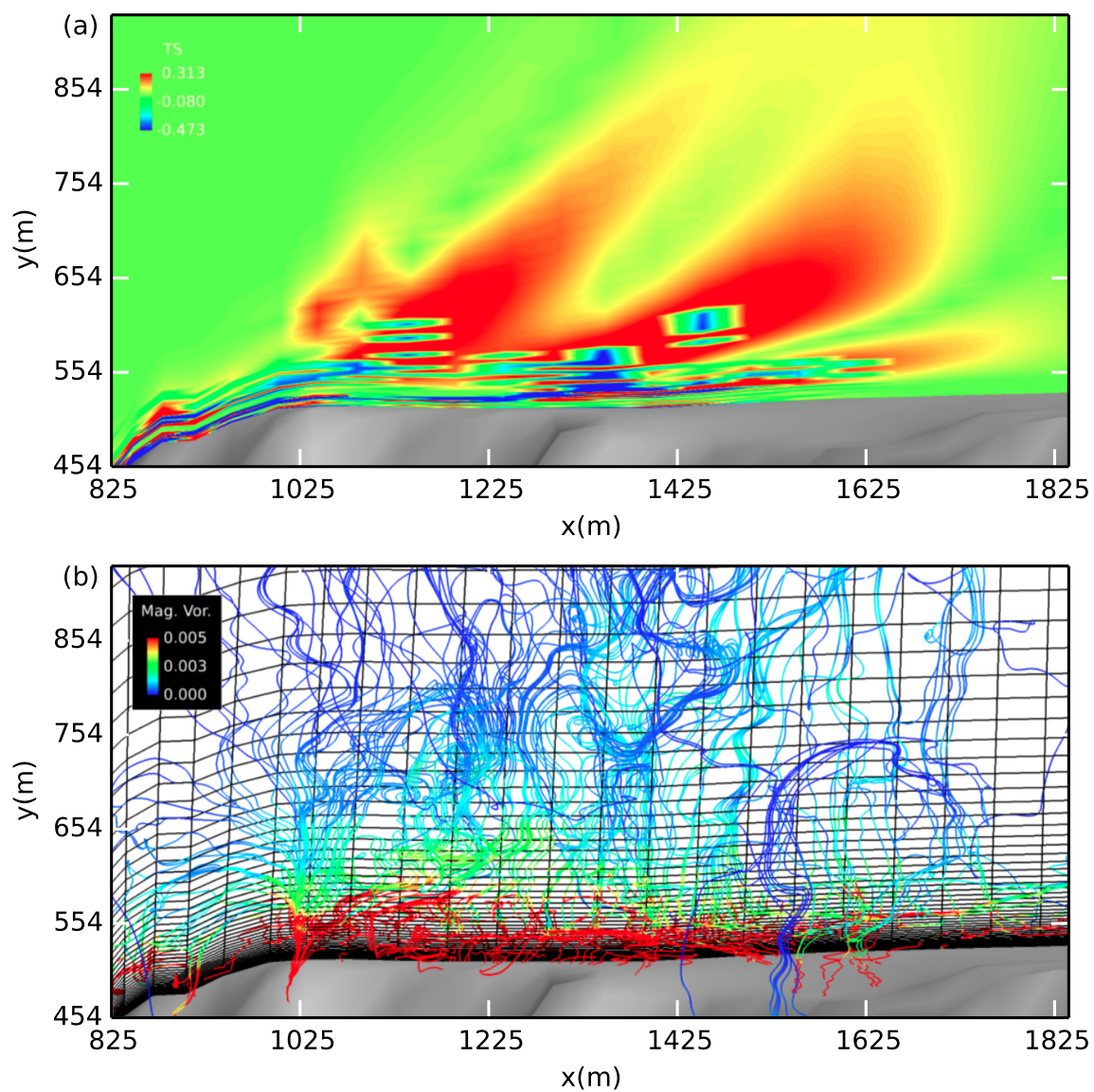


Figure 7.11: Small-scale behaviors at $z=145$ m: (a) Small-scale temperature contours; (b) Small-scale streamlines.

this meso-scale case (Fig. 7.10), implying that grid spacings of 50 m in x , z directions or/and 1.5–167 m in y direction may be too large to capture the small-scale behaviors. Note that grid spacings of 20 m in x and z directions, 1.5–40 m in y direction have also been attempted for a forest fire spread on a $2\text{ km} \times 2\text{ km} \times 2\text{ km}$ flat terrain (not shown here), but large-scale turbulence is still not present, even with different scalings of small-scale variables for synthetic-velocity LES. Since the small-scale part of the synthetic-velocity is dependent on the high-pass filtered velocity calculated from the large-scale grids, adjusting the scalings may not be sufficient. Figure 7.11 may suggest that grid spacings in y direction need to be further refined at the expense of more computation time.

7.4. Forest fire with firebrands (simulation 4)

As discussed in Ch. 3, Sec. 3.6, firebrands have large effects on wildfire spread. In particular, they play an important role in the transition from canopy fire to surface fire through the “landing” phase, and/or surface fire to canopy fire through the “lofting and transport” phase. In the current work, several numerical experiments are conducted to observe the influence of the fire-induced circulations and eddies in the LES on the trajectories of combusting spherical firebrand particles. The ignition region of simulation 4 is the same as that of simulation 2. Both one-way coupling (fixed flow field) and two-way coupling (time-dependent flow field) cases are investigated.

In all experiments, firebrands are released randomly from burning fuels in the canopy. Specifically, a certain number of random and non-repetitive grid points are chosen from grid cells in the canopy that are identified as “burning.” The coordinates of these chosen grids are used as initial positions for the firebrands. The burn time of such fuels required for launching firebrands can also be specified in the code. Firebrand sizes collected from real wildfires or observed from experiments (see [57] and [184]) are $\sim 5\text{--}50$ mm in diameter (for cylinder), or in thickness (for shingle).

Spherical particles of diameter $d_{fb}=50$ mm were used here. Since firebrands are often of irregular shape with embers from leaves, twigs, or branches, the spherical firebrand particles are assumed to be porous, with a porosity of approximately 0.96. The projected cross-sectional area of the particle A_{fb} is calculated to be 0.002 m^2 divided by the porosity. Assume the density of the particle is 400 kg/m^3 (Table 7.2), the initial mass is calculated as $\sim 0.00105 \text{ kg}$, which is similar to values used in [184] in milligrams units, and in [57]. Air density of 1.086 kg/m^3 at a temperature of 40°C is used to calculate the drag coefficient. The mass loss rate, diameter regression rate of a combusting particle, convective and radiative heat transfer, and other air properties are as described in Sec. 3.6. Other firebrand properties are provided in Table 7.2.

Table 7.2: Firebrand properties.

Property	Value
Density, Sycamore	400 kg/m^3
Specific heat, wood	1.466 kJ/kg/K
Emissivity, wood	0.95
Burning rate constant	$4.8 \times 10^{-7} \text{ m}^2/\text{s}$

Figure 7.12 shows firebrand trajectories within a fixed flow field at 100 s of simulation 4. At this time, many fuel particles in the canopy are burning, as seen from the high temperature (orange) in the upper part in Fig. 7.12 (a). A number of 200 firebrands were released randomly from the canopy at one time (100 s) in order to mimic a real intense wildfire. The number of firebrand generation is not thoroughly studied yet, but a range of 2–584 brands is obtained from an example of firebrand collection results in house-burning tests [57], and a number of 45 firebrands were used in [176] for numerical computations. Part (a) also shows that firebrands are lifted through the fire plume. Plumes at the two sides (z direction) lift firebrands much higher with parabolic-like trajectories, while plumes in the middle region lift firebrands only to lower altitudes with trajectories exhibiting more curvature. Most

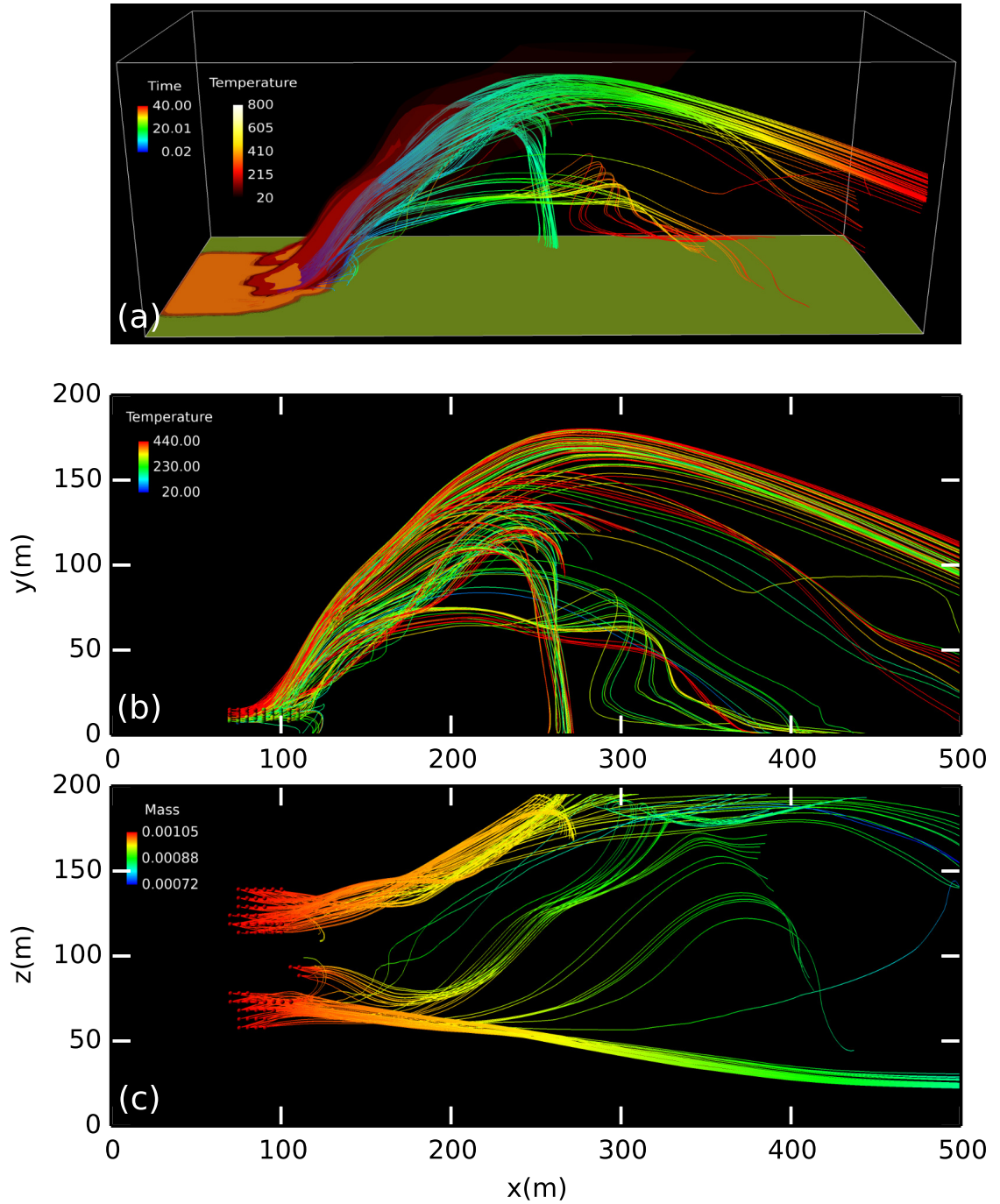


Figure 7.12: Firebrand trajectories (200) at 100 sec. of simulation 4: (a) 3-D depiction of firebrands with coloring in travel time (second); iso-surfaces of temperature (transparency): 100 °C (75%), 160 °C (75%), 230 °C (62.5%), 500 °C (0%), 600 °C (0%) (b) side view of the trajectories with coloring in temperature; (c) top view of the trajectories with coloring in mass.

firebrands fly towards the downwind boundary of the domain with a travel time of over 40 s, except for those which fell to the ground in the middle of the domain (x direction) with a lifetime of ~ 20 s.

Part (b) of Figure 7.12 shows a sideview of part (a). It is seen that firebrands are launched from different heights in the canopy. Firebrands lifted higher travel further. The travel distance in the x direction ranges from ~ 20 m to over 440 m, which is mainly dependent on the releasing position (with different flow velocity) since the initial mass of the firebrands is the same. The initial temperature of these firebrands ranges from 230°C to 800°C according to releasing position. It is assumed that a temperature of roughly 440°C is sufficient to ignite unburned fuel once the firebrand lands since the average value of 440°C and 20°C is the ignition temperature of grass. Thus, Fig. 7.12 (b) shows that only a small number of firebrands are able to ignite unburned fuels. Part (c) of Fig. 7.12 is a top-view of these firebrands. The randomly chosen points are obvious when seen from above. More points are chosen from the two sides since fire burns more intense in these regions. It is seen that trajectories of firebrands are largely altered by the turbulent flow field, especially in the z direction, implying that a three-dimensional firebrand study, as performed here, is necessary. Also, since the mass of a firebrand decreases as it travels downwind due to combustion, firebrands traveling longer distances are lighter in weight, as expected. However, the lowest mass is still 68% ($\geq 24\%$ as discussed in Sec. 3.5) of the original mass, so extinction because of this does not usually occur.

Figure 7.13 displays trajectories of 200 randomly initiated firebrands in a different fixed flow field (150 s of simulation 4). It is seen in part (a) that fire at this time becomes more turbulent and more fuels in the canopy are burning. The fire plume is quite different from that shown in Fig. 7.12 (a). Accordingly, firebrand trajectories are different. Firebrands are not lifted as high as those in Fig. 7.12 because the plumes are more inclined in this case, and trajectories follow the shape of the plume.

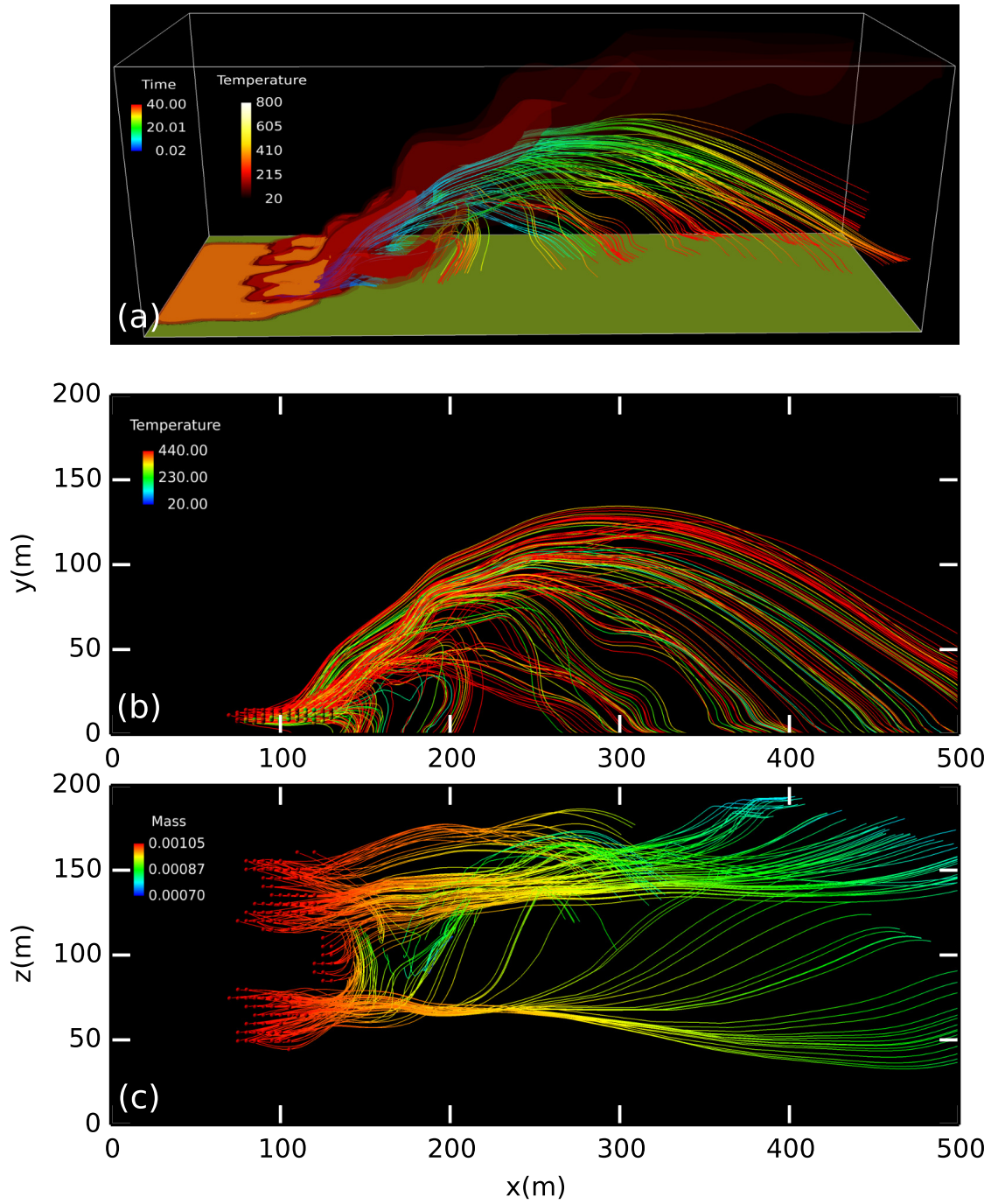


Figure 7.13: Firebrand trajectories (200) at 150 s of simulation 4: (a) 3-D depiction of firebrands with coloring in travel time (second); iso-surfaces of temperature (transparency): 100 °C (75%), 160 °C (75%), 230 °C (62.5%), 500 °C (0%), 600 °C (0%) (b) side view of the trajectories with coloring in temperature; (c) top view of the trajectories with coloring in mass.

Therefore, more firebrands will land on the ground with an airborne lifetime of only slightly over 40 s. Several firebrands also travel toward the downwind boundary for over 40 s. The sideview is shown in part (b). The travel distance in the x direction is more uniformly distributed than seen in Fig. 7.12 (b), with more irregular trajectories. Also, more firebrands have a temperature greater than 440°C when they land, since they have a higher initial temperature from the initial launching position. Part (c) shows a top-view of these firebrands analogous to part (c) of Fig. 7.12. Since more fuel particles in the canopy are available to release firebrands, the randomly chosen points are more evenly distributed and produce various trajectories, unlike in the previous case where firebrands are concentrated in areas with heavily burning crowns. Also, it is observed that firebrands released from the middle portion of the plume travel much shorter distances, and that all trajectories are altered by the fire-induced flow in the z direction.

Lastly, Fig. 7.14 presents a comparison of firebrands calculated in fixed (a) and time-dependent flow fields (b) (c). In both cases, only 20 firebrands are launched from the canopy for the sake of simplicity and clarity. The flow field shown in part (a) is at 100 s of simulation 4 (as in Fig. 7.12 (a)), but for only 20 trajectories calculated in this fixed flow field with an integration time of over 40 s. It is seen that only two firebrands fell to the ground, while all others exceeded either spanwise or horizontal boundaries.

Part (b) of Fig. 7.14 shows the temperature field at 120 s of simulation 4; but firebrands have been released at 100 s (as in Fig. 7.14 (a)), and trajectories are calculated along with the flow and temperature fields for 20 s. Note that the time shown in the legend also includes the cold flow calculation time before the initiation of a wildfire, as stated in Sec. 7.1. Trajectories in part (b) are different from those in part (a) for the first 20 s, not only because of effects from the evolving flow field, but also because of the difference in release points chosen in these two separate

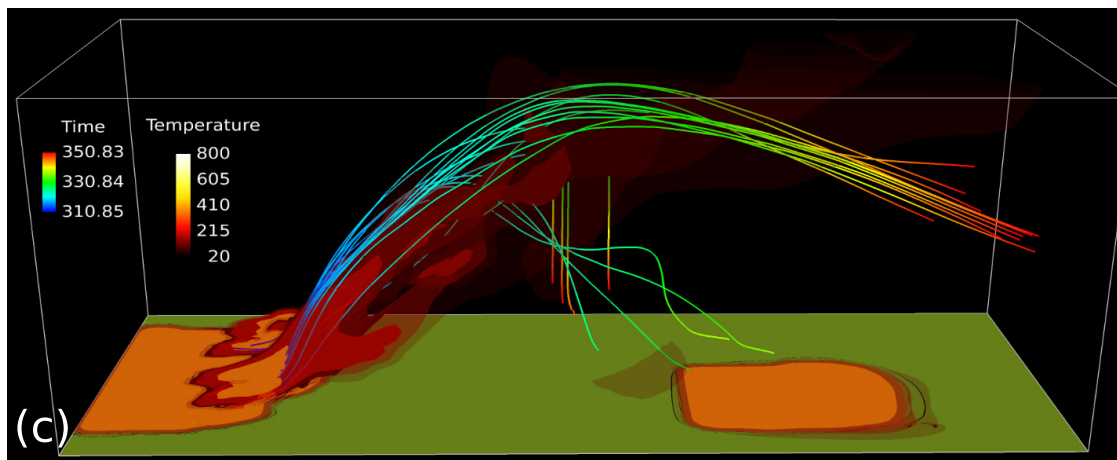
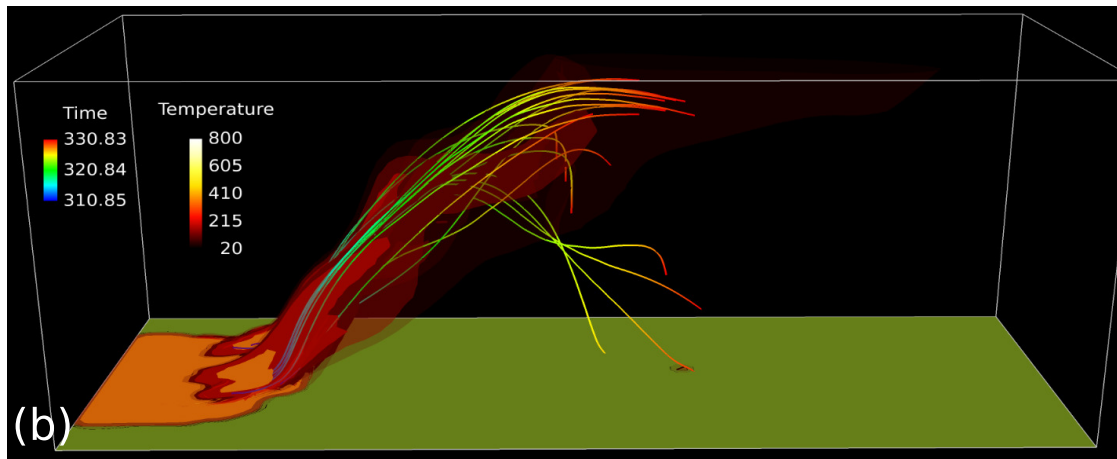
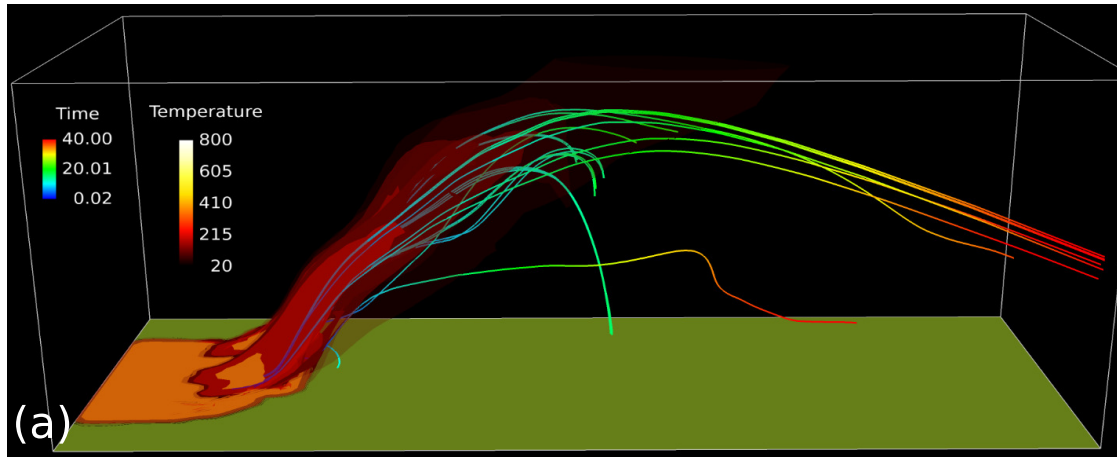


Figure 7.14: 3-D depiction of 20 firebrand trajectories with iso-surfaces of temperature (transparency): 100°C (75%), 160°C (75%), 230°C (62.5%), 500°C (0%), 600°C (0%): (a) in fixed flow field at 100 s with coloring in travel time; (b) in flow field at 20 s with coloring in temperature; (c) in flow field at 40 s with coloring in temperature.

calculations. In part (b), there are at least two firebrands that have landed although most have not. As is seen, one of the two firebrands has initiated a new fire since it has a temperature greater than 440°C , while the other does not. Part (c) shows temperature field at 140 s, and firebrand trajectories 40 s after launch. The flow and temperature fields have become much different by this time, but firebrand trajectories expected to be changed by the moving fluid flow is not noticeably seen. The trajectory is somewhat similar to part (a), but since firebrand launch points are different, the comparison is not rigorous. In addition, the fire ignited by the firebrand has spread a significant distance of ~ 100 m by this time, and the spread rate is much larger than that of the main fire. This is possibly because the fire plume has changed the whole computational flow field at this later time, and velocity at the undergrowth level is much larger—resulting in larger convective heat transfer and subsequent ignition and spread.

7.5. Summary and conclusions

In this chapter, four simulations are performed to provide an initial implementation of the forest fire modeling approach proposed in this study. First, grassland fire simulations are carried out by using three different ignition lines. These show good agreement with results with previous experiments and simulations, accounting for fire line shape and spread rates. Second, surface fire is ignited in a forest region. The transition from surface to canopy fire is presented. Canopy fire is also compared with grassfire. Third, the forest fire in a meso-scale domain is simulated. Large fire plumes due to buoyancy are predicted along with reasonable fire spread rates. Fourth, firebrands in a forest fire are investigated. Both fixed and time-dependent flow fields are used to calculate trajectories. Re-ignition due to firebrands is also studied.

It is concluded that the modeling approach is able to produce qualitatively (some quantitatively) correct fire spread results. Rather complicated vortices can be cap-

tured even on a rather course grids. The effect of canopy drag terms is also considered. The model incorporates physics that is important in real fire predictions. Simulation results are compared, in a qualitative way, to similar wildfire spread simulations or experiments, but not to actual forest fires, due to lack of “benchmark” results (which are difficult to obtain because of the complexity of wildfires.) It will be intriguing to further investigate details of several aspects of the model. Fire spread under different inlet flow velocities and heat sources (size, shape, number, positions) are to be investigated. Also, atmospheric boundary-layer velocity profiles with chaotic oscillations should be used for the inlet boundary conditions.

Chapter 8: Final Summary, Conclusions and Future Work

8.1. Summary

This dissertation will be summarized in the sequence of chapters it contains. After introducing wildland fires and the scope of current work in Ch. 1, a literature review of wildfire science and modeling is given in Ch. 2 in order to provide a context for the development and investigation of the wildfire model of this work. Several physical processes are introduced, e.g., ignition, heat transfer, and turbulence. In particular, it is learned that convective heat transfer may be dominant in wildfires. Wildfire models ranging from purely empirical to purely physical are discussed, with special attention given to turbulence modeling using RANS and LES.

A proposed wildfire spread model with several physics-based sub-models is discussed in detail in Ch. 3. The governing equation is the incompressible N.-S. equation in porous media with the Boussinesq approximation for buoyancy. Synthetic-velocity LES is employed for modeling turbulence. Porosities and heat release rates are estimated from extant botanical literature data. A rather comprehensive physical ignition modeling being used is introduced. Firebrand equations are also presented.

The flow-field solver is introduced in Ch. 3. The projection method is employed to maintain the divergence free constraint and generalized coordinates are used. In particular, solution and parallelization of both momentum equation and the pressure Poisson equation (PPE) are presented in detail. Douglas & Gunn [203] time splitting is used for the momentum and energy equations. Optimal point SOR is used for the (pseudo) PPE.

In Ch. 5, the poor man’s N.–S. (PMNS) equation in porous media is derived via a Galerkin procedure. A detailed numerical investigation focusing on the bifurcation parameters due to these additional terms is provided in the form of regime maps, time series, power spectra, phase portraits and basins of attraction, which indicate system behaviors in agreement with expected physical fluid flow through porous media.

Chapter 6 discusses a general porosity-permeability model. The model is derived based on a general non-equilibrium thermodynamic stability theory. The resulting formula is in a form similar to previous empirical equations, but with calculable coefficients. Both three-dimensional cubicle lid-driven cavity and natural convection problems have been computed for numerical investigations of its performance.

Computational results of wildfires are presented in Ch. 7. Both simple grassland fire and rather complex forest fires are simulated. Results of computed spread rates and fire front line are compared with available resources (experimental or numerical) with similar problem configurations, and results are found to be in reasonable agreement. Firebrand trajectories and ignition of spot fires for both fixed and time-dependent flow fields are calculated.

8.2. Conclusions

There are four main original contributions in this work, and conclusions are drawn from each of them. First, the current model produces reasonably accurate results with regards to wildfire line shape and spread rate, which agree well with previous experiments and simulations, but using coarser grids than utilized previously which still presenting complicated subgrid-scale behaviors. The proposed wildfire model and numerical scheme are capable of exhibiting important wildfire physics such as large buoyant plumes, fire whirls, and firebrand transport, incorporating effects of meteorology and topography. In particular, the difference between grassland and forest fires, the transition from surface to crown fires, and the effects of firebrands in

an evolving fluid flow field are presented. Also, the code is able to simulate meso-scale forest fires in a qualitative correct way. In addition, the synthetic-velocity LES incorporating the PMNS equations in porous media is able to produce complicated small-scale behaviors of wildfire to enhance resolution below the large-grid scale, and to capture the complex interaction of vegetation and atmosphere within and above porous media fuel beds. The general permeability model is also applied to the flow through forests producing damped velocities. Also, parallel performance of the ILES code for a typical fire spread problem implies a promising future of the current model for faster-than-real-time simulation without losing important physics. It is concluded that such a model has the potential to be a predicting tool for forest fire spread since it is based on the current understanding of physics and is implemented via parallelization.

Second, the PMNS equations in porous media derived from the generalized N.-S. equation is demonstrated to exhibit more complicated bifurcation behaviors, since it contains six additional bifurcation parameters beyond those of the original 3-D PMNS. These additional parameters can be calculated from porosity and permeability and are related to physical variables directly, which are different from closures required in usual turbulence modeling (e.g., RANS and typical LES). It is concluded that the PMNS equations for porous media have the potential to provide temporal fluctuations in SGS models for synthetic-velocity LES of turbulence through porous media; and this is demonstrated in the wildfire modeling results.

Third, the general permeability model calculates variable permeability through porosity, velocity strain rates, and effective viscosity. It can be simplified to the same form as the well-known K-C equation for laminar flows, but now with calculable coefficients. Also, it automatically satisfies the constraints relating porosity and permeability. It can potentially be used in general situations for flow in both homogeneous and inhomogeneous porous media since no additional empirical parameters

appear. Furthermore, variable permeabilities are obtained to account for influences from solid walls in the LDC problem. In the natural convection problem, noticeably different results are shown for velocity and temperature from those calculated with constant, fixed permeabilities, and these results are consistent with expected flow physics for situations with different porosities.

Fourth, it is found that point SOR with optimal parameter performs very well for parallelization of the PPE using OpenMP with regard to nearly-perfect linear speedups with increasing number of cores. The momentum and energy equations are parallelized with OpenMP in the context of the D–G time splitting method. The overall performance of this parallelization scheme is tested by employing a canonical lid-driven cavity (LDC) problem. It is found that OpenMP is quite efficient across cores since it does not require explicit information exchanges within the shared-memory architecture.

8.3. Future work

The wildfire modeling approach proposed in this work not only shows a promising future, but also has a fairly rigorous theoretical and mathematical underpinning for its sub-models. However, there is clearly much additional work to be done in order to develop such models to the point of operational status in real fire predictions. Therefore, an extensive study for each of the four aspects discussed in Sec. 8.2 is proposed.

First, it is noted that this comprehensive wildfire model with several novel sub-models is explorative and needs to be further tested. Field experiments with the same configuration and/or the previously well-documented wildfires can be used for more rigorous comparisons. The model should be tested under conditions such as different inflow velocity, ignition shape, forest moisture content, and atmospheric humidity. Also, planetary boundary layers with chaotic behavior (probably based on

the PMNS equations) are to be considered to add more realistic ingredients. Variable viscosity and thermal conductivity are also required to account for large temperature differences and non-unity tortuosities. More specific studies are proposed for firebrands and fire whirls such as firebrands launched by small fire whirls, and the intensity of fire whirls. In addition, in order to be operational, a forest fire model should also be able to predict density and distribution of smoke and effects of fire suppressants with faster-than-real-time simulations.

Second, the PMNS equation in porous media has been thoroughly discussed in terms of bifurcation behaviors, but its application in simple geometrical models has not been attempted. The application in wildfire scenarios shows qualitatively good results, but rigorous verification and evaluation of this model should also be conducted. Especially, comparisons of such a model with RANS and eddy-viscosity based LES methods are proposed. Furthermore, bifurcation behaviors of the PMNS equation with buoyancy and the energy equation in porous media should also be analyzed, as done in current work for cold flows. Qualitative or quantitative comparison for PMNS with and without porous media in the application of forest fires.

Third, results from the general permeability model for different fluid flow problems should be quantitatively verified by future experiments. The general model for calculating permeability of compressible flow should be obtained via the same derivation procedure. Also, the geometry-related effective viscosity should be further studied in the context of an inhomogeneous porous medium. Furthermore, this model has been applied to the problems of blood flow in choriocapillaris of the human eye and cerebrospinal fluid flow in brain tissue. The results are qualitatively correct, even without using empirical parameters. The strain rate results for blood flow compare quantitatively well with values obtained from experiments. Other applications, such as gas seepage and underground water flow, will be studied in the future.

Fourth, since only 16 cores within one node are used in this study, the scalability

of the parallelization model needs to be improved for implementation using many more cores. One possible solution is using hybrid OpenMP and MPI, but OpenMP needs an extra operation to work on distributed memory systems. Also, a comparison of SOR and multigrid methods under such parallelization should be performed.

Appendix

Source code for PPE parallelization

```
0      subroutine sor(sortlrnc,sorparm,icrtsn,maxitsor,msor,
1          nx,ny,nz,kregf,krega,ippe)
2      use three_d_data, only: mnx,mny,kstrt,klnth,nreg,jbs,
3          jts,kfs,kas,nregbrd,nmombdtp,amatrix,bmatrix,p3d
5      implicit real*8 (a-h,o-z)
6      msor = 0
7      ccc evaluate right-hand side of ppe
8      call rhsppe(icrtsn,kregf,krega,nx,ny,nz)
9      kreg = 1
10     jreg = 1
11     ireg = 1
12     il=nregbrd(ireg,jreg,kreg,1)
13     ir=nregbrd(ireg,jreg,kreg,2)
14     jb=nregbrd(ireg,jreg,kreg,3)
15     jt=nregbrd(ireg,jreg,kreg,4)
16     kf=nregbrd(ireg,jreg,kreg,5)
17     ka=nregbrd(ireg,jreg,kreg,6)
18     do m=1,maxitsor
19         dif = 0.d0
20     !$omp parallel private(i,j)
21     !$omp do
22         do j=jb+1, jt
23             do i=il+1,ir
24                 p3d(i,j,kf) =pijksor(ireg,jreg,kreg,kf,
25                     1          i,j,kf+1,nz,ippe)
26                 p3d(i,j,ka+1)= pijkasor(ireg,jreg,kreg,
27                     1          ka,i,j,ka,ippe)
28             end do
29         end do
30     !$omp end do
31     !$omp end parallel
32
33     !$omp parallel private(j,k)
34     !$omp do
35         do k=kf+1,ka
36             do j=jb+1, jt
37                 p3d(il,j,k) = pimjksor(ireg,jreg,kreg,il,il+1
38                     1          ,j,k,nx,ippe)
39                 p3d(ir+1,j,k) = piajksor(ireg,jreg,kreg,ir,
40                     1          i,j,k,ippe)
41             end do
42         end do
43     !$omp end do
44     !$omp end parallel
45
46     !$omp parallel private(i,k)
47     !$omp do
48         do k=kf+1,ka
49             do i=il+1,ir
```



```

50      p3d(i,jb,k) = pijmksor(ireg,jreg,kreg,jb,
1          i,jb+1,k,ny,ippe)
      p3d(i,jt+1,k) =pijaksor(ireg,jreg,kreg,
1          jt,i,jt,k,ippe)
      end do
55  end do
!$omp end do
!$omp end parallel

!$omp parallel
60 !$omp do private (i,j,k,ndx,dp3d,p3d0)
      do k=kf+1,ka
        do j=jb+1,jt
          do i=il+1,ir
            ndx = (k-2)*(ny-1)*(nx-1) + (j-2)*(nx-1)+i-1
65            p3d0=p3d(i,j,k)
            p3d(i,j,k) = (bmatrx(ndx) - amatrnx(ndx,1)*
1              p3d(i,j,k-1)-
1              amatrnx(ndx,7)*p3d(i,j,k+1)-
1              amatrnx(ndx,2)*p3d(i,j-1,k)-
70            amatrnx(ndx,6)*p3d(i,j+1,k)-
2              amatrnx(ndx,3)*p3d(i-1,j,k)-
1              amatrnx(ndx,5)*p3d(i+1,j,k))/amatrx(ndx,4)
            p3d(i,j,k) = p3d0*(1-sorparm)+ sorparm*p3d(i,j,k)
            dp3d=p3d(i,j,k)-p3d0
75            if(dabs(dp3d).gt.dif)dif = dabs(dp3d)
          end do
        end do
      end do

!$omp end do
80 !$omp end parallel
ccc      wtime = omp_get_wtime ( )-wtime
ccc      write(*,*)'wall time is', wtime
      if(m.gt.1.and.dif.lt.sortlrnc)then
        msor = m
85      return
      end if
    end do !---> end sor iterations
    msor = maxitsor
    write(*,*)'sor iterations failed to converge after',
90    1    msor,'iterations; maximum error is:', dif
    return
  end

```

Bibliography

- [1] F. E. Council. Guidance for implementation of federal wildland fire management policy. US Department of Agriculture and US Department of the Interior, Washington, D.C., USA, 2009.
- [2] S. Palley. Terra flamma. Photograph, 2014. Retrieved Aug 21, 2016 from the website <http://stuartpalley.photoshelter.com/index>.
- [3] S. M. Stein, J. Menakis, M. A. Carr, S. J. Comas, S. I. Stewart, H. Cleveland, L. Bramwell, and V. C. Radeloff. Wildfire, wildlands, and people: understanding and preparing for wildfire in the wildland-urban interface. Technical report, RMRS-GTR-299, US Department of Agriculture, 2013.
- [4] D. Guha-Sapir, F. Vos, R. Below, and S. Ponserre. Annual disaster statistical review 2010: The numbers and trends. Technical report, Centre for Research on the Epidemiology of Disasters, Université catholique de Louvain: Brussels, Belgium, 2011.
- [5] R. I. Emori and K. Saito. Model experiment of hazardous forest fire whirl. *Fire Technology*, **18**(4):319–327, 1982.
- [6] Statista. Number of fatalities due to major forest, brush or wild-fires between 1900 and 2016. Retrieved Aug 21, 2016 from the website <http://www.statista.com/statistics/234723/fatalities-due-to-the-most-significant-wildfires/>.
- [7] S. L. Stephens, J. K. Agee, P. Z. Fulé, M. P. North, W. H. Romme, T. W. Swetnam, and M. G. Turner. Managing forests and fire in changing climates. *Science*, **342**(6154):41–42, 2013.
- [8] C. Topik. Wildfires burn science capacity. *Science*, **349**(6254):1263–1263, 2015.
- [9] P. Tullis. Into the wildfire. The New York Times Magazine, September 19, 2013. Available from the website <http://www.nytimes.com/2013/09/22/magazine/into-the-wildfire.html?pagewanted=all&r=0>.
- [10] S. L. Stephens. Forest fire causes and extent on united states forest service lands. *International Journal of Wildland Fire*, **14**(3):213–222, 2005.
- [11] K. Miyanishi. *Forest Fires: Behavior and Ecological Effects*. Ed. Edward A. Johnson. Academic Press, 2001.
- [12] B. J. Stocks, M. E. Alexander, and R. A. Lanoville. Overview of the International Crown Fire Modelling Experiment (ICFME). *Canadian Journal of Forest Research*, **34**(8):1543–1547, 2004.

- [13] R. Linn, K. Anderson, J. Winterkamp, A. Brooks, M. Wotton, J. Dupuy, F. Pimont, and C. Edminster. Incorporating field wind data into FIRETEC simulations of the International Crown Fire Modeling Experiment (ICFME): preliminary lessons learned. *Canadian Journal of Forest Research*, **42**(5):879–898, 2012.
- [14] M. A. Finney, J. D. Cohen, S. S. McAllister, and W. M. Jolly. On the need for a theory of wildland fire spread. *International Journal of Wildland Fire*, **22**(1):25–36, 2013.
- [15] M. A. Finney, J. D. Cohen, J. M. Forthofer, S. S. McAllister, M. J. Gollner, D. J. Gorham, K. Saito, N. K. Akafuah, B. A. Adam, and J. D. English. Role of buoyant flame dynamics in wildfire spread. *Proceedings of the National Academy of Sciences*, **112**(32):9833–9838, 2015.
- [16] R. C. Rothermel. A mathematical model for predicting fire spread in wildland fuels. Research Paper INT-115, USDA Forest service, 1972.
- [17] J. L. Coen and P. J. Riggan. Simulation and thermal imaging of the 2006 Esperanza Wildfire in southern California: application of a coupled weather–wildland fire model. *International Journal of Wildland Fire*, **23**(6):755–770, 2014.
- [18] E. Kintisch. Computing a better fire forecast. *Science*, **341**(6146):609–611, 2013.
- [19] J. L. Coen, M. Cameron, J. Michalak, E. G. Patton, P. J. Riggan, and K. M. Yedinak. WRF-Fire: coupled weather–wildland fire modeling with the weather research and forecasting model. *Journal of Applied Meteorology and Climatology*, **52**(1):16–38, 2013.
- [20] K. McGrattan, S. Hostikka, R. McDermott, J. Floyd, C. Weinschenk, and K. Overholt. *Fire Dynamics Simulator Technical Reference Guide Volume 1: Mathematical Model*. NIST Special Publication 1018 Sixth Edition, 2013.
- [21] R. Linn, J. Reisner, J. J. Colman, and J. Winterkamp. Studying wildfire behavior using FIRETEC. *International Journal of Wildland Fire*, **11**(4):233–246, 2002.
- [22] E. Weinan and B. Engquist. Multiscale modeling and computation. *Notices of the AMS*, **50**(9):1062–1070, 2003.
- [23] J. M. McDonough, V. E. Garzón, and K. Saito. Parallel simulation of forest fire spread due to firebrand transport. In D. R. Emerson, J. Periaux, A. Ecer, N. Satofuka, and P. Fox, editors, *Parallel Computational Fluid Dynamics 1997: Recent Developments and Advances Using Parallel Computers*, pages 115–121. Elsevier, 1998.

- [24] J. M. McDonough and T. Yang. Parallel performance of a new model for wildland fire spread predictions. In G. Winter, A. Ecer, P. Fox, J. Periaux, and N. Satofuka, editors, *Parallel Computational Fluid Dynamics 2004: Multidisciplinary Applications*, pages 45–51. Elsevier, 2004.
- [25] W. L. Fons. Analysis of fire spread in light forest fuels. *Journal of Agricultural Research*, **72**(3):93–121, 1946.
- [26] R. O. Weber. Modelling fire spread through fuel beds. *Progress in Energy and Combustion Science*, **17**(1):67–82, 1991.
- [27] T. L. Clark, M. Griffiths, M. J. Reeder, and D. Latham. Numerical simulations of grassland fires in the northern territory, Australia: A new subgrid-scale fire parameterization. *Journal of Geophysical Research: Atmospheres*, **108**(D18), 2003.
- [28] M. A. Finney, J. Forthofer, et al. A study of flame spread in engineered cardboard fuelbeds: Part I: Correlations and observations. In K. Saito, A. Ito, Y. Nakamura, and K. Kuwana, editors, *Progress in Scale Modeling, Volume II*, pages 71–83. Springer, 2013.
- [29] B. A. Adam. *Incorporating Dynamic Flame Behavior into the Scaling Laws Wildland Fire Spread*. PhD dissertation, University of Kentucky, 2014.
- [30] T. D. of Agriculture. Fire behavior, fuels and topography. Texas Department of Agriculture Prescribed Burn School Manual v1.3 5-2002, Chapter 6, 2002. Available from the website http://campus.extension.org/file.php/475/ Fire_Characteristics_and_Behavior/Firebehavior-fuels.pdf.
- [31] I. Vermesi, N. Roenner, P. Pironi, R. M. Hadden, and G. Rein. Pyrolysis and ignition of a polymer by transient irradiation. *Combustion and Flame*, **163**:31–41, 2016.
- [32] V. Babrauskas. Ignition of wood: A review of the state of the art. *Journal of Fire Protection Engineering*, **12**(3):163–189, 2002.
- [33] J. D. Engstrom, J. K. Butler, S. G. Smith, L. L. Baxter, T. H. Fletcher, and D. R. Weise. Ignition behavior of live california chaparral leaves. *Combustion Science and Technology*, **176**(9):1577–1591, 2004.
- [34] V. Kuznetsov and A. Fil’kov. Ignition of various wood species by radiant energy. *Combustion, Explosion, and Shock Waves*, **47**(1):65–69, 2011.
- [35] R. E. Lyon and J. G. Quintiere. Criteria for piloted ignition of combustible solids. *Combustion and Flame*, **151**(4):551–559, 2007.

- [36] J. Torero. Flaming ignition of solid fuels. In M. J. Hurley and et al., editors, *SFPE Handbook of Fire Protection Engineering*, pages 633–661. Fifth edition, Springer, 2016.
- [37] D. Morvan, S. Méradji, and G. Accary. Physical modelling of fire spread in grasslands. *Fire Safety Journal*, **44**(1):50–61, 2009.
- [38] F. A. Albini. A model for fire spread in wildland fuels by-radiation. *Combustion Science and Technology*, **42**(5-6):229–258, 1985.
- [39] F. A. Albini. Wildland fire spread by radiation-a model including fuel cooling by natural convection. *Combustion Science and Technology*, **45**(1-2):101–113, 1986.
- [40] B. Butler, M. Finney, P. Andrews, and F. Albini. A radiation-driven model for crown fire spread. *Canadian Journal of Forest Research*, **34**(8):1588–1599, 2004.
- [41] P. G. Baines. Physical mechanisms for the propagation of surface fires. *Mathematical and Computer Modelling*, **13**(12):83–94, 1990.
- [42] M. A. Finney, J. D. Cohen, I. C. Grenfell, and K. M. Yedinak. An examination of fire spread thresholds in discontinuous fuel beds. *International Journal of Wildland Fire*, **19**(2):163–170, 2010.
- [43] R. I. Emori and K. Saito. A study of scaling laws in pool and crib fires. *Combustion Science and Technology*, **31**(5-6):217–231, 1983.
- [44] G. Pagnini and L. Massidda. Modelling turbulence effects in wildland fire propagation by the randomized level-set method. CRS4 Technical Report 2012/PM12a, 2014. Available from the website http://publications.crs4.it/pubdocs/2012/PM12a/pagnini_massidda-levelset.pdf.
- [45] W. E. Heilman and X. Bian. Turbulent kinetic energy during wildfires in the north central and north-eastern us. *International Journal of Wildland Fire*, **19**(3):346–363, 2010.
- [46] C. B. Clements, S. Zhong, X. Bian, W. E. Heilman, and D. W. Byun. First observations of turbulence generated by grass fires. *Journal of Geophysical Research: Atmospheres*, **113**(D22), 2008.
- [47] J. P. Strodbeck. *A Filter-Forcing Turbulence Model for Large Eddy Simulation Incorporating the Compressible ‘Poor Man’s Navier–Stokes Equations’*. PhD dissertation, University of Kentucky, 2012.
- [48] H. Tennekes and J. L. Lumley. *A First Course in Turbulence*. MIT press, 1972.

- [49] W. J. Bos and J.-P. Bertoglio. Dynamics of spectrally truncated inviscid turbulence. *Physics of Fluids (1994-present)*, **18**(7):071701, 2006.
- [50] U. Piomelli, W. H. Cabot, P. Moin, and S. Lee. Subgrid-scale backscatter in turbulent and transitional flows. *Physics of Fluids A: Fluid Dynamics (1989-1993)*, **3**(7):1766–1771, 1991.
- [51] D. W. Goens. *Fire Whirls*. National Weather Service, Western Region, 1978.
- [52] B. R. Morton. Geophysical vortices. *Progress in Aerospace Sciences*, **7**:145–194, 1966.
- [53] A. Y. Snegirev, J. Marsden, J. Francis, and G. Makhviladze. Numerical studies and experimental observations of whirling flames. *International Journal of Heat and Mass Transfer*, **47**(12):2523–2539, 2004.
- [54] M. A. Jenkins, T. Clark, and J. Coen. *Coupling Atmospheric and Fire Models*. Academic Press, San Diego, CA, USA, 2001.
- [55] A. M. Grishin. *Mathematical modeling of Forest Fires and New Methods of Fighting Them*. Publishing house of the Tomsk state university, Tomsk, Russia, 1997.
- [56] E. Pastor, L. Zarate, E. Planas, and J. Arnaldos. Mathematical models and calculation systems for the study of wildland fire behaviour. *Progress in Energy and Combustion Science*, **29**(2):139–153, 2003.
- [57] E. Koo, P. J. Pagni, D. R. Weise, and J. P. Woycheese. Firebrands and spotting ignition in large-scale fires. *International Journal of Wildland Fire*, **19**(7):818–843, 2010.
- [58] G. L. W. Perry. Current approaches to modelling the spread of wildland fire: a review. *Progress in Physical Geography*, **22**(2):222–245, 1998.
- [59] D. Morvan, M. Larini, J. L. Dupuy, P. Fernandes, A. I. Miranda, J. Andre, O. Sero-Guillaume, D. Calogine, and P. Cuinas. Behaviour modelling of wildland fires: a state of the art. EUFIRELAB (Rapport N° EVR1-CT-2002-40028/D-03-01), 2002. Available from the website <http://prodinra.inra.fr/record/17384>.
- [60] A. L. Sullivan. Wildland surface fire spread modelling, 1990–2007. 1: Physical and quasi-physical models. *International Journal of Wildland Fire*, **18**(4):349–368, 2009.
- [61] A. L. Sullivan. Wildland surface fire spread modelling, 1990–2007. 2: Empirical and quasi-empirical models. *International Journal of Wildland Fire*, **18**(4):369–386, 2009.

- [62] A. L. Sullivan. Wildland surface fire spread modelling, 1990–2007. 3: Simulation and mathematical analogue models. *International Journal of Wildland Fire*, **18**(4):387–403, 2009.
- [63] W. Mell, M. A. Jenkins, J. Gould, and P. Cheney. A physics-based approach to modelling grassland fires. *International Journal of Wildland Fire*, **16**(1):1–22, 2007.
- [64] T. Clark, M. Jenkins, J. Coen, and D. Packham. A coupled atmosphere-fire model: Role of the convective froude number and dynamic fingering at the fireline. *International Journal of Wildland Fire*, **6**(4):177–190, 1997.
- [65] T. L. Clark, J. Coen, and D. Latham. Description of a coupled atmosphere–fire model. *International Journal of Wildland Fire*, **13**(1):49–63, 2004.
- [66] I. Noble, A. Gill, and G. Bary. McArthur’s fire-danger meters expressed as equations. *Australian Journal of Ecology*, **5**(2):201–203, 1980.
- [67] A. G. McArthur. Weather and grassland fire behaviour. Forest Research Institute, Forest and Timber Bureau of Australia, Leaflet no. 100, Canberra., 1966.
- [68] N. Cheney, J. Gould, and W. R. Catchpole. Prediction of fire spread in grasslands. *International Journal of Wildland Fire*, **8**(1):1–13, 1998.
- [69] F. Williams. Mechanisms of fire spread. In *Symposium (International) on Combustion, Combustion Institute*, volume 16, pages 1281–1294. Elsevier, 1977.
- [70] W. H. Frandsen. Fire spread through porous fuels from the conservation of energy. *Combustion and Flame*, **16**(1):9–16, 1971.
- [71] P. L. Andrews. BehavePlus fire modeling system: past, present, and future. In *Proceedings of 7th Symposium on Fire and Forest Meteorology*. American Meteorological Society, 2007.
- [72] M. A. Finney. FARSITE: Fire Area Simulator–model development and evaluation. Technical report, USDA Forest service, 2004.
- [73] J. H. Balbi, F. Morandini, X. Silvani, J. B. Filippi, and F. Rinieri. A physical model for wildland fires. *Combustion and Flame*, **156**(12):2217–2230, 2009.
- [74] A. Sullivan, P. Ellis, and I. Knight. A review of radiant heat flux models used in bushfire applications. *International Journal of Wildland Fire*, **12**(1):101–110, 2003.
- [75] A. Grishin, A. Gruzin, and V. Zverev. Mathematical modeling of the spreading of high-level forest fires. *Soviet Physics, Doklady*, **28**(4):328–330, 1983.

- [76] F. A. Williams. Scaling mass fires. *Fire Research Abstracts and Reviews*, **11**(1):1–23, 1969.
- [77] J. G. Quintiere. Scaling applications in fire research. *Fire Safety Journal*, **15**(1):3–29, 1989.
- [78] S. Soma and K. Saito. Reconstruction of fire whirls using scale models. *Combustion and Flame*, **86**(3):269–284, 1991.
- [79] D. B. Spalding. Colloquium on modeling principles. In *Symposium (International) on Combustion*, *Combustion Institute*, volume 9, page 833, 1963.
- [80] M. Larini, F. Giroud, B. Porterie, and J.-C. Loraud. A multiphase formulation for fire propagation in heterogeneous combustible media. *International Journal of Heat and Mass Transfer*, **41**(6):881–897, 1998.
- [81] B. Porterie, J.-L. Consalvi, J.-C. Loraud, F. Giroud, and C. Picard. Dynamics of wildland fires and their impact on structures. *Combustion and Flame*, **149**(3):314–328, 2007.
- [82] D. Morvan and J. L. Dupuy. Modeling the propagation of a wildfire through a mediterranean shrub using a multiphase formulation. *Combustion and Flame*, **138**(3):199–210, 2004.
- [83] S. Meradji, G. Accary, D. Morvan, O. Bessonov, and D. Fougere. Numerical simulation of grassland-fires behavior using FIRESTAR3D model. In *Proceedings of Topical Problems of Fluid Mechanics*, 2016.
- [84] D. Morvan, C. Hoffman, F. Rego, and W. Mell. Numerical simulation of the interaction between two fire fronts in grassland and shrubland. *Fire Safety Journal*, **46**(8):469–479, 2011.
- [85] E. G. Patton. *Large-eddy Simulation of Turbulent Flow above and within a Plant Canopy*. PhD dissertation, University of California Davis, 1997.
- [86] T. Duman, G. G. Katul, M. B. Siqueira, and M. Cassiani. A velocity–dissipation lagrangian stochastic model for turbulent dispersion in atmospheric boundary-layer and canopy flows. *Boundary-Layer Meteorology*, **152**(1):1–18, 2014.
- [87] J. Smagorinsky. General circulation experiments with the primitive equations: I. the basic experiment*. *Monthly Weather Review*, **91**(3):99–164, 1963.
- [88] W. Mell, J. Charney, M. A. Jenkins, P. Cheney, and J. Gould. Numerical simulations of grassland fire behavior from the LANL-FIRETEC and NIST-WFDS models. In J. Qu, W. Sommers, R. Yang, A. Riebau, and M. Kafatos, editors, *Remote Sensing and Modeling Applications to Wildland Fires*, pages 209–225. Springer, 2013.

- [89] C. M. Hoffman, J. Canfield, R. R. Linn, W. Mell, C. H. Sieg, F. Pimont, and J. Ziegler. Evaluating crown fire rate of spread predictions from physics-based models. *Fire Technology*, **52**(1):221–237, 2016.
- [90] J. L. Coen. Simulation of the Big Elk Fire using coupled atmosphere–fire modeling. *International Journal of Wildland Fire*, **14**(1):49–59, 2005.
- [91] G. L. Achtemeier. Field validation of a free-agent cellular automata model of fire spread with fire–atmosphere coupling. *International Journal of Wildland Fire*, **22**(2):148–156, 2013.
- [92] U. Frisch. *Turbulence: the Legacy of AN Kolmogorov*. Cambridge university press, Cambridge, 1995.
- [93] D. C. Wilcox. *Turbulence Modeling for CFD*. 2nd edition, DCW industries, Inc., La Canada, CA, 1998.
- [94] V. Yakhot and S. A. Orszag. Renormalization-group analysis of turbulence. *Physical Review Letters*, **57**(14):1722, 1986.
- [95] Z. Li, H. Zhang, J. Hoagg, S. C. Bailey, and A. Martin. Turbulence simulation using direct gradient adaptive k- ω model. In *54th AIAA Aerospace Sciences Meeting, AIAA SciTech Forum, (AIAA 2016-0587)*, 2016.
- [96] J. W. Deardorff. A numerical study of three-dimensional turbulent channel flow at large reynolds numbers. *Journal of Fluid Mechanics*, **41**(02):453–480, 1970.
- [97] J. A. Domaradzki and E. M. Saiki. A subgrid-scale model based on the estimation of unresolved scales of turbulence. *Physics of Fluids (1994-present)*, **9**(7):2148–2164, 1997.
- [98] S. Basu and F. Porté-Agel. Large-eddy simulation of stably stratified atmospheric boundary layer turbulence: a scale-dependent dynamic modeling approach. *Journal of the Atmospheric Sciences*, **63**:2074–2091, 2005.
- [99] M. Germano. Turbulence: the filtering approach. *Journal of Fluid Mechanics*, **238**:325–336, 1992.
- [100] W. Thurston, K. J. Tory, R. J. Fawcett, and J. D. Kepert. Large-eddy simulations of bushfire plumes in the turbulent atmospheric boundary layer. In J. Piantadosi, R. Anderssen, and B. J., editors, *20th International Congress on Modelling and Simulation*, 2013.
- [101] J. Bardina, J. H. Ferziger, and W. C. Reynolds. Improved turbulence models based on large eddy simulation of homogeneous, incompressible, turbulent flows. AIAA Paper 80-1357, 1983.

- [102] S. Liu, C. Meneveau, and J. Katz. On the properties of similarity subgrid-scale models as deduced from measurements in a turbulent jet. *Journal of Fluid Mechanics*, **275**:83–119, 1994.
- [103] U. Piomelli, J. H. Ferziger, and P. Moin. Model consistency in large eddy simulation of turbulent channel flows. *Physics of Fluids*, **31**(7):1884, 1988.
- [104] C. Fureby and F. F. Grinstein. Large eddy simulation of high-reynolds-number free and wall-bounded flows. *Journal of Computational Physics*, **181**(1):68–97, 2002.
- [105] S. Stolz and N. A. Adams. An approximate deconvolution procedure for large-eddy simulation. *Physics of Fluids (1994-present)*, **11**(7):1699–1701, 1999.
- [106] P. Sagaut. *Large Eddy Simulation for Incompressible Flows*. Springer, 2002.
- [107] J. A. Domaradzki and N. A. Adams. Direct modelling of subgrid scales of turbulence in large eddy simulations. *Journal of Turbulence*, **3**(024):1, 2002.
- [108] A. R. Kerstein. Linear-eddy modelling of turbulent transport. part 3. mixing and differential molecular diffusion in round jets. *Journal of Fluid Mechanics*, **216**:411–435, 1990.
- [109] T. Echekki, A. R. Kerstein, T. D. Dreeben, and J.-Y. Chen. ‘One-dimensional turbulence’ simulation of turbulent jet diffusion flames: model formulation and illustrative applications. *Combustion and Flame*, **125**(3):1083–1105, 2001.
- [110] J. M. McDonough, Y. Yang, and E. C. Hylin. Modeling time-dependent turbulent flow over a backward-facing step via additive turbulent decomposition and chaotic algebraic maps. In *Proc. First Asian Computational Fluid Dynamics Conference*, pages 747–752, Hong Kong, 1995.
- [111] E. C. Hylin. *A Stochastic Model for Small-Scale Turbulence*. PhD dissertation, University of Kentucky, 1997.
- [112] R. N. Meroney. Fires in porous media: natural and urban canopies. In Y. A. Gayev and J. C. Hunt, editors, *Flow and Transport Processes in Complex Obstructed Geometries: from Cities and Vegetative Canopies to Industrial Problems*, pages 271–310. Springer, 2007.
- [113] V. E. Garzon, J. M. McDonough, and K. Saito. Time-dependent model of forest fire spread in turbulent gusting winds. In N. R. Keltner, N. J. Alvares, and S. J. Grayson, editors, *Very Large-Scale Fires*. ASTM International, 1998.
- [114] O. Séro-Guillaume and J. Margerit. Modelling forest fires. Part I: a complete set of equations derived by extended irreversible thermodynamics. *International Journal of Heat and Mass Transfer*, **45**(8):1705–1722, 2002.

- [115] P. Nithiarasu, K. N. Seetharamu, and T. Sundararajan. Natural convective heat transfer in a fluid saturated variable porosity medium. *International Journal of Heat and Mass Transfer*, **40**(16):3955–3967, 1997.
- [116] D. A. Nield. Modelling fluid flow in saturated porous media and at interfaces. In D. B. Ingham and I. Pop, editors, *Transport Phenomena in Porous Media II*, pages 1–19. Elsevier Science, Oxford, 2002.
- [117] D. A. Nield and A. Bejan. *Convection in Porous Media*. Springer-Verlag, New York, 2006.
- [118] H. Brinkman. A calculation of the viscous force exerted by a flowing fluid on a dense swarm of particles. *Applied Scientific Research*, **1**(1):27–34, 1949.
- [119] J. Bear and Y. Bachmat. *Introduction to modeling of transport phenomena in porous media*, volume 4. Springer Science & Business Media, 2012.
- [120] E. Spiegel and G. Veronis. On the boussinesq approximation for a compressible fluid. *The Astrophysical Journal*, **131**:442, 1960.
- [121] D. D. Gray and A. Giorgini. The validity of the boussinesq approximation for liquids and gases. *International Journal of Heat and Mass Transfer*, **19**(5):545–551, 1976.
- [122] C. K. Law. *Combustion Physics*. Cambridge University Press, 2006.
- [123] H. Darcy. *Les Fontaines Publiques de la Ville de Dijon*. Victor Dalmont, Paris, 1856.
- [124] T. Tang and J. M. McDonough. A theoretical model for the porosity-permeability relationship. *International Journal of Heat and Mass Transfer*, **103**:984–996, 2016.
- [125] D. D. Joseph, D. A. Nield, and G. Papanicolaou. Nonlinear equation governing flow in a saturated porous medium. *Water Resources Research*, **18**(4):1049–1052, 1982.
- [126] S. Ergun. Fluid flow through packed columns. *Chemical Engineering Progress*, **48**:89–94, 1952.
- [127] K. Hooman, F. Hooman, and S. R. Mohebpour. Entropy generation for forced convection in a porous channel with isoflux or isothermal walls. *International Journal of Exergy*, **5**(1):78–96, 2008.
- [128] S. Whitaker. *The Method of Volume Averaging*. Dordrecht: Kluwer Academic Publishers, 1999.

- [129] K. Sbutega. *Modeling and Optimization of Spatially Evolving Heat Sinks Using Volume Averaging Theory*. PhD dissertation, University of California Los Angeles, 2015.
- [130] V. Travkin and I. Catton. Transport phenomena in heterogeneous media based on volume averaging theory. *Advances in Heat Transfer*, **34**:1–144, 2001.
- [131] E. Weinan and B. Engquist. The heterognous multiscale methods. *Communications in Mathematical Sciences*, **1**(1):87–132, 2003.
- [132] E. C. Hylin and J. M. McDonough. Chaotic small-scale velocity fields as prospective models for unresolved turbulence in an additive decomposition of the Navier-Stokes equations. *International Journal of Fluid Mechanics Research*, **26**(5-6), 1999.
- [133] J. M. McDonough. A different approach to large-eddy simulation with advantages for computing turbulence-chemical kinetics interactions. In K. Matsuno and et al., editors, *Parallel Computational Fluid Dynamics 2002: New Frontiers and Multi-Disciplinary Applications*, pages 23–32, Amsterdam, 2002.
- [134] J. M. McDonough and T. Yang. A new SGS LES model applied to an internally-heated, swirling buoyant plume. In *Western States Section, Combustion Institute*, Los Angeles, 2003.
- [135] W. Zeng. Low-order discrete dynamical system for H₂-air finite-rate combustion process. Master’s thesis, University of Kentucky, 2015.
- [136] J. M. McDonough. Lectures on computational numerical analysis of partial differential equations. Available from the website <http://www.engr.uky.edu/~acfd/me690-lctr-nts.pdf>, 2008.
- [137] J. M. McDonough. *Introductory Lectures on Turbulence Physics, Mathematics and Modeling*, 2007. Available from the website <https://www.engr.uky.edu/~acfd/lctr-notes634.pdf>.
- [138] F. G. Shuman. Numerical methods in weather prediction: II. smoothing and filtering. *Monthly Weather Review*, **85**(11):357–361, 1957.
- [139] Z. Liu, Q. Huang, Z. Zhao, and J. Yuan. Optimized compact finite difference schemes with high accuracy and maximum resolution. *International Journal of Aeroacoustics*, **7**(2):123–146, 2008.
- [140] J. Bardina, J. H. Ferziger, and W. Reynolds. Improved subgrid-scale models for large-eddy simulation. In *American Institute of Aeronautics and Astronautics, Fluid and Plasma Dynamics Conference, 13th, Snowmass, Colo., July 14-16, 1980, 10 p.*, volume 1, 1980.

- [141] W. Liu. Investigation of filtering methods for large-eddy simulation. Master's thesis, University of Kentucky, 2014.
- [142] J. M. McDonough. A 'synthetic scalar' subgrid-scale model for large-eddy simulation of turbulent combustion. In *Spring Technical Meeting Central States Section, Combustion Institute*, pages 7–9, Knoxville, TN, 2002.
- [143] J. M. McDonough and J. C. Holloway. An alternative approach to subgrid-scale modeling of LES of turbulent combustion. In *Proceedings of Third Joint Meeting of the US Sections, Combustion Institute*, The University of Illinois at Chicago, IL, 2003.
- [144] J. M. McDonough and M. T. Huang. A 'poor man's Navier–Stokes equation': derivation and numerical experiments—the 2-D case. *International Journal for Numerical Methods in Fluids*, **44**(5):545–578, 2004.
- [145] S. Bible and J. M. McDonough. Basins of attraction of the two-dimensional 'poor man's Navier–Stokes equation'. *International Journal of Bifurcation and Chaos*, **14**(07):2381–2386, 2004.
- [146] J. M. McDonough, S. Bible, and J. Scoville. Response to strain rate in a discrete dynamical system model of the high-wavenumber Navier–Stokes equations. *Journal of Turbulence*, **4**(4):25, 2003.
- [147] J. Polly. Numerical experiments of the 3-D 'poor man's Navier–Stokes equations'. Master's thesis, University of Kentucky, 2011.
- [148] J. B. Polly and J. M. McDonough. Application of the poor man's navier-stokes equations to real-time control of fluid flow. *Journal of Applied Mathematics*, **2012**, 2012.
- [149] J. M. McDonough. Three-dimensional poor man's Navier–Stokes equation: A discrete dynamical system exhibiting $k^{-5/3}$ inertial subrange energy scaling. *Physical Review E*, **79**(6):065302, 2009.
- [150] J. P. Strodtbeck, J. M. McDonough, and P. D. Hislop. Characterization of the dynamical behavior of the compressible 'poor man's Navier–Stokes equations'. *International Journal of Bifurcation and Chaos*, **22**(01):1230004, 2012.
- [151] A. Bejan. *Convection in Porous Media*. Wiley Online Library, 1999.
- [152] B. Pekin and C. Macfarlane. Measurement of crown cover and leaf area index using digital cover photography and its application to remote sensing. *Remote Sensing*, **1**(4):1298–1320, 2009.
- [153] M. E. Dubrasich, D. W. Hann, and J. C. Tappeiner II. Methods for evaluating crown area profiles of forest stands. *Canadian Journal of Forest Research*, **27**(3):385–392, 1997.

- [154] H. Eriksson, L. Eklundh, K. Hall, and A. Lindroth. Estimating LAI in deciduous forest stands. *Agricultural and Forest Meteorology*, **129**(1):27–37, 2005.
- [155] S. C. Thomas and W. E. Winner. Leaf area index of an old-growth Douglas-fir forest estimated from direct structural measurements in the canopy. *Canadian Journal of Forest Research*, **30**(12):1922–1930, 2000.
- [156] E. F. Frank. Crown volume estimates. Technical report, The Native Tree Society, 2010.
- [157] E. Witkowski and B. B. Lamont. Leaf specific mass confounds leaf density and thickness. *Oecologia*, **88**(4):486–493, 1991.
- [158] L. B. Leopold. Trees and streams: the efficiency of branching patterns. *Journal of Theoretical Biology*, **31**(2):339–354, 1971.
- [159] K. J. Niklas. Size-dependent allometry of tree height, diameter and trunk-taper. *Annals of Botany*, **75**(3):217–227, 1995.
- [160] T. Satoo and H. A. L. Madgwick. *Forest Biomass*. Martinus Nijhoff/Dr. W. Junk Publishers, The Hague, Boston, London, 1982.
- [161] K. J. Niklas. Plant height and the properties of some herbaceous stems. *Annals of Botany*, **75**(2):133–142, 1995.
- [162] D. A. Dokken and L. C. Hulbert. Effect of standing dead plants on stem density in bluestem prairie. In D. C. Glenn-Lewin and R. Q. J. Landers, editors, *Fifth Midwest Prairie Conference*, pages 78–81. Iowa State University, Ames, Iowa, 1976.
- [163] H. Biteau, T. Steinhaus, A. Simeoni, C. Schemel, G. Marlair, N. Bal, and J. L. Torero. Calculation methods for the heat release rate of materials of unknown composition. Technical report, International Association for Fire Safety Science, 2008.
- [164] S. McAllister and M. Finney. The effect of wind on burning rate of wood cribs. *Fire Technology*, **52**(4):1035–1050, 2016.
- [165] C. Heskestad. Modeling of enclosure fires. In *Symposium (International) on Combustion, Combustion Institute*, volume 14, pages 1021–1030, 1972.
- [166] Phyllis2. database for biomass and waste. Energy research Centre of the Netherlands, Available from the website <https://www.ecn.nl/phyllis2/>.
- [167] H. C. Tran and R. H. White. Burning rate of solid wood measured in a heat release rate calorimeter. *Fire and Materials*, **16**(4):197–206, 1992.

- [168] L. Orloff and J. De Ris. Froude modeling of pool fires. In *Symposium (International) on Combustion, Combustion Institute*, volume 19, pages 885–895. Elsevier, 1982.
- [169] K. Himoto and T. Tanaka. Transport of disk-shaped firebrands in a turbulent boundary layer. In M. A. Boston, D. T. Gottuk, and B. Y. Lattimer, editors, *Proceedings of Eighth International Symposium on Fire Safety Science, International Association for Fire Safety Science (IAFSS)*, pages 18–23, 2005.
- [170] C. Countryman. Heat—its role in wildland fire, part 3: heat conduction and wildland fire. Technical report, USDA Forest service, 1978.
- [171] P. F. Ellis. *The Aerodynamic and Combustion Characteristics of Eucalypt Bark: a Firebrand Study*. PhD dissertation, The Australian National University, 2000.
- [172] N. Sardoy, J.-L. Consalvi, B. Porterie, and A. C. Fernandez-Pello. Modeling transport and combustion of firebrands from burning trees. *Combustion and Flame*, **150**(3):151–169, 2007.
- [173] A. Tohidi, N. Kaye, and W. Bridges. Statistical description of firebrand size and shape distribution from coniferous trees for use in Metropolis Monte Carlo simulations of firebrand flight distance. *Fire Safety Journal*, **77**:21–35, 2015.
- [174] S. L. Manzello, A. Maranghides, and W. E. Mell. Firebrand generation from burning vegetation. *International Journal of Wildland Fire*, **16**(4):458–462, 2007.
- [175] S. L. Manzello, A. Maranghides, J. R. Shields, W. E. Mell, Y. Hayashi, and D. Nii. Measurement of firebrand production and heat release rate (HRR) from burning Korean pine trees. *Fire Safety Science*, **7**:108–108, 2007.
- [176] S. Bhutia, M. Ann Jenkins, and R. Sun. Comparison of firebrand propagation prediction by a plume model and a coupled-fire/atmosphere large-eddy simulator. *Journal of Advances in Modeling Earth Systems*, **2**(1), 2010.
- [177] E. Koo, R. R. Linn, P. J. Pagni, and C. B. Edminster. Modelling firebrand transport in wildfires using HIGRAD/FIRETEC. *International Journal of Wildland Fire*, **21**(4):396–417, 2012.
- [178] D. T. Stephen and A. C. Fernandez-Pello. On the flight paths of metal particles and embers generated by power lines in high winds—a potential source of wildland fires. *Fire Safety Journal*, **30**(4):333–356, 1998.
- [179] A. Haider and O. Levenspiel. Drag coefficient and terminal velocity of spherical and nonspherical particles. *Powder Technology*, **58**(1):63–70, 1989.
- [180] P. K. Kundu and I. M. Cohen. *Fluid Mechanics*. Fourth Edition, Burlington, MA: Elsevier Inc, 2008.

- [181] R. Montgomery. Viscosity and thermal conductivity of air and diffusivity of water vapor in air. *Journal of Meteorology*, **4**(6):193–196, 1947.
- [182] R. S. Davuluri, H. Zhang, and A. Martin. Numerical study of spallation phenomenon in an arc-jet environment. *Journal of Thermophysics and Heat Transfer*, **30**(1):32–41, 2015.
- [183] N. Frössling. Über die verdunstung fallender tropfen. *Gerlands Beiträge zur Geophysik*, **52**:170–215, 1938.
- [184] C. S. Tarifa. *Transport and Combustion of Firebrands*. Instituto Nacional de Tecnica Aeroespacial Esteban Terradas, 1967.
- [185] J. M. McDonough, T. Yang, and M. Sheetz. Parallelization of a modern CFD incompressible turbulent flow code. In A. Ecer, N. Satofuka, J. Periaux, and P. Fox, editors, *Parallel Computational Fluid Dynamics 2003: Advanced Numerical Methods Software and Applications*, pages 473–479. Elsevier, 2004.
- [186] O. Bessonov, V. Brailovskaya, V. Polezhaev, and B. Roux. Parallelization of the solution of 3D Navier-Stokes equations for fluid flow in a cavity with moving covers. In V. Malyskin, editor, *Parallel Computing Technologies Third International Conference (PaCT-95)*, pages 385–399. Springer, 1995.
- [187] L. Dagum and R. Menon. OpenMP: an industry standard API for shared-memory programming. *Computational Science & Engineering, IEEE*, **5**(1):46–55, 1998.
- [188] J. Leray. Etude de diverses équations intégrales non linéaires et de quelques problèmes que pose l’hydrodynamique. *Thèses françaises de l’entre-deux-guerres*, **142**:1–82, 1933.
- [189] A. J. Chorin. On the convergence of discrete approximations to the navier-stokes equations. *Mathematics of computation*, **23**(106):341–353, 1969.
- [190] J. Kim and P. Moin. Application of a fractional-step method to incompressible navier-stokes equations. *Journal of computational physics*, **59**(2):308–323, 1985.
- [191] P. M. Gresho. On the theory of semi-implicit projection methods for viscous incompressible flow and its implementation via a finite element method that also introduces a nearly consistent mass matrix. Part 1: Theory. *International Journal for Numerical Methods in Fluids*, **11**(5):587–620, 1990.
- [192] M. Fortin, R. Peyret, and R. Temam. Résolution numérique des équations de navier-stokes pour un fluide incompressible. *J. Mécanique*, **10**(3):357–390, 1971.

- [193] J. B. Bell, P. Colella, and H. M. Glaz. A second-order projection method for the incompressible navier-stokes equations. *Journal of Computational Physics*, **85**(2):257–283, 1989.
- [194] N. N. Yanenko. *The Method of Fractional Steps*. Springer, 1971.
- [195] F. H. Harlow and J. E. Welch. Numerical calculation of time-dependent viscous incompressible flow of fluid with free surface. *Physics of Fluids*, **8**(2182), 1965.
- [196] J. M. McDonough. *Lectures in Computational Fluid Dynamics of Incompressible Flow: Mathematics, Algorithms and Implementations*, 2007. Available from the website <http://www.engr.uky.edu/~acfd/me691-lctr-nts.pdf>.
- [197] J. Shen. On error estimates of some higher order projection and penalty-projection methods for navier-stokes equations. *Numerische Mathematik*, **62**(1):49–73, 1992.
- [198] Pointwise v17.1 release 4 [computer software]. Available from the website: <http://www.pointwise.com/>.
- [199] J. F. Thompson, Z. U. Warsi, and C. W. Mastin. *Numerical grid generation: foundations and applications*, volume 45. North-holland Amsterdam, 1985.
- [200] S. Patankar. *Numerical Heat Transfer and Fluid Flow*. CRC press, 1980.
- [201] W. F. Ames. *Numerical Methods for Partial Differential Equations*. Academic Press, 1992.
- [202] L. V. Kantorovich and G. P. Akilov. *Functional Analysis*. Pergamon Press, Oxford, 1982.
- [203] J. Douglas and J. E. Gunn. A general formulation of alternating direction methods. *Numerische Mathematik*, **6**(1):428–453, 1964.
- [204] J. M. McDonough and S. J. Dong. 2-D to 3-D Conversion for Navier—Stokes Codes: Parallelization Issue. In C. Jenssen, T. Kvamdal, H. Andersson, P. F. B. Pettersen, N. Satofuka, A. Ecer, and J. Periaux, editors, *Parallel Computational Fluid Dynamics 2000: Trends and Applications*, 2000.
- [205] D. M. Young. *Iterative Solution of Large Linear Systems*. Elsevier, 2014.
- [206] O. Axelsson. *Iterative Solution Methods*. Cambridge university press, 1996.
- [207] Y. Saad. *Iterative Methods for Sparse Linear Systems*. Siam, 2003.
- [208] D. D. McCracken. *Computing for Engineers and Scientists with Fortran 77*. John Wiley & Sons, Inc., 1984.
- [209] B. Stroustrup. *The C++ Programming Language*. Pearson Education India, 1986.

- [210] T. Tang, W. Liu, and J. M. McDonough. Parallelization of linear iterative methods for solving the 3-D pressure Poisson equation using various programming languages. *Procedia Engineering*, **61**:136–143, 2013.
- [211] G. Accary, O. Bessonov, D. Fougère, S. Meradji, and D. Morvan. *Optimized parallel approach for 3D modelling of forest fire behaviour*. Springer, 2007.
- [212] A. Basumallik, S.-J. Min, and R. Eigenmann. Programming distributed memory systems using OpenMP. In *2007 IEEE International Parallel and Distributed Processing Symposium*, pages 1–8. IEEE, 2007.
- [213] T. Tang, Z. Li, J. M. McDonough, and P. D. Hislop. Numerical investigation of the “poor man’s navier–stokes equations” with darcy and forchheimer terms. *International Journal of Bifurcation and Chaos*, **26**(05):1650086, 2016.
- [214] C. Hutter, A. Zenklusen, S. Kuhn, and P. R. von Rohr. Large eddy simulation of flow through a streamwise-periodic structure. *Chemical engineering science*, **66**(3):519–529, 2011.
- [215] R. B. Kazerooni and S. K. Hannani. Simulation of turbulent flow through porous media employing a v2f model. *Sci. Iran., Trans. B*, **16**(2):159–167, 2009.
- [216] F. Kuwahara, T. Yamane, and A. Nakayama. Large eddy simulation of turbulent flow in porous media. *International Communications in Heat and Mass Transfer*, **33**(4):411–418, 2006.
- [217] J. Ward. Turbulent flow in porous media. *Journal of the Hydraulics Division*, **90**(5):1–12, 1964.
- [218] N. Ahmed and D. K. Sunada. Nonlinear flow in porous media. *Journal of the Hydraulics Division*, **95**(6):1847–1858, 1969.
- [219] P. Venkataraman and P. R. M. Rao. Darcian, transitional, and turbulent flow through porous media. *Journal of Hydraulic Engineering*, **124**(8):840–846, 1998.
- [220] R. M. May. Simple mathematical models with very complicated dynamics. *Nature*, **261**(5560):459–467, 1976.
- [221] J. Kozeny. *Über Kapillare Leitung des Wassers im Boden:(Aufstieg, Versickerung und Anwendung auf die Bewässerung)*. Hölder-Pichler-Tempsky, Vienna, 1927.
- [222] P. C. Carman. Permeability of saturated sands, soils and clays. *Journal of Agricultural Science*, **29**(02):262–273, 1939.

- [223] M. J. Feigenbaum. Quantitative universality for a class of nonlinear transformations. *Journal of Statistical Physics*, **19**(1):25–52, 1978.
- [224] D. Ruelle and F. Takens. On the nature of turbulence. *Communications in Mathematical Physics*, **20**(3):167–192, 1971.
- [225] J. Gollub and S. Benson. Many routes to turbulent convection. *Journal of Fluid Mechanics*, **100**(03):449–470, 1980.
- [226] P. Bergé, Y. Pomeau, and C. Vidal. *Order within Chaos*. Wiley and Sons, New York, 1984.
- [227] S. A. Bible. Study of the ‘poor man’s Navier–Stokes’ equation turbulence model. Master’s thesis, University of Kentucky, 2003.
- [228] E. V. Mueller, W. Mell, and A. Simenoi. Large eddy simulation of forest canopy flow for wildland fire modeling. *Canadian Journal of Forest Research*, **44**(12):1534–1544, 2014.
- [229] F. Coletti, K. Muramatsu, D. Schiavazzi, C. J. Elkins, and J. K. Eaton. Fluid flow and scalar transport through porous fins. *Physics of Fluids*, **26**(5):055104, 2014.
- [230] A. Liakopoulos. Darcy’s coefficient of permeability as a symmetric tensor of second rank. *Transactions of the ASAE*, **8**(2):216–0218, 1965.
- [231] G. A. Bayles, G. E. Klinzing, and S.-H. Chiang. Fractal mathematics applied to flow in porous systems. *Particle & Particle Systems Characterization*, **6**(1-4):168–175, 1989.
- [232] A. Costa. Permeability-porosity relationship: A reexamination of the Kozeny–Carman equation based on a fractal pore-space geometry assumption. *Geophysical Research Letters*, **33**(2), 2006.
- [233] E. Rodriguez, F. Giacomelli, and A. Vazquez. Permeability-porosity relationship in RTM for different fiberglass and natural reinforcements. *Journal of Composite Materials*, **38**(3):259–268, 2004.
- [234] P. Glansdorff and I. Prigogine. Non-equilibrium stability theory. *Physica*, **46**(3):344–366, 1970.
- [235] P. Glansdorff and I. Prigogine. *Thermodynamic Theory of Structure, Stability and Fluctuations*. John Wiley & Sons Ltd, 1971.
- [236] A. Liapunov, V. Pliss, and F. Abramovici. *Stability of Motion*. Elsevier, 1967.
- [237] A. Bejan and J. Kestin. Entropy generation through heat and fluid flow. *Journal of Applied Mechanics*, **50**:475, 1983.

- [238] A. C. Clairaut. *Théorie de la Figure de la Terre, Tirée des Principes de L’Hydrostatique*. Paris Courcier, 1743.
- [239] W. Breugem. The effective viscosity of a channel-type porous medium. *Physics of Fluids*, **19**(10):103104–103104, 2007.
- [240] Z. Guo and T. Zhao. Lattice Boltzmann model for incompressible flows through porous media. *Physical Review E*, **66**(3):036304, 2002.
- [241] S. Albensoeder and H. C. Kuhlmann. Accurate three-dimensional lid-driven cavity flow. *Journal of Computational Physics*, **206**(2):536–558, 2005.
- [242] T. R. Mahapatra, D. Pal, and S. Mondal. Natural convection in a lid-driven square cavity filled with Darcy-Forchheimer porous medium in the presence of thermal radiation. *International Journal of Nonlinear Science*, **11**(3):366–379, 2011.
- [243] E. Tric, G. Labrosse, and M. Betrouni. A first incursion into the 3D structure of natural convection of air in a differentially heated cubic cavity, from accurate numerical solutions. *International Journal of Heat and Mass Transfer*, **43**(21):4043–4056, 2000.
- [244] D. C. Wan, B. S. V. Patnaik, and G. W. Wei. A new benchmark quality solution for the buoyancy-driven cavity by discrete singular convolution. *Numerical Heat Transfer: Part B: Fundamentals*, **40**(3):199–228, 2001.
- [245] R. H. Shaw and U. Schumann. Large-eddy simulation of turbulent flow above and within a forest. *Boundary-Layer Meteorology*, **61**(1-2):47–64, 1992.
- [246] T. Yamada. A numerical model study of turbulent airflow in and above a forest canopy. *Journal of the Meteorological Society of Japan*, **60**:439–454, 1982.
- [247] P. Aumond, V. Masson, C. Lac, B. Gauvreau, S. Dupont, and M. Berengier. Including the drag effects of canopies: real case large-eddy simulation studies. *Boundary-Layer Meteorology*, **146**(1):65–80, 2013.
- [248] R. Shaw, G. Den Hartog, and H. Neumann. Influence of foliar density and thermal stability on profiles of reynolds stress and turbulence intensity in a deciduous forest. *Boundary-Layer Meteorology*, **45**(4):391–409, 1988.
- [249] S. Dupont, J.-M. Bonnefond, M. R. Irvine, E. Lamaud, and Y. Brunet. Long-distance edge effects in a pine forest with a deep and sparse trunk space: in situ and numerical experiments. *Agricultural and Forest Meteorology*, **151**(3):328–344, 2011.
- [250] J. Finnigan. Turbulence in plant canopies. *Annual Review of Fluid Mechanics*, **32**(1):519–571, 2000.

- [251] G. Crasto. *Numerical Simulations of the Atmospheric Boundary Layer*. PhD dissertation, Università di Cagliari, 2007.

Tingting Tang

Professional Preparation

Ph.D. Student, Mechanical Engineering, University of Kentucky, Lexington, Kentucky, USA, Aug. 2011-pres.

Bachelor of Engineering, Energy and Power Engineering, Central South University, Changsha, Hunan Province, China, Sept. 2007 -Jun. 2011

Journal Article

T. Tang, J. M. McDonough, “Parallel performance of an implicit LES code for wild-fire spread,” *Procedia Engineering*, 2016 (under review).

T. Tang and J. M. McDonough. A theoretical model for the porosity-permeability relationship. *International Journal of Heat and Mass Transfer*, **103**:984-996, 2016.

T. Tang, Z. Li, J. M. McDonough, and P. D. Hislop. Numerical investigation of the “poor man’s Navier–Stokes equations” with Darcy and Forchheimer terms. *International Journal of Bifurcation and Chaos*, **26**(05):1650086, 2016.

T. Tang, W. Liu, and J. M. McDonough. Parallelization of linear iterative methods for solving the 3-D pressure Poisson equation using various programming languages. *Procedia Engineering*, **61**:136-143, 2013.

Conference Abstracts:

J. M. McDonough, T. Tang, Wildfire simulation using LES with synthetic-velocity SGS models, 69th American Physical Society Division of Fluid Dynamics Meeting, Portland, OR, Nov. 20-22, 2016.

T. Tang, J. M. McDonough, Parallel performance of an implicit LES code for wild-land fire spread, 28th International Conference on Parallel CFD, Kobe, Japan, May 9-12, 2016 (peer reviewed).

J. M. McDonough, D. Bradley, T. Tang, Investigation of a porous media model for blood flow in the choriocapillaris of the human eye, 8th International Conference on Porous Media, Cincinnati, Ohio, May 9-12, 2016.

T. Tang, J. M. McDonough, A general permeability model for incompressible flow through porous media, 41th Dayton-Cincinnati Aerospace Sciences Symposium, Day-

ton, OH, Mar. 2, 2016.

T. Tang, J. M. McDonough, Improved parallelization of an implicit large-eddy simulation code with OpenMP, 27th International Conference on Parallel CFD, Montreal, Canada, May 17-21, 2015 (peer reviewed).

P. Gao, T. Tang, J. M. McDonough, CFD of the mammalian lymphatic system, 27th International Conference on Parallel CFD, Montreal, Canada, May 17-21, 2015 (peer-reviewed).

P. Gao, T. Tang, J. M. McDonough, Glymphatic system simulation, 40th Dayton-Cincinnati Aerospace Sciences Symposium, Dayton, OH, Mar. 4, 2015.

B. Alipova, T. Tang, J. M. McDonough, Optimal SOR parameters for non-Dirichlet elliptic boundary-value problem, 40th Dayton-Cincinnati Aerospace Sciences Symposium, Dayton, OH, Mar. 4, 2015.

J. M. McDonough, T. Tang, A theoretical relationship between porosity and permeability, 67th American Physical Society Division of Fluid Dynamics Meeting, San Francisco, CA, Nov. 23-25, 2014.

J. M. McDonough, T. Tang Parallelization of an implicit large eddy simulation code with OpenMP, 26th International Conference on Parallel Computational Fluid Dynamics, Trondheim, Norway, May 20-22, 2014 (peer reviewed).

T. Tang, Weiyun Liu, J. M. McDonough, Parallelization of linear iterative methods for solving the 3-D pressure Poisson equation using various programming languages, 25th International Conference on Parallel Computational Fluid Dynamics, Changsha, Hunan, May 20-24, 2013 (published)

T. Tang, J. M. McDonough, The exploration of a general relationship between porosity and permeability, presented at the 38th Dayton-Cincinnati Aerospace Symposium, Dayton, OH, Mar. 6, 2013.

Honors and Certificate:

Lyman T. Johnson Academic Year Fellowship, University of Kentucky (2013–2016)

The Graduate Certificate in Computational Fluid Dynamics, University of Kentucky (received in 12/2013)

Teaching Experience:

Teaching Assistant, Department of Mechanical Engineering, University of Kentucky (9/2011–12/2016)